Spinel-Type Transition Metal Oxides as Heterogeneous Water Oxidation Catalysts

---

Dissertation

zur

Erlangung der naturwissenschaftlichen Doktorwürde
(Dr. sc. nat.)

vorgelegt der

Mathematisch-naturwissenschaftlichen Fakultät

der

Universität Zürich

von

Karla Lienau

von

Aadorf TG

Promotionskommission

Prof. Dr. Greta R. Patzke (Vorsitz und Leitung der Dissertation)
Prof. Dr. David Tilley
Prof. Dr. Anthony Linden

Zürich, 2020

Table of Contents

Abstract

Water oxidation, the bottleneck of the water splitting reaction, requires the development of stable, economic but also efficient water oxidation catalysts. Spinel-type Co_3O_4 is amongst the most promising materials in this context, due to its low cost and robustness. However, there is not only one clearly defined, unique compound referred to as Co_3O_4: the material in fact can exhibit very different characteristics, with respect to crystallinity, defects, doping, particle size, oxidation state, or surface area, just to name the most important ones. These parameters were found to largely influence the catalytic behavior of the corresponding spinels and they can be tuned by varying and adapting the synthetic conditions. Therefore, three different approaches were applied throughout this thesis to investigate the influence of synthesis parameters on the emerging spinels and the resulting relationships between materials properties and catalytic activity.

First, spinel-type Co_3O_4 materials prepared by nine different, well-established synthetic protocols are compared. The resulting cobalt oxides were characterized with a wide range of analytical methods, including XAS, XPS, PXRD, Raman, BET, and TEM to investigate the connections between materials properties and efficient catalysis. Going beyond most literature reports, the catalytic activity was tested with all of the three typical water oxidation methods: electrocatalytically, chemically and photocatalytically. Different activity trends were found for the three test methods. Whereas no clear influence of the synthetic protocol on the electrocatalytic activity was evident, the chemical and photocatalytic approaches showed significant differences between the samples. Especially for chemical water oxidation, the importance of the surface area, the increase in disorder and the decrease in oxidation states of the materials exhibited by samples synthesized at lower temperatures, was unequivocal.

The next study was in fact a close-up investigation, following up on the previous one: microwave hydrothermal synthesis, which is a very attractive and time-saving synthesis method that can accelerate reaction times and reduce reaction temperatures significantly, was applied. Hence, the parameters were varied only within a single preparative approach. The resulting spinels were examined with respect to materials characteristics like crystallinity, oxidation state and surface area with various analytical methods. Furthermore, their water oxidation activity in electrocatalytic and chemical oxidation setups was investigated. For both oxidation methods the same trends regarding the synthesis parameters were found, showing higher activity for lower synthesis temperatures, lower precursor concentrations, addition of hydrogen peroxide and shorter ramping and reaction time.

In the last part of this thesis, synergistic effects between cobalt and other transition metals as well as the influence of the addition of redox inert gallium ions into the spinel matrix were studied. Especially the incorporation of around one third of iron was slightly beneficial for the water oxidation activity. However, most metal combinations were not able to compete with the plain Co_3O_4 matrix, also not with the use of Ga^{3+} as a redox-inert mimic of Ca^{2+} in photosystem II.

Interestingly, metallic cobalt, which was formed as a side product in one synthesis, increased the activity significantly and was shown to exhibit considerable water oxidation abilities. These results merit deeper investigations with respect to the interplay and relative activities of cobalt materials with oxidic and metallic properties.

Overall, the influence of spinel properties, which were varied through synthesis conditions or starting materials, on different approaches of catalytic water oxidation is reported in the main part of this thesis. It was shown that less-crystalline materials with more defects and higher surface area exhibit the highest water oxidation activities. All in all, the investigations demonstrate that both preparative approach and selected water oxidation test assays can exert substantial influence on the catalytic activity and assessment of cobalt oxide catalysts. These results are significant for future comparative studies on the optimization of oxide-based water oxidation catalysts with respect to technical applications.

Acknowledgement

In the course of my PhD thesis, I received a lot of help and support in all possible ways from many people; professors, co-workers, students, technical employees and of course friends and family. Therefore, I want to thank everyone mentioned in the following.

I especially want to acknowledge Prof. Greta Patzke, who enabled me to work on this topic as a PhD in her group and was very supportive throughout the whole time, be it with advice on research problems, new input and ideas, technical issues as well as with personal topics. Furthermore, I want to thank Prof. David Tilley and Prof. Anthony Linden for being supportive, straightforward and uncomplicated PhD committee members.

For the organisational framework as well as for many educational and fun events I want to acknowledge the graduate school CMSZH.

I also want to thank my group members – former and present, namely Dr. Franziska Conrad, Dr. Debora Ressnig, Dr. Pierre-Emmanuel Car, Dr. Fabio Evangelisti, Dr. Hongfei Liu, Dr. Kim von Allmen, Dr. René Moré, Dr. Shan Yu, Dr. Carlos Triana, Dr. Christos Mavrokefalos, Dr. Fabian von Rohr, Dr. Sima Heidari, Dr. Roger Jacot, Dr. Qian Zhang, Dr. Matteo Croce, Dr. Rafael Müller, Robin Güttinger, Wenchao Wan, Madhusudhan Jarpla, Fangyuan Song, Jingguo Li, Michael Olah, Sayedesmael Balaghi, Mauro Schilling, Dr. Simona Conti, Lukas Reith, Lucia Fagiolari, Lara Pestrin, Catherine Witteveen, Keyuan Ma, Younggui Zhao, Giann Wiprächtiger and Faezeh Pazoki. I received a lot of support from all of them and I think we often enjoyed great teamwork. I especially want to thank my lab mates Esmael, Catherine and Michael for the great supportive and often funny working atmosphere and friendly relationship. Furthermore, I also want to specially thank Lukas for the good teamwork and Christos for his help and thesis corrections.

Furthermore, I want to emphasis all the help I received for technical and administrative issues and collaborations. For the Regarding measurement techniques I want to thank Dr. Sebastian Siol (Empa Dübendorf) and Dr. Zbynek Novotny (PSI) for XPS measurements, Dr. Olga Safanova (PSI) for XAS measurements, Dr. Ferdinand Wild for the help with thermogravimetric analysis, Dr. Andres Käch for all the help with SEM measurements and Dr. Eszter Judit Barthazy Meier for the help with TEM measurements. For the help with other technical problems I would like to thank Hanspeter Stalder and Serkan Sariyildiz from the mechanical workshop, Thomas Jacoby and generally the staff from UZH Irchel Service Center. For a lot of help with IT problems I want to acknowledge Mirko Hofer and Sascha Giger. Regarding administrative support, I want to thank Dr. Jae Kyoung Pak, Natzyieli Rupprecht, Petra Westermann, Nathalie Melunsky-Fichter, Dr. Sabine Stockhause, Chantal Henningsen-Conus, Maja Gossweiler and Larissa Mostacciuolo. My special thanks go to Ramona Erni for her commitment and devotion for all of us. She really helped me a lot and many times with daily but numerous issues.

Of course, I also want to thank many other people here from the University of Zurich, who made this time very special and enjoyable. Above all Robin Güttinger and Giuseppe Meola for countless conversations in coffee breaks, sports sessions and after work beers. For the latter also our former neighbours, the Koushik group: Tobias von Arx, Dominik Suter, Dr. Alexander Szentkuti, Dr. Michael Bachmann, Florian Gribi Robert Malmberg, Sandro Soom and Jasmin Terreni and of course the Irchel bar team, especially Dominik Schenk and Kyra Stocker. Furthermore I want to thank many people from the building number 34, who brightened up the daily life: René Wick, Laurent Sévery, Rajiv Prabhakar, Ji Hye Sue, Xi Zhang, Wei Cui, Jonas Zurflüh, Connor Firth, Dr. Thomas Möhl, Dr. Magdalena Marszalek, Dr. Thomas Fox, Mathias Mosberger, Nicola Weder, Dr. Evelyne Joliat-Wick, Carla Gotzmann, Robin Bolliger, Dr. Angelo Frei and Dr. Michel Wuillemin.

Furthermore, I want to thank my friends outside UZH for always having a great time. My biggest fan Stefanie Bauleo, my fellow sufferer Fabia Canonica, my bosom friend Bardha Emerllahu, my ETH friends Philip Caspari, Johannes Löckinger, Johanna Scoul, Ceren Yilmaz, Lukas Lutz, Melanie Zechner and Elias Arturo Halabi and my friends from high school Ramona Reiser, Fabienne Meienberger, I-Hsiang Hung, Martin Tischhauser, Remo Haag and Josua Suter.

Last but not least I want to express my gratitude to my family, my father Wolfram Lienau, my mother Angelika Lienau-Gukelberger, my stepparents Sandra Gansner-Lienau und Armin Gukelberger, my grandparents Detlef and Uta Lienau and my step siblings Marianne and Matthias Gansner for always being there for me. Especially I want to thank my sister Marlene Lienau, my deceased sister Sirkka Lienau and my boyfriend Lewe Eggers for our very open, frank and loving relationships.

Financial Support

I am grateful to the University Research Priority Program “Solar Light to Chemical Energy Conversion” (URPP LightChEC) for funding.

List of Abbreviations

AC	Alternating current
ALD	Atomic layer deposition
BET	Brunauer-Emmett-Teller
BM	Ball milling
Bpy	2,2’-bipyridine
CAN	Cerium ammonium nitrate
CV	Cyclic voltammetry
CVD	Chemical vapor deposition
DC	Direct current
EDX	Energy dispersive X-ray
EIS	Electrochemical Impedance Spectroscopy
EtOH	Ethanol
EXAFS	Extended X-ray absorption fine structure
FEG	Field emission gun
FT-IR	Fourier transform infrared
FTO	Fluorine-doped tin oxide
FWHM	Full width at half maximum
GC	Gas chromatography
HER	Hydrogen evolution reaction

List of Abbreviations

HOMO	Highest occupied molecular orbital
HT	Hydrothermal
IEA	International Energy Agency
ITO	Indium tin oxide
JMAK	Johnson Mehl Avrami Kolmogorov
LDH	Layered double hydroxide
LDO	Luminescent dissolved oxygen
LED	Light-emitting diode
LUMO	Lowest unoccupied molecular orbital
MS	Molten salt
MW	Microwave
NHE	Normal hydrogen electrode
NIST	National Institute of Standards and Technology
NP	Nanoparticle
OEC	Oxygen evolving centre
OER	Oxygen evolving reaction
PEC	Photoelectrochemical
PM	Precipitation method
POM	Polyoxometalate
PS	Photosystem
PTFE	Polytetrafluoroethylene
PV	Photovoltaics

List of Abbreviations

PXRD	Powder X-ray diffraction
RHE	Reversible hydrogen electrode
SEM	Scanning electron microscopy
SG	Sol-gel
(HR-)TEM	(High resolution) Transmission electron microscopy
TCD	Thermal conductivity detector
TD	Thermal decomposition
TON	Turnover number
WOC	Water oxidation catalyst
WT	Wavelet-Transformed
XANES	X-ray absorption near edge structure
XAS	X-ray absorption spectroscopy
XPS	X-ray photoelectron spectroscopy

Symbols

Symbol	Definition	Units
A	adsorption cross section	$Å^2$
b	Tafel slope	V
c	BET constant	-
d	distance between adjacent lattice planes	Ångstrom
E_g	band gap	eV
ΔG	Gibbs free energy	kJ mol^{-1}
h, k, l	Miller indices	-
j	Current density	mA cm^{-2}
j_0	Exchange current density	mA cm^{-2}
K	Shape factor	-
K_α	X-ray emission	nm
m	Mass	g
N	Avogadro number	-
N	Atomic coordination numbers	-

p	Equilibrium pressure	Pa
p_0	Saturation pressure	Pa
S	Specific surface area	$m^2 g^{-1}$
U	Potential	V
V	Volume of adsorbed gas	m^3
V_m	Volume of monolayer	m^3
x	Degree of inversion	-

Greek letter	**Definition**	**Units**
β	Instrumental broadening	°
η	Overpotential	V
θ	Bragg angle	°
λ	Wavelength	nm
τ	Crystallite size	nm
Φ	Work function	eV

Publications & Contributions

List of publications

Major parts of this thesis are published and have been submitted to scientific journals (see I and II).

I. Preparative History vs Driving Force in Water Oxidation Catalysis: Parameter Space Studies of Cobalt Spinels, Karla Lienau, Lukas Reith, C. A. Triana, Sebastian Siol, and Greta R. Patzke, *ACS Omega* **2019**, *4*, 15444−15456.

II. Microwave-Hydrothermal Tuning of Spinel-type Co_3O_4 Water Oxidation Catalysts, Karla Lienau, C. A. Triana, Lukas Reith, Sebastian Siol, and Greta R. Patzke, *Front. Chem.* accepted, Manuscript ID: 508534

Co-author publications

III. R. J. Müller, J. Lan, Karla Lienau, R. Moré, C. A. Triana, M. Iannuzzi, G. R. Patzke, Monitoring surface transformations of metal carbodiimide water oxidation catalysts by *operando* XAS and Raman spectroscopy, *Dalton Trans*. **2018**, *47*, 10759-10766.

IV. L. Reith, K. Lienau, D. S. Cook, R. Moré, R. I. Walton, G. R. Patzke, Monitoring the hydrothermal growth of cobalt spinel water oxidation catalysts - From preparative history to catalytic activity, *Chem. Eur. J.* ***2018****, 24,* 1-12 *(Renewable Energy Special Issue).*

V. D. S. Cook, Y, Wu, K. Lienau, R. Moré, R. J. Kashtiban, O. V. Magdysyuk, G. R. Patzke, R. I. Walton, Time-Resolved Powder X-ray Diffraction of the Solvothermal Crystallization of Cobalt Gallate Spinel Photocatalyst Reveals Transient Layered Double Hydroxides, *Chem. Mater.,* **2017**, *29* (12)*,* 5053-5057.

List of contributions by co-authors

Lukas Reith, Patzke group, Department of Chemistry, University of Zurich:

Synthesis and Characterization of Co_3O_4 samples (Shared first author in Publication I; Chapter 3).

Dr. Carlos A. Triana, Patzke group, Department of Chemistry, University of Zurich:

XAS characterization of Co_3O_4 (Publication I & II; Chapter 3 & 4).

Dr. Sebastian Siol, Juergens group, Empa Dübendorf:

XPS characterization of Co_3O_4 samples (Publication I & II; Chapter 3 & 4).

S. Esmael Balaghi, Patzke group, Department of Chemistry, University of Zurich:

EIS characterization of Co_3O_4 samples (Publication II).

1 Introduction

1.1 Energy Supply – Development, Current Status & Outlook

Climate change is one of the main global challenges of our age. To bring global warming under control is an indispensable necessity to prevent further rise in the sea level, extinction of animal and plant species and endangering food supply to name a few consequences.[1–4] A substantial portion of CO_2 emissions is caused by fuel combustion for electricity production (Figure 1-1).[5,6] According to the International Energy Agency (IEA), 82% of primary energy supply is covered by fossil fuels, which did not decrease significantly, but only by 4%, in the past 50 years.[5] Even though the need for energy is rising slower than in the past, the absolute energy demand is still increasing, according to the "new policies scenario", which models current and announced energy policies, including those in the Paris Agreement, namely by 30% until 2040. This is also, but not solely, due to the increase in world population.[7,8] Therefore, the only way to tackle this problem of global warming is to shift from fossil fuels to renewable energy sources.

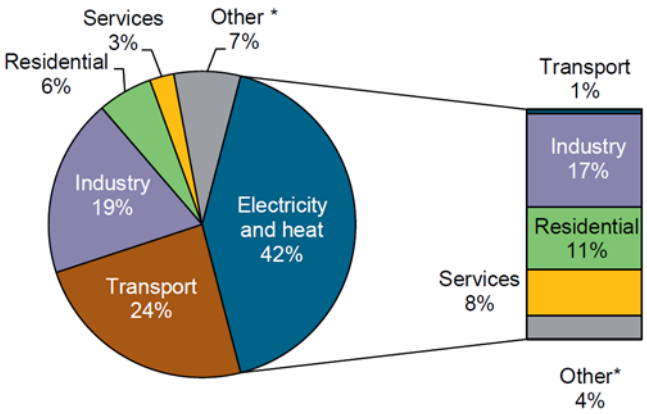

Figure 1-1 World CO_2 emissions from fuel combustion by sector, 2015.[5]* Other includes agriculture/forestry, fishing, energy industries other than electricity and heat generation, and other emissions not specified elsewhere

Although capacity from coal-fired power plants increased by nearly 900 GW since 2000 the era of coal slowly draws to an end. From today to 2040, only 400 GW more will be produced from mainly plants, which are already under construction, according to the IEA.[8] The oil and natural gas demand is foreseen to grow for the next 20 years. Renewables already cover a substantial portion (40%) of the increase in primary energy demand and make up for two-third of global investment in power plants for the next 20 years.[8] In 2016, 2017 GWe were produced by renewable energy sources,[9] whereas hydroelectric energy makes up for the biggest part, 83% of global electricity production from renewable sources (see Figure 1-2)[10]. The reason for this clear dominance is probably the reliable technology for harnessing water, which dates back to the early 20th century.[10] The second largest player is wind energy with 4%, exceeding biowaste and biomass energy (2%), followed by solar photovoltaics (PV) (1.5%) geothermal energy, tidal and wave energy (<1%).[10] This is too

little considering the fact that the sun provides enough energy in about one hour to cover the global energy needs of >9000 Mtoe and has therefore huge potential to increase this small share[11,12]. The development of PV for electricity production started with the oil crisis in 1973, when alternative energy sources were more and more in the limelight.[13]

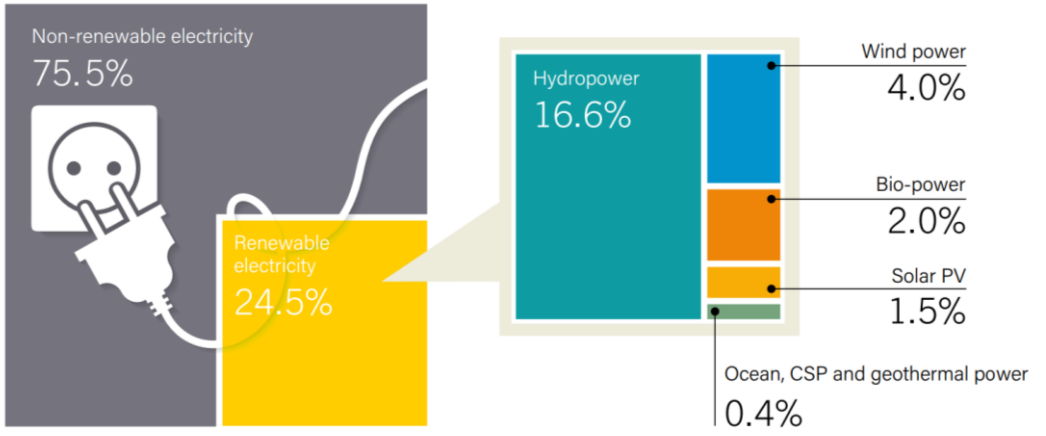

Figure 1-2 Estimated Renewable Energy Share of Global Electricity Production, End-2016.[9]

After the nuclear catastrophe in Chernobyl 1986 the research and development as well as production of solar cells was further increased. Efficiency of PV has increased over the last years, but what is even more important is that it had become much cheaper due to improvements in technology and the implementation of polycrystalline silicon besides the expensive monocrystalline silicon. Whereas one Watt from a solar module cost 96$ on mid-1970s, the costs decreased by 99% to 0.68$ in 2016.[14] This is quite promising, since there are much more technologies developing and entering the market. However, PV has one major drawback: the energy from sunlight is directly converted to electricity, therefore inverters are needed to convert the direct current (DC) to alternating current (AC) and, more importantly, they also require storage batteries, which increase the cost considerably, or other storage possibilities. For example, the Tesla Powerwall 14kWh battery costs $7'100 (with installation) and to back-up the energy for one house for one day, three of these batteries are required, adding up to $18'300.[15] Therefore it is desirable to convert the energy of solar light into chemical energy, called artificial photosynthesis, thus synthesizing fuels. This process is inspired by nature's photosynthesis.

1.1.1 Water Oxidation in Nature

Photosynthesis, namely the oxidation of water to oxygen by the manganese-containing oxygen evolving centre (Mn-OEC) in the chloroplasts and the following back-reduction of oxygen to water in the aerobic respiration by cytochrome c oxidase in mitochondria is essential for plant and also animal and human life on earth.[16] Pirson could show in 1937 that this oxidation seems to be dependent on manganese since plants and algea in which manganese was removed were unable to evolve oxygen.[17] Owing to its accessible oxidation states of II, III, IV and V, manganese is perfectly suited for its central role in this redox catalysis. The Kok cycle, which is a widely accepted theory proposed in 1970, describes the water oxidation in photosynthesis in five intermediate states, known as S states (Figure 1-3), which is based on the observation of Joliot, that Chloroplasts, excited by short flashes after adapted to the dark, evolve oxygen in discrete pulses with a periodicity of four.[18,19] Kok proposed that through this cycle of the intermediate states ($S_{0\text{-}4}$), the oxidizing equivalents of four absorbed photons by pigment P680 are stored on the OEC of photosystem II (PS II).[18]

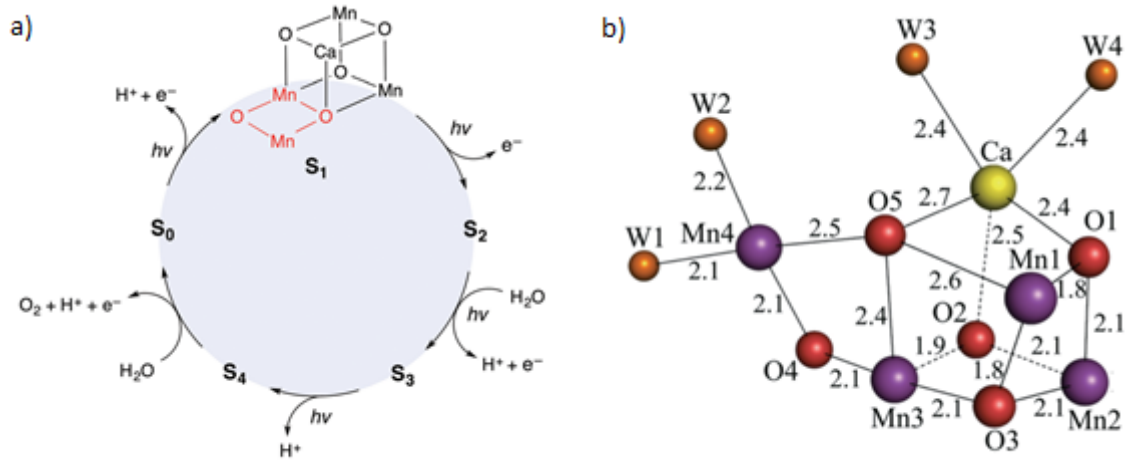

Figure 1-3. a) Water oxidation through different S-states.[20] b) Crystal structure of Mn_4O_4 cluster of OEC.[21]

Figure 1-3 b) shows the structure of the PS II core, the cuboidal $\{Mn_4O_4\}$ cluster. It consists of four manganese atoms, three of them plus one calcium atom in four corners of a distorted cube, whereas the rest of the corners are occupied by oxygen atoms. This structural motif is widely discussed in the community for the design of catalysts for artificial photosynthesis, as described below.

1.1.2 Artificial Photosynthesis

Splitting water by solar light can be a clean, abundant and sustainable way to produce hydrogen as energy carrier. This process is inspired by nature's photosynthesis, i.e. the way plants convert light into chemical energy.

1.1.2.1 Photocatalytic Water Oxidation

Inspired by natural photosynthesis, intense worldwide design and testing of artificial solar water-splitting catalysts and devices is now ongoing. Solar-to-chemical energy conversion would be highly desirable and even though many international scientific consortia are working on this topic, it remains a significant challenge to construct an efficient device capable of producing hydrogen at a scale that can compete with fossil fuels. The efficiency is determined by the thermodynamics and kinetics of three processes: the light-harvesting, the charge generation and separation and the catalytic reaction.

In nature's photosynthesis, the reaction is proceeding stepwise, accumulating enough energy to split water by exciting two subsequent chlorophylls (P680 and P700) connected in series with an electron transfer chain according to the Z-scheme[22] (Figure 1-4 a). In artificial photosynthesis, the reaction can be carried out in two ways: either with one light-absorbing species reducing and oxidizing both corresponding catalysts for water oxidation (Figure 1-4 b) and reduction, or by a two-step technique which is analogous to the Z-scheme, where the oxidation and reduction of water are separated into two systems (Figure 1-4 c). For light absorption, dye molecules or semiconductors are used whose light-absorbing properties can be tuned by changing the HOMO-LUMO distance or the bandgap. They should efficiently absorb sunlight and convert it to an excited state, which is followed by a charge-separation step to generate the required driving force for the water splitting reaction. The energy level of the oxidation catalyst (electron donor) must be lower than the excited state of the light-absorbing materials and higher than the water oxidation potential. The advantage of the single-step technique is the simplicity of the structure compared to the two-step technique. However, often the two-step technique is preferred due to the lower charge carrier recombination through direct separation into the two different materials and because of the higher flexibility in the materials choice. The advantage of the latter is that the chromophores energy levels have to match only one side of the reaction, and a higher fraction of the sunlight can be harvested with two different band gaps.

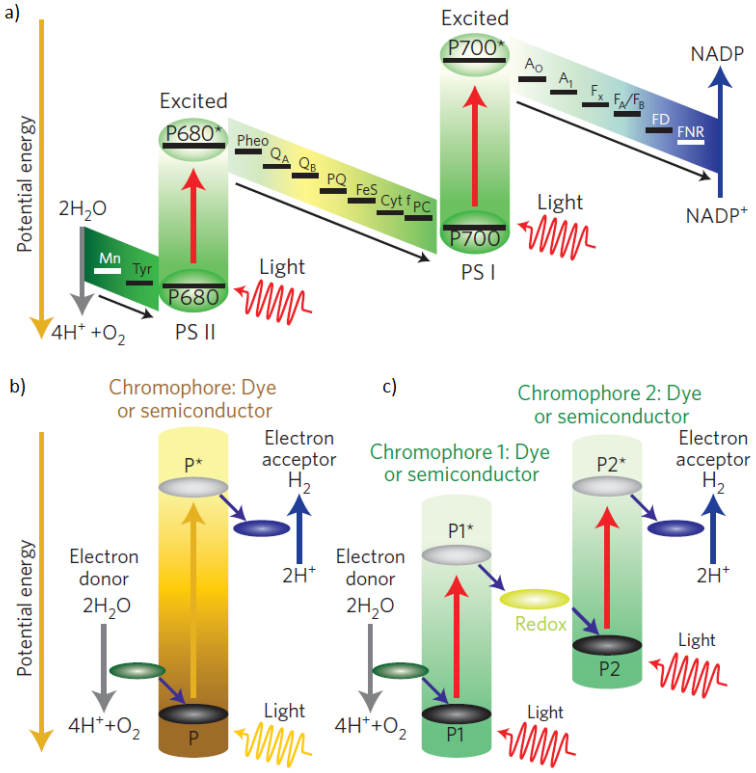

Figure 1-4. Comparison between Z-scheme from natural photosynthesis (a) and artificial photosynthesis (b and c).[23] a) Z-scheme process is driven by the absorption of two photons, one at PSII and the other at PSI. A series of electron transfer pathways are indicated by black arrows. b,c) Artificial photosynthesis charge-separation processes: single-step reactions (b) and two-step (Z-scheme) reactions (c).[23]

In this chapter, the focus is placed on the water oxidation part (formula (1)) of the reaction and different catalyst types are discussed. The overall water splitting (formula (3)) will be discussed in the following chapters. The four-electron transfer process of oxidizing H_2O to O_2 is not as easy as it might seem from the simplicity of educt and products. Most redox processes in nature are only one or two electron transfer reactions. For this four electron transfer, multiple bonds have to be rearranged and finally the O-O bond has to be formed. Therefore, the Gibbs free energy (ΔG) of ~237 kJ mol^{-1} of this process is correspondingly high. The {Mn_4O_4}-core of PS II is an operational solution to this challenge and therefore it inspired many catalyst designs.

$$O_2 + 4\,H^+ + 4\,e^- \leftrightarrows 2\,H_2O \qquad (1)$$

$$4\,H^+ + 4\,e^- \leftrightarrows 2\,H_2 \qquad (2)$$

$$2\,H_2O \leftrightarrows 2\,H_2 + O_2 \qquad (3)$$

Artificial water oxidation catalysts (WOC) can be mainly divided into two types: homogeneous and heterogeneous. Homogeneous catalysts are generally transition metal based complexes while heterogeneous catalysts nowadays consist of different materials like metal oxides, metals, carbon-based materials, chalkogenides. Homogeneous catalysts are easier to investigate and thus optimize due to their direct accessibility for a broad range of possible spectroscopic, crystallographic and computational methods. These methods allow also mechanistic studies at operational conditions, whereas for operando studies of heterogeneous catalysts often ultrahigh vacuum and advanced setups are required.[24–28] The first molecular water oxidation catalyst was a ruthenium complex, the so-called "Blue-Dimer".[29] It was the starting point for a now large group of Ru-based catalysts, one of the most important besides Ir-based WOCs, and first-row transition metal-based complexes.[30] Intense Ir-based molecular catalyst investigations started 2008, after the corresponding oxide was known as the most active and stable catalyst for many years, with the discovery of Bernhard et al. that single-site cyclometalated iridium complexes could mediate H_2O oxidation.[30,31] Due to nature's use of manganese in the oxygen evolving complex, lots of efforts are dedicated to the design and synthesis of manganese-based WOCs. Advantages like high abundance and therefore low cost make these materials even more interesting. Furthermore, manganese can access a wide range of oxidation states, which might be helpful for this four-electron transfer. Unfortunately, the intrinsic stability of these high-valent species is very low and has to be stabilized with effective ligands, which have to be stable against oxidative degradation as well.[32–34]

Inspired by the fact that the $\{Mn_4O_4\}$-cluster of PS II contains not only active manganese ions but also a redox inert Ca^{2+}-ion, cubane complexes containing Ln^{3+} as redox inert Ca^{2+} mimic and flexible aqua-/acetate ligands were investigated in our group and showed good performance (Figure 1-5 a)).[35,36] This was further developed to cubanes containing the widely discussed $\{H_2O\text{-}Co_2(OR)_2\text{-}OH_2\}$ edge-site motif, which is considered the sine qua non for cobalt oxide-based WOCs. They showed high performance and stability (Figure 1-5 a)).[37–40]

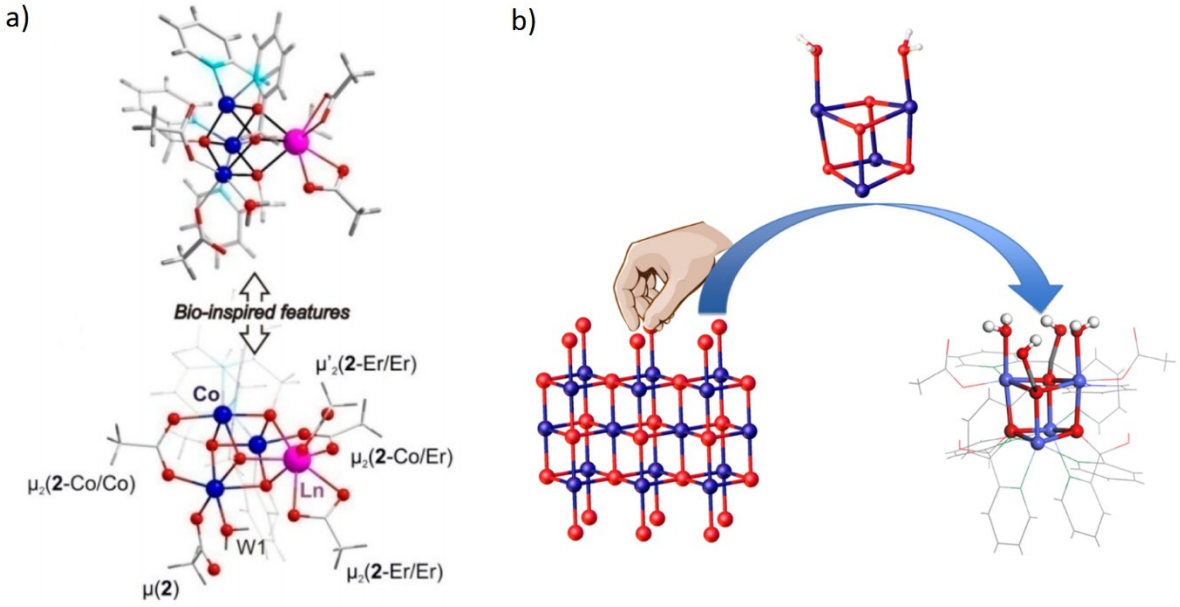

Figure 1-5. Cubane WOCs a) with Ln^{3+} as Ca^{2+}-mimic[36] and b) with the $\{H_2O\text{-}Co_2(OR)_2\text{-}OH_2\}$ edge-site motif.[37]

Since molecular WOCs often suffer from instability, often due to oxidation of the organic ligands, polyoxometalates (POMs) with very stable, inorganic ligands have been developed as active catalysts.[41–44]

Homogeneous WOCs often show increased reactivity compared and generally a higher fraction of accessible catalytic sites compared to their heterogeneous counterparts and allow more detailed kinetic studies as well as accurate structural determinations which are not hampered by amorphization as in solids.[45] However, many molecular catalyst face challenges in terms of synthetic costs, stability – or the in situ formation of oxide nanoparticles which raises the crucial question of the true catalyst.[46] There are many pathways of deactivation, degradation and inhibition which have been reported and even if the catalysts are stable, the practicability of molecular complexes is under debate.[47] Heterogeneous catalysts on the other hand usually have high oxidative stability and further advantages like low cost and more feasible applications.[43] As already mentioned above, IrO_2 is the most efficient metal oxide catalyst, producing O_2 in >99% yield with a fast rate of 190 $\mu Ms^{-1}g^{-1}$ (see Table 1-1).[48–50] Like in homogeneous catalysis, ruthenium is also a very efficient WOC component in the form of RuO_2, for example as NPs supported on mesoporous silica (SBA-15) with a yield of 95%.[51] However, to achieve global scalability, Ir and Ru are not an option; commercial WOCs must consist of earth-abundant elements.[52]

Table 1-1 Turnover number (TON) and yield in photocatalytic water oxidation by persulfate using heterogeneous catalysts.[48]

Catalyst	pH	Rate [a]	Yield [%] [b]	Ref.
IrO_2	5.4[c]	190	>99	49
IrO_2 [d]	10	18	73	53
RuO_2	5	–	27	54
RuO_2 NP[e]	5.4	–	95	55
RuO_x /Y-zeolite[f]		–	31	56
$NiFe_2O_4$ [g]	8	2.7	74	57
Co_3O_4 [g]	8	2.4	64	57
Co_3O_4 -150[h]	7	-	27	58
Co_3O_4 -750[h]	7	-	16	58
NiO[g]	8	1.5	52	57
α-NiO nanorods[i]	8.5	1.8	44	59
Fe_3O_4 [g]	9	0.95	55	57
Fe_2O_3 [g]	8.5	0.65	24	57
Fe_2O_3 (nanocubes)	8	–	13.4	60
Fe_2O_3 (nanoplates)	8	–	4.5	60
Fe_2O_3 (nanoflakes)	8	–	3	60
Fe_2O_3 (nanoarticle)	8	–	17.7	60
$CuFe_2O_4$	8.5	11	73	61
$LaCoO_3$	7	5.5	74	62
$CoWO_4$ [j]	7	1.3	19	62
$La_{0.7}Sr_{0.3}CoO_3$ [j]	7	3.6	59	62
$NdCoO_3$ [j]	7	4.6	59	62
$YCoO_3$ [j]	7	1.8	24	62
CoNCN [k]	9	–	76	63
$NiMnO_3$	7	9.6	52	64
α-MnO_2	7	5	24	64
Mn_2O_3	7	2.5	18	64
Mn_2O_3 (bixbyite)	7	2.4	–	65
Mn_3O_4	7	1	4	64
Mn_3O_4 (hausmannite)	7	1	–	65
γ-MnO_2	7	0.94	–	65
$NiO/CoO/Fe_2O_3$	8.5	–	64	66
$NiO+CoO+Fe_2O_3$	8.5	–	47	66
$[Co^{II}(H_2O)_{1.79}]_{1.42}[(Co^{III}_{0.85}Pt^{IV}_{0.15})(CN)_6]$	8	62	100	67

[a] O_2 evolution rate: $\mu Ms^{-1}g^{-1}$ (catalyst weight: g). [b] Yield is defined as twice the number of moles of O_2 per mole of $Na_2S_2O_8$. [c] 5.0×10^{-2} M (1.0:1.3) Na_2SiF_6 -$NaHCO_3$ buffer. [d] Photoirradiation (300 W Xe lamp, $\lambda > 400$ nm) of a buffer solution (100 mL, pH 10) containing $Na_2S_2O_8$ (42.9 mmol) and IrO_2 (3.7 mg). [e] RuO_2 supported on mesoporous silica SBA-15. [f] Obtained starting from zeolite Y and $Ru_3(CO)_{12}$. [g] Photoirradiation ($\lambda > 420$ nm) of an aqueous buffer solution (pH 8.0, 2.0 mL) containing the catalyst (0.50 gL^{-1}), $Na_2S_2O_8$ (5.0 mm), and $[Ru(bpy)_3]^{2+}$ (0.25 mm). [h] The number denotes the calcination temperature. [i] α-NiO nanowires and α-NiO nanoplates exhibited similar catalytic reactivity. [j] Photoirradiation (Xe lamp, $\lambda > 420$ nm) of a phosphate buffer solution (50 mM, 2.0 mL, pH 7.0) containing the catalyst (0.25 gL^{-1}), $Na_2S_2O_8$ (5.0 mM), and $[Ru(bpy)_3]^{2+}$ (0.25 mM). [k] Cobalt carbodiimide.[48]

A major share of these catalysts is covered by first row transition metal oxides. Among them, $NiFe_2O_4$ shows the best catalytic performance as shown in Table 1-1, which lists some representative catalysts of these earth-abundant materials.[48] With 74% yield it outperforms cobalt, iron and nickel oxides.[57] The same yield was achieved by $LaCoO_3$, showing the highest activity of the Co-containing WOCs in Table 1-1.[62] Besides transition metal oxides, there are also some other WOC-types like carbodiimides, also listed in Table 1-1,[63] or polymeric carbon nitride.[68] Very high activity and quantum efficiency was obtained by the incorporation of Ca^{2+} into a polymeric cobalt cyanide complex.[69] Therefore, a wide variety of different WOCs is investigated and still it is not entirely clear which requirements must be met precisely to get the highest possible efficiency. Some articles claim that, besides surface area, high crystallinity is important whereas other studies found that amorphous materials seem to be the best working catalysts - and still others show that specific structural motifs are giving rise to the highest performance.[37,70–75] Recently, Co_3O_4 and CoO were found to split water when their size is reduced to small nanoparticles (NPs) of several nanometers.[76,77] Therefore, further studies are required to determine the decisive criteria for all types of highly active WOCs.

In general, heterogeneous catalysts, compared to homogeneous analogues, have the advantages of good oxidative stability, some also of high abundance and therefore low cost, and easier handling, which means better upscaling options. Unfortunately, they suffer from one major disadvantage compared to molecular WOCs: they are, especially mechanistically, much harder to study and request more demanding in situ/operando setups.[33,43,78,79]

1.1.2.2 Chemical Water Oxidation

To conduct water oxidation catalysis, usually a sacrificial oxidant is used. The most frequently used in chemical water oxidation is ceric ammonium nitrate (CAN, $Ce(NH_4)_2(NO_3)_6$) with a redox potential of 1.70 V vs NHE.[80,81] For Meyer's blue dimer, introduced in the previous chapter, CAN was originally used to test the water oxidation activity.[29] Due to its weak UV-Vis absorption CAN can also be used in mechanistic studies with different spectroscopic techniques.[32] Furthermore, it is directly commercially available and for all these reasons it is widely used as sacrificial oxidant for water oxidation promoted by a WOC (Formula (4)).[82]

$$4\,Ce^{IV} + 2\,H_2O \leftrightarrows 4\,Ce^{III} + O_2 + 4\,H^+ \qquad (4)$$

The biggest drawback of this system is the necessity of very acidic solutions (pH < 1), which makes it unsuitable for acid sensitive WOCs. Furthermore, it was shown recently, that the nitrate anion can promote the oxygen atom transfer, therefore influencing the evolution mechanism of O_2 since one oxygen atom can possibly come from nitrate instead of water.[83]

Another powerful oxidant is peroxymonosulfate (Oxone) which is very stable in solutions up to pH 6. It can act as a two-electron oxidant with an oxidation potential of 1.82 V vs NHE.[84] However, like CAN it can also promote oxygen atom transfer and since it is a two-electron oxidant, its practicability in water splitting catalysis, which is carried out through one-electron transfer

reactions, is questionable.[82,85] Another two-electron oxidant with a similar oxidation potential of around 1.6 V vs NHE (at pH 1) is sodium periodate. It can be applied to determine H_2O oxidation activity under neutral conditions since it can be used up to pH 7.5.[86] If alkaline pH is required, sodium hypochlorite, also a two-electron oxidant, can be utilized.[82]

1.1.2.3 Electrocatalytic Water Oxidation

The Gibbs free energy (ΔG) of 237 kJ mol^{-1} is converted by the Nernst equation into an electrochemical potential of 1.23 V vs NHE at standard conditions. The real electrode potential for the four sequential one-electron steps of water oxidation is higher than the potential for four-electron, four-proton oxidation.[87] This usually rather large difference between these applied potentials and the thermodynamic potential of 1.23 V vs NHE is referred to as overpotential, which is a kinetic phenomenon.[32] This implies high activation barriers, and therefore a catalyst is required to promote water splitting.

The electrocatalytic oxidation of water is strongly pH dependent. The reaction as shown in formulas (1) and (2) is only possible in acidic solution. If the water oxidation is conducted in basic solution, the water splitting proceeds via different half reaction types (formulas (5) & (6)).

$$O_2 + 2\,H_2O + 4\,e^- \leftrightarrows 4\,OH^- \qquad (5)$$

$$4\,H_2O + 4\,e^- \leftrightarrows 2\,H_2 + 4\,OH^- \qquad (6)$$

Already back in 1966, Pourbaix described the electrochemical equilibria of metals in aqueous solution.[88] The data from this atlas were summarized by Müller et *al*. in Figure 1-6. They colour-coded the non-gaseous group 1−16 elements of the Periodic Table depending on their stability in low, neutral and high pH for applied high anodic potentials (which are required for water oxidation). From this figure, it is obvious that in general, more earth abundant metal oxides or hydroxides exist at high pH values. A method to circumvent these stability issues of certain metals at one pH region is to use binary systems which deviate from the Pourbaix prediction. For example manganese, which is not stable at basic pH, can be stabilized in the $Ca_2Mn_2O_5$ perovskite structure or in nickel-containing double hydroxides.[89,90]

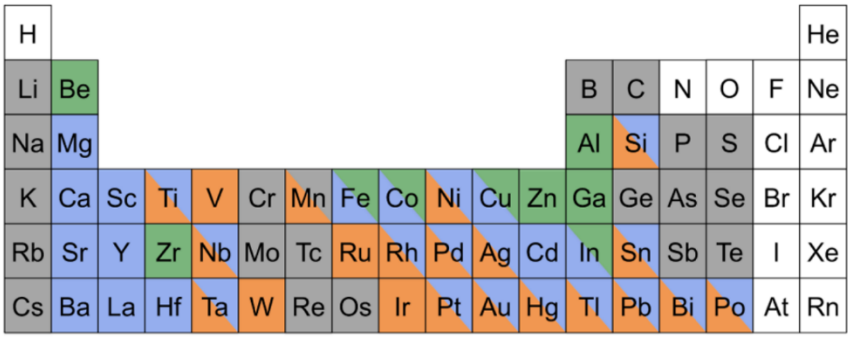

Figure 1-6. Corrosion stability of nongaseous group 1−16 elements for element−water systems at 25 °C under positive applied potentials; adapted from the Pourbaix Atlas. Color code: stable against corrosion by innate immunity or the formation of an oxide or hydroxide layer at low (orange), around neutral (green), and high (blue) pH. Elements that corrode under applied oxidative potentials are depicted in gray. Multiple colors (blue/orange, blue/green) indicate stability over a wide pH range. The combination orange/gray is for stability at low pH but only for moderately positive potentials.[87]

As for light-driven catalysts, electrocatalytic water splitting is inspired as well by nature's use of manganese. In 1977 it was already shown that MnO_2 works as an electrocatalyst for water splitting and one decade later, Mn_2O_3 was established for this application.[33,34] A recent study on different manganese oxides, however, showed that the "best catalyst" actually depends on the employed test method.[91] In this study, nine crystalline MnO_x samples were tested chemically using CAN at pH 0.8, photocatalytically at pH 8 with the $Ru(bpy)_3^{2+}/S_2O_8^{2-}$ approach and electrocatalytically in acidic, neutral and basic pH. Some years ago, Jaramillo et al. introduced nanostructured manganese oxides with activities close to noble metals for water oxidation as well as for oxygen reduction.[92]

Besides manganese, iron, nickel and cobalt catalysts were heavily investigated as well.[87] Considering scalability for clean energy conversion methods, iron oxides are very attractive materials due to their low cost and abundance. Electrochemical studies on passive oxide covered polycrystalline Fe electrodes suggested a physisorbed peroxide pathway for these compounds and a stabilized Fe^{VI} species as active site.[93] One very important approach to increase the activity of these catalysts is nano-structuring, which will be also further discussed later.[94] The first nickel oxide was found to catalyse water oxidation in 1966 by Bode.[95] For oxide passivated nickel anodes, Lyons et al. suggested also a physisorbed peroxide mechanism based on electrochemical investigations including Ni^{III} or Ni^{IV}.[93] The well-known beneficial effect of improving water oxidation activity of nickel oxide catalysts already by very small amounts of iron was discovered in 1984 by Radniecka et al.[96] The same was also found by Corrigan around the same time.[97] Therefore, mixed Ni-Fe oxides gained a lot of interest for electrochemical water oxidation and were, with a few others, discussed as one of the benchmarking electrocatalysts for water splitting.[98] Recently, the activity of mixed NiFe-OOH was further increased by introducing oxygen vacancies, which lowered the energy barrier and increased the conductivity of the material.[99]

Cobalt oxides were as well shown to be an active anode material for water oxidation in alkaline electrolyte, usually KOH.[100–104] A study of Stahl et al. explored catalysts being heterogeneous to a pH as low as 3.5. In more acidic electrolyte the reaction proceeds homogeneously.[105] In 1950 the formation of CoO, Co_2O_3 and CoO_2 upon anodic polarization prior to oxygen evolution was already discovered.[106] Alternative cobalt oxide types, like Co_3O_4 have then gained a lot of interest and will be discussed in larger extent in chapter 1.2.3.

Another very important and famous Co-based WOC is CoPi, discovered by Nocera and Kanan in 2008.[107] It is formed upon anodic polarization of the inert indium tin oxide (ITO) electrode in phosphate buffer containing Co(II) ions.[107] This catalytic film was able to split water at neutral pH with low overpotential and exhibits self-healing properties, which arise from a dynamic equilibrium between the dissolving of the film during water oxidation and the redeposition upon oxidation of Co^{2+} ions from the solution to Co^{3+}.[108]

Recent research also focused on the development of layered double hydroxides (LDHs), which contain sheets of $M^{2+/3+}(OH)_6$ edge-sharing octahedras that are intercalated by anions and water.[109] For example a Zn-Co-LDH showed lower overpotential than the corresponding Co-based solid state materials (e.g. $Co(OH)_2$ and Co_3O_4) according to the authors.[110] Also more sophisticated structures like CoFe-LDH nanosheets coated with CoFe-Borate layer demonstrated considerable efficiency and long-time stability.[111] Based on the success of the already mentioned class of nickel-iron oxides, NiFe-LDHs also attracted a lot of interest. Boettcher et al. detected the in situ transformation from oxide to LDH which was accompanied by an increase in catalytic activity.[112] The highest activity in this study was exhibited by $Ni_{0.9}Fe_{0.1}O_x$, outperforming IrO_2 in basic media. Also more advanced designs like mixed NiFe-LDH immobilized on graphene, carbon nanotubes or quantum dots showed high activity in water oxidation.[113–115]

Nowadays, thin films become more and more important, also in electrocatalysis. These catalysts have the major advantage to avoid bulk materials problems like the materials conductivity, originating from various factors, or depletion regions.[116,117]

Bifunctional catalysts for overall water splitting. The preceding sections mainly focused on one half reaction of water splitting, namely the water oxidation, but the ultimate goal is a full water splitting system wherefore this is discussed briefly in this section. In practice, platinum catalysts are currently used for HER whereas iridium and ruthenium-based catalysts accelerate the oxygen evolution. Due to the high cost of these metals, non-precious metal catalysts are very desirable. Therefore, bifunctional catalysts are investigated, which are mainly first-row transition-metal based. The advantage of bifunctional catalysts is the simplification of the system and operation with one electrolyte at distinct pH. Alkaline electrolytes enable the replacement of expensive precious metal catalysts with transition metals and favour the more complex oxygen evolution reaction compared to acidic electrolytes. [118]

A simple preparation for such a bifunctional catalyst is electrodeposition from Co-salts in phosphate buffer yielding metallic cobalt covered with a cobalt-oxo/hydroxo-phosphate layer, which can reversibly convert into an amorphous cobalt oxide film for oxygen evolving reaction (OER), as published by Cobo et al.[119] Another cobalt phosphate electrolyzer was also shown to exhibit high activity and stability.[120] Zhu et al. presented mesoporous nanorod arrays of CoP supported on Ni foam for enhanced conductivity and mass transport. Besides Co-P catalysts, also Co-Se and Co-B were shown to be active towards overall water splitting.

Other examples are NiFe-LDH immobilized on $Co_{0.85}Se$ sheets which were grown on exfoliated graphene sheets or CoO with $CoSe_2$ nanobelts on Ti which were introduced recently.[121,122] Amorphous cobalt boride (Co_2B), which exhibit increased lattice strain, facilitating the formation of OOH* intermediates and therefore showing exceptional activity for OER, also showed to be active for hydrogen evolution reaction (HER).[123] For enhanced conductivity, supporting on graphite carbon can improve the performance of catalysts. A very successful representative of this method was obtained by Jin et al. with their cobalt-cobalt oxide and N-doped carbon hybrids.[124] Also Ni-based phosphates and chalcogenides can be applied as water electrolyzers.[125–127] Along these lines, catalysts based on iron are investigated as well. Applications of such catalysts would be very eligible due to its very high abundance. Recently an iron-only catalyst was introduced which splits water by interconversion between Fe under cathodic bias and FeO_x under anodic bias.[128] Besides the above mentioned catalysts, also bimetallic oxides are investigated. A few examples are Ni-incorporated hierarchical hollow $NiCo_2O_4$ microcuboids, carbon-coated Co-Mn oxide nanoparticle superlattices, $NiCo_2S_4$ nanowire arrays on Ni foam, $NiCo_2O_4$ and $Ni_{0.33}Co_{0.67}S_2$ nanowires on Ti and assembled $CoNi(OH)_x/NiN_x$ nanotubes, all showing significant performance.[129–133]

1.1.2.4 Photo-Electro-Chemical Water Splitting (PEC)

Gray et al. differentiated between three architectures of solar water splitting devices (Figure 1-7) based on their level of development and projected manufacturing cost.[134] Photovoltaic (PV) modules connected to discrete electrolyzers is the most mature technique among them. It was concluded by Westerik et al. that, in the short-term, this architecture is the only economical option for niche applications, whereas in the long term, a broader application might be possible, but for that still require advances in technology as well as cost reduction.[135]

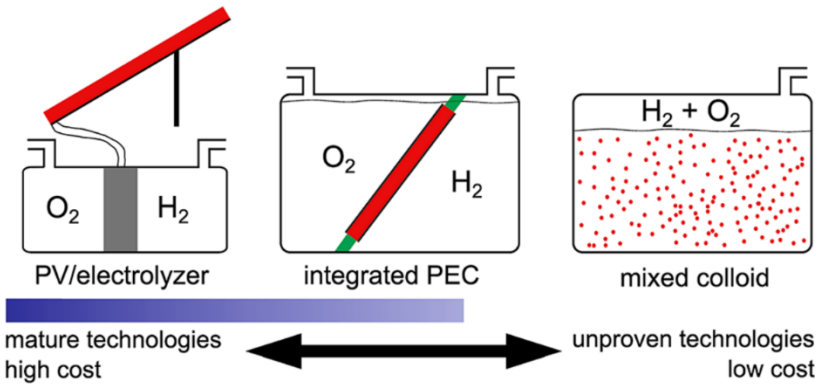

Figure 1-7. Three device architectures of solar water splitting devices.[134]

Nonetheless, it is possible to surpass this design by fully integrated devices, since the efficiency of the system is not only made up by the PV module and the electrolyzer but the required power electronics (e.g. DC-DC and AC-DC converters) to enable transmission from PV modules into the electricity grid lower the system efficiency and also add to the cost of this approach. The connection to the grid is necessary because the electrolyzers require constant energy supply, which is not possible to cover just by solar irradiation.

The mixed colloid architectures, where heterogeneous catalysts are in suspension (or homogeneous catalysts in solution) have the problem of forming explosive H_2 and O_2 mixtures when hydrogen and oxygen evolution occur together. A more promising method regarding applicability is the second architecture in Figure 1-7, integrated photo-electro-chemical (PEC) water splitting. This setup has the advantage of separating hydrogen and oxygen evolution reactions and also directly converting sunlight to hydrogen, therefore avoiding the ohmic losses discussed for PV/electrolyzer architectures. One approach is shown in Figure 1-8 which illustrates the Honda-Fujishima effect of water splitting by TiO_2 discovered in 1972.[136] TiO_2 acts as UV-light absorbing semiconductor, generating electrons and holes upon illumination which are separated due to the band bending at the semiconductor/electrolyte interface. The corresponding reactions are driven by an applied external bias between anode and cathode: oxygen evolution reaction (OER) by water oxidation at the TiO_2-working electrode and hydrogen evolution reaction (HER) at the Pt counter electrode.

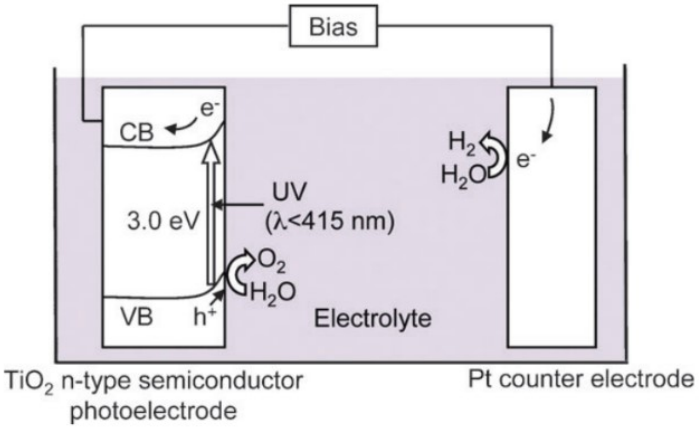

Figure 1-8 Honda–Fujishima effect of water splitting using a TiO_2 photoelectrode.[136,137]

The important processes which have to be fulfilled in these systems are first the absorption of photons, generating electron-hole pairs with sufficient potential for the water splitting reaction. Furthermore, also the position of conduction and valence band have to be consistent with the water oxidation and reduction potentials; the bottom of the conduction band needs to be more negative than the H^+/H_2O redox potential, whereas the top of the valence band has to be more positive than the H_2O/O_2 redox potential. Therefore, the minimum bandgap energy required is 1.23 eV, corresponding to light with a wavelength of 1100 nm. Few semiconductors like ZrO_2, $KTaO_3$, $SrTiO_3$ and TiO_2 exhibit this suitable bandgap, but many more are able to carry out one of the two half reactions.[137] The electrons and holes should be separated to minimize recombination processes and migrate to the corresponding surface sites where the reactions take place. Therefore, band bending between semiconductor and electrolyte and - if there are extra catalyst particles - also between semiconductor and catalyst has to be appropriate. Migration of carriers strongly depend on grain boundaries and defects, which increase the recombination probability, and on particle size.

After the discovery of the Honda-Fujishima effect of light-driven water splitting, photoelectrodes were further developed. Due to the large bandgap of TiO_2 only ultraviolet light is absorbed by these electrodes. Therefore, many different light absorbers/semiconductors were investigated, like multijuntion photoelectrodes, which drastically increase the light absorption and carrier generation efficiency. Improving absorption of single junction devices by using dyes like $Ru(bpy)_3^{2+}$ was also successful. [138–140] The probably most famous one is the Ru-dye-sensitized TiO_2 oxygen evolving electrode introduced by Grätzel et al.[141,142] The beneficial effect of dyes drove the development of mesoscopic semiconductors forward.[143] Bio-inspired cubic Mn-oxo-cluster catalysts were used to improve such a dye-sensitized water-splitting cell in the short term, before suffering from instability issues.[144] Besides improving the photoelectrode, like by using solid solutions of gallium and zinc oxynitrides, very often, co-catalysts are immobilized at the electrode surface to increase the water splitting efficiency.[140,145]

For overall water splitting a bandgap of 1.23 eV and suitable band positions are required as mentioned above. Many photocatalysts therefore show only activity for one of the reactions, H_2 or O_2 evolution. These photocatalysts can be combined constructing a Z-scheme like in nature's photosynthesis, using electron mediators which shuttle the electron between the two catalysts. [146,147] Successful examples for such Z-schemes are the Pt/$SrTiO_3$:Cr,Ta and Pt/TaON or Pt/$MTaO_2N$ (M=Ca, Sr, Ba) as water reduction catalysts with Pt/WO_3 as water oxidation catalyst and IO_3^-/I^- used as electron mediator or Pt/$SrTiO_3$:Rh WRC and $BiVO_4$ WOC with a Fe^{3+}/Fe^{2+} redox couple as an electron relay.[146–149] A system of semiconductor nanoparticles, Ru/$SrTiO_3$:Rh for HER and $BiVO_4$ for OER, without electron mediator, was introduced by Kudo et al.[150] Another possibility for this two-step system is the tandem cell configuration.[141,142] In a tandem device, two photosystems are connected in series, e.g. a WO_3 or Fe_2O_3 as the top electrode, absorbing the high-wavelength part of the solar spectrum and catalysing the water oxidation, is connected to a second electrode, such as to the famous dye-sensitized TiO_2, which absorbs the more in the red part of the visible light spectrum and drives the evolution of hydrogen.[151,152] A very efficient way to increase the activity of electrode materials is nanomaterial development or nanostructuring.[23] A very interesting property of very small features is the so-called quantum confinement – a physical effect which results in an increased bandgap for nanoparticles compared to the bulk material. One example for quantum-confined nanostructures with optimized bandgap and tuned band edges is shown in Figure 1-9; nanorods made out of a solid solution of ZnO–ZnS (ZnOS) exhibit significantly improved efficiency compared to the plain electrodes or not-sensitized ZnO nanowire array.[153]

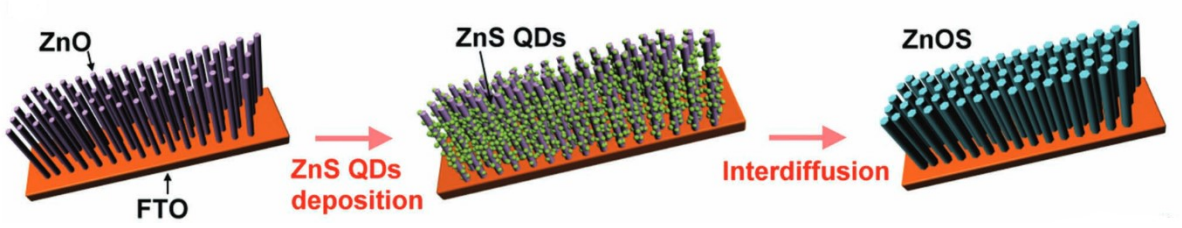

Figure 1-9. New concept of nanomaterial development: fabrication of ZnOS nanowire array electrode on fluorine-doped tin oxide (FTO).[153]

1.2 Spinels in Materials Science

1.2.1 Structure, Properties and Applications

Spinels are well-known for their use as gemstones. They can adapt different colours: the Cr^{3+}-containing are red whereas spinels with Fe^{2+} or Zn^{2+} can be blue.[154] The spinel structure was first discovered in 1915 when Bragg and Nishikawa found the composition of spinels to consist of A-O tetrahedra and B-O octahedra.[155,156] Nowadays, spinel is a very important and flexible structure type, constituted of a cubic closed packing of oxygen with both interstices, tetrahedral and octahedral, partially occupied. Oxide spinels have the general composition AM_2O_4 with the possibility that A and M can be nearly all main group metals and transition metals.[154] There are also some spinels which are not oxides but sulphides, selenides, halides and pseudohalides, but they are less important in materials science. Regarding the oxidation state there are also two possibilities, namely the $A^{2+}M^{3+}{}_2O^{2-}{}_4$ and the $A^{4+}M^{2+}{}_2O^{2-}{}_4$. In this chapter only the first type is discussed. Two-third of the metal ions occupy the octahedral voids and one-third the tetrahedral voids. In the normal spinel the tetrahedral voids are occupied by the A ions and the octahedral voids by the M ions. For this to happen, the A ions should be smaller since the tetrahedral interstices are smaller than the octahedral ones. If this is not the case, the formation of an inverse spinel, where one half of the M ions is in tetrahedral and one half in octahedral voids, or an intermediate state, called complex spinel, with some M ions in tetrahedral voids occurs. This is described by the degree of inversion x in $A_{1-x}M_x(A_xM_{2-x})O_4$: for a normal spinel $x = 0$, for an inverse spinel $x = 1$ and for complex spinels $0 < x < 1$. Examples for normal and inverse spinels with different oxidation state combinations are depicted in Table 1-2.

Table 1-2 Examples of spinel types.[157]

Oxidation state combination	Normal spinels $A_T[M_2]_OX_4$	Inverse spinels $M_T[AM]_OX_4$
II, III	$MgAl_2O_4$	$MgIn_2O_4$
II, III	Co_3O_4	Fe_3O_4
IV, II	$GeNi_2O_4$	$TiMg_2O_4$
II, I	$ZnK_2(CN)_4$	$NiLi_2F_4$
VI, I	WNa_2O_4	

However, it is rather difficult to understand the cation distribution, because λ is not only dependent on the ionic radii but also on the ligand field stabilization energy (LFSE) and the temperature. The ligand field stabilization energy corresponds to the crystal field effect of the octahedral site preference energy i.e. the energy difference between tetrahedral and octahedral fields. It is an essential parameter for transition metal compounds. Depending on octahedral or tetrahedral coordination of the cation, the energies of the d-orbitals are split as a consequence of the interaction between the bonding electrons and the nonbonding d-electrons as shown in Figure 1-10. The energy difference of the e_g and t_{2g} orbitals arising from repulsion of the bonding electron pairs is referred to as Δ_O and Δ_T respectively. Due to the stronger interaction of the e_g orbitals with the binding orbitals in octahedral coordination compared to the interaction of the t_{2g} orbitals with the binding orbitals in tetrahedral coordination, the splitting of e_g and t_{2g} is smaller in tetrahedral than in octahedral geometry, namely $\Delta_T = \frac{4}{9}\Delta_O$.

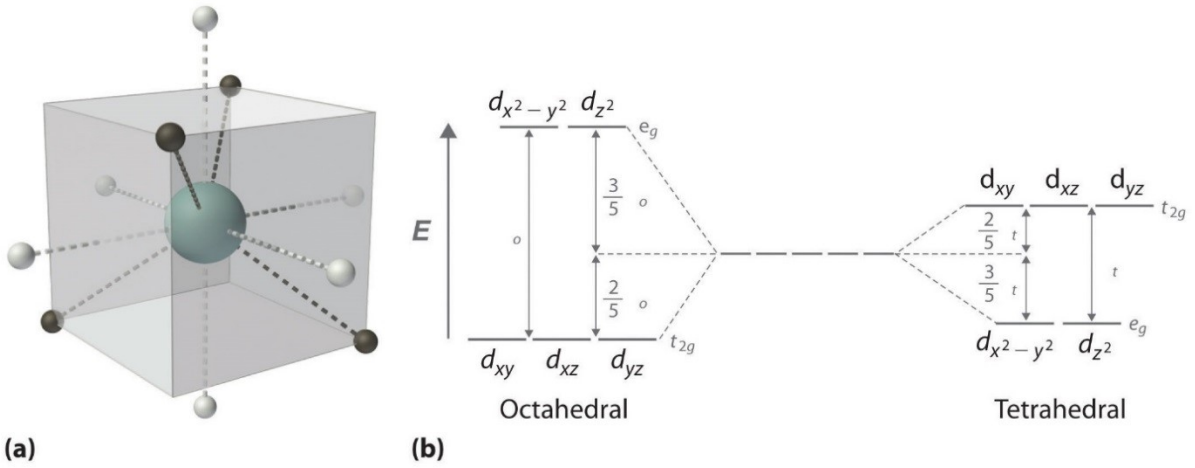

Figure 1-10. (a) In a tetrahedral complex, none of the five *d* orbitals points directly at or between the ligands. (b) d-orbitals energy distribution with ligands arranged in a regular octahedron around the transition-metal ion (6 ligands) or tetrahedrally (4 ligands) with $\Delta_T = \frac{4}{9}\Delta_O$.[158]

The examples of Mn_3O_4, Fe_3O_4 and Co_3O_4 are discussed to illustrate this effect. For Mn_3O_4, both, Mn(II) and Mn(III) are in their low-spin states. Mn(II) has d^5configuration and therefore both normal and inverse spinel would be possible since all orbitals are half occupied. But considering Mn(III), which is in d^4 configuration, the octahedral sites are favourable with Δ_O = 0.6 instead of 0.18 and therefore Mn_3O_4 is a normal spinel. For Fe_3O_4 the inverse spinel configuration is favoured. Fe(III) is isoelectronic to Mn(II) and therefore both configurations would be energetically the same, but since Fe(II) has d^6 configuration, it is better stabilized in the octahedral voids (Δ_O = 0.4 instead of 0.27) and therefore Fe_3O_4 is adopting the inverse spinel structure. In the case of Co_3O_4, which is a normal spinel, Co(II) exhibits d^7 configuration. Therefore the inverse spinel with Co(II) in octahedral voids would be favourable (only according to ligand field theory, not based on ionic

radii; due to its small radius of 75 pm it usually favours tetrahedral configuration), since $\Delta_O = 0.8$ for octahedral vs $\frac{6}{5} \times \frac{4}{9} = 0.53$ for tetrahedral geometry. However, since Co(III) has d^6 configuration, the maximum ligand field stabilization of 2.4 is achieved with octahedral low-spin configuration which outweighs the weaker stabilization of Co(II) in the tetrahedral voids. If Co(III) would occur as high-spin complex, which is usually not the case for octahedral coordinated Co(III), then Co_3O_4 would be an inverse spinel.[157]

The spinel structure is shown in Figure 1-11. Starting from the Al_4O_4-cube, aluminium being represented by the dark spheres and oxygen by the white spheres, the corners of this cube are alternately occupied by Al and O^{2-}. Each Al^{3+} is part of two such cubes, therefore every Al_4O_4-cube is connected to four others, sharing one corner. Each O^{2-}, therefore four per cube, is connected to a tetrahedron constituted of four O^{2-} with Mg^{2+} in the centre. One unit cell contains eight Al_4O_4-cubes and also eight MgO_4-tetrahedra. This structure allows a lot of flexibility since partially and full inversion is possible and not all interstices are occupied.

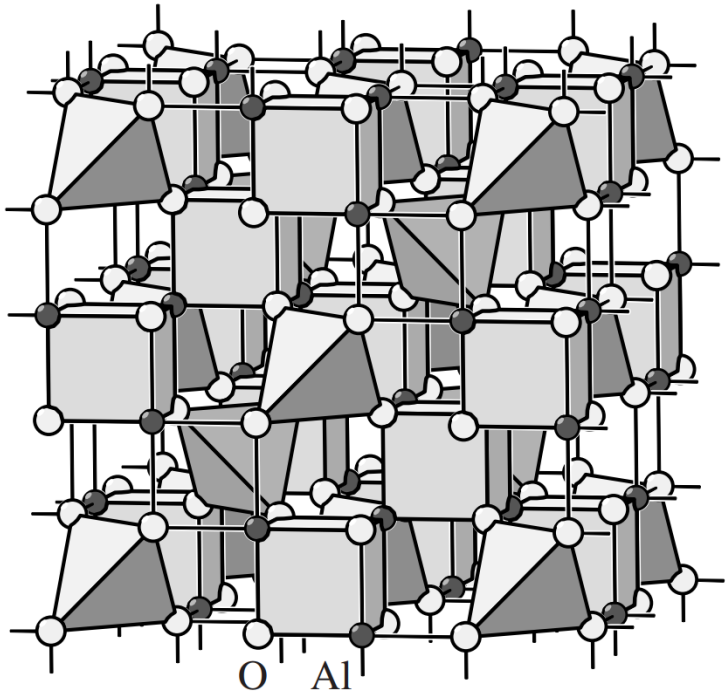

Figure 1-11. Spinel structure with Mg^{2+} located in the centres of the tetrahedrons, O^{2-} represented by white and Al^{3+} by black spheres.[157]

The probably most important property exhibited by some spinels is magnetism, appearing in the inverse spinel ferrites MFe_2O_4 with M being a divalent ion like Fe^{2+}, Ni^{2+}, Cu^{2+}, Mg^{2+}. The first practical application of magnetism was the development of compass needles with magnetite or Iodestone, Fe_3O_4, which was discovered many centuries ago in China.[159] Magnetite is related to γ-Fe_2O_3, which is also a spinel but it is Fe-deficient and therefore easily oxidises to magnetite. The

latter is very important for the application in magnetic data storage.[159] In ferrites, the magnetic spins of the ions on octahedral sites are antiparallel to the magnetic spins of the ions on tetrahedral sites, therefore ferrites are either antiferromagnetic or ferrimagnetic.

Other spinels also show paramagnetism, with cobalt ferrite even exhibiting superparamagnetism.[160] Applications of these magnetic spinels are in data storage, as mentioned above, but also envisaged in biotechnology or electronic industry. Since spinels exist in many different compositions, also other very interesting properties besides magnetism have been observed which enable them for applications in other fields. They were shown to exhibit optical, electrical and also catalytic properties, and the latter will be broadly discussed for the case of water oxidation in chapter 1.2.3.[161–166] The optical properties of some spinels, like electrochemical luminescence, or photoluminescence, make them interesting candidates for laser applications.[161,167] Due to their electrical properties, spinels are already applied for example in Li-ion batteries and investigated for Na-ion, Mg-ion and Zn-ion batteries.[168–170] Defects often increase the performance of spinels and also of other oxides for battery or catalytic applications.[170–172] One can differentiate between intrinsic and extrinsic defects. Intrinsic defects can be Schottky defects, which are point defects in crystal lattices, Frenkel defects, i.e. dislocation defects, and interstitial defects. Extrinsic defects are often caused by doping the materials with extra ions which usually substitute the A or M ions of the spinel.

1.2.2 Synthetic Methods for Spinels

Traditionally, spinels are synthesized using high temperature methods like calcination of the grinded precursors for a long period to overcome the diffusion barrier. With less energy consuming methods like sol-gel, coprecipitation, hydrothermal or solvothermal synthesis, these high temperatures and long reaction times can be circumvented. In this chapter, only the most important and common methods and those applied in the present thesis are discussed.

In high-temperature solid phase synthesis, the corresponding metal precursor like nitrates, halides, sulfates, oxides, hydroxides or carbonates are heated to temperatures ranging from about 550 °C to more than 1500 °C.[173–178] The most widely used compounds for thermal decomposition are nitrates. Often, two or more steps are applied with crushing the powders in between to redistribute the grains. This method can be easily applied in large-scale applications but with the major drawbacks of the high temperature and long reaction times. Often ball milling is used to increase the reaction rate and sometimes ball milling itself provides enough energy to decrease the synthesis temperature.[179] By reducing oxygen pressure during the calcination or treating the sample with hydrogen, defects can be introduced into the materials.[180,181]

A milder method is the so-called sol-gel approach. In this method, metal salts and a chelating agent are dissolved. As chelating agents, e.g. citric acid, propionic acid or ethylene glycol can be used.[182–184] For pore-formation, also glucose is often added to the mixture. The solution is heated up and reactions like hydrolysis and condensation start. Due to continuous heating, the solvent is slowly evaporated, and a gel is formed, which will then be calcinated to obtain the corresponding spinels.

A method where no calcination and therefore no high temperature at all is needed is hydrothermal synthesis. In this method, metal salt precursors are dissolved in water and the solution is sealed in an autoclave, usually a Teflon liner within some robust reactor, usually made of stainless steel. Upon heating, either in the oven or by microwaves with wavelengths from 1 mm to 1 m, the solvent heats up differently at different areas in the autoclave, leading to gradients in solubility and convective flows. In hotter areas there is an increased solubility, which can lead to precipitation by convection in colder areas. Upon more heating, the solvent start to evaporate and pressure is built up, which enables the reaction to generally proceed at lower temperatures. Spinels of various morphologies are obtained with this method ranging from 1D structures, nanorods and nanowires, over 2D features like squares, hexagons or other nanosheets to 3D spinels in octahedral or cubic shapes.[185–190] To increase monodispersity, the application of surfactants like ethyl alcohol seems to be useful.[191] Obviously, hydrothermal synthesis is a powerful method to obtain spinels in all kinds of shapes and with different morphologies, which can therefore be useful for various applications. As it cannot be applied for water sensitive compounds, solvothermal synthesis is then an alternative option. The principle is the same but instead of water, solvents like ethanol, ethylene glucol or isopropanol can be used.[192–194] Sol-gel and hydrothermal syntheses will be mentioned again in Chapter 2.1.

Another possibility to synthesize spinels is the precipitation method. The method starts from a solution from which the precursor precipitates after adding an according precipitant. Then, the precursor is annealed at high temperature to yield the spinel.[195] Often, NaOH or KOH are used as precipitants, but also Na_2CO_3, ammonia and others were applied.[196–199] To achieve porous structures, CO_2-forming agents like carbonates can be added.[200]

A very important synthesis method to yield films is electrodeposition, which is especially useful if the spinel is needed on a surface, e.g. as electrode materials. It is a cheap and fast synthesis and spinels with various morphologies can be obtained, like a 3D, self-assembled Mn_3O_4 hierarchical network but also quite compact films.[201,202] The morphology and structure can be adjusted by varying different precursor salts and the carbon source to salt ratio.[203]

A completely different method is chemical vapor deposition (CVD), where gaseous precursor decompose or react directly on a solid substrate, forming a high quality film. This method is similar to atomic layer deposition (ALD), which was developed by Suntola et al. in the 1970s.[204] This deposition is carried out in vacuum, where stepwise first a precursor adsorbs on a substrate then a second precursor is added, which reacts with the first precursor. Residues are always flushed away so that the desired thin film is formed layer by layer.

Another deposition technique, which is carried out in vacuum is magnetron sputtering. In ultrahigh vacuum, Argon ions (plasma), which are ionized by high-energy electrons are accelerated towards a target from which particles are then ejected and deposited on a substrate.

1.2.3 Co-containing Spinels as Water Oxidation Catalyst

As mentioned in chapter 1.1.2.3, the formation of CoO, Co_2O_3 and CoO_2 from metallic cobalt electrodes prior to oxygen evolution, indicating the oxides being the catalysts, was observed already in 1950.[106] Later, almost 40 years ago now, spinel-type Co_3O_4 was first used as an electrocatalyst for water oxidation. [205] A comparison of electrocatalytic activity for oxygen evolution from different metal oxides was published in 1984 by Trasatti et *al.*, showing considerably lower activity of Co_3O_4 compared to RuO_2 or IrO_2 (Figure 1-12).[206]

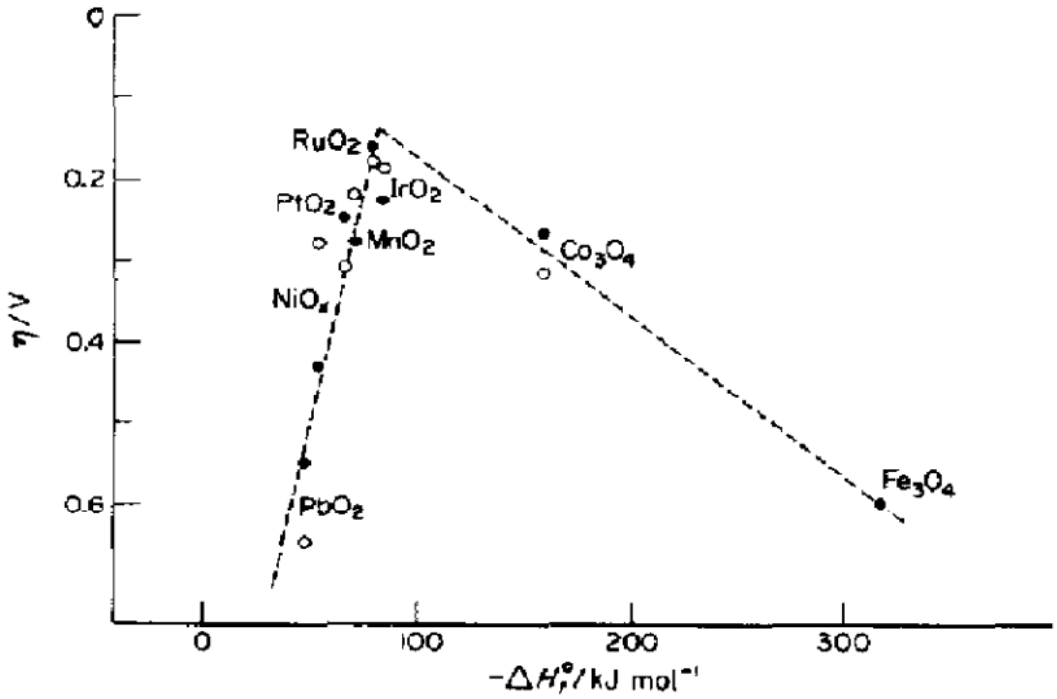

Figure 1-12. Electrocatalytic activity of O_2 evolution on metal oxide surfaces versus the enthalpy of transition in alkaline (°) and acid (•) solutions.

Spinel-type Co_3O_4 was also compared to other cobalt-containing metal oxide types, namely perovskite and wolframite whereof perovskite, or rather $LaCoO_3$, showed the highest activity, followed by Co_3O_4 (see also Table 1-1).[62] However these oxides are bulk materials and there are many possibilities to improve their activity by micro- or nanostructuring, integrated architecture designs, composition, crystallinity and morphology control. Kang et al. found Co(III) to play the more important role in electrocatalytic OER compared to Co(II) by comparing Co_3O_4 cubes which exhibit their (100) facets, and therefore only Co(II) on these surfaces, with (112) facets which partially also display Co(III).[207]

Co_3O_4 was synthesized in a wide variety of structures and morphologies, like nanoparticles, nanocubes, nanorods, nanotubes, nanosheets or with porous structures, to address the influence of architecture and facet exposure.[165,208–214] The advantage of nanostructures and porous materials is

the higher surface area with shorter diffusion lengths. Morphologies like interconnected mesoporous nanoflakes or defect-rich mesoporous cobalt oxide, obtained through Mg-leaching from Mg-substituted Co_3O_4, clearly outperformed bulk Co_3O_4.[215,216] The electrical structure of Co_3O_4 can be changed by doping with other metal ions, like Ni, Mn, Fe, Cu, but also Li, to improve the properties.[217–223] Another possibility is to load the catalyst on a conductive matrix. Electrochemically grown Co_3O_4 on an Au electrode was easier to be oxidized and therefore showed higher oxygen evolution activity due to the high electronegativity of the Au substrate and therefore resulting increased oxidation state of the Co cations.[224] This effect of substrate electronegativity contributes to the activity trend of cobalt oxide deposited on metal substrates, namely Au > Pt > Pd > Cu > Co, in line with electronegativity trends. But not only deposition on Au surfaces but even the construction of more advanced composites like Au@Co_3O_4 core-shell nanocrystals increase the efficiency of pure cobalt oxide.[225] Besides gold and the other mentioned metals as substrates, also highly conductive oxides like Tl_2O_3 or PbO_2 were used and recently, more and more carbon materials were identified as powerful supports as well.[226] Especially graphene with its high conductivity and chemical and mechanical stability is often combined with Co_3O_4 catalysts for increased performance.[227,228] This beneficial effect could even be improved by doping graphene and other carbonaceous materials with nitrogen.[229,230] The improved activity was explained by Fellinger et al. with a synergistic effect between the Co_3O_4 particles and the very conductive heteroatom doped carbon support, in which the electron transfer from the Co_3O_4 to the support may be facilitated by these heterojunctions and therefore preventing charge accumulation.[231] Besides the above discussed parameters like structure, architecture, and composition it is also important to consider the crystallinity of the discussed materials. In addition to the famous amorphous CoPi catalyst of Nocera discussed earlier, Switzer et al. also found amorphous Co_3O_4 to be more active than the crystalline form, whereas in our group it was shown that higher crystallinity is beneficial for the OER.[70,107,232] An essential distinction is that in these two studies the activity was examined by different methods. Switzer et al. tested the material for electrochemical OER whereas in our works the photocatalytic assay was used. The importance of oxidation method was also outlined by Stahl et al. and will also be a topic later in chapter 3.[91]

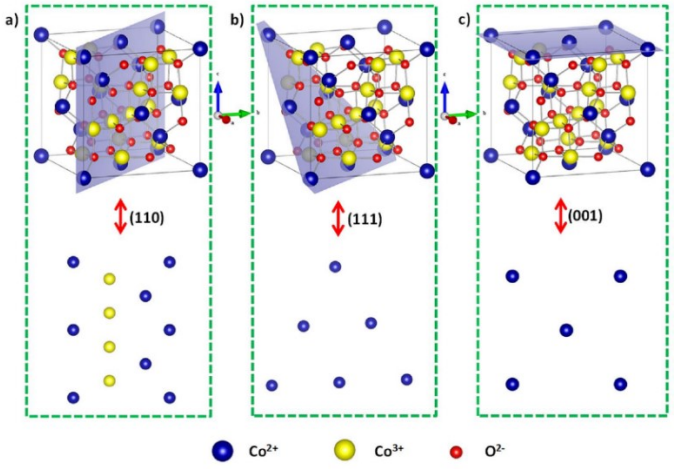

Figure 1-13. The 3D and 2D surface atomic configurations in (a) the (110) plane, (b) the (111) plane, and (c) the (001) plane of Co_3O_4.[233]

Water Oxidation Mechanism. A distinction must be made for the mechanisms proceeding in different pH regions. Here, only basic environments are considered since they are more important for the following results. Two possible mechanistic pathways were proposed in 2014 by Heinz Frei et *al.* and are shown in Figure 1-14.[39] In the fast mechanism two neighbouring oxo-bridged Co(III) cations catalyse the oxygen evolution by two first consecutive hole injections and proton emission steps, whereby both Co ions are oxidized to Co(IV)=O centers. In the next step, both Co(IV) centers are reduced to Co(III) again by the addition of H_2O, forming one Co-OH and one Co-O-OH peroxide species. The hydroperoxide is then oxidized by a further hole injection to the superoxide species, before the catalyst is returning to its ground state by the nucleophilic attack of another H_2O and hole injection by releasing O_2. The Co(IV)=O-O-Co(III)-OH resting state followed by the oxidation to Co(IV)=O-O-Co(IV) is in accordance with other studies.[38,105] Dau et al. investigated several catalytically active cobalt oxide structures and found that they all featured edge-sharing CoO_6 octahedra, corresponding to Co(III) in the normal spinel.[234] This is also consistent with results from Sun and his group, who found the (110) planes, which contain Co(III), to be more active than the (001) planes, which only contain Co(II) (see Figure 1-13).[235] The study of Fukuzumi et *al.* supports this finding due to the fact that the highest activity is attributed to $LaCoO_3$ in which Co(III) is stabilized in the perovskite structure.[62] Furthermore, Koel et al. investigated the facet dependence of catalysis and also found the cubes ((100) planes) to be less active but compared to the (111) planes, which he explained by the absence of Co(III) in 100 planes.[236]

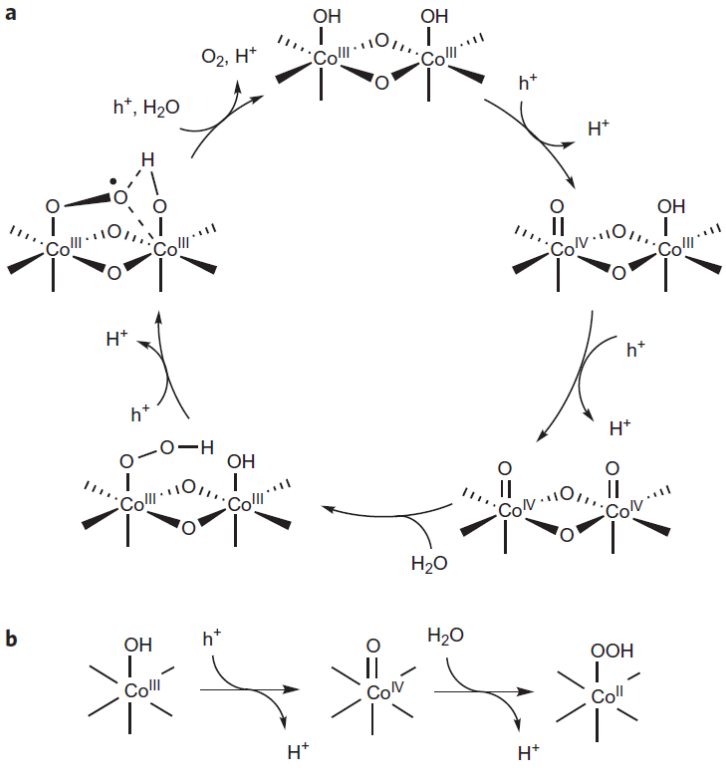

Figure 1-14. Proposed photocatalytic mechanism. a) Water oxidation mechanism of the fast Co_3O_4 surface site. b) Mechanism of the slow Co_3O_4 surface site. The OO bond-forming step with H_2O in the fast cycle features the cooperative effect of adjacent electronically coupled Co(IV)=O sites, which is absent in the H_2O addition reaction at the slow site.[39]

1.3 Scope of the Thesis

As outlined in the intrdoduction, the development of stable, efficient and affordable water oxidation catalysts is crucial for large-scale water splitting applications. Regarding practical applicability and stability, heterogeneous catalysts are superior to homogeneous catalysts. Therefore, catalytic performance optimization of heterogeneous materials is the most direct pathway to enable forthcoming water splitting applications. The target of this thesis was therefore to determine the most important materials characteristics for successful water oxidation with spinels, starting from Co_3O_4 as a competent catalyst and valid model system. Moreover, hitherto underexplored connections between the preparative history of cobalt spinels and their resulting relations between materials properties and performance were newly investigated in this thesis. To this end, a systematic study of the influence of different synthetic protocols on the detailed properties of cobalt spinels was conducted on different levels of detail, employing various water oxidation catalyst assessment methods. Additionally, mixed spinel-type transition metal (Mn, Fe, Co, and Ni) oxides were synthesized and characterized to explore the emerging intrinsic materials properties and synergisms with metallic components. The ultimate goal of such studies are general oxide catalyst design guidelines through identification of (1) the most influential parameters for water oxidation catalysis and (2) of the optimal synthetic procedures to achieve them.

2 Experimental Techniques and Background

2.1 Catalyst Preparation

The synthesis methods applied were already briefly discussed in the previous chapter but some more details will be given here.

2.1.1 Hydrothermal Synthesis

For the hydrothermal synthesis of pure Co_3O_4 or mixed spinels, the transition metal salts (usually acetates or nitrates) were dissolved in water before the addition of ammonia solution upon which the hydroxides were formed. The dispersions were filled in Teflon liners and sealed in stainless steel autoclaves which were heated in regular lab ovens to different temperatures up to 220°C. Growth mechanisms of cobalt oxide spinel were monitored with in situ powder X-ray diffraction (PXRD) in a previous study of our group.[165] It was found that the spinel phase is formed without crystalline intermediate but via amorphous oxides, as suggested from ex situ quenching experiment analyses. The growth mechanism was found to be but temperature dependent as indicated by two different slopes in the corresponding Sharp-Hancock plots and also by fitting the extent of reaction with the Gualtieri approach. The samples synthesized at the lowest temperature, 170 °C, were most probably formed by a mechanism related to phase boundary control. At 185°C the growth could best be described by the first-order model and for the highest temperature, 200°C, a Johnson Mehl Avrami Kolmogorov (JMAK) growth kinetic was most likely taking over, which is a phenomenological model for the growth kinetics proceeding via nucleation and growth at constant temperature.

2.1.2 Microwave Hydrothermal Synthesis

Microwave (MW) synthesis of various materials is becoming more and more important after the first article on the topic was published in 1986, since it is generally faster than standard previous methods and often proceeds at lower temperatures, giving rise to more diverse morphologies.[237] Many materials with industrial importance have now been synthesized by this technique like zeolites, complex oxides, silicides, apatite, carbides, nitrides, and others.[238–243] MW hydrothermal synthesis is related to hydrothermal synthesis carried out in an oven, but instead of direct heating, interactions of reactants and/or solvents with microwaves generated by magnetrons are speeding up the reaction. Microwaves are electromagnetic waves with very long wavelengths of 1-300 mm which interact with dielectric dipole moments resulting in chaotic motion and thereby generating heat. They are unable to break chemical bonds or to cause a shift in the chemical equilibrium due to the electric field. [244] Not all materials interact with microwaves. There are three different classes of materials regarding the interaction with microwaves; (1) materials that reflect MWs like brass and other bulk metals and alloys, which are therefore used in making microwave guides, (2) materials that transmit MWs like Teflon, several glasses, ceramics without transition metals and some more, which are employed as reactor materials and (3) the above-mentioned class of MW absorbers which thereby generate heat.[245] The microwaves used for the syntheses carried out during

this thesis have a wavelength of 12 cm and are randomly dissipated in the device by being reflected at the inside of the walls (Figure 2-1). The advantage of MW in comparison with infrared radiation from standard ovens is the shortening of reaction times. The synthesis of oxide nanoparticles is believed to occur through the formation of an amorphous gel by association of hydroxides followed by nucleation and growth.[244] The interactions between ions with water in solvation complexes are believed to be perturbed by MW energy, thereby enhancing the formation rate of M-O bonds. It is clear that the different species differ with respect to their absorption properties and it is also known that so called "hot spots" can form in a microwave reactor. What remains questionable is if this leads to significant variations in temperature in the reaction mixture or whether the heat dissipation is fast enough for the reaction mixture to be deemed isothermal. Microwaves generate an alternating field. If the dipoles of the medium cannot re-orientate fast enough a phase lag of the orientation results - and therefore a polarization current in phase with the applied field. Consequently, resistive heating occurs. In liquids (or other materials in which the dipoles rotate freely) the frequency of the dipole rotation determines the heat dissipation. The dielectric constant is frequency-dependent due to the characteristic relaxation times. For water at 20 °C, 2.45 GHz is the most efficient frequency regarding heat dissipation and therefore commercial MW ovens and also the laboratory CEM MARS 5 applied in the present thesis operate at this frequency.[245] As a last point, the reactor geometry is influential. The volume of the dielectric materials exposed to MWs has an effect on the electric field. It is maximized when dielectric resonance, which is possible for sufficiently large samples, can occur. For the synthesis of zeolite NaA, low crystallization and higher impurity level was found for the use of vessels with higher surface-to-volume ratio, attributed to the low penetration depth and the resulting energy build-up on the outside of the reaction mixture.[246]

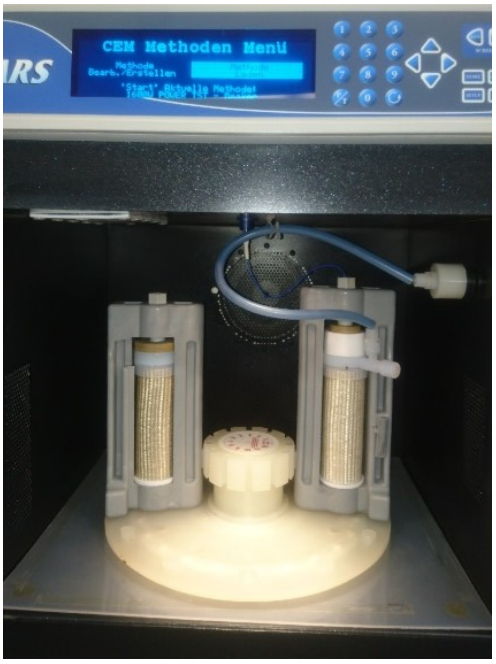

Figure 2-1. Inside of CEM MARS 5 microwave oven used for synthesis of Co_3O_4. Depicted is the rotary disk which can be equipped with up to 12 autoclaves. The autoclaves consist of a Teflon reaction vessel which is protected by a Kevlar cover and closed with a Teflon lid with an overpressure membrane. The reference vessel is equipped with a temperature glass fibre (blue cable) sensor and a pressure sensor (blue hose).

2.1.3 Sol-Gel Synthesis

Analogous to the two aforementioned hydrothermal methods, sol-gel synthesis has the advantage of comparable low reaction temperatures and in this case even lower costs since typical lab equipment without pressure resistant vessels is more convenient. Historically, metal alkoxides were employed as precursors in the sol-gel method since they readily undergo hydrolysis and condensation, forming a nanometre-sized metal oxide sol.[247] A sol or colloidal suspension is a suspension of very small particles, in which gravitational forces are negligible. Therefore the value of short-range forces like van der Waals or surface charge interactions is increased. From these colloids, ceramics can be produced via the sol-gel process. Typical precursors are nitrate or acetate salts and also metal alkoxides since they readily undergo full or partial hydrolysis. Partially hydrolysed precursors can undergo condensation reactions, forming larger structures, particles or even polymers; for bifunctional monomers (typical oxide monomers) into rings or chains, for functionalities > 2 random, three-dimensional structures are formed. These polymeric sols are for example formed by silica, whereas other oxides preferably give rise to particles. [248] Figure 2-2 shows the complete sol-gel process scheme. In this thesis, only the pathway from 'Sol' to 'Wet Gel' to 'Dense Ceramic' was applied with cobalt nitrate precursor and citric acid as chelating agent to yield Co_3O_4 nanoparticles of about 50 nm. This is not the traditional 'gels via hydrolysis and condensation' approach but the formation of small molecule gel approach, similar to the Pechini method.[249]

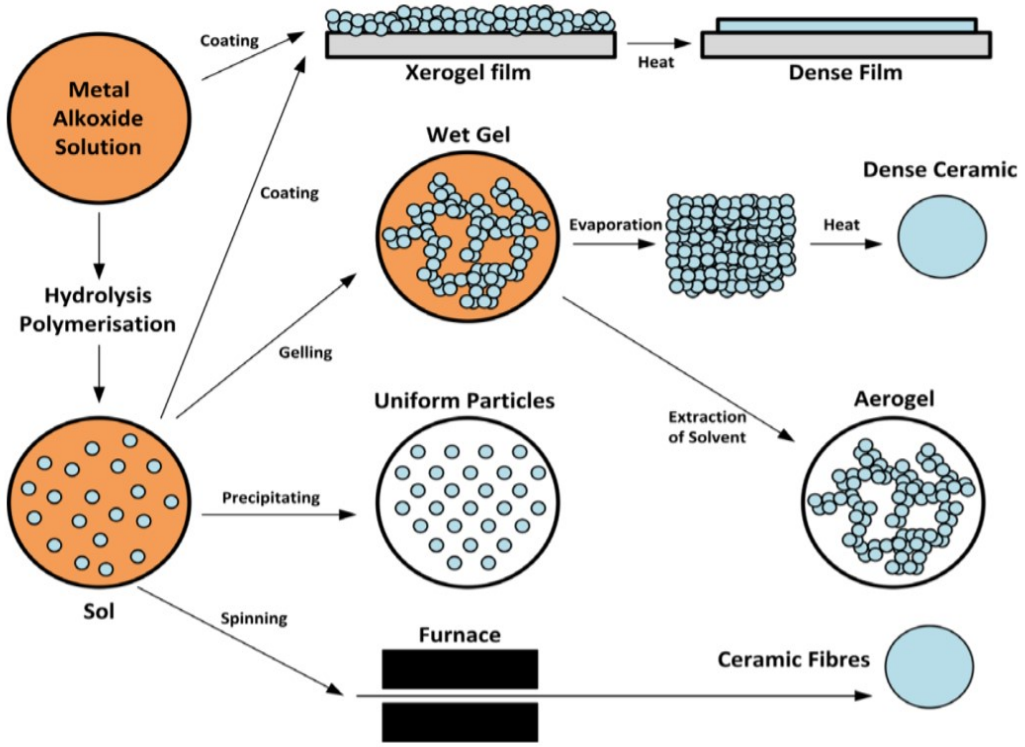

Figure 2-2. The sol-gel method for fabrication of nanoparticles.[250]

This approach is very common since many alkoxides cannot be formed or are not stable. Therefore, the strategy of using small molecules, most often chelating agents, is frequently applied. In aqueous solutions, water molecules coordinate to metal ions, thereby the O-H bond is weakened and deprotonation or hydrolysis, depending on the metal and pH, occurs (formula (7)).

$$[M(OH_2)]^{z+} \leftrightarrow [M-OH]^{(z-1)+} + H^+ \leftrightarrow [M=O]^{(z-2)+} + 2H^+ \qquad (7)$$

Non-aqueous solvents with low water content might be necessary for highly reactive metals. Usually the reaction in water can be controlled by adjusting the pH, shifting the equilibrium to the right at more basic pH and to the left under acidic conditions. This solution or suspension, however, is not the same as the gel of sol-gel synthesis, and by simply drying these solutions or suspensions either the applied precursor salts or some amorphous oxides/hydroxides are obtained. To obtain the desired products, small molecules are applied. They stabilize the formed structures in solution through gels. Chelating agents change the equilibria of formula (7), thereby making hydrolysis less favourable. Citric acid, a readily available and cheap triprotic acid, is one of the most common chelating agents for the small molecular gel method. The stability and homogeneity of the precursor solution strongly depends on the pH since cation binding of citric acid is enhanced or reduced.[251] This consideration is even more important in binary, ternary etc. compounds to ensure homogeneity of the resulting materials.[252,253] For the synthesis of metal oxide powders, this method is often applied. The gel is converted by pyrolysis in air at elevated temperatures, usually yielding to very homogeneous products owing to the organic matrix controlling the uniformity of dispersion of nucleation sites. The multitude of these sites ensure the small particle size of the products. The use of nitrates as precursors, besides being the transition metal source, has the advantage of being the oxidant in the self-propagating combustion with the citrate being the organic fuel.[254]

2.2 Analytical Methods

2.2.1 Powder X-ray diffraction (PXRD)

PXRD is an essential and very powerful characterization method for crystalline materials. It provides information about crystal system, lattice parameters and in certain cases the crystallite size or structure of the analysed materials. In PXRD, usually Cu, Mo or Co K_α radiations are used which have wavelengths similar to atomic distances in crystals.

Electrons of atoms are set into vibration when hit by an X-ray therefore emitting radiation coherent with the incident wave, without change of wavelength and energy loss, therefore being secondary point sources of X-rays. In crystals, since they are a periodically arrangement of atoms, incident coherent waves get scattered at different planes and interfere, either constructive or destructive, depending of the wavelength, the angle and the spacing of the planes. The constructive interference is described by Bragg's law

$$2dsin(\theta) = n\lambda \qquad (8)$$

where d is the distance between adjacent lattice planes, θ the angle of the X-ray and λ the wavelength. Under these conditions, the scattered waves interfere constructively showing a signal of the corresponding planes. By measuring X-ray diffraction, the angle is changed giving rise to a diffraction pattern; reflection peaks at certain angles. After the measurement, the powder pattern has to be indexed, meaning assigning the peaks to the h, k, l indices and obtaining the unit cell symmetry and dimensions. Structural details of measured powders can be confirmed by the so-called Rietveld refinement.

Another possible gain from PXRD is the size determination by means of Scherrer equation. Scherrer found that the peak broadening in PXRD pattern correlate to the size of sub-micrometre particles.[255] The particle size correlate to the peak broadening like in formula (9) with the crystallite size τ being dependent on a shape factor K (usually close to 1), the X-ray wavelength λ and the Bragg angle θ besides the peak broadening at full with half maximum (FWHM) β (without instrumental broadening).[256]

$$\tau = \frac{K\lambda}{\beta cos\theta} \qquad (9)$$

2.2.2 Brunauer-Emmett-Teller (BET) surface analysis

In heterogeneous catalysis the measurement of the surface area of the catalyst is important to compare and to standardize different catalysts, especially nanomaterials, where fraction of surface atoms is significantly higher than in bulk materials. The BET analysis is the most common surface area measurement method. It is named after Stephen Brunauer, Paul Hugh Emmett and Edward Teller who published the theory utilized for this measurement 80 years ago, namely the multi-molecular adsorption process.[257] The extended Langmuir's derivation for unimolecular layers to a concept for multimolecular layers and correlated the adsorption not only to surface area, but also to porosity, pore-size distribution and micro-pore analysis. The first underlying assumption is that the surface is homogeneous and the adsorption has no preferential site and occurs with maximum one molecule per site. Molecular interactions are neglected. The adsorption and desorption are in equilibrium. The reaction is not diffusion- but kinetically limited with the required energy provided as heat and each layer requiring the same energy for adsorption. The adsorption at saturation pressure (p_0) is assumed to be infinite, meaning the material is surrounded by condensed liquid-phase adsorbent. To model the adsorbed layers, an Arrhenius equation is used for adsorption/desorption rate kinetics regarding the surface coverage, resulting in the following formula:

$$V = \frac{V_m c p}{(p_0 - p)[1 + (c-1)\frac{p}{p_0}]} \tag{9}$$

With V being the volume of adsorbed gas, V_m the volume of the adsorbed monolayer, p the equilibrium and p_0 the saturation gas pressure and c the BET constant. For data evaluation, this equation is rearranged as a linear function of $\frac{p}{p_0}$:

$$\frac{1}{V\left[\frac{p}{p_0} - 1\right]} = \frac{(c-1)}{V_m c}\left(\frac{p}{p_0}\right) + \frac{1}{V_m c} \tag{10}$$

By plotting the left side of formula (10) against $\frac{p}{p_0}$ the intercept of the straight line is $\frac{1}{V_m c}$ and the slope is $\frac{(c-1)}{V_m c}$, therefore V_m and c can be easily evaluated. The specific surface area S (in m^2/g) can then be calculated using the following formula:

$$S = \frac{V_m N A}{22.4 \times m} \tag{11}$$

N is the Avogadro number, A the adsorption cross section of the adsorbed gas, m the mass of the measured compound and 22.4 the molar volume of a gas at standard temperature and pressure.[258]

2.2.3 Electron Microscopy

Electron microscopy is a very powerful and versatile characterization method for solids. It can provide different kind of information, like structure/morphology but also crystal structure or composition are possible to investigate. As depicted in Figure 2-3, scanning electron microscopy (SEM) starts at the upper range of optical microscopy at ~ 10 µm and works up to a resolution of almost 10 nm. For higher resolution, transmission electron microscopy (TEM) or even high-resolution TEM (HR-TEM), which makes it possible to see crystal planes or even atoms, is then used.

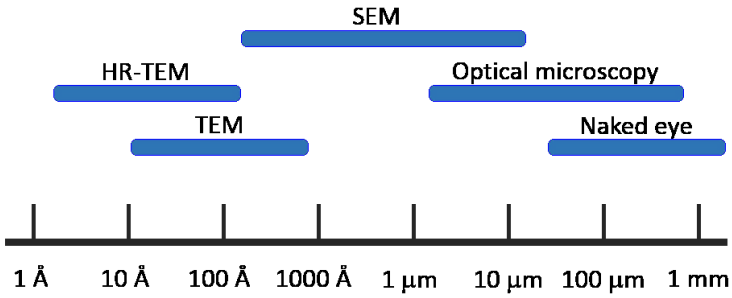

Figure 2-3. Working ranges of different microscopy techniques; adapted from Anthony R. West.[159]

Scanning electron microscopy (SEM). In SEM, mainly the texture and morphology of the surface is studied, but also the chemical composition can be investigated. A focused electron beam of 50-500 Å diameter is moved over the sample surface with a penetration depth of ≤ 1 µm.

Measuring the secondary electrons, generated when the electron beam hits an atom at the sample surface and an electron from the outer shell is emitted, is the most common imaging mode. If the irradiated atoms are heavier, backscattering of incident electrons is getting more frequent. Due to elastic scattering, these electrons maintain their incident energy and areas of different chemical composition can be detected, since the heavier atoms are backscattering more strongly and therefore appear brighter.

If the electrons of the electron beam hit the sample atom with enough energy, also electrons from inner shells can be ejected and because they occupied a lower energy level which is now vacant, outer electrons relax back to this level, emerging characteristic X-rays from which the involved atom can be determined. [159,259] If the device is equipped with and energy dispersive X-ray detector (EDX) the ratio of involved elements can be measured at high enough acceleration voltages. [159]

Transmission electron microscopy (TEM). TEM detects transmitted electrons and radiation and is a very powerful method so view the samples at very high resolution. Since the electrons have to penetrate through the sample, the sample thickness should not exceed 200 nm in order to not get completely absorbed by the sample.

For TEM imaging and diffraction, a parallel beam is used. To achieve the parallel beam, either the C2 lens is set to far underfocus, which produces a pseudo-parallel beam or it is set to overfocus to produce the cross-over on the front focal plane of the upper objective lens. From the forward elastic scattered electrons, two different kind of information can be obtained, which are contained in two different planes, the diffraction and the image plane. For the imaging mode, the objective aperture is put into the first intermediate diffraction plane and the intermediate lens projects the first onto the second intermediate image plane which is then magnified and projected on the fluorescent screen or detector by the projector lens.

In the diffraction mode, the objective aperture is removed from the beam and the selected area electron diffraction aperture is inserted to define an area of the sample from which the diffraction pattern is recorded. Compared to X-ray diffraction, the intensities of the diffracted beams in TEM are sample thickness dependent and therefore cannot be used for crystal structure determination. Still, unit cell information and space group data and can be obtained by this technique. [159,260]

2.2.4 X-ray Photoelectron Spectroscopy (XPS)

XPS measures the kinetic energy of electrons that are emitted from the sample after irradiation with X-rays. The high energy of the X-rays ionize electrons from different shells of the atoms. As X-ray sources, usually Mg K_α (1254 eV) or Al K_α (1487 eV) are used. After electrons from inner shells are photoemitted, electrons from outer shells relax to these lower energy levels, emitting X-ray fluorescence. This radiation can cause the emission of outer shell electrons, the so-called Auger electrons (see Figure 2-4). Depending on the binding energy of the ionized electrons, which is determined by the nucleus and the valence shell of origin, the resulting energy of the emitted electrons is different and distinct. From the spectra, the binding energies can be determined according to the following formula:

$$E_K = hv - E_B - \varphi \qquad (12)$$

with E_K being the kinetic energy of the measured electrons, E_B the binding energy of the electron, hv the photon energy and φ the work function, which depends on the materials as well as the spectrometer. Therefore, every element has a characteristic spectrum, allowing for the identification of the involved atoms. Since not only the energy but also the number of electrons is measured, the quantity of the measured elements can be determined, indicating the sample composition. XPS is a surface sensitive technique since the low energy of ejected electrons does not allow them to travel long distances through matter, which absorbs the electrons. In addition to the element composition, also the local environment of a surface atom can be investigated. This is possible due to the change in binding energy depending on the interactions of the surface atoms to ligands like for example surface bound water or –OH. This change slightly shifts the peaks depending on the electron density change caused by the ligand. Consequently, also oxidation states have an influence on the peak position.[159]

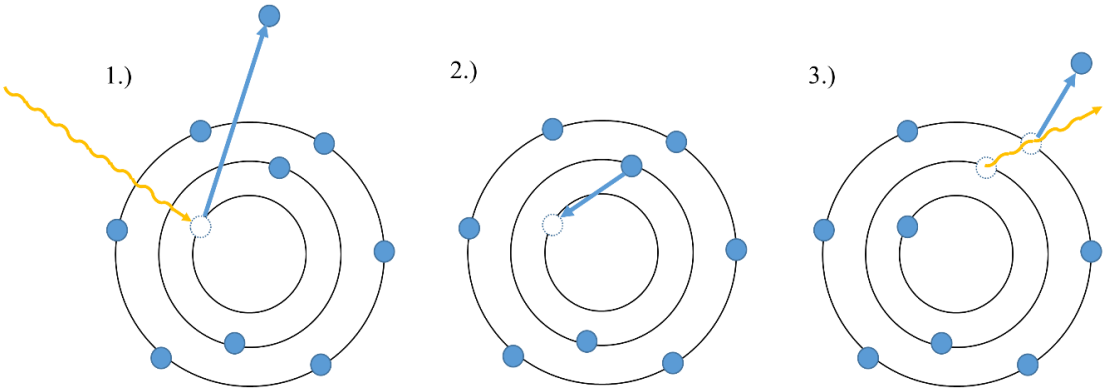

Figure 2-4. 1.) Excitation of core level electron followed by 2.) relaxation of outer electron and 3.) emission of Auger electron or X-ray fluorescence.

A bit more emphasis is laid on shake-up satellites, Auger parameter and Wagner plot, since the materials in the next chapters are characterized accordingly. Shake-up satellites occur, when the emerging electron interacts with another valence electron, thereby reducing its kinetic energy. This gives rise to a smaller peak, the shake-up satellite, up to 15 eV lower than the main peak, usually in the 2p spectra of first row transition metals.[261] The origin of Auger electrons is already explained above. A core electron is emitted due to photoexcitation, an outer electron relaxes into that core level releasing energy, which can cause the emission of another outer electron, an Auger electron. Auger peaks are named according to the shell from which the first electron was ejected (e.g. K, L, M), the shell from which an electron relaxed back into the first vacancy (e.g L, M, N) and the shell from which the Auger electron is emitted (e.g. L, M, N). In solids this can also be the valence band (V). The Wagner plot shows measured values of kinetic energies of a specified Auger peak versus the measured binding energies of a specified photoelectron peak and therefore is a good analytical tool for chemical state analysis.[262] The same element contained in different materials can thus be compared. The sum of the photoelectron binding energy and the Auger electron kinetic energy is called the modified Auger parameter, which is insensitive to charging of a non-conducting specimen, and can be included as diagonal lines in the Wagner plot.[263] The magnitudes of chemical shifts of these energies can assist in the identification of chemical state.

2.2.5 X-ray Absorption Spectroscopy (XAS) EXAFS/XANES

To obtain information of the oxidation states and local environment of the bulk materials, XPS cannot be used. As an alternative method, X-ray absorption can provide this information. X-ray absorption techniques are very powerful to study local structures, but they require high energy radiation which usually is generated at synchrotrons. Electrons from different shells are excited by absorbing X-rays but also intershell transitions occur. Exciting electrons from the inner K shell requires much more energy (almost 9 keV for Cu) than from the L shell (~ 1 keV) which corresponds to the 2*s* and 2*p* electrons. Atoms give rise to characteristic X-ray absorption spectra depending on the local environment as explained for XPS analysis. For the XAS measurements, the the X-ray energy is increased steadily. Only after the energy is sufficiently high to eject an inner electron, the absorption increases rapidly. For non-centrosymmetric atom coordinations, the otherwise forbidden 1*s* to 3*d* transition can occur at slightly lower energies, which is visible in the spectra from the pre-edge peak (Figure 2-5).

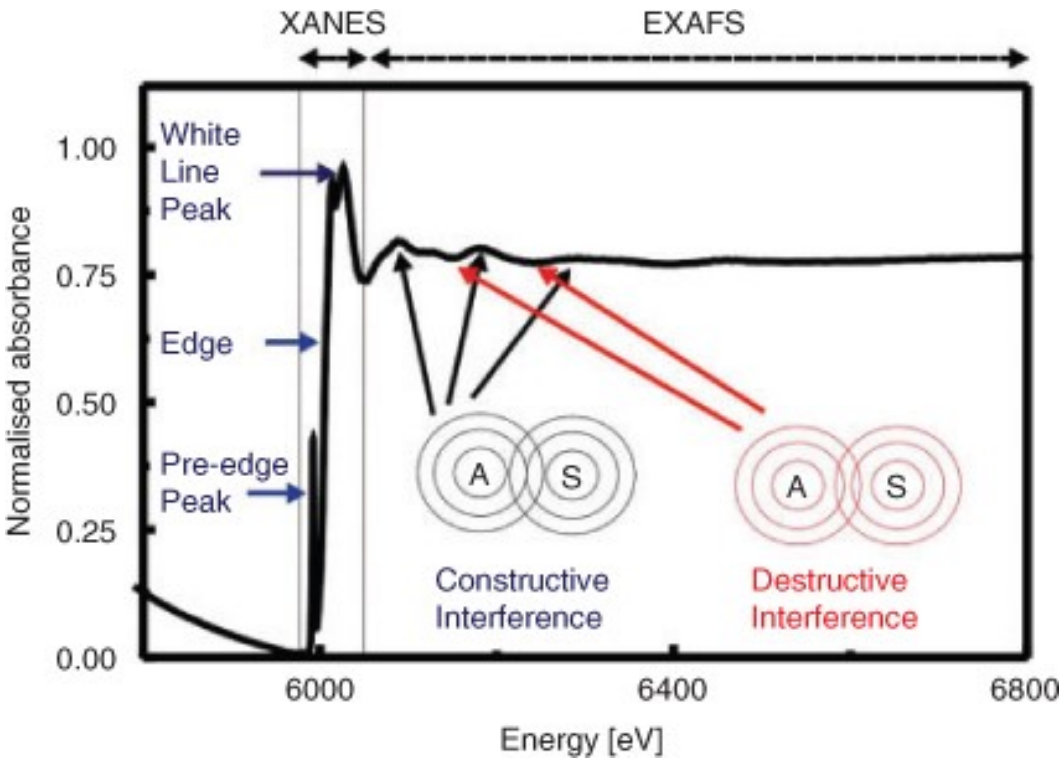

Figure 2-5. Typical XAS spectrum defining the XANES and EXAFS regions and showing key spectroscopic features.[264]

Figure 2-5 shows a typical XAS K edge spectrum with the X-ray absorption near edge structure (XANES) and extended X-ray absorption fine structure (EXAFS). From both regions, different information can be obtained. In XANES spectra, inner shell transitions become visible. In Figure 2-5 for example, the pre-edge is caused by the $1s \rightarrow 3d$ transition in Cr, and the edge arises from the $1s \rightarrow 4p$ transition. The edge position therefore depends on the oxidation state of the investigated element, the surrounding ligands and the symmetry. If the atom has a higher oxidation state or less electron density than the neutral element, the electrons more strongly bound to the nucleus and therefore more energy is needed to ionize them, shifting the edge to the right. At higher energies compared to the edge, the EXAFS region starts in which the absorption with increasing energy over a wide range is measured. This provides information about the local structure around the investigated atom and the bond lengths. When electrons get ejected, their wave properties interact with neighbouring atoms which then act as secondary scattering sources. Depending on constructive or destructive interference of this scattering, peaks or valleys of absorption are measured. From the periodicity of the EXAFS curve, the bond length can be determined due to the proportionality with the X-ray wavenumber and the intensity of this curve provides information about the neighbouring atoms.[265] By Fourier transformations the FT$|k^3\chi(k)|$spectra are obtained and then fitted with possible scattering paths, leading to interatomic distances, atomic coordination number (N) and Debye-Waller factors (σ^2) which correlate with the disorder of the material.

2.3 Water Oxidation

2.3.1 Photocatalytic Water Oxidation

An overview of photocatalytic water oxidation was already given in chapter. However, in this chapter, the focus is placed on the applied method, the $Ru(bpy)_3^{2+}$ /$S_2O_8^{2-}$ (bpy=2,2'-bipyridine) approach with heterogeneous water oxidation catalysts. $Ru(bpy)_3^{3+}$ is often used as primary oxidant for the water oxidation reaction due to its high quantum yield of photogeneration and a wide range of reduction potentials which can be adjusted by ring substitutions and also as a one-electron oxidant. The primary oxidant $Ru(bpy)_3^{3+}$ is generated in situ by light-driven excitation and subsequent quenching of the photoexcited state $Ru(bpy)_3^{2+*}$. For this oxidation, a sacrificial electron acceptor is used – in this case $Na_2S_2O_8$ or $S_2O_8^{2-}$.

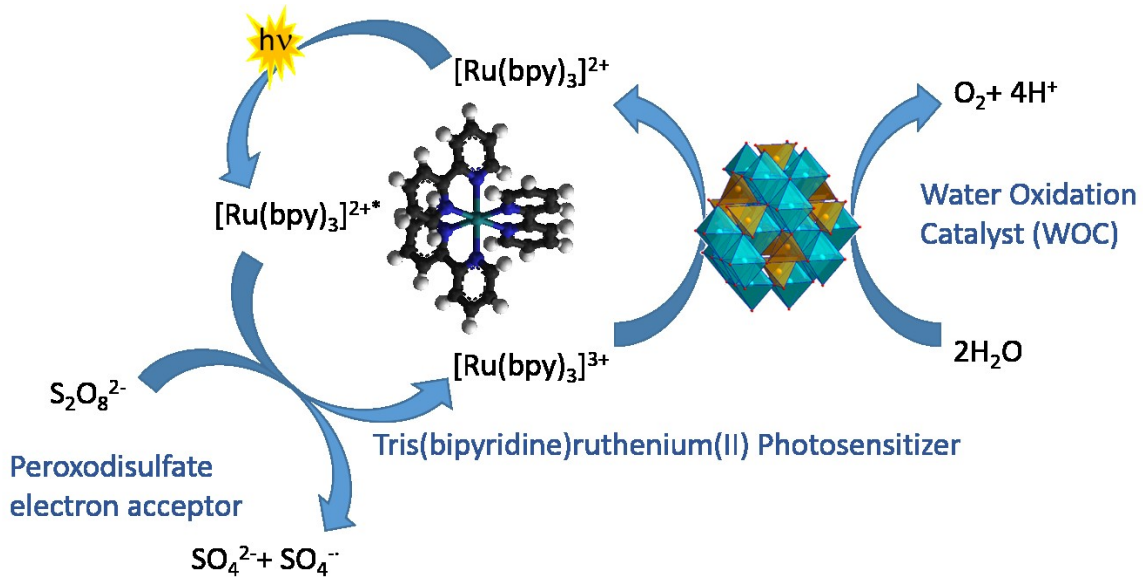

Figure 2-6. Scheme of photocatalytic water oxidation with the $Ru(bpy)_3^{2+}/S_2O_8^{2-}$ assay and spinel type Co_3O_4 as WOC.

The scheme of these reactions is depicted in Figure 2-6. $Ru(bpy)_3^{2+}$ is excited by visible light, therefore being easily oxidized to $Ru(bpy)_3^{3+}$ by $S_2O_8^{2-}$ forming a sulfate ion and a sulfate radical by dissociative electron transfer. This radical is also a strong oxidant and can either oxidize another $Ru(bpy)_3^{2+*}$ but also the WOC directly, wherefore the concentration of the photosensitizer has to be considerable higher than the concentration of the WOC to ensure the preferential oxidation of the photosensitizer. The so-generated $Ru(bpy)_3^{3+}$ then oxidizes the WOC in four consecutive electron transfer steps which thereby oxidizes water to oxygen.[32,48]

Besides reagent concentrations, other parameters like light source, pH and buffer play an important role. The pH-dependence can be clearly seen from Figure 1-14 by the removal of an H^+ by OH^- forming water and the generation of H^+, which gives rise to the need for a buffer. Various buffer solutions have been studied, e.g. by Mallouk et *al.*, who found Na_2SiF_6-base buffers to improve the turnover number of IrO_2 catalyst whereas phosphate-borate buffers increase the effect of photosensitizer degradation.[266] However, Na_2SiF_6 works for slightly acidic solutions and is poorly soluble, therefore phosphate and borate buffers are still frequently used.[266,267] In this thesis, borate buffer was always used since the phosphate buffer was found to coordinate to the WOC and to lower the systems' activity whereas with borate buffer the IR spectra of the WOC did not change significantly.[37]

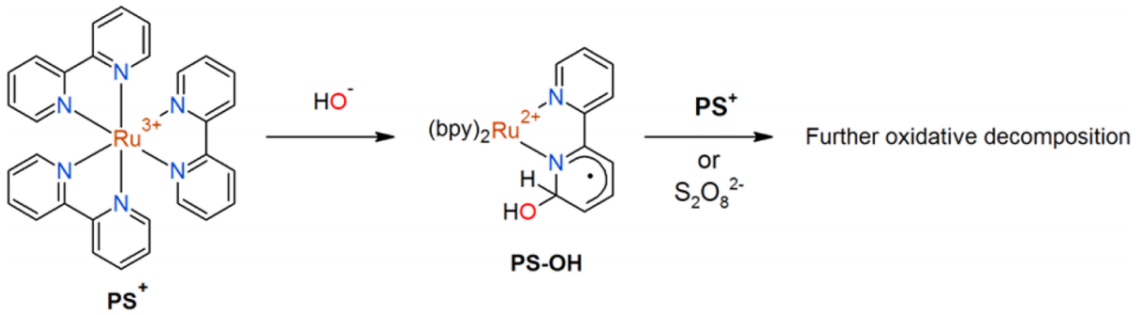

Figure 2-7. Decomposition of the photosensitizer: after the attack of a hydroxide anion to a bipyridine, the molecule undergoes further oxidations which can be performed either by another molecule of $Ru(bpy)_3^{3+}$ or by $S_2O_8^{2-}$.[268]

A major drawback of this method is the instability and decomposition of the photosensitizer in neutral to basic solutions according to Figure 2-7. The α-carbon of a pyridine ligand gets attacked by a hydroxide anion which then undergoes further oxidation reactions with either $Ru(bpy)_3^{3+}$ or $S_2O_8^{2-}$ as was already described in 1984 by Gosh et al.[269] This problem becomes less relevant if the catalyst kinetics are slow and the water oxidation to oxygen is the rate limiting step. If, however, the catalysts are fast enough and the electron transfer from WOC to photosensitizer becomes the rate determining step, $Ru(bpy)_3^{3+}$ builds up and can therefore decompose to a higher extent.[268] Another decomposition pathway is induced by light. Not only $Ru(bpy)_3^{2+}$ but also $Ru(bpy)_3^{3+}$ becomes photoexcited and can then produce Ru μ-oxo dimers via decomposition of an intermediate formed by a reaction with $S_2O_8^{2-}$. These dimers are still active but if they oligomerize they become inactive.[270] Overall, the $Ru(bpy)_3^{2+}$ /$S_2O_8^{2-}$ approach is a quite complex one compared to e.g. chemical oxidation with CAN (discussed in the next chapter) due to the interplay of WOC, photosensitizer, electron acceptor and also buffer and light.

2.3.2 Chemical Water Oxidation

The most straightforward (dark) water oxidation test method is the chemical oxidation using CAN as already introduced in chapter 1.1.2.2. This method was also applied in the course of this thesis. The measurements were conducted in a two-necked round bottom flask equipped with a luminescent dissolved oxygen (LDO) sensor directly measuring the oxygen concentration of the previously degassed solution. The exposure of the solution to atmospheric oxygen is prevented by an Ar stream during the addition of the WOC. After the addition of WOC to the solution, the sacrificial oxidant CAN with a sufficient redox potential (1.7 V vs NHE) can oxidize the catalyst which then oxidizes water to O_2 in four consecutive steps, since CAN is a one-electron oxidant. Like with the ruthenium photosensitizer in the photocatalytic protocol, there are as well drawbacks with the CAN system: upon reduction from Ce^{IV} to Ce^{III} insoluble cerium oxide can be formed with increasing pH, therefore the CAN method can only be applied in very acidic pH regions.[82,271] Also its high reduction potential of ~1.75 V vs. NHE at the commonly used pH region of 0.9 can be considered as a drawback since the resulting high overpotential not only successfully drives the water oxidation but it also makes side reactions more likely to occur.[82] Finally, the systems using sacrificial reagents, such as the photocatalytic system described above, are of course only an approximation of the final version water oxidation device and even if they can give a good indication of functionality, their limitations as model systems have to be kept in mind.

2.3.3 Electrocatalytic Water Oxidation

In this chapter, the electrochemical measurement techniques applied in this thesis are introduced. Before measurements, the catalyst has to be immobilized on a conductive electrode surface. Generally, the WOC was dispersed in water, drop-casted on fluorine-doped tin oxide (FTO) and fixated with Nafion after drying. The measurements were carried out in a standard three-electrode setup with Pt as counter and Ag/AgCl as reference electrode. Both electrode types were recently under discussion due to possible stability issues.[272,273] However, the applicability of the counter – and reference electrodes depend on the applied conditions as well as on the scope of the study. Pt dissolution is an issue in acidic conditions, whereas in basic conditions the effect is much smaller.[274] Furthermore, Pt is not quite active for water oxidation in the potential range which is usually applied as shown in chapter 4.4.2. In addition to the fact that Ag/AgCl is still used as reference electrode also in basic media, we showed with control experiments its applicability for comparison studies (chapter 4.4.2).[275–277]

The first measurement technique applied was cyclic voltammetry (CV). In CV, the potential against the reference electrode is swept back and forth between fixed potentials in defined steps and the current is measured. If the applied potential plus the necessary overpotential correspond to a redox potential of the catalyst, a peak can be observed and if the redox potential of water oxidation is reached, oxygen is formed and the current increases significantly. The overpotential is the potential which has to be applied additionally to the thermodynamically necessary potential due to the resistance and mass-transport limitations in an electrocatalytic cell.[278] Since the system conditions are kept constant, the overpotential is then a feature of the working electrode and therefore the catalyst attached to it. In that respect, the Tafel equation, which relates the rate of an electrochemical reaction to the overpotential, provided an important benchmarking method.[279] The rate is represented by the current density j, to which the overpotential η is logarithmically related as

$$\eta = a + b \log (j) \qquad (12)$$

The Tafel slope b relates to the mechanisms on the electrode surface. A high Tafel slope b indicates that the overpotential has to be increased drastically to increase the reaction rate by a factor of ten. Therefore, a small b and a high so-called exchange current density j_0 at $\eta = 0$ are desirable for a catalyst. For the comparison of exchange current density, the number of active sites is an important factor. Therefore often the overpotential required to obtain a certain current density, like 1 or 10 $mAcm^{-1}$ is provided instead.[280]

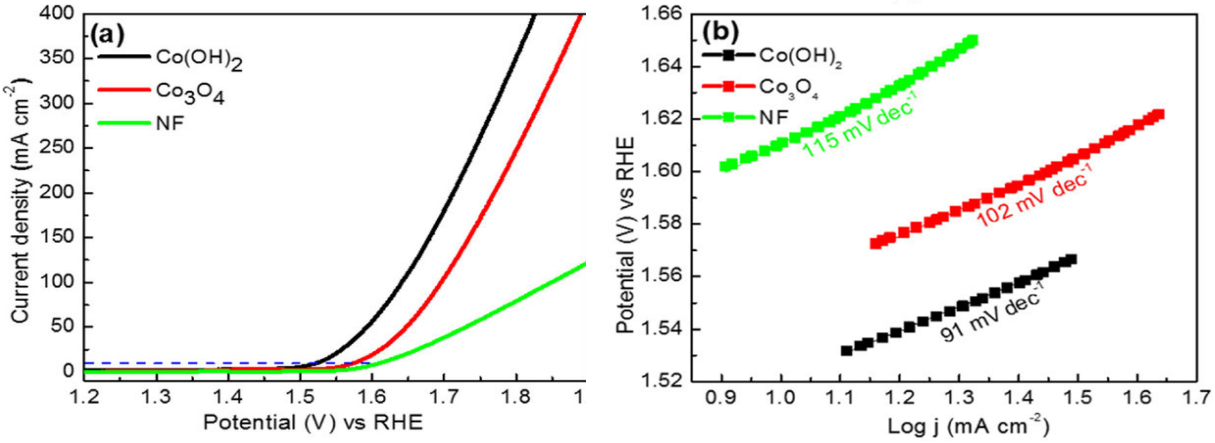

Figure 2-8. (a) OER polarization curves scan rate of 5 mV s^{-1} (b) corresponding OER Tafel plots of $Co(OH)_2$ and Co_3O_4 on nickel foam (NF).[281]

The other technique applied in this thesis is chronoamperometry. Here, the potential is fixed or stepwise adjusted and the current is measured as a function of time. The fixation of the potential allows for stability monitoring of the electrode since the current also should be constant for a stable electrode. The stepwise increase allows for the activity determination as in CV, but the diffusion current is circumvented, and the Faradaic current can be determined for sufficiently long holding times.

Generally, electrocatalytic water oxidation is a complex reaction regarding the mechanism and pathways, which can change for different surface structures.[282] If the thickness or structure of oxides with identical composition show some differences, this can already be enough to exhibit different electro-kinetic profiles, thus rendering the development and testing of electrocatalysts a challenging task.[280] Another important finding that has to be considered for electrocatalytic assessment of WOCs besides stability and synthetic history of the catalyst is the reversible formation of a thin amorphous surface layer, as found for Co_3O_4 by Dau et *al.*[283]

3 Preparative History vs Driving Force in Water Oxidation Catalysis: Parameter Space Studies of Cobalt Spinels

This chapter is based on the following publication:

Preparative History vs Driving Force in Water Oxidation Catalysis: Parameter Space Studies of Cobalt Spinels, Karla Lienau, Lukas Reith, C. A. Triana, Sebastian Siol, and Greta R. Patzke, *ACS Omega* **2019**, *4*, 15444−15456.[284]

Author Contributions: Lukas Reith performed the hydrothermal, precipitation method, thermal decomposition and molten salt syntheses as well as nitrogen sorption measurements, Raman and PXRD characterization and TEM imaging of some samples. Furthermore, he carried out the photocatalytic measurements. C. A. Triana evaluated the XAS data measured by S. Esmael Balaghi. Sebastian Siol performed and analysed XPS measurements of selected samples.

3.1 Introduction

As mentioned in chapter 1.1.2.1 development of stable, economic and efficient water oxidation catalysts is a major goal. However, it is still under investigation, which parameters are decisive for high water oxidation activity in heterogeneous catalysis. Furthermore the problem of predictivity of synthetic protocols is still a limiting factor, so that frequently no exact control of crucial parameters like crystallinity, defects, surface area and exposed planes or even structural motifs is possible.[285–288] Another problem is that the key parameters required for optimal performance in turn can often depend on the catalytic test method.[82,91,289] Few systematic studies to date shed light on these essential foundations of catalyst production, and in the following we discuss them for Co_3O_4 as a binary WOC model system.

In chapter 1.2.3, the investigations on spinel-type Co_3O_4 as abundant, low-cost and robust alternatives to the "gold standard WOCs" containing noble metals, i.e. Ru, Pt, and Ir, were discussed. Furthermore, Co_3O_4 attracts intense research interest in a wide range of other applications, e.g. in battery electrodes, sensors, data storage, as well as general heterogeneous catalysis as briefly mentioned in chapter 1.2.1.[290–296] Therefore, considerable attempts have been made to improve the moderate oxygen evolution reaction (OER) performance of pristine Co_3O_4, which is attributed to poor conductivity and a low number of exposed surface active sites, by adjusting a diverse range of performance parameters, such as crystallinity, oxidation states, surface area and particle/crystallite size, defects, crystal structure and morphology.[39,71,76,283,297–310] The crystallinity is clearly an important factor but how exactly it affects the performance is still under

investigation. Whereas some studies studies claim that higher crystallinity improves the WOC activity, others came to the conclusion that amorphous catalysts perform better.[70,71,283,311] A very interesting work of Dau, Strasser et *al.* even show reversible amorphization of the Co_3O_4 electrocatalyst during water oxidation.[283] Furthermore, the results on the impact of oxidation state, i.e. the Co^{2+}/Co^{3+} ratio, in literature are sometimes contradictory.[298,299] For surface and/or particle size, however, the trend is towards the smaller the particle size, the better the performance. For quantum dots it was shown that in addition to the increased surface area and therefore the higher number of exposed catalytic sites, also the intrinsic electroactivity could be improved due to quantum confinement.[76,300,305] Recently, defects, especially oxygen vacancies but also cobalt defects, were shown to create reactive sites in catalysts, improving the activity compared to the corresponding bulk material considerably. These defects, which can be generated post-synthetically e.g. by plasma engraving, but also by simple annealing at different temperatures and atmospheres, have a great influence on the interaction between the reactants and the catalyst surface. But not only exposed sites were influenced by the defective structures but also the electronic conductivity was improved.[301,308–310] Regarding the crystal structure, the discussions are quite similar to the discussions on the oxidation states mentioned above. Higher activity attributed to certain crystal planes is mainly explained by the amount of exposed Co^{2+}/Co^{3+} sites, but diverse opinions are represented in literature. For example, it was shown that the {100} crystal planes are inferior compared to {110} and {112} regarding the WOC activity due to their Co^{2+}-Co^{2+} sites. However, many studies support the responsibility of Co^{3+} for higher activity, thereby supporting the proposed mechanism of Heinz Frei described in chapter 1.2.3 and shown in Figure 1-14.[39,302,303]

With the aim to influence the aforementioned performance parameters, a wide range of different synthetic methods have been applied in the course of various independent roads to Co_3O_4, including molten salt, ball milling, sol-gel, thermal decomposition, precipitation and classic or microwave hydrothermal synthesis.[154,312–320] However, the impact of the various preparations on the catalytic efficiency of Co_3O_4 in different assays has not been evaluated coherently to date. Generally, deriving clear synthesis-activity trends from comparisons between different studies remains difficult due to the underlying variations in the obtained materials properties.[321–323] To facilitate forthcoming synthesis planning for WOCs, (a) studies on coherent synthesis-properties relationships are required which are (b) correlated with the results for the most important catalytic tests for water oxidation performance. The three most common routine tests are: (1) photochemical oxidation through the use of the well-established $[Ru(bpy)_3]^{2+}/S_2O_8^{2-}$/visible light assay (chapter 1.1.2.1, Figure 2-6), (2) chemical oxidation typically performed with ceric ammonium nitrate (CAN) (chapter 1.1.2.2), and (3) electrochemical methods (chapter 1.1.2.3). To date, however, studies presenting critical comparisons between two or more catalytic test results for a given WOC remain quite rare, and activity trends for one assessment method were often implicitly assumed to be valid for another. Only in 2015, a pioneering study by S. S. Stahl et al. provided the first critical assessment of the influence of the employed oxidation method for different manganese oxides and demonstrated that the “best catalyst” indeed depends on the selected oxidation method.[91]

We here developed this methodological approach further by selecting one target material, namely spinel-type cobalt oxide WOC, and first applying a spectrum of synthetic methods that can be roughly classified in high and low temperature methods. Next, the influence of these preparative routes on the WOC activity was specifically assessed with the three aforementioned catalytic test methods. The emerging synthesis-activity trends were then substantiated with thorough characterizations of the different Co_3O_4 materials with a wide analytical repertoire, including diffraction, spectroscopy, and microscopy techniques. This three-step strategy provides insight into the correlations between the preparative history of Co_3O_4 specimens and their emerging materials properties with the resulting catalytic performance in different test setups. Our results provide highly sought-after comprehensive guidelines for selecting the best preparative approach for a given water oxidation catalysis route

3.2 Aims of the project and principal outcomes

As mentioned above, spinel-type Co_3O_4 is amongst the most promising materials for water oxidation, due to its low cost and robustness. However, Co_3O_4 can be prepared by a variety of different methods and therefore, we synthesized cobalt oxide with 9 different well-established synthesis strategies. The cobalt oxides were characterized by a number of analytical methods, including XAS, XPS, PXRD, Raman, BET, and TEM to investigate their influence towards materials properties and efficient catalysis. Furthermore, in literature water oxidation catalysts are routinely tested by only one of the three typical oxidation methods: photocatalytically, electrocatalytically or by chemical oxidation. Hence, we also evaluate the synthesized Co_3O_4 with the three oxidation methods, resulting in diverging trends for each oxidation method. The importance of the surface area, the increase in disorder and the decrease in oxidation states of the material for superior catalytic activity was found specifically for chemical oxidation. These properties were found for samples synthesized at lower temperatures ($\leq$ 180 °). For photocatalytic water oxidation the correlation was not as clear but in general, also the samples synthesized at lower temperature were more active. In electrocatalysis, no such trend was found and all samples showed similar activity towards water oxidation. Therefore, we illustrate the importance of preparative methods for catalytic materials as well as the major influence of the applied oxidation method.

3.3 Experimental

Syntheses and measurements are marked with * if completely or with (*) if partially carried out by Lukas Reith. XAS measurements were performed by S. Esmael Balaghi and Wenchao Wan and analysed by Dr. Carlos A. Triana ($^{\Delta}$). XPS spectra were measured and evaluated by Sebastian Siol ($^{\nabla}$).

3.3.1 Synthetic Procedures

In order to obtain a broad range of different samples, spinel-type Co_3O_4 was synthesized by nine different methods:

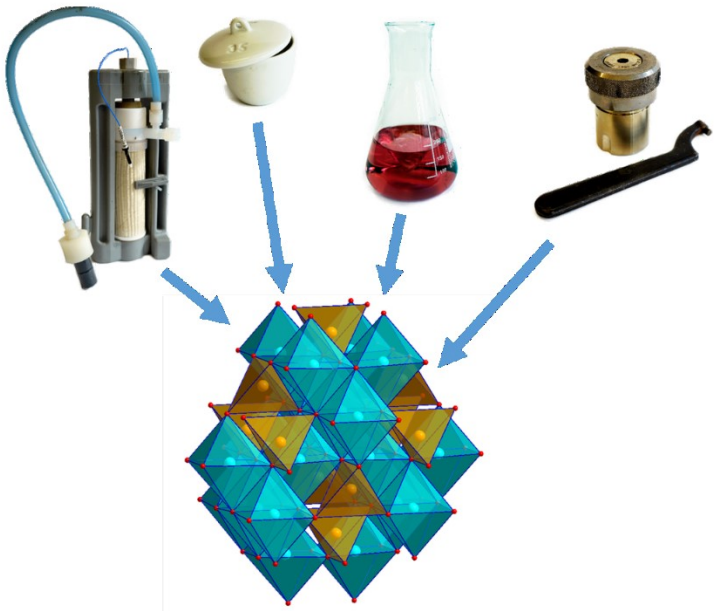

Figure 3-1. Different synthesis methods were applied to produce spinel-type Co_3O_4 (Figure adapted from ref 284).

***Hydrothermal synthesis (HT-A).**[318] For the hydrothermal synthesis, 0.24 g urea (4 mmol) and 0.2328 g $Co(NO_3)_2{\cdot}6H_2O$ (0.82 mmol) were dissolved in 10 mL of H_2O_2 (30 wt%) solution under vigorous stirring. The homogeneous reaction solution was transferred to a 15 mL polytetrafluoroethylene(PTFE)-lined stainless steel autoclave and heated to 150 °C (4.5 C° min^{-1}). The holding temperature was maintained for 3 h. The autoclaves were cooled down rapidly under cold running water (10 °C) for 8 min. The black precipitate was purified by centrifugation/resuspension (5000 rpm, 8 min, 2 x H_2O and 2 x EtOH) and dried at 78 °C for 16 h in air.

***Alternative hydrothermal synthesis (HT-B).**[324] The alternative hydrothermal synthesis was carried out according to the following procedure: 291 mg $Co(NO_3)_2{\cdot}6H_2O$ (1 mmol) and 42.5 mg $NaNO_3$ (0.5 mmol) were solved in 15 mL H_2O. After 10 min of stirring, 15 mL of an NH_3 (25 %) solution was slowly added and after 10 more minutes of stirring 1.5 mL H_2O_2 (30 wt%) solution

was added. The reaction solution was transferred to a 15 mL PTFE-lined stainless-steel autoclave and heated to 140 °C (4.5 C° min^{-1}). The holding temperature was maintained for 6 h and then cooled to room temperature naturally. The black precipitate was purified by centrifugation/resuspension (5000 rpm, 8 min, 2 x H_2O and 2 x EtOH) and dried at 78 °C for 16 h in air.

Microwave hydrothermal synthesis (MW-A). For the microwave hydrothermal synthesis of Co_3O_4, 1.8 mmol of $Co(NO_3)_2{\cdot}6H_2O$ was dissolved in 15 mL H_2O and the pH was adjusted to 11 with NH_3 (25 %) solution. The resulting dispersion was filled into a 50 mL Teflon liner, which can be closed and fixed inside a frame before introducing into the microwave. Reactions were carried out in a MARS5 microwave (CEM cooperation). The synthesis was conducted by controlling the temperature; 30 min ramping to 180°C and then holding this temperature for 60 min under constant stirring. The temperature and pressure were measured from the reference vessel, which was equipped with appropriate sensors. After letting the dispersions cool down to room temperature, the product was separated by centrifugation and washed with H_2O.

Microwave alternative hydrothermal synthesis (MW-B). 100 mM $Co(NO_3)_2{\cdot}6H_2O$ and 50 mM $NaNO_3$ were dissolved in 5 mL H_2O. 5 mL NH_3 (25 %) solution and 0.5 mL H_2O_2 (32 wt-%) was added before sealing the solution in the corresponding vessels as described in the above section. The reaction was carried out at 140°C for 1 h after 30 min of ramping time.

***Mild oxidative synthesis/Precipitation method (PM).**[317] The nitrate-salt-mediated precipitation method was carried out according to a previously reported procedure. $NaNO_3$ (15 g, 176 mmol) was added to a 50 mL two-necked round-bottom flask, equipped with a water-cooled reflux condenser containing 25 mL NaOH solution (0.3 M). The reaction mixture was heated to 95 °C and an aqueous solution of $Co(NO_3)_2$ (5.0 mL, 1.0 M) was added within 1 min which led to instantaneous precipitation. Throughout the precipitation and aging period, the reaction mixture was stirred vigorously and purged with air, while keeping the temperature at a constant 95 °C for 16 h. Afterward, the suspension was cooled to room temperature naturally under ambient conditions. The black precipitate was purified by centrifugation/resuspension (5000 rpm, 8 min, 2 x HCl (2 M), 1 x H_2O and 1 x EtOH) and dried at 78 °C for 16 h in air.

***Thermal decomposition (TD).** For the synthesis of Co_3O_4 through thermal decomposition $Co(NO_3)_2{\cdot}6H_2O$ was added to a crucible, heated in a muffle furnace to 450 °C (4.5 °C/min) and kept at this temperature for 3 hours. Afterwards, the product was cooled down to room temperature.

Ball milling and thermal decomposition (BM). $Co(NO_3)_2{\cdot}6H_2O$ was ground in a planetary ball mill (Retsch) at a speed of 500 rpm for 2 h. The ball-milled powder was calcined in air at 450 °C for 1 h to obtain larger Co_3O_4 nanoparticles.

Sol-Gel (SG).[325] A variation of the sol-gel method from the Pechini method[249] was applied: 1.8 mmol of $Co(NO_3)_2{\cdot}6H_2O$ and 2.7 mmol of citric acid were dissolved in 25 mL H_2O. The solution

was heated up slowly while stirring until a gel was formed. It was heated up to 400 °C for 1h, then transferred into a ceramic crucible and heated to 700 °C for 10 h yielding Co_3O_4.

***Molten salt method (MS).**[312] $Co(NO_3)_2{\cdot}6H_2O$ (0.291 g,1 mmol) was mixed with $LiNO_3$ (6.895 g, 100 mmol), ground and transferred to an alumina crucible. The crucible was put into a muffle furnace, heated to 400 °C (12.6 °C/min) and kept at this temperature for 30 min. Afterward, the mixture cooled to room temperature naturally and was washed (2 x H_2O and 1 x EtOH) and dried at 78 °C for 16 h in air.

3.3.2 Catalytic Measurements

The three above-mentioned water oxidation test protocols (chapter 2.3) were performed for each sample to not only compare the catalysts amongst each other, but also to compare the influence of the catalytic test methods.

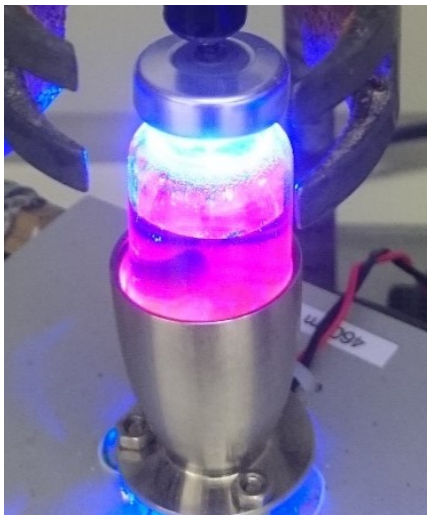

Figure 3-2. Photocatalytic measurement setup with LED, closed vial and inserted LDO**.**

***Photocatalytic tests.** Photocatalytic water oxidation tests were performed using a standard $[Ru(bpy)_3]^{2+}/S_2O_8^{2-}$ protocol.[165] Photocatalytic reaction suspensions were handled in a dark environment while shielded from light. According to the protocol introduced in chapter 2.3.1, Co_3O_4 photocatalyst (2.00 mg, 8.3 mmol), $Na_2S_2O_8$ sacrificial electron acceptor (9.5 mg, 5 mM), and $[Ru(bpy)_3]Cl_2 \cdot 6H_2O$ photosensitizer (6.0 mg, 1 mM) were mixed with borate buffer (8 mL, 80 mM, pH 8.5) in a 10 mL headspace glass vial. The glass vial was subsequently sealed gastight with a rubber septum (PTFE) and an aluminium crimp cap and sonicated for 3 min. To remove all the oxygen before starting the test, the suspension was degassed through purging with helium (purity 5.0) for 10 min. Afterward, the catalytic suspension was illuminated with a 460 nm high flux light-emitting diode (LED) (26.1 mW cm^{-2}, Rhopoint Component LTD) under constant stirring (1200 rpm) for 25 min. For evaluating the amount of evolved oxygen a 100 µL gas sample was taken from the headspace with a gastight microliter syringe (Hamilton-1825RN) and injected into the gas chromatograph (GC). GC measurements were recorded with an Agilent Technologies 7820A equipped with a thermal conductivity detector (TCD) and a

30 m×0.53 mm packed HP molecular sieve column with a 50.0 µm film and He carrier gas (purity 6.0).

A previously determined linear GC calibration curve was used to quantify the oxygen evolution (air contamination was corrected). The error for the O_2 yield was determined by the standard deviation of minimum three photocatalytic tests for each sample.

Chemical water oxidation. The standard CAN method was used to evaluate the chemical water oxidation activity of the catalysts.[82] With a standard potential of about 1.7 V vs NHE, CAN is a suitable one-electron oxidant to promote the water oxidation. CAN (2 g) was dissolved in milli-Q water (40 mL) and the solution was degassed with argon. The respective catalysts (2 mg each) were added and the oxygen evolution was recorded by a luminescent dissolved oxygen sensor (LDO) in the stirred solution for about 45 min. The highest obtained value was used for the evaluation. A Hach HQ40d multimeter with LDO 101 sensor was used for oxygen determination.

Electrocatalytic tests. Electrocatalytic measurements were carried out in 1 M KOH, using an Ag/AgCl reference- and a Pt counter electrode. First, cyclic voltammetry cycles from 0-0.7 V vs. reference with 0.005 mV step size were measured, prior to conducting chronoamperometry. For comparison, only the second cycle was considered at the data evaluation. The potential was stepwise increased starting from 0.45 V to 0.65 V in 0.01 V steps and held for 5 min each to eliminate diffusion currents. The stabilized current after 5 min was used for further evaluation. After the steps, a potential of 0.6 V vs. reference electrode was applied for 2 h for stability tests. Electrochemical measurements were carried out with a Bio-Logic SAS SP-150 potentiostat. As reference electrode, an Aldrich® glass reference electrode Ag/AgCl with 3 M KCl and as counter electrode, a Pt-foil were used. The working electrodes were produced by dispersing 2 mg of the catalyst in 100 µL H_2O, applying 40 µL of this dispersion on 1 cm^2 FTO, and drying the electrodes at 80°C for 30 min before covering with 10 µL of Nafion 1%-solution.

3.3.3 Materials and Methods

Ultrapure H_2O (18.2 MΩ) was generally used for synthesis (Merck, Milli-Q® Type 1 Ultrapure Water Systems). All chemicals and solvents were purchased from commercial suppliers: CoO (Aldrich, ≥99.99% metals basis), $LiCoO_2$ (Alfa Aesar, 99.5% metals basis), $Co(NO_3)_2 \cdot 6H_2O$ (Sigma-Aldrich, 99.999% trace metal basis), $[Ru(bpy)_3]Cl_2 \cdot 6H_2O$ (Sigma–Aldrich, 99.95 %), $Na_2S_2O_8$ (Sigma–Aldrich, 99.0 %), H_2O_2 30 wt.% in H_2O (Sigma–Aldrich, ACS reagent), urea (Sigma-Aldrich, 98 %), $NaNO_3$ (Sigma-Aldrich, ≥99.0 %), NaOH (Acros Organics, 97+%), $LiNO_3$ (Sigma-Aldrich, ReagentPlus®), ammonia solution 25 % (Merck, for analysis), ethanol (VWR Chemicals, absolute). NH_3 (Merck, for analysis), citric acid (Merck, anhydrous for synthesis), KOH (Honeywell, pellets, extra pure), HCl (Fluka Analytical), Nafion® perfluorinated resin solution 5 wt.% in a mixture of lower aliphatic alcohols and water (Sigma-Aldrich).

(*)Powder X-ray diffraction (PXRD) patterns were recorded with a STOE STADI P diffractometer in transmission mode (flat-plate sample holder, Ge monochromator, and $MoK_{\alpha 1}$ radiation) using a position-sensitive microstrip solid-state detector (MYTHEN 1K).

***Raman spectroscopy** was performed with a Renishaw inVia Qontor confocal Raman microscope equipped with a diode laser (785 nm).

***Nitrogen sorption isotherms** were recorded with a Quantachrome Quadrasorb SI porosimeter at 77 K after degassing at 100 °C for 20 h under vacuum. The Brunauer-Emmet-Teller (BET) model was applied for adsorption branch points ($0.05>p/p_0<0.3$) to calculate the apparent surface area.

(*)Transmission electron microscopy (TEM) images were taken with a JEOL JEM-1400 Plus equipped with a JEOL CCD camera Ruby (8 M pixel) and a LaB6 crystal as an emitter (120 kV).

$^{\Delta}$X-ray absorption spectroscopy XANES and EXAFS at the Co K-edge on solid powder samples dispersed in cellulose of the synthesized Co_3O_4 oxides and reference samples $Co^{II}O$, $LiCo^{III}O_2$ were carried out at the European Synchrotron Radiation Facility (ESRF), Swiss-Norwegian Beamline BM31, Grenoble-France. The storage ring was run in top-up mode (average current 40 mA). The X-ray beam was collimated using a Si coated mirror and energy was scanned using a double crystal Si[111] monochromator. Measurements were performed at room temperature using a three-ionization chamber configuration in transmission mode using a 13-element Ge detector. For energy calibrations, spectra of a metal Co foil were measured simultaneously at the second ionization chamber. The measured EXAFS spectra $k^3\chi(k)$ were extracted by data reduction, absorption edge energy calibration and background subtraction as realized in ATHENA. The spectra were reduced in the range $\Delta k \approx 3\text{-}14$ Å-1 and Fourier transformed to $FT|k^3\chi(k)|$ into the real-space interval of $\Delta R \approx 0\text{-}6$ Å. To calculate main values for interatomic distances, coordination numbers, and Debye-Waller factors σ^2 nonlinear least-squares fitting of the experimental $FT|k^3\chi(k)|$ spectra was carried out by ARTEMIS using atomic clusters of Co_3O_4 (ICSD code 27498), generated by ATOMS as implemented in IFEFFIT.[326] The amplitudes and phases shift for single and multiple scattering paths were calculated using FEFF6.[327]

$^{\nabla}$X-ray photoelectron spectroscopy (XPS) was conducted using a Physical Electronics (PHI) Quantum 2000 spectrometer featuring monochromatic Al-K_{α} radiation, generated from an electron beam operated at 15 kV and 35.8 W. The energy scale of the instrument was calibrated using Au and Cu reference samples. The analysis was conducted at 10^{-8} mbar, with an electron take off angle of 45° and a pass-energy of 23.5 eV for all samples. Charge compensation during the measurement was achieved using a low energy electron source. The acquired spectra were then aligned using the main (C-C) component of the C1s core level emission. The modified Auger parameter was calculated by adding the kinetic energy of the Co L3VV and Co $2p_{3/2}$ binding energies.

3.4 Results & Discussion

3.4.1 Characterization of the Co_3O_4 materials emerging from different synthetic methods

Raman and PXRD measurements were mainly performed by Lukas Reith. XAS measurements were performed by S. Esmael Balaghi and Wenchao Wan and analysed by Dr. Carlos A. Triana. XPS spectra were measured and evaluated by Sebastian Siol.

The materials properties were investigated with a set of different methods to characterize them extensively. PXRD patterns revealed obvious differences between the samples (Figure 3-3). Whereas some samples show peak broadening, indicating smaller crystallite size as described in chapter 2.2.1, others exhibit very clear and sharp peaks pointing towards larger particles of higher crystallinity. This correlation described before is defined by the Scherrer equation (formula (9)) and the calculated particle sizes are shown in a values for smaller particles.

Table 3-1.[255,256] It should be noted that the instrumental broadening becomes the limiting factor for calculations of very narrow full width at half maximum (FWHM) values and therefore large crystallite domain sizes.

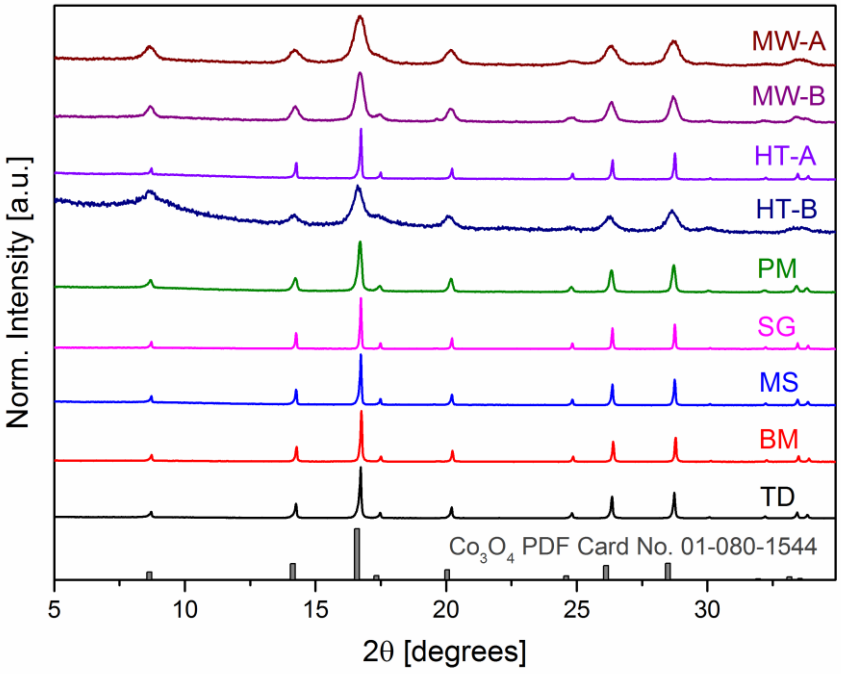

Figure 3-3. PXRD patterns of spinel Co_3O_4 synthesized by different methods (Figure created by Lukas Reith).

As expected, the cobalt oxides synthesized at higher temperatures (≥ 400 °C), namely SG, MS, BM, and TD, display a high crystallite domain size from ≈ 91 nm (SG) and up to ≈ 141 nm (MS). The cobalt oxide samples obtained at lower temperature (≤ 180 °C), i.e. MW-A, MW-B, HT-B, and -

PM show a much lower crystallite domain size with values below ≈ 25 nm (PM) and down to ≈ 7 nm (MW-A). HT-A is the only exception to this trend with a higher τ_{XRD} of ≈ 96 nm. Apart from that, all Bragg reflections are in agreement with the given reference (PDF Card No.: 01-080-1544) indicating phase purity of the synthesized spinel-type Co_3O_4 (space group $Fd\bar{3}m$ (No.: 227)) for all samples. In the normal spinel structure, the O^{2-} anions form a cubic close-packed lattice, where octahedral and tetrahedral sites are occupied by the Co^{3+} and Co^{2+} cations, respectively as discussed before in chapter 1.2.1. To determine the surface area, BET measurements were performed. The surface area measurement by N_2-sorption is described in more detail in chapter 2.2.2. The obtained values are given in a values for smaller particles.

Table 3-1 and are in good agreement with the calculated crystallite sizes τ from Scherrer equation, showing larger surface area values for smaller particles.

Table 3-1 Specific surface area of the synthesized cobalt oxides determined from the Brunauer-Emmet-Teller (BET) model and the crystallite domain size DXRD, calculated from the Scherrer equation.

	MW-A	**MW-B**	**HT-A**	**HT-B**	**PM**	**SG**	**MS**	**BM**	**TD**
BET [m^2/g]	99	146	18	203	42	28	2	8	11
τ_{XRD} [nm]	7.3 ±0.1	11.3 ±0.3	97 ±14	8.1 ±1.3	25 ±2.0	91 ±27	141 ±20	126 ±35	108 ±28

TEM images of all samples were recorded and are shown in Figure 3-4. It can be clearly seen that the synthetic protocol has a major influence on the resulting morphologies. In Figure 3-4 (a), samples synthesized by the fist microwave hydrothermal synthesis, MW-A, are depicted. Compared to another microwave hydrothermal synthesis, MW-B, the particles are a slightly larger, in the range of 10-20 nm and mainly show a cubic shape. The shape of the MW-B Co_3O_4 particles is not clearly visible as they seem to agglomerate even stronger, but it is less defined than for MW-A and the smaller particle size is clearly visible. Figure 3-4 (c) shows much larger particles of different shapes, which were synthesized similarly to MW-A Co_3O_4 but with conventional hydrothermalsynthesis. The TEM image of the other hydrothermal synthesis, HT-B, which has a similar protocol like MW-B, shows the smallest particle size and a strong agglomeration. The most separated particles are the ones synthesized by the precipitation method, resulting in Co_3O_4-particles of about 50 nm and without a clear shape. The sol-gel synthesis yielded in much larger particles of 100 nm up to 400 nm, which are highly agglomerated (Figure 3-4 (f)). Similar size but more cubic shape was obtained by the particles synthesized from molten salt synthesis (Figure 3-4(g)). The Co_3O_4 samples

synthesized by thermal decomposition (Figure 3-4 (i)) and especially the ones prepared by ball milling followed by thermal decomposition (Figure 3-4 (h)) show elongated nanoparticles with an average size distribution around 50 nm. These findings more or less match with the measured BET and calculated crystallite size τ (a values for smaller particles.

Table 3-1).

No clear size-temperature correlation can be found but in general, the samples synthesized at lower temperatures, so MW-A, MW-B, HT-A, HT-B and PM exhibit smaller particle size compared samples synthesized at higher temperature

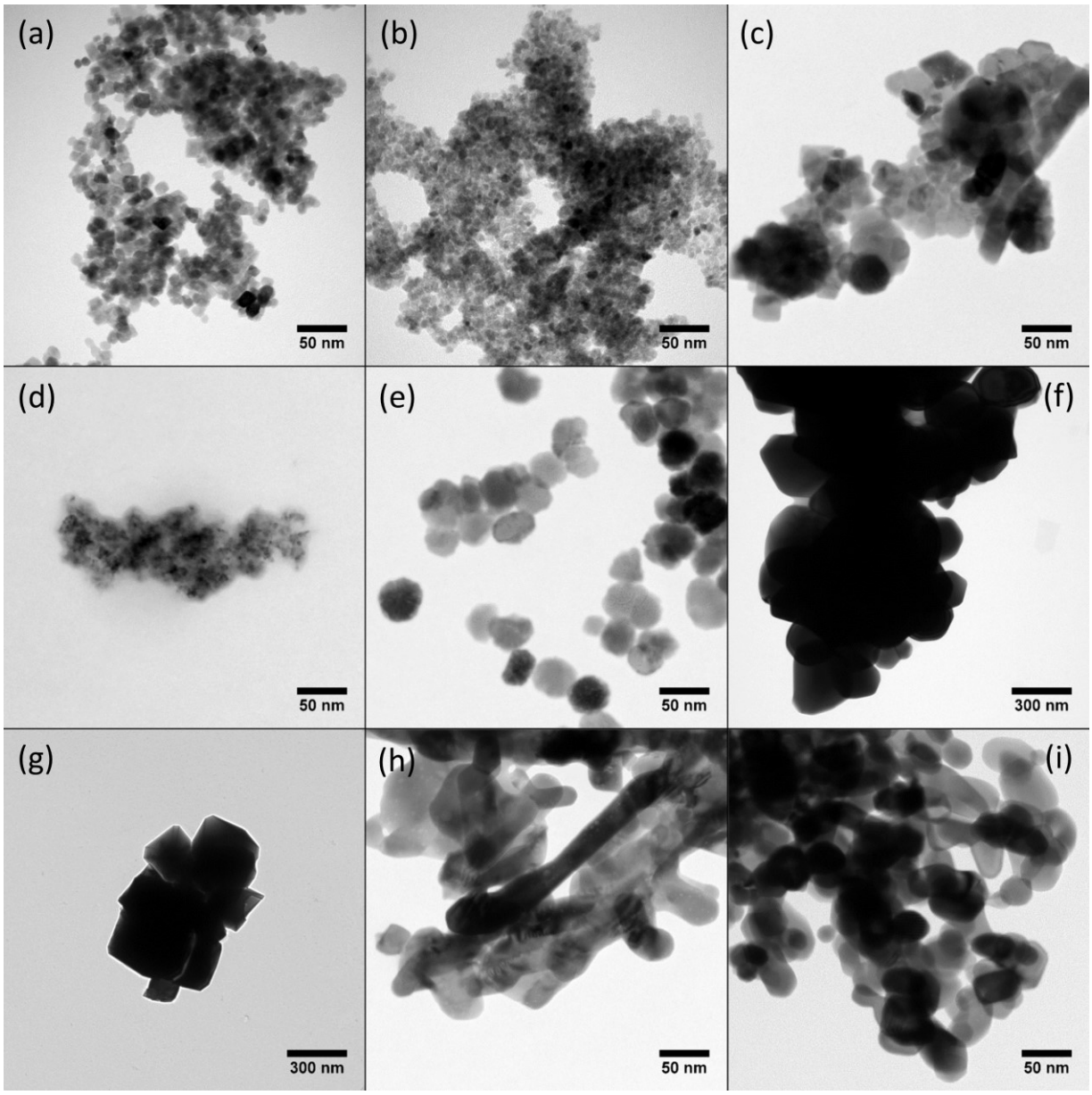

Figure 3-4. TEM images of Co_3O_4 samples prepared by different synthesis methods: (a) MW-A, (b) MW-B, (c) HT-A, (d) HT-B, (e) PM, (f) SG, (g) MS, (h) BM, (i) TD (Figure created by Lukas Reith).

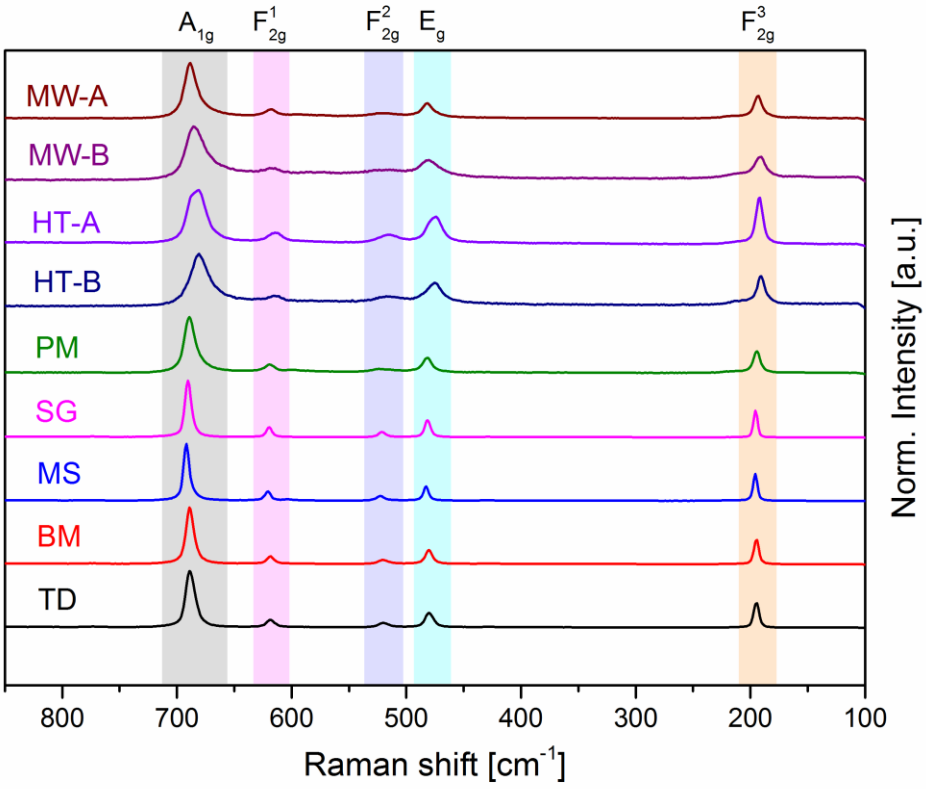

Figure 3-5. Raman spectra of the synthesized spinel cobalt oxides (Figure created by Lukas Reith).

Raman spectra of all synthesized cobalt oxides are shown in Figure 3-5. Group theory predicts five Raman active vibrational modes for Co_3O_4, consisting of A_{1g}, E_g and three F_{2g} modes.[328] These five main phonon excitations were observed for all spectra and match well with theoretical and experimental reports on spinel type cobalt oxide.[329,330] The symmetric Co^{3+}-O stretching vibration of octahedrally coordinated CoO_6 is attributed to A_{1g} in O^7_h symmetry and is assigned to the most intense band at ≈ 690 cm^{-1}. The medium/low intensity bands at ≈ 620 cm^{-1}, ≈ 520 cm^{-1}, and ≈ 480 cm^{-1} correspond to F^1_{2g}, F^2_{2g}, and E_g symmetry, respectively. The band at ≈ 190 cm^{-1} arises from tetrahedrally coordinated $Co^{2+}O_4$ units with F^3_{2g} symmetry. These results further confirm the formation of phase pure cubic spinel Co_3O_4 from all applied synthesis methods.

Generally, narrow and intense Raman-active modes are characteristic for well-ordered structures. In the present system, the oxides emerging from low temperature methods (MW-A, MW-B, HT-B, PM) exhibit Raman peaks shifted toward higher-frequency values, displaying lower intensity and peak-broadening (see **Table 3-2**), with respect to the oxide samples obtained at higher temperatures (SG, MS, BM, TD). This result indicates a decrease in the long-range order of oxides synthesized at low temperature (MW-A, MW-B, HT-B, PM). This result agrees with the low intensity and peak broadening observed in the corresponding PXRD patterns (MW-A, MW-B, HT-B, P) (Figure 3-3).[331]

Table 3-2 Line positions and full width at half maximum (FWHM) for Raman modes A_{1g} and F^3_{2g} of spinel-type Co_3O_4 synthesized with different methods (Table created by Lukas Reith).

Sample	A_{1g}		F^3_{2g}	
	Raman shift [cm^{-1}]	FWHM [cm^{-1}]	Raman shift [cm^{-1}]	FWHM [cm^{-1}]
MW-A	687.8	13.3	193.4	8.8
MW-B	684.0	19.6	192.0	16.2
HT-A	682.5	18.9	192.1	7.0
HT-B	680.3	19.5	190.8	10.2
PM	688.7	11.5	194.4	7.2
SG	690.1	6.8	195.5	4.2
MS	691.6	6.1	195.6	4.3
BM	688.6	8.1	194.7	5.1
TD	688.3	9.7	194.8	5.7

To acquire deeper insight into the atomic short-range order of the as-synthesized Co_3O_4 oxides, X-ray absorption near edge structure (XANES) and extended X-ray absorption fine structure (EXAFS) analyses were carried out. Figure 3-6 shows the fitting of the Fourier-Transformed FT|$k^3\chi(k)$|spectra of the experimental Co K-edge EXAFS spectra $k^3\chi(k)$, for oxides displaying remarkable differences in their short-range order, i.e. Co_3O_4-SG, -MS, -PM, -MW-A, -MW-B and -HT-B. The Co_3O_4-BM, -TD and -HT-A oxides showed similar short-range order to that of Co_3O_4-PM. Calculated main values for interatomic distances, atomic coordination numbers (N), and Debye-Waller factors (σ^2) are given in Table 3-3. All synthesized Co_3O_4 samples show four prominent peaks arising from backscattering from neighboring O and Co atoms. The first peak in the FT|$k^3\chi(k)$| spectra at r ≈ 1.55 Å relates to Co^{2+} and Co^{3+} cations in tetrahedral {CoO_4} and octahedral {CoO_6} coordination with oxygen atoms at interatomic distances of ≈ 1.914 Å and ≈ 1.899 Å, respectively. However, since those two shells are too close to be resolved in the FT|$k^3\chi(k)$| spectra, they convolute to a first Co-O shell having a main interatomic distance Co-O ≈ 1.907 Å and an averaged atomic coordination number N = 5.333. The second and third peaks in the FT|$k^3\chi(k)$| spectra, at r ≈ 2.49 Å and r ≈ 2.95 Å, correspond to the Co_{Octa}-Co_{Octa} ≈ 2.86 Å [N = 4] and Co_{Tetra}-Co_{Octa} ≈ 3.35 Å [N = 8] coordination shells, respectively. The fourth peak at r ≈ 4.70 Å relates to higher Co and O coordination shells (see Figure 3-6, Table 3-3). Remarkably, while the relative amplitude of the first Co-O coordination shell in the FT|$k^3\chi(k)$| and Wavelet-Transformed (WT) spectra (r ≈ 1.55 Å), do not change too much among the different Co_3O_4 oxides, the FT|$k^3\chi(k)$| and WT spectra show a decreasing relative magnitude of the Co_{Octa}-Co_{Octa}, Co_{Tetra}-Co_{Octa} and higher Co-Co(-O) coordination peaks from high to low temperature synthesis methods in the order Co_3O_4-SG > -MS > -PM> -MW-A > -MW-B > -HT-B (see Figure 3-6). The amplitude decay in the FT|$k^3\chi(k)$| and WT spectra is correlated with a decrease of the coordination number or an increase in the mean-square disorder parameter $\sigma^2=\sigma^2_{thermal}+\sigma^2_{static}$. Here, structural disorder arises from static disorder σ^2_{static}, i.e. crystal defects due to slightly different interatomic distances in the same coordination shell. The vibrational

disorder $\sigma^2_{thermal}$ is not crucial since the spectra have been all measured at the same temperature. Hence, the decline in the relative amplitude of high coordination peaks in the FT|k$^3\chi$(k)| and WT spectra provide a direct indication of the extent of crystalline long-range order around the cobalt center. The results in Figure 3-6 and Table 3-3 suggest the existence of static-disorder and the presence of Co and O vacancies in the structure of the cobalt oxides synthesized at low temperature, namely Co_3O_4-HT-B, -MW-B, -MW-A and -PM. While the atomic coordination number N for Co_{Octa}-Co_{Octa}, Co_{Tetra}-Co_{Octa}, and higher Co-Co(-O) coordination shells remains quite the same for Co_3O_4-SG, -MS, -PM, -BM, -TD and -HT-A (Table 3-3), the mean-square disorder σ^2 of those oxides increases steadily. The static local-disorder σ^2 increases more notably for Co_3O_4-MW-A, -MW-B and -HT-B. Additionally, for those oxide materials the atomic coordination number N of the Co-O, Co_{Octa}-Co_{Octa}, Co_{Tetra}-Co_{Octa} and higher Co-Co(-O) coordination shells is slightly smaller than those values of more crystalline Co_3O_4-SG, -MS, and -PM. The bond length Co-O ≈ 1.912 Å in Co_3O_4-MW-A is slightly larger with respect to the other oxides, suggesting lattice expansion and relaxation of Co-O bonds. These findings agree with results from PXRD and Raman spectra, in which Co_3O_4-MW-A, -MW-B and -HT-B show lower intensity and broadened diffraction and Raman peaks due to the local-structural dispersion of the Co and O atoms in the spinel structure (Figure 3-3 and Figure 3-5).

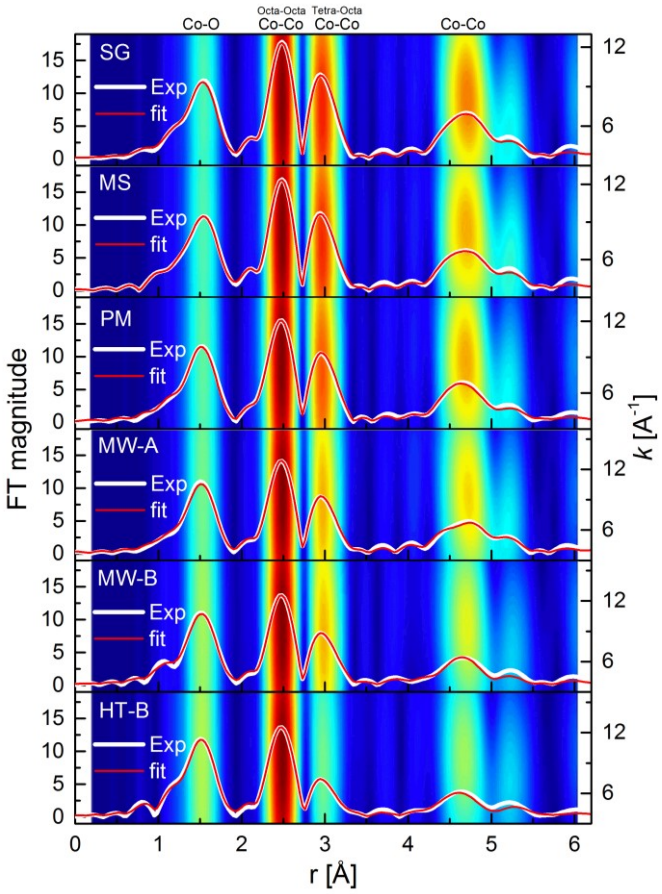

Figure 3-6. Fitting (colored-spectra) of the Fourier Transforms FT|$k^3\chi(k)$| of the experimental Co *K*-edge EXAFS spectra $k^3\chi(k)$ (gray) of Co_3O_4-SG, -MS, -PM, -MW-A, -MW-B and -HT-B, phase uncorrected. The background 2D contour plots are the Wavelet-Transformed (WT) of the $k^3\chi(k)$ spectra and their shaded regions highlight the decreasing of the peak intensity associated with the increasing disorder parameter σ^2 for Co-O, , Co_{Octa}-Co_{Octa}, Co_{Tetra}-Co_{Octa} and higher Co-Co(-O) coordination shells (Figure created by Carlos Triana).

Table 3-3 Main interatomic distances, atomic coordination numbers (*N*) and Debye-Waller factors (σ^2) calculated from the fitting of the experimental Co *K*-edge FT|$k^3\chi(k)$| spectra of Co_3O_4-SG, -MS, -PM, -MW-A, -MW-B, -HT-B, -BM, -TD and -HT-A. Amplitude reduction factor $S_0^2 \approx 0.784$, $\Delta E_0 \approx -7.82$ eV (Table created by Carlos Triana).

Sample	Bond	*N*	σ^2	**r** (A)
Co_3O_4-SG	Co-O	5.33	0.00366	1.9094
	Co_{Octa}-Co_{Octa}	4.00	0.00307	2.8555
	Co_{Tetra}-Co_{Octa}	8.00	0.00577	3.3599
	Co-Co	8.00	0.00546	4.9643
Co_3O_4-MS	Co-O	5.31	0.00310	1.9080
	Co_{Octa}-Co_{Octa}	3.98	0.00309	2.8523
	Co_{Tetra}-Co_{Octa}	7.98	0.00587	3.3559
	Co-Co	7.98	0.00565	4.9548
Co_3O_4-PM	Co-O	5.31	0.00327	1.9105
	Co_{Octa}-Co_{Octa}	3.96	0.00316	2.8544
	Co_{Tetra}-Co_{Octa}	7.95	0.00625	3.3604
	Co-Co	7.96	0.00571	4.9625
Co_3O_4-MW-A	Co-O	5.28	0.00344	1.9115
	Co_{Octa}-Co_{Octa}	3.92	0.00336	2.8589
	Co_{Tetra}-Co_{Octa}	7.93	0.00701	3.3671
	Co-Co	7.92	0.00722	4.9562
Co_3O_4-MW-B	Co-O	5.27	0.00313	1.9097
	Co_{Octa}-Co_{Octa}	3.86	0.00346	2.8567
	Co_{Tetra}-Co_{Octa}	7.90	0.00740	3.3655
	Co-Co	7.83	0.00728	4.9652
Co_3O_4-HT-B	Co-O	5.23	0.00283	1.9051
	Co_{Octa}-Co_{Octa}	3.85	0.00359	2.8560
	Co_{Tetra}-Co_{Octa}	7.71	0.00861	3.3631
	Co-Co	7.79	0.00739	4.9571
Co_3O_4-BM	Co-O	5.31	0.00385	1.9080
	Co_{Octa}-Co_{Octa}	3.96	0.00310	2.8549
	Co_{Tetra}-Co_{Octa}	7.95	0.00609	3.3598
	Co-Co	7.96	0.00566	4.9637
Co_3O_4-TD	Co-O	5.31	0.00367	1.9102
	Co_{Octa}-Co_{Octa}	3.96	0.00313	2.8556
	Co_{Tetra}-Co_{Octa}	7.95	0.00614	3.3612
	Co-Co	7.96	0.00568	4.9649
Co_3O_4-HT-A	Co-O	5.31	0.00295	1.9120
	Co_{Octa}-Co_{Octa}	3.96	0.00315	2.8571
	Co_{Tetra}-Co_{Octa}	7.95	0.00621	3.3624
	Co-Co	7.96	0.00569	4.9667

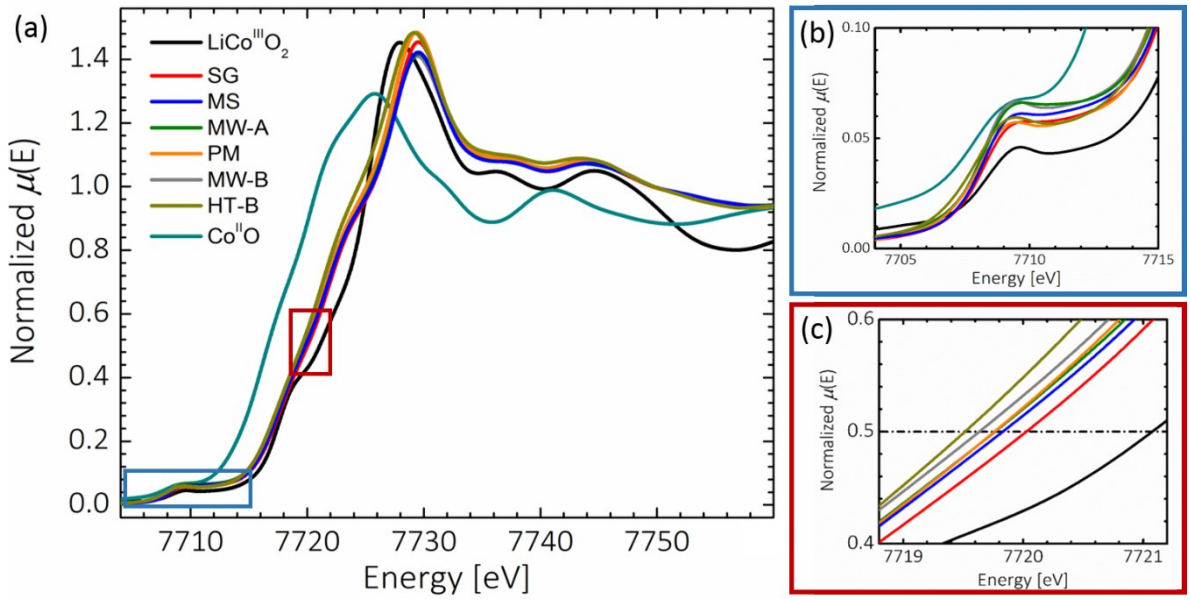

Figure 3-7. a) XANES spectra of synthesized Co_3O_4-SG, -MS, -PM, -MW-A, -MW-B, -HT-B oxides, and reference compounds $Co^{II}O$ and $LiCo^{III}O_2$. The inset shows the calculated Co valance states, b) zoom of changes in the pre edge intensity of XANES spectra, c) zoom of the shifts of the Co K-edge absorption edge to higher energy at μ(E)=0.5 of the normalized XANES spectra (Figure adapted from ref 284).

Figure 3-7 shows XANES spectra for as-synthesized Co_3O_4-SG, -MS, -PM, -MW-A, -MW-B, -HT-B and those of reference compounds $Co^{II}O$ and $LiCo^{III}O_2$. The Co K-edge absorption edge is gradually shifted to higher energy from ≈ 7719.1 eV for -HT-B to ≈ 7720.36 eV for -SG (Figure 3-7c), which suggests that distinct Co_3O_4 samples were slightly oxidized when proceeding from low to high synthesis temperatures. The average oxidation state of Co was estimated from the linear dependence of the Co K-edge position at the energy corresponding to a μ(E)-value of 0.5 of the normalized XANES spectra.[332] Consequently, Figure 3-8 show that, based on the absorption edge energy position (μ(E) ≈ 0.5) of the reference compounds $Co^{II}O$ and $LiCo^{III}O_2$, the Co valence states for the as-synthesized Co_3O_4 oxides were calculated to slightly increase from ≈ 2.654 for -HT-B to ≈ 2.778 for -SG. The average cobalt oxidation state in an ideal spinel is 2.67. In order to maintain electroneutrality, formation of oxygen vacancies for lower and formation of cobalt defects (or interstitial oxygen) for higher oxidation states would be a reasonable explanation for these deviating values.[308,310]

As shown in Figure 3-7, the XANES spectra of all synthesized oxides exhibit a characteristic pre-edge peak at ≈ 7709.6 eV whose intensity lightly increases from high to low temperature synthesis methods according to Co_3O_4-MW-B > -MW-A > -MS > -HT-B > PM > SG. The pre-edge peak is more intense for tetrahedral sites and broader and less intense for octahedral symmetry.[332] Therefore, the result in Figure 3-7b suggests that the degree of inversion, as introduced in chapter 1.2.1 is slightly higher for low temperature synthesized oxides Co_3O_4-MW-B and -MW-A. Qualitative information on the degree of inversion x was obtained from EXAFS fitting by estimating the fraction of Co^{3+} in tetrahedral (X_a) and octahedral (X_b) sites given by $X_a = 1 - X_b$, which corresponds to the degree of inversion (x).[332] Calculated values range from x=0.007 ± 2 for Co_3O_4-SG to x=0.021 ± 2 for Co_3O_4-MW-B. These values agree with previous reported values of

inversion degree for spinel Co_3O_4 oxides.[333,334] However, those values should be taken conservatively since the interatomic distances for tetrahedral Co^{2+}-O_4 ≈ 1.914 Å and octahedral Co^{3+}-O_6 ≈ 1.899 Å coordination shells are too close to be well-resolved in the FT|$k^3\chi(k)$| spectra. While the energy position and line shape of the white line intensity in the XANES spectra is sensitive to experimental beam stability, the change in the white line intensity and the slightly shift to lower energy (Figure 3-7a) further indicates the presence of structural disorder and an increasing of the inversion degree *x*. This result also suggests that the density of unoccupied *d*-states and oxidation states of Co atoms are indeed different among the synthesized Co_3O_4-SG, -MS, -PM, -MW-A, -MW-B, and -HT-B oxides. These trends agree with those of PXRD and Raman spectra and further support that low temperature synthesis of Co_3O_4 promotes the formation of a charge imbalance, Co and/or O vacancies or unsaturated chemical bonds on the spinel surface-structure.

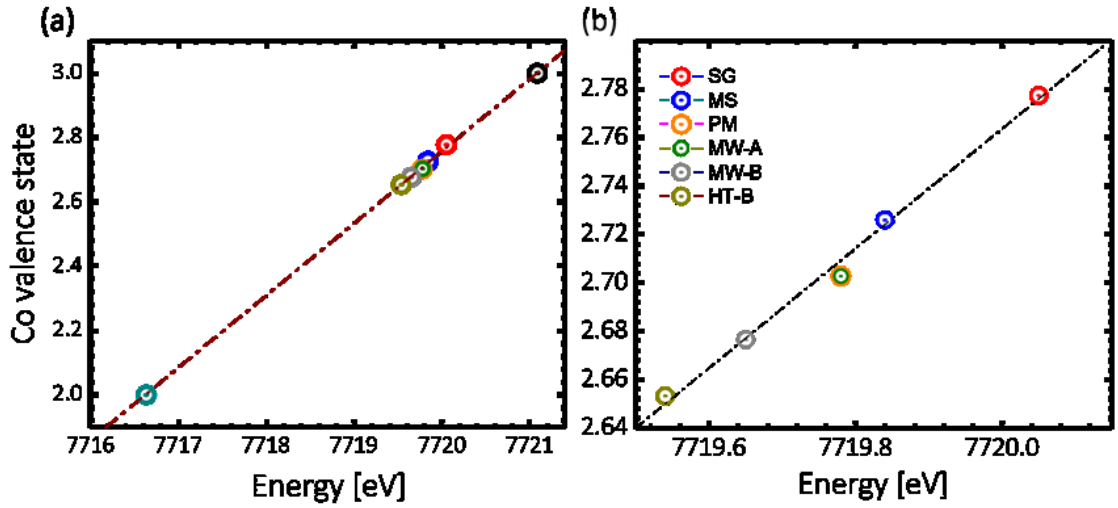

Figure 3-8. Cobalt valence states calculated at μ(E)=0.5 of the normalized XANES spectra (Figure adapted from ref [284]).

XPS data for Co_3O_4-MW-B, -HT-B, -SG, and –PM are plotted in Figure 3-9 together with those of the reference samples of $Co^{II}O$ and $LiCo^{III}O_2$ for representative core level spectra of Co^{2+} and Co^{3+}, respectively. The binding energies of the Co $2p_{3/2}$ emission are similar for all investigated cobalt oxides at ≈780 eV (Figure 3-9a), which is in good agreement with literature reports.[335] Whereas the peak positions for Co^{2+} and Co^{3+} are hard to distinguish, samples containing Co^{2+} show an additional characteristic shake-up satellite emission at roughly 786 eV.[336] The intensity of this satellite emission (inset of Figure 3-9a) can be used to assess the relative amount of Co^{2+} present in the sample. By comparing the intensity of the satellite emission of the synthesized cobalt oxides with that of the reference compounds $LiCo^{III}O_2$ and $Co^{II}O$ the following trend for the average Co valence states was derived: HT-B < PM ≈ MW-B < SG. This trend is in good agreement with the XANES data shown in Figure 3-7a,c. Whereas the Co $2p_{3/2}$ core level binding energies are similar for CoO and Co_3O_4, the shift in the kinetic energy of the L3VV Auger emission is considerable for different oxidation states. Figure 3-9b shows a Wagner plot featuring both Co $2p_{3/2}$ binding energies as well as L3VV Auger kinetic energies. The Wagner plot is a helpful analytical tool for chemical state

analysis, because it provides a comprehensive display of both Auger electron kinetic energies as well as photoelectron binding energies. It can be applied for different materials containing the same element, by plotting the kinetic energies of an Auger peak over the binding energies of a photoelectron peak.[262] The sum of the Auger kinetic energies and the binding energies, the modified Auger parameters, are illustrated as diagonal lines.[263]

The Auger parameter is insensitive to charging and particularly useful when comparing spectra of insulating samples with results from literature. Modified Auger parameters from the National Institute of Standards and Technology (NIST) are given for references (Co_3O_4*, Co*, and CoO*) as indicated by the orange lines.[335] The modified Auger parameters for the as-synthesized Co_3O_4-MW-B, -HT-B, and PM samples are on the same line with the Co_3O_4* reference. Interestingly, the measured $Co^{II}O$ also coincides with this line, implying oxidation of the surface. The SG sample is closer to the $LiCo^{III}O_2$ line, which is in good agreement with the absence of a strong satellite emission as shown in Figure 3-9a. These findings correlate well with the previous spectroscopic measurements, showing the same trends, namely lower average oxidation states for samples synthesized at lower temperatures.

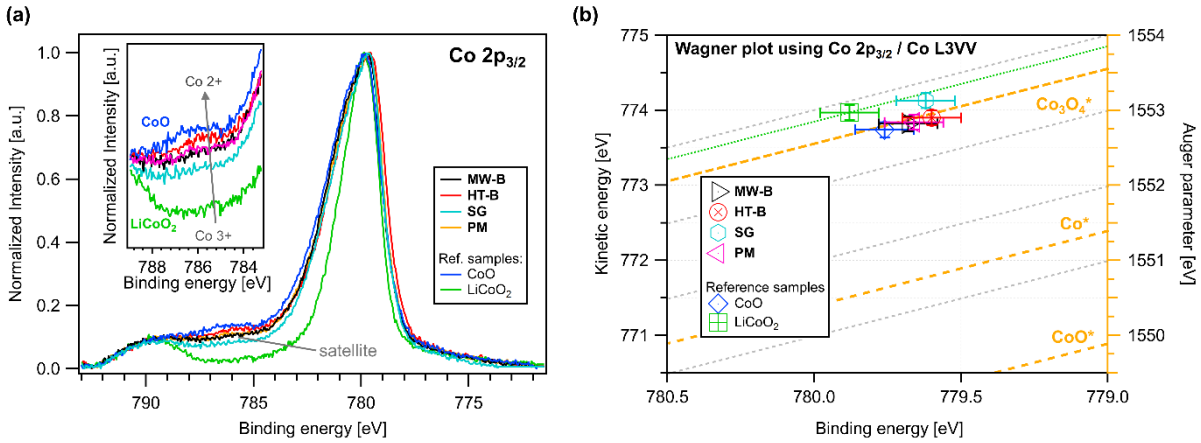

Figure 3-9. (a) XPS spectra of the Co $2p_{3/2}$ peak of the synthesized Co_3O_4-MW-B, -HT-B, -SG, -PM samples, and of reference compounds $Co^{II}O$ and $LiCo^{III}O_2$ (inset: satellite of the Co $2p_{3/2}$ peak), (b) Wagner plot using the Co $2p_{3/2}$ core level binding energy and the Co L3VV Auger electron kinetic energy. References (Co_3O_4*, Co*, and CoO*) were obtained from the NIST database[335] (Figure created by Sebastian Siol).

3.4.2 Water Oxidation Activity

Photocatalytic water oxidation experiments were performed by Lukas Reith.

The water oxidation performance of Co_3O_4 samples synthesized by nine different methods was tested using the three most widely applied approaches, namely photocatalytic, chemical and electrocatalytic oxidation as introduced in chapters 1.1.2 and 2.3. The results are shown in Figure 3-15, and for a better assessment of the activity, the BET surface area and the mean-square disorder parameter σ^2 values are included as well.

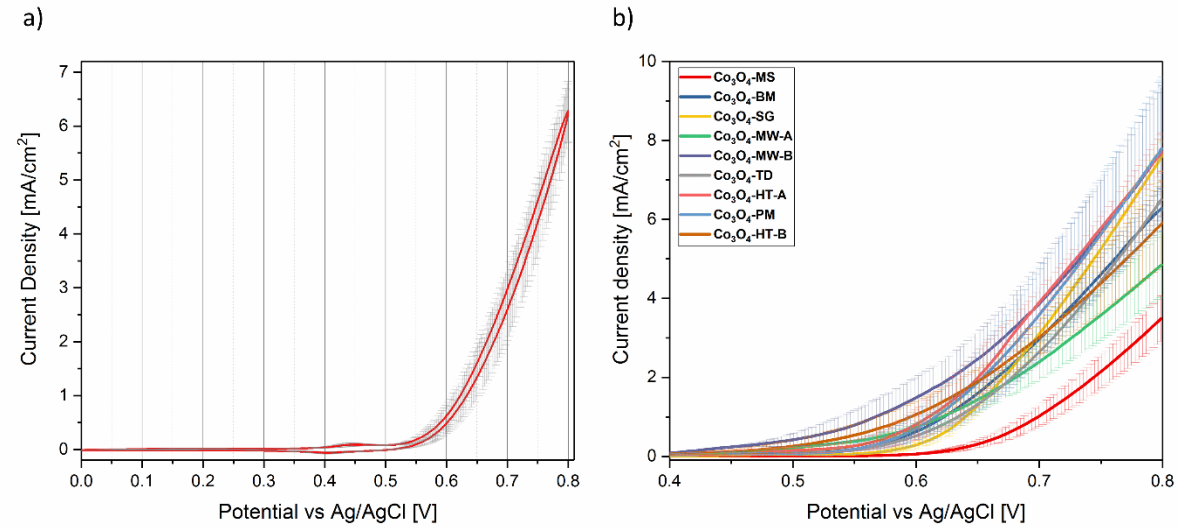

Figure 3-10. Cyclic voltammetry performed in 1 M KOH from 0 – 0.8 V vs. Ag/AgCl with 5 mV/s. A single cycle (the second) is shown in a) and the section showing the onset potential of all samples is shown in b).

To evaluate the electrocatalytic water oxidation performance, the spinel samples were coated on FTO (blank FTO showed catalytic properties inferior to all Co_3O_4 samples except Co_3O_4-MS, therefore allowing for comparison of the catalyst activities) and measured in a standard three electrode setup in 1 M KOH, using Ag/AgCl as reference and Pt as counter electrodes. The use of Pt counter electrodes was recently under debate since it was shown that small amounts dissolve in the electrolyte and influence the activity of water reduction catalysts.[337–339] However, this is not the case for water oxidation as Pt does not produce any Faradaic current in this region (see Figure 3-11) and since the measurements were performed at pH 14 the dissolution is minimized.[274]

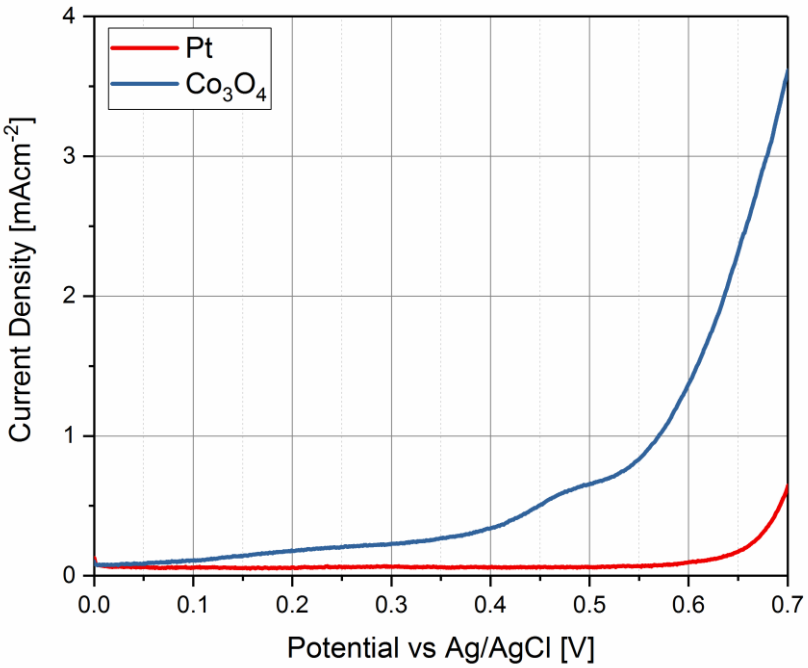

Figure 3-11. LSV measurements of standard MW-Co_3O_4 in comparison with a Pt electrode in 1 M KOH.

Furthermore, the stability of Ag/AgCl reference electrodes in alkaline media was recently questioned due to the possible formation of silver oxide.[273] To address this issue, control experiments were performed. First, the stability of the used Ag/AgCl electrode in 1 M KOH was tested by measuring CV of the $[Fe^{II}(CN)_6]^{4-}$ / $[Fe^{III}(CN)_6]^{3-}$ redox pair every hour for 12 hours. After that, a CV of fresh $[Fe^{II}(CN)_6]^{4-}$ / $[Fe^{III}(CN)_6]^{3-}$ solution was recorded to check the stability of the redox pair itself. The redox peak positions over time are shown in Figure 3-12. These results confirm the stability of the measured redox pair as well as the instability of the Ag/AgCl reference electrode since the redox peaks shift over time. However, as indicated with the green area in Figure 3-12, this stability shift is within the error margin of the performed experiments, especially since the measurement time of the performed oxidation tests is less than 2 hours. This justifies the use of a Ag/AgCl reference electrode for the performed experiments explained below. Furthermore, no new catalyst is introduced here but the influence of single synthesis parameters on the activity of the resulting well-known catalyst, spinel-type Co_3O_4, are investigated by comparing them using standard electrochemical measurement techniques.

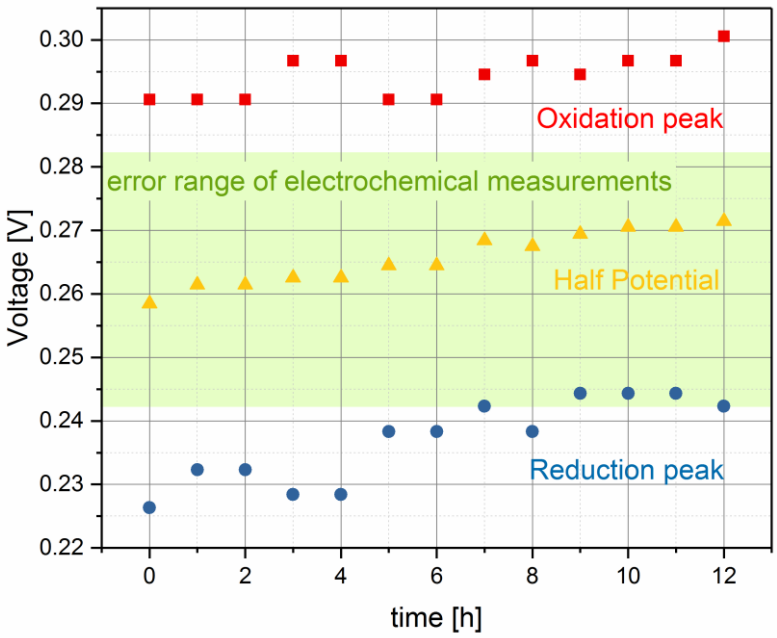

Figure 3-12. Oxidation, reduction and half potential changes of the $[Fe^{II}(CN)_6]^{4-}$/ $[Fe^{III}(CN)_6]^{3-}$ redox pair in 1 M KOH over time vs. Ag/AgCl; green area: standard deviation of the potential at 1 mA/cm^2 given in **Figure** 3-15.

Cyclic voltammetry as well as chronoamperometry were performed, first stepwise from 0.45 to 0.65 V vs. Ag/AgCl, then for 2 h at 0.6 V. From the cyclic voltammograms, which were performed in 1 M KOH from 0 – 0.8 V vs. Ag/AgCl with 5 mV/s steps, always the second cycle (Figure 3-10a) was taken for comparison. Figure 3-10b shows the section of the onset potential from second cycle of all samples. All samples showed an onset potential in the range of 0.45 – 0.6 V vs. Ag/AgCl (1.49 – 1.64 V vs. RHE) with significant standard deviations of 0.03 V, no clear trend is visible (see Figure 3-10b). The only remarkable feature is that Co_3O_4-MS, with an overpotential of 0.6 V vs. Ag/AgCl (1.64 V vs RHE), is outperformed clearly by all other materials.

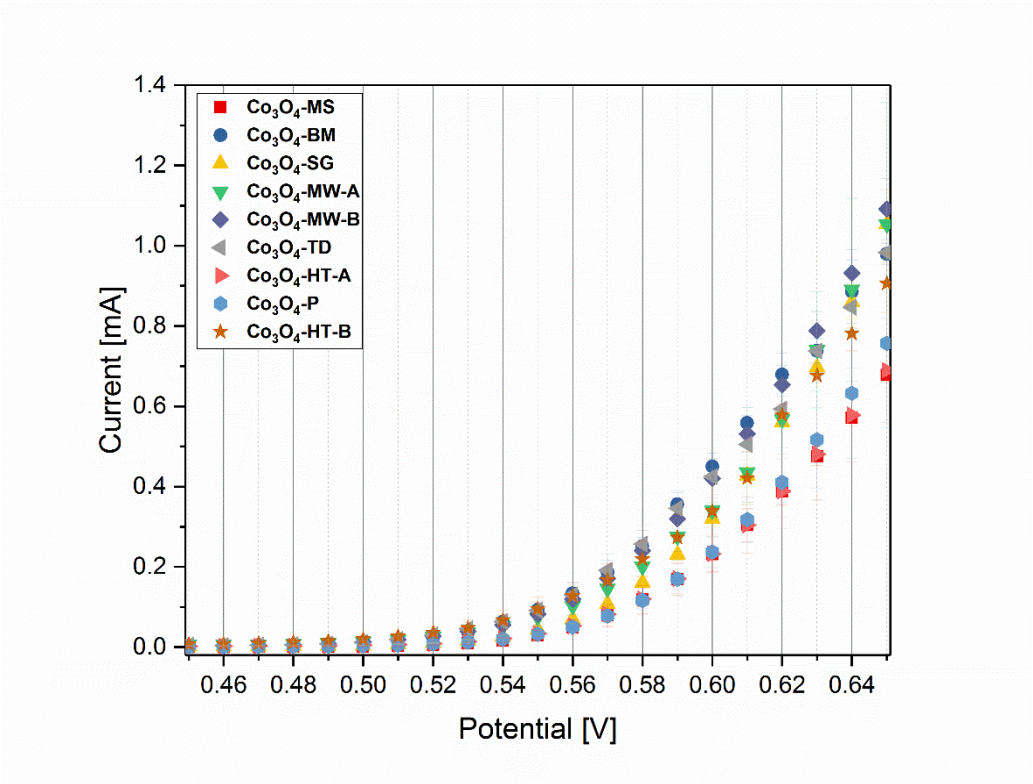

Figure 3-13. Chronoamperometry measurements of all cobalt oxide samples from 0.45 – 0.65 V vs. Ag/AgCl (0.1 V steps and holding time of 5 min for each step). For clarity of presentation, only the stabilized current after 5 min holding is plotted against the potential.

For a better comparison of the pure material, stepwise chronoamperometry, from 0.45 to 0.65 V vs. Ag/AgCl with 0.01 V steps and 5 min per step, was conducted. To eliminate the diffusion current, therefore representing the catalytic activity more reliably, always the current density after keeping the potential for 5 min was taken and plotted in Figure 3-13. For comparison, the potentials at 1 mA/cm^2 are determined from Figure 3-13 and plotted in Figure 3-15. Even from these more accurate measurements, no clear influence on the electrocatalytic performance is evident. All potentials at 1 mA/cm^2 are in the range of 0.55 – 0.59 vs Ag/AgCl (1.59 – 1.62 V vs. RHE) with a comparatively large error of 0.024 V.

To investigate the stability of Co_3O_4-MW-A as a representative of the different samples on FTO electrodes, different characterizations were performed before and after electrocatalytic measurements (see Figure 3-14). Representative SEM images recorded of Co_3O_4-MW-A before and after electrocatalytic measurements (Figure 3-14a) do not show significant morphology changes. Likewise, Raman spectroscopy (Figure 3-14c) reveals the stability of the catalyst. Only PXRD patterns recorded in reflectance mode on a Rigaku SmartLab device using a Ge monochromator and CuK_α radiation showed some changes (Figure 3-14b), namely an increased FTO:Co_3O_4 ratio which can be explained by partial detachment of electrode material but not by a change in the catalyst itself. Justification of the use of Pt as a counter electrode is provided in the next chapter.

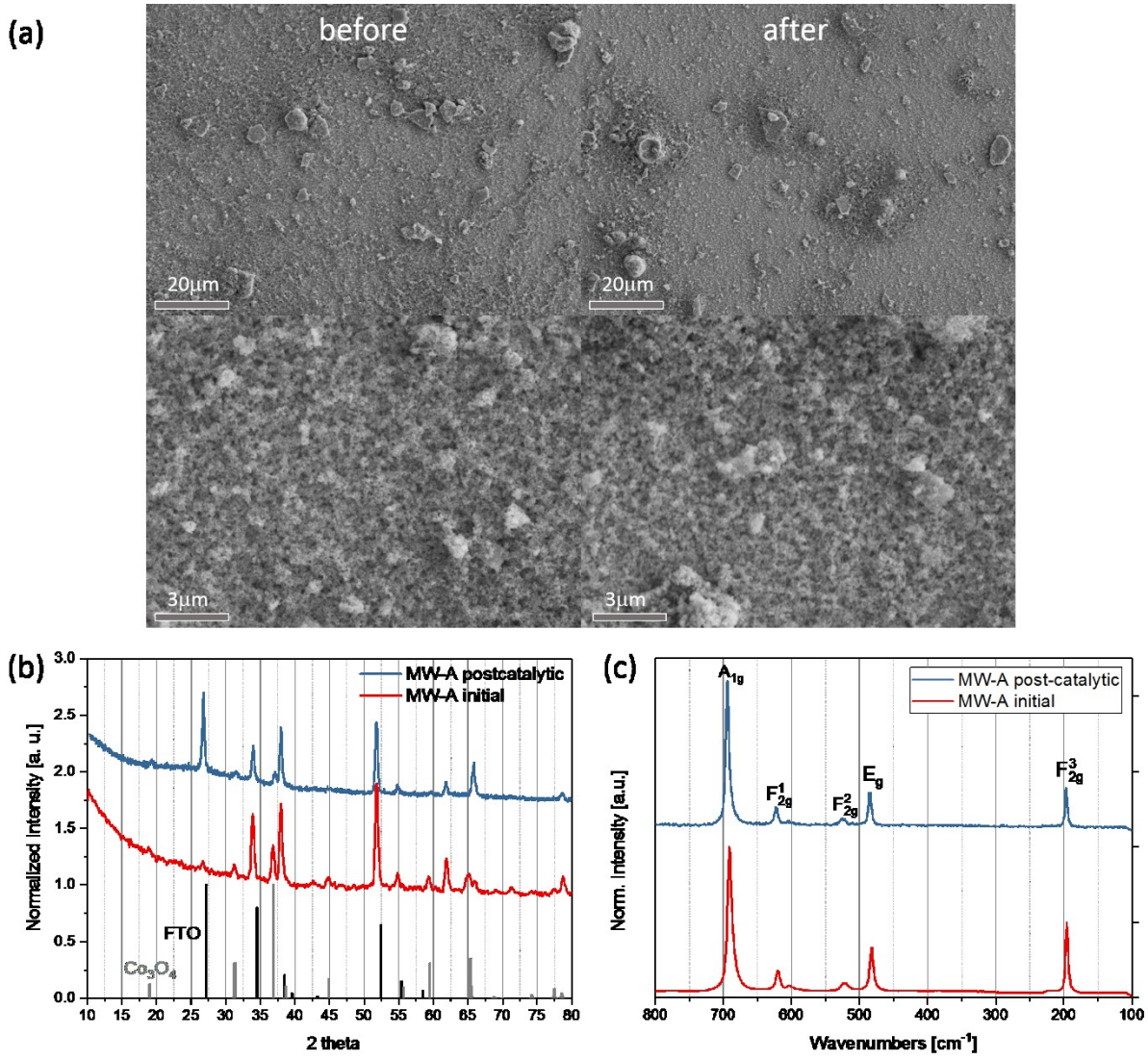

Figure 3-14. SEM images (a), PXRD pattern (b) and Raman spectra (c) of Co_3O_4-MW-A deposited on FTO electrodes before and after electrocatalytic measurements.

For photocatalytic water oxidation, a standard $[Ru(bpy)_3]^{2+}/S_2O_8^{2-}$/light assay was used at pH 8.5. In this case, through visible-light excitation of $[Ru(bpy)_3]^{2+}$ and subsequent oxidative quenching by persulfate, the one electron oxidant $[Ru(bpy)_3]^{3+}$ is generated in situ ($E° = 1.26$ V vs NHE)[340]. Figure 3-15 shows a quite significant difference in activity between the most active catalyst Co_3O_4-HT-B with 77.7 % ± 6.4 / 203 m^2g^{-1} and the least active catalyst Co_3O_4-MS with 12.4 % ± 0.4 / 2 m^2g^{-1}. The samples synthesized at lower temperatures generally show higher OER activity, with the hydrothermally synthesized Co_3O_4-HT-B demonstrating the highest activity with an O_2-yield of 77.7 % ± 6.4, compared to the samples obtained at high temperature. This goes in hand with the high surface areas of MW-A (99 m^2g^{-1}), MW-B (146 m^2g^{-1}) and HT-B (203 m^2g^{-1}). However, HT-A and PM, which exhibit relatively low surface areas, also show increased performance. Considering only the high-temperature samples, Co_3O_4-MS, -BM, and -SG show a trend towards higher activity for increasing surface area. Co_3O_4-TD is an exception with a rather high activity of 46.9 % ± 4.6 for its comparably low surface area of 11 m^2g^{-1}. Note that the disorder among the

samples follows a related trend to the surface area. No clear correlation between the activity and either surface area, disorder, or valence state can be seen in photocatalytic water oxidation. The general performance trend reveals a higher activity for materials synthesized through low temperature hydrothermal or precipitation methods (≤ 180°C) than for materials synthesized at high temperature (≥ 400°C) (Co_3O_4-TD being the above-mentioned exception). Consequently, the synthetic method itself exerts a clear effect on photocatalytic water oxidation activity.

Chemical water oxidation was tested with the strong one electron oxidant cerium ammonium nitrate (CAN) with an E° of 1.7 V vs NHE.[80,81] Using CAN is a relatively simple and straightforward protocol for WOC assessment since the kinetics are driven in one electron steps and commercially available O_2 sensors can be used. However, CAN is only sufficiently stable at low pH values of typically 0.9, which limits its applicability.[271] Even though chemical and photochemical water oxidation tests are thus performed at very different pH values, their "overpotentials" for water oxidation correspond to comparable E° at the given pH values.[91] In our case, water oxidation was tested by a standard method, measuring O_2 production by a luminescent dissolved oxygen electrode (LDO) with results between 5 x 10^{-4} and 10^{-2} mmol oxygen per milligram catalyst. Co_3O_4-HT-B was the most active catalyst (1.05 x 10-2 mmol oxygen per mg) and Co_3O_4-MS showed the lowest activity (6.45 x 10-4 mmol oxygen per mg) (see Figure 3-15), as observed for photocatalytic oxidation. Despite this similarity and the comparable "overpotentials", the activities of the other cobalt oxides vary drastically between both test methods. In contrast to the photochemical oxidation, the activities for the chemical oxidation display the expected correlations with the materials parameters. A clear increase of the activity with higher BET surface area can be seen. Likewise, the increasing disorder among the sample series results in continuously higher activity. As BET surface area and disorder show similar trends, both being linked to the preparative history, a plausible further differentiation into one key performance parameter is not possible from the present data set. Additionally, the valence states derived from XANES and XPS data showing lower general oxidation states could be a key performance parameter. Generally, samples synthesized at lower temperatures show higher activities than the high temperature samples, such as Co_3O_4-MS, -BM, and -SG (see Figure 3-15).

The observation that WOC activity shows significant differences for chemical and photocatalytic but not for electrocatalytic water splitting indicates that the differences among the materials, such as in surface area, disorder or oxidation state, are less important for electrocatalytic water oxidation, i.e. the influence of the synthetic method is rather negligible here. A possible explanation for this observed leveling is the reversible pre-catalytic formation of a thin amorphous shell of $CoO_x(OH)_y$, since the post-catalytic investigations still show the presence of Co_3O_4 (see Figure 3-14). This supports the in-situ X-ray study of Dau et *al*., who observed the formation of a sub-nanometer $CoO_x(OH)_y$ shell containing di-μ-oxo-bridged $Co^{3+/4+}$ ions. In this study it is furthermore shown, that the catalytically active $CoO_x(OH)_y$ crystallizes back to Co_3O_4 after returning to non-catalytic electrode conditions, showing a reversible formation of the active electrocatalyst.[283] Dau et *al.* found a reversibly formed intermediate sub-nanometer shell containing di-μ-oxo-bridged $Co^{3+/4+}$ ions by advanced in-situ X-ray techniques. A very similar study, published by Chen & Cheng et *al*. in the

same year, support these results as well with in-situ X-ray diffraction techniques, showing the formation of α- and β-COOH thin layer from CoO on Co_3O_4 nanocubes.[311] These findings would relativize the influence of pristine surface composition and structure.

All in all, a different behaviour was observed for all three catalytic methods. This agrees with the results of Stahl et *al.* comparing different manganese oxides for photocatalytic, chemical and electrocatalytic water oxidation.[91] The present study narrowed this approach further down to a single material type which was subjected to different preparative histories. Notwithstanding this systematic strategy, the observed differences in activity show clear deviations between the different oxidation methods. Although photochemical and chemical oxidation should presumably show a similar trend, the comparably sluggish kinetics through the more complicated photocatalytic cycle could be the reason for the observed deviations.

Regardless of these specific differences in assessment, the preparative method exerts a clear influence on the WOC for both photochemical and chemical water oxidation. Surface area, oxidation state, and disorder were identified as the most important parameters for the chemical oxidation performance. In contrast, no clear trend for these parameters could be found for the photochemical oxidation. However, in both test methods, Co_3O_4 samples synthesized at higher temperatures generally show lower activity, than those obtained at notably lower synthesis temperatures. As for electrochemical water oxidation, no significant trends were derived, i.e. the choice of the synthesis method exerts a rather negligible effect on the catalytic performance.

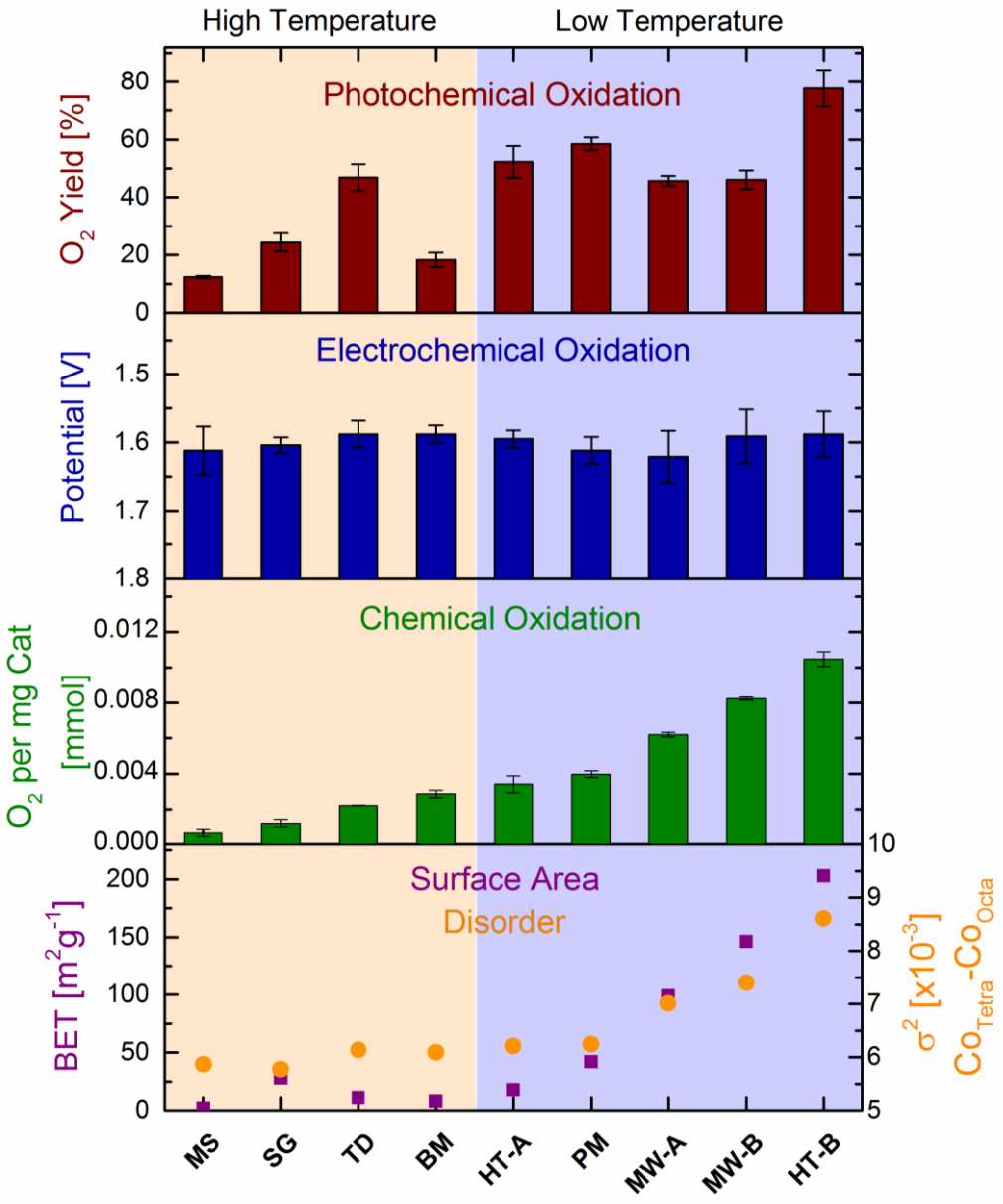

Figure 3-15. Comparison of the water oxidation activity of spinel Co_3O_4 synthesized by different methods by applying photochemical, electrochemical, and chemical oxidation methods, as well as the BET surface area and the mean-square disorder parameter σ^2. For the photochemical oxidation a standard $[Ru(bpy)_3]^{2+}/S_2O_8^{2-}$ protocol was used with a borate buffer (pH 8.5). Electrocatalytic activity is compared by the potentials vs RHE at 1 mA/cm^2 in 1 M KOH, and the chemical oxidation was tested in 146 mM ammonium cerium (IV) nitrate (CAN) (Figure created by Lukas Reith).

3.5 Conclusion

In this chapter, a two-step strategy using spinel-type Co_3O_4 water oxidation catalysts (WOCs) as a model system was introduced to investigate the fundamental issue of the influence of the preparative method on the WOC activity determined with different catalytic test methods. To this end, nine different synthetic approaches to obtain Co_3O_4 were first applied, and the as-synthesized products were compared with respect to their key physical properties, such as crystallinity, disorder, oxidation state, and particle size. Second, this spectrum of cobalt oxide materials was subjected to a critical comparison of their WOC activity using the three most widely applied test methods, namely photocatalytic, electrocatalytic and chemical water oxidation.

The Co_3O_4 samples synthesized at lower temperatures show higher disorder as determined from EXAFS fitting, which strongly correlated with the observed peak broadening in their Raman spectra. These more disordered samples are also found to contain lower fractions of Co(III), indicating a higher amount of oxygen vacancies, than those exhibiting a higher degree of crystallinity, as evident from XPS and XANES data. Generally, cobalt oxides synthesized at low temperatures (≤ 180 °C) show higher water oxidation activities in the chemical and photocatalytic assessment protocols than those obtained at higher temperatures, with molten salt synthesis giving rise to lowest and hydrothermal approaches to highest WOC activity.

Chemical oxidation as the most direct test protocol brought forward the clearest correlation between increasing surface area/disorder along with lower average cobalt oxidation states and increasing catalytic activity. However, such straightforward trends were not observed in photochemical water oxidation. In contrast, the electrochemical water oxidation activity was far less sensitive to variations in the materials properties. The underlying reason for this leveling effect is most likely the formation of an active thin amorphous $CoO_x(OH)_y$ shell during electrocatalysis, as observed in previous studies.

We here demonstrate that the synthetic method exerts a crucial influence on the materials characteristics of Co_3O_4 WOCs which in turn leads to significant differences in their catalytic activity in chemical and photochemical assays. These trends have an impact on the general ranking of WOC activity which should be unambiguously differentiated with respect to the specific applied protocol. Further studies are under way to explore the optimization of ternary and higher WOCs, such as perovskites, through fine-tuned synthetic methodologies addressing individual materials parameters.

4 Microwave-Hydrothermal Tuning of Spinel-type Co_3O_4 Water Oxidation Catalysts

This chapter is based on the following publication:

Microwave-Hydrothermal Tuning of Spinel-type Co_3O_4 Water Oxidation Catalysts, Karla Lienau, C. A. Triana, Lukas Reith, Sebastian Siol, and Greta R. Patzke, *Frontiers in Chemistry* **accepted,** Manuscript ID: 508534

Author contributions: Parts of the Raman and TEM measurements were performed by Lukas Reith. XAS analysis was performed with the help of S. Esmael Balaghi and C. A. Triana and evaluation was performed by C.A. Triana. XPS measurements were conducted and analysed by Sebastian Siol. EIS and long-term chronoamperometry measurements were conducted and evaluated by S. Esmael Balaghi

4.1 Introduction

The role of Co_3O_4 as water oxidation catalyst was already laid out in the previous chapters. It was mentioned that not only the type of catalyst, but also its crystallinity, morphology, size, facets, oxidation states and maybe even more parameters play important roles in the water oxidation activity.[154] In previous studies, a wide range of different synthesis methods has been applied to obtain Co_3O_4 in various morphologies and forms.[39,71,76,283,298–307] In the last chapter, spinel-type Co_3O_4 samples prepared by a broad spectrum of different synthesis methods and the resulting materials were compared regarding their characteristics and photo-, electro- and chemical water oxidation activity. Indeed, it was found that the synthesis method exerts a major influence on the catalytic activity for water oxidation. Furthermore, large deviations of these activity trends were found by comparing the three water oxidation methods. Whereas a strong correlation between the activity and surface area, crystallinity and disorder of the corresponding materials was found for chemical oxidation, electrocatalytic oxidation was barely influenced by these parameters. This trend was in part ascribed to the in situ cobalt oxyhydroxide formation observed by other groups.[283,298,311]

In the present study, we conduct an in-depth investigation of the influence of microwave-hydrothermal synthesis parameters on the WOC activity of Co_3O_4 nanocubes, thereby narrowing the parameter range further down in search of optimization guidelines. Microwave synthesis, which is already well established in organic synthesis, attracts increasing interest in inorganic synthesis, especially for different oxide materials.[76,341–347] Microwaves as non-ionizing and long-wavelength electromagnetic radiation enable high penetration depths and fast heating, thus rendering syntheses economically attractive by decreasing reaction times and temperatures. Due to optimization of the microwave reactor conditions, such as shape, constant motion of the reactor vessels and stirring,

thermal gradients and "hot spots" can be largely prevented leading to uniform growth and dimensions of the oxide particles.[348] This renders microwave synthesis a crucial option for well-defined particle fabrication in nanoscience and technology.[341] However, little is still known about the growth mechanisms of metal oxides under the influence of microwaves.[349–351] More information about microwave synthesis are provided in chapter 1.2.2.

In the case of Co_3O_4 we recently demonstrated that the growth mechanism can play a key role in the resulting water oxidation activity.[165] Therefore, we here started from a well-defined microwave protocol for microwave-assisted spinel-type Co_3O_4 and systematically studied the influence of the synthetic parameters on the properties and catalytic performance of the emerging materials to demonstrate the importance of these parameters in microwave-hydrothermal WOC synthesis.[320,352,353] To this end, the Co_3O_4 spinel samples were characterized with a wide range of analytical methods and subsequently compared with respect to their chemical and electrocatalytic water oxidation activity. The results of this study shed detailed and practical light on our recent work presented in the previous chapter by illustrating that a given Co_3O_4 catalyst cannot be simply compared to another specimen without taking the preparative history into account.

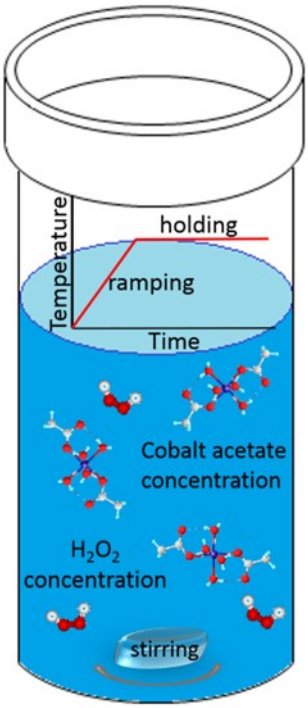

Figure 4-1. Scheme of varied microwave-hydrothermal synthesis parameters throughout this chapter.

4.2 Aims of the project and brief summary

Co_3O_4 as a promising candidate for water oxidation is a highly investigated candidate. As clearly explained in the previous chapter, the preparation method does influence the resulting materials properties and therefore water oxidation activities. We here prepared Co_3O_4 by microwave hydrothermal synthesis, which offers attractive features of fast kinetics and parameters, while varying several synthesis parameters. The resulting spinels were examined with respect to materials characteristics like crystallinity, oxidation state and surface area using various analytical methods. Furthermore, their water oxidation activity in electrocatalytic and chemical oxidation setup was investigated. For both oxidation methods we demonstrate in the following that the same trends regarding the synthesis parameters were found, showing higher activity for lower synthesis temperatures, lower precursor concentrations, addition of hydrogen peroxide and shorter ramping and reaction time.

4.3 Experimental

EIS measurements were performed by S. Esmael Balaghi.

4.3.1 Synthetic procedure

All Co_3O_4 samples were obtained from microwave-hydrothermal synthesis. $Co(CH_3COO)_2{\cdot}4H_2O$ (Sigma-Aldrich, reagent grade) was dissolved in 15 mL water and the pH was adjusted to 11 by addition of aqueous ammonia (25% NH_3, Merck, GR for analysis). The dispersion was poured into a 95 mL CEM Omni Teflon vessel equipped with a stirring bar and sealed accordingly. Always, two reactions were conducted simultaneously, and temperature and pressure were monitored for the reaction in the reference vessel. The reaction was temperature controlled, i.e. the microwave power was adjusted according to the reference vessel temperature. The reaction mixture was heated to 180 °C in 30 min (referred to as ramping time) and kept at this temperature for 45 min (referred to as holding time), followed by a cooling period of approximately 30 min, before separation of the product by centrifugation. The samples were air-dried at 80 °C prior to further characterization. The parameters were varied as summarized in Table 2 and the samples were labelled accordingly.

The parameters were varied according to Table 4-1 and the samples are labelled accordingly.

Table 4-1 Synthesis parameters of the investigated spinel-type Co_3O_4 samples.

Sample Name	$Co(ac)_2$ amount [mmol]	H_2O_2 amount [ml]	T [° C]	Ramping time [min]	Holding time [min]	Stirring speed
0.18 mmol	**0.18**	0	180	30	60	slow
0.6 mmol	**0.6**	0	180	30	60	slow
1.2 mmol	**1.2**	0	180	30	60	slow
Standard	**1.8**	**0**	**180**	**30**	**60**	**slow**
1.5 ml H_2O_2	1.8	**1.5**	180	30	60	slow
3 ml H_2O_2	1.8	**3**	180	30	60	slow
160° C	1.8	0	**160**	30	60	slow
140° C	1.8	0	**140**	30	60	slow
20 min ramping	1.8	0	180	**20**	60	slow
10 min ramping	1.8	0	180	**10**	60	slow
30 min holding	1.8	0	180	30	**30**	slow
Fast stirring	1.8	0	180	30	60	**fast**

4.3.2 Catalytic measurements

Electrocatalytic measurements were carried out in a standard three-electrode setup with an Ag/AgCl (Aldrich® glass reference electrode Ag/AgCl with 3 M KCl) as reference- and a Pt-foil as counter electrode. The working electrode was prepared by first dispersing the WOC in water (2 mg in 100 mL) and 40 mL of this dispersion were drop casted on 1 cm^2 FTO (Aldrich, ~7 Ω/sq). After 30 min drying at 80 °C, Nafion solution (10 mL, 1wt-% diluted from 5 wt-%, Nafion® perfluorinated resin solution, Aldrich) was drop-casted on the surface to fix the WOC. For the measurements, 1 M KOH was used as electrolyte. A Bio-Logic SAS SP-150 potentiostat was used. The standard measurement protocol consisted of three steps: (1) Cyclic voltammetry (CV) was measured from 0-0.7 V vs. Ag/AgCl with 0.005 mV step size. For data evaluation, only the second cycles were compared to each other. (2) Stepwise chronoamperometry increasing the potential from 0.45 V to 0.65 V in 0.01 V steps and held for 5 min. The stabilized current at the end of each step was used for further evaluation to eliminate diffusion currents. (3) Chronoamperometry in which a potential of 0.6 V vs. Ag/AgCl was applied for 2 h for stability testing.

For electrochemical impedance spectroscopy (EIS) and long-term chronoamperometry studies in 1.0 M KOH, 2 mg of the obtained cobalt oxide powders were dispersed in 100 µL of 2% Nafion (ethanol solution) and sonicated for 15 min. A total of 40 µL of the suspension was drop-cast on the carbon cloth (Toray Carbon Paper, TGP-H-60, 1 cm2) and kept at 60 °C for 15 min.

To evaluate the chemical water oxidation activity of the catalysts, the following standard CAN method was applied: Prior to addition of WOC, CAN (2 g) was dissolved in milli-Q water (40 mL) and the solution was degassed with argon. After subsequent addition of WOC (2 mg) the oxygen evolution was recorded for 45 min while stirring the solution, using a luminescent dissolved oxygen sensor (LDO). For data evaluation, only the peak concentration was used. A Hach HQ40d multimeter with LDO 101 sensor was used for these measurements.

4.3.3 Materials and methods

Powder X-ray diffraction (PXRD). The spinels were characterized by powder X-ray diffraction (PXRD) measurements on a STOE STADI P diffractometer in transmission mode (Ge monochromator Mo $K_{\alpha 1}$ radiation).

Fourier transformed infrared spectra (FT-IR). FT-IR spectra were recorded on a Bruker Opus spectrometer.

Nitrogen sorption. The surface area was measured using Brunauer−Emmett−Teller (BET) measurements on a Quadrasorb SI machine in N_2-adsorption mode. Samples were degassed at 100 °C overnight under vacuum prior to the measurements.

Raman. Raman spectra were measured on a Renishaw inVia Qontor confocal Raman microscope with a diode laser (785 nm).

Microscopy. SEM was measured on a Zeiss SUPRA 50VP SEM equipped with a Schottky field emitter and an inlens secondary electron (SE) detector. An acceleration voltage of 10 kV and a working distance of 5.4-6 mm were applied, TEM images were taken on a JEOL JEM-1400 Plus. The camera was a JEOL CCD camera Ruby (8 M pixel) and the electron beam source a LaB6 crystal operated at 120 kV. HR-TEM images were obtained from a FEI Tecnai F30 FEG device, equipped with a CCD Gatan 794 MultiScan Camera and a Schottky emitter (300 kV).

X-ray photoelectron spectroscopy (XPS). XPS measurements were performed by Sebastian Siol on a Physical Electronics (PHI) Quantum 2000 spectrometer. The monochromatic Al-K_α radiation was generated from an electron beam (15 kV, 35.8 W). For energy scale calibration, Au and Cu reference samples were used. The measurements were carried out at 10^{-8} mbar, with an electron take off angle of 45° and a pass-energy of 23.5 eV. A low energy electron source was used for charge compensation throughout the measurements. The alignment of the acquired spectra was performed using the the main (CC) component of the C1s core level emission. The modified Auger parameter was calculated by adding the kinetic energy of the CoL3VV and Co 2p3/2 binding energies.

X-ray absorption spectroscopy (XAS). XANES-EXAFS spectra at the Co *K*-edge on solid powder samples dispersed in cellulose of the synthesized Co_3O_4 and reference oxides $Co^{II}O$ and $LiCo^{III}O_2$ were carried out at the SuperXAS beamline at the Swiss Light Source (SLS), Paul Scherrer Institute (PSI) Villigen, Switzerland. Measurements were carried out by quick-scanning (QEXAFS) acquisition data protocols using a three-ionization chamber configuration in transmission mode and a 5-element Silicon Drift Detector. For energy calibration, the spectrum of a metal Co foil was measured simultaneously at the second ionization chamber. The X-ray beam was collimated using a Si coated mirror and the energy was scanned using a channel-cut Si[111] monochromator. A Rh coating toroidal mirror was used after the monochromator to focus the incident X-rays with a spot size of 400×200 μm^2 on the samples and a photon flux of 5.0×10^{11} photons. The measured EXAFS spectra $k^3\chi(k)$ were extracted by standard data reduction, absorption edge energy calibration and background subtraction as implemented in ATHENA.[326] The spectra were reduced into the range $\Delta k \approx$ 3-14 $Å^{-1}$ and Fourier transformed to FT$|k^3\chi(k)|$ into the real-space interval of $\Delta R \approx$ 0-6 Å. To calculate main values for interatomic distances, coordination numbers (*N*), and Debye-Waller factors (σ^2) nonlinear least-squares fitting of the FT$|k^3\chi(k)|$ spectra was carried out by ARTEMIS using atomic clusters of Co_3O_4 (ICSD code 27498), generated by ATOMS as implemented in IFEFFIT.[326] The amplitudes and phases shift for single and multiple scattering paths were calculated using FEFF6.[327]

4.4 Results & Discussion

4.4.1 Materials characterization

XAS measurements were performed and analysed by Dr. Carlos A. Triana.

In order to screen the parameter influence on the WOC activity of cobalt oxide nanoparticles, the selected standard microwave hydrothermal protocol was varied with respect to: temperature, precursor concentration, amount of hydrogen peroxide added to the synthesis mixture, the ramping and holding times of the synthesis and the stirring speed (see Table 4-1). Samples were labelled with respect to the single varied parameter.

Powder X-ray diffraction (PXRD) pattern show the formation of phase pure spinel structure (space group $Fd\bar{3}m$ (No.: 227)) for all samples (see Figure 4-2a). Co_3O_4 crystallizes in the normal spinel structure, i.e. the Co^{2+} ions occupy one eight of the tetrahedral voids of cubic close packed oxygen anions and Co^{3+} occupy half of the octahedral voids. The general structural model is in accordance with the obtained Raman spectra shown in Figure 4-2b, where five phonon excitations can be observed: the A_{1g}, E_g, and the three F_{2g} modes are Raman active.[328] The symmetric Co-O stretching vibration of the octahedrally coordinated cobalt centers appearing at 693 – 685 cm^{-1} is assigned to the A_{1g} mode.[329] The Co-O stretching vibration of tetrahedrally coordinated cobalt centers is attributed to the F^3_{2g} mode at 196 – 193 cm^{-1}. The two remaining F_{2g} modes and the E_g mode are located at 621 – 618 cm^{-1}, 523 – 519 cm^{-1} and 484 – 480 cm^{-1}, respectively. The relative shifts of the Raman peaks as well as the different peak broadening indicate a difference in the short-range order of the synthesized Co_3O_4 spinel samples, analogous to the peak broadening observed in the PXRD patterns. Only very small shifts of the Raman peak centers of A_{1g} and F^3_{2g} modes are observed for the investigated samples, indicating the presence of very similar sample structures.

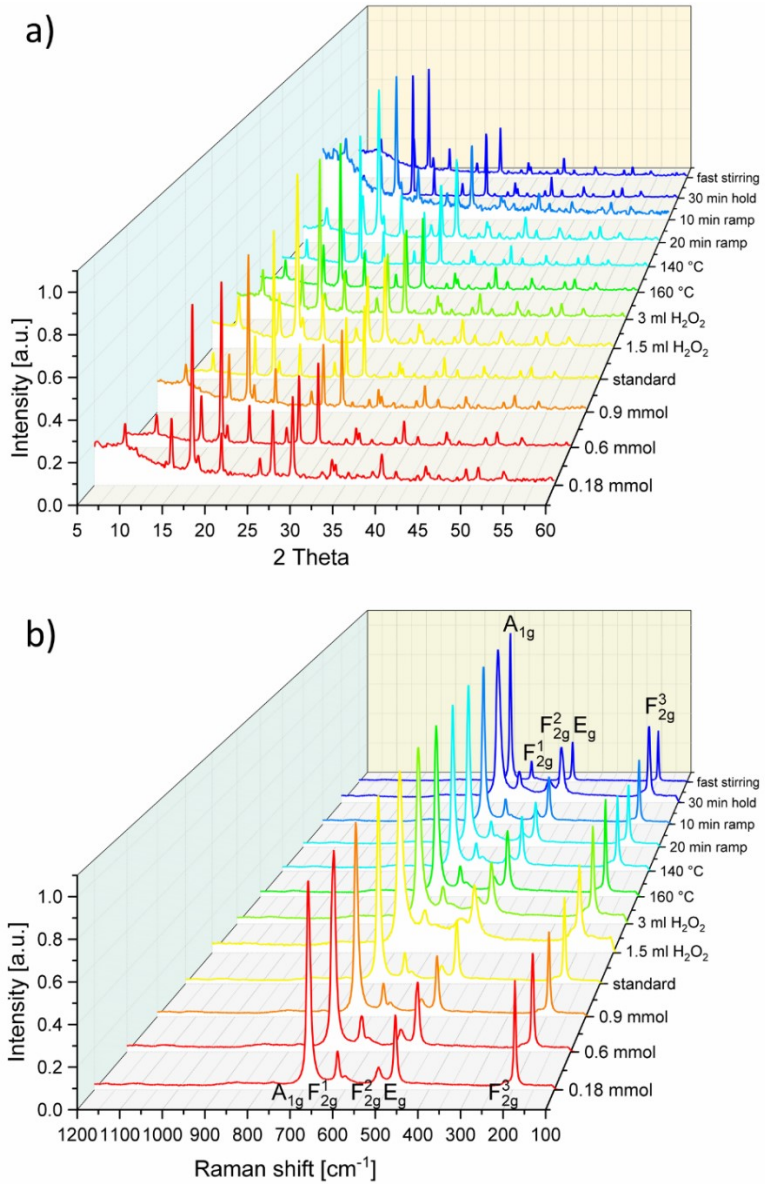

Figure 4-2. (a) PXRD patterns and (b) Raman spectra of the different spinel-type Co_3O_4 samples obtained from parameter variations of the standard microwave protocol.

Even though showing the same structure, the Bragg reflections of the different samples in Figure 4-2a exhibit slightly different full width half maxima (FWHM), from which the crystallite domain size can be calculated by means of the Scherrer equation.[255,256] The according calculated crystallite sizes τ are compared in Table 4-2. Broader reflections than obtained from the standard synthesis procedure were observed for the materials synthesized with the lowest precursor concentration, with addition of H_2O_2 and with more rapid heating. Interestingly, the temperature, the stirring speed and the reaction time (holding time) did not exert a significant impact on the FWHM of the Bragg reflections. The value of the surface area obtained from Brunauer-Emmet-Teller (BET) analyses (Table 4-2) moderately correlate with the crystallite sizes obtained from Scherrer analysis but appear generally quite low taking the particle sizes into account. This may indicate that the obtained Co_3O_4 particles were agglomerated to a large extent.

Table 4-2 Surface area measured by N_2-sorption and determined from BET and crystallite size determined from PXRD measurement calculated from Scherrer equation.

Sample Name	**BET surface area [m^2/g]**	τ_{XRD} **[nm]**
0.18 mmol	169	16
0.6 mmol	33	22
0.9 mmol	44	17
1.2 mmol	25	22
Standard	30	23
1.5 ml H_2O_2	67	12
3 ml H_2O_2	75	14
160° C	22	18
140° C	39	25
20 min ramping	75	14
10 min ramping	35	15
30 min holding	16	23
Fast stirring	18	32

SEM images of the obtained spinels show generally similar morphology but still visible differences (see Figure 4-3). Probably the most significant morphology differences can be observed in Figure 4-3 g) and i) representing the samples with H_2O_2 added to the reaction mixture, and also j) and k) which correspond to the samples that were heated more rapidly. Interestingly, the surface of the spinel material shown in Figure 4-3 j), emerging from a ramping time of 20 min, looks more rough than the one in k) which was heated up even faster, namely in 10 min. This is consistent with the BET surface area measurement results as shown in Table 4-2. Compared to the sample obtained under standard conditions shown in the middle (Figure 4-3 f)), many samples are less agglomerated. This is especially the case for the samples obtained from lower Co-concentrations (a) and b)), lower temperatures (c) and e)), faster stirring speed (d)) and shorter holding time (h)). To a large extend, this is not reflected in the obtained BET values.

Therefore, to provide a better comparison of the particles themselves and not only of how they agglomerate, TEM images were recorded as well and are shown in Figure 4-4. For the most different samples, HR-TEM was recorded as well and is shown in Figure 4-5.

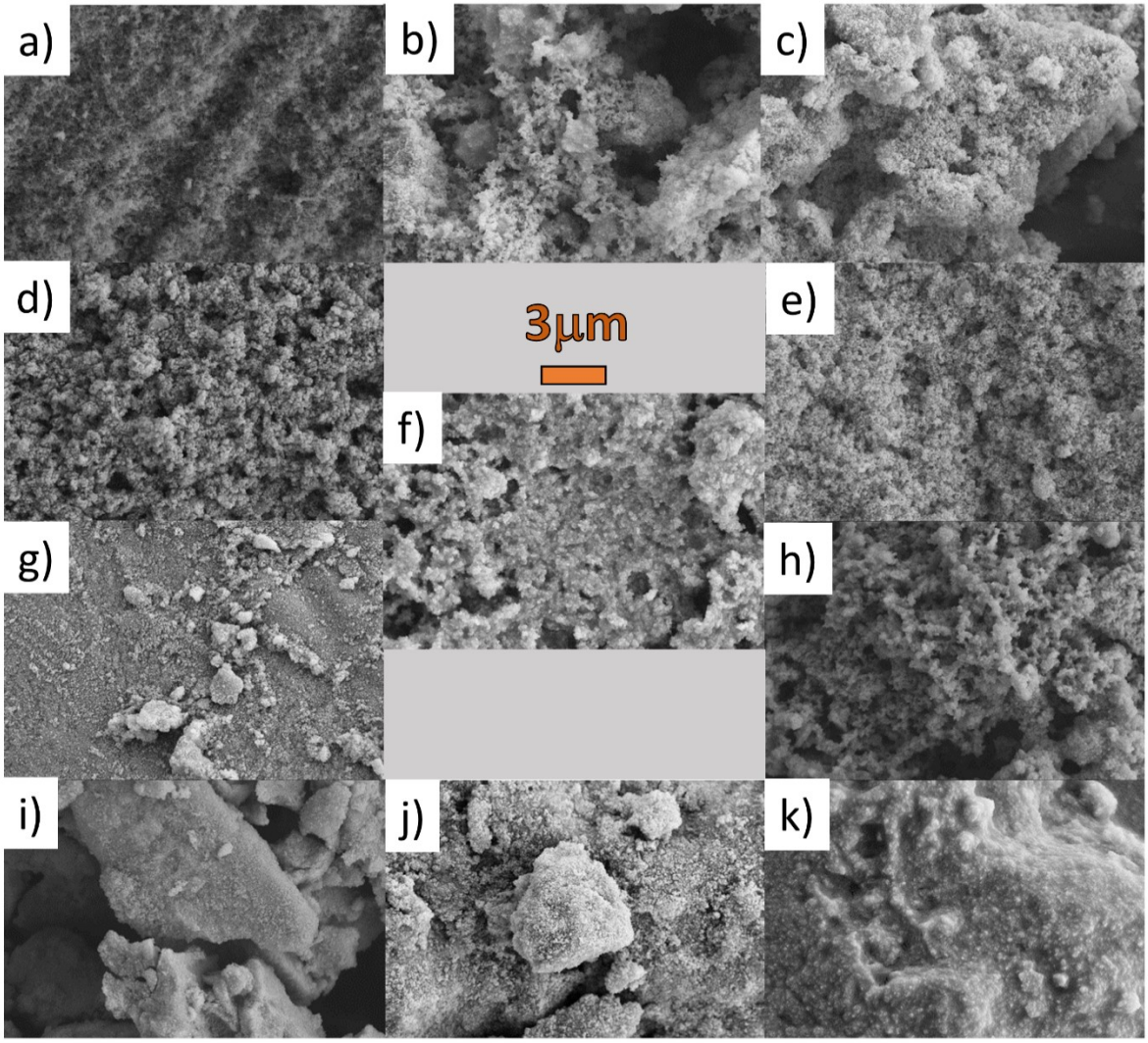

Figure 4-3. SEM images of the spinel samples synthesized with one parameter varying from the standard synthesis method (f)): a) and b) with 0.18 and 0.9 mmol cobalt precursor respectively, c) and e) with 140°C and 160°C synthesis temperature, d) with a faster stirring speed, g) and i) with addition of 1.5 and 3 ml H_2O_2 (30wt-%), h) with 30 min holding time and j) and k) with 20 and 10 min ramping time. For all images, the same magnification was applied (scale bar = 3 µm).

TEM images (see Figure 4-4) show moderately aggregated particles but this might be due to the different sample preparation for TEM and BET analysis. Whereas for BET measurements, the pestled powder is heated under vacuum to remove adsorbed gases, TEM sample are crushed in a mortar, followed by homogeneous dispersion in ethanol. Furthermore, it is obvious from TEM images that variation of the synthesis parameters exerts a notable influence on the resulting morphologies. Especially shorter ramping times (Figure 4-4d and g) and the addition of hydrogen peroxide (j and k) result in much smaller particles with diameters around 10-20 nm, whereas particle sizes of 30-40 nm were obtained from the standard synthesis.

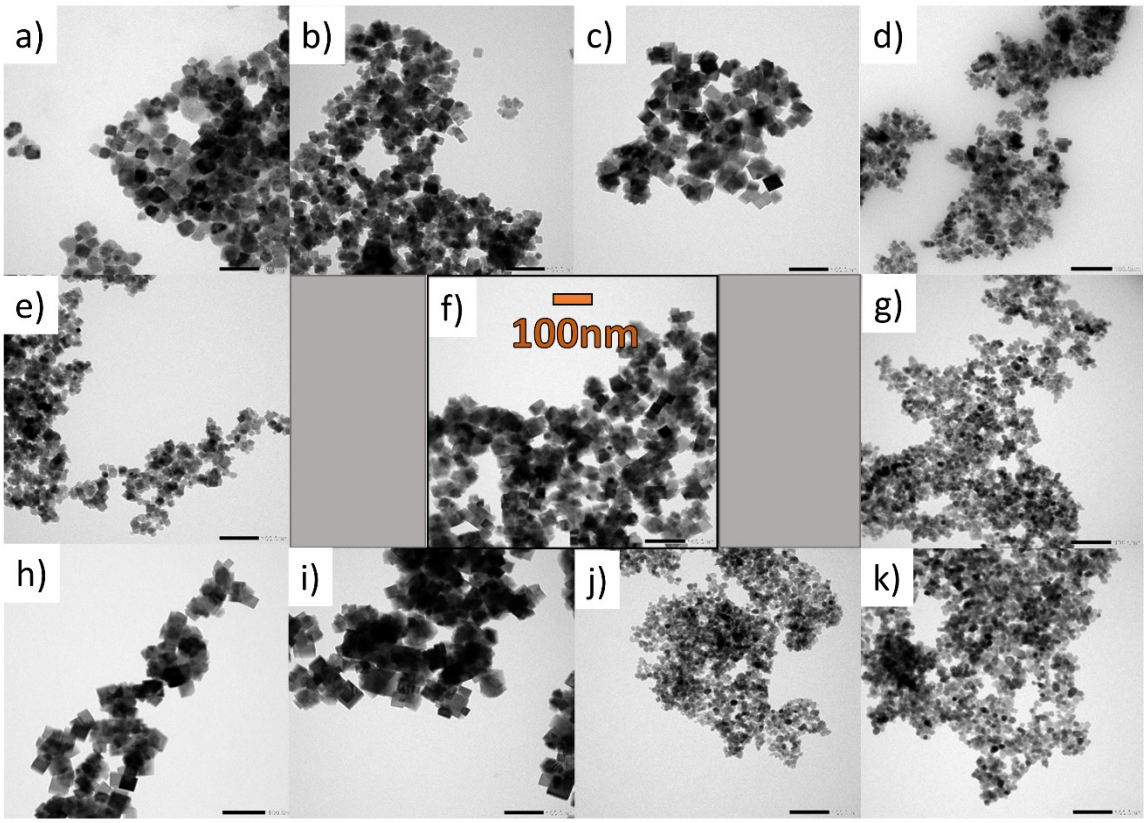

Figure 4-4. TEM images of the spinel samples synthesized with one parameter varying from the standard synthesis method (f)): a) and b) with 140°C and 160°C synthesis temperature, c) with 30 min holding time, d) and g) with 10 and 20 min ramping time, e) and h) with 0.9 and 0.18 mmol cobalt precursor respectively, i) with a faster stirring speed and j) and k) with addition of 1.5 and 3 ml H_2O_2 (30wt-%). For all images, the same magnification of 50 k was applied (scale bar = 3 µm).

High resolution images of four different samples were measured; obtained from the standard synthesis, from the lowest synthesis temperature (140°C), from lower Co-concentration (0.9 mmol) and obtained from addition of the highest H_2O_2 amount added to the reaction mixture (3 mL). Representative images are shown in Figure 4-5. For all these samples, the (111), (202), (311) and (404) planes were observed, except for the (404) being absent in the spinel obtained from standard synthesis. However, it cannot be concluded that the (404) plane is not present in this sample since the observed area is very small. From these measurements it can be assumed that the influence of the exposed plane and – most likely – also of the number of specific Co^{2+}/Co^{3+}-sites on the water oxidation activity can be neglected. This plane-dependency of water oxidation activity was shown to be an important effect in recent studies of Ding et *al.* and Sun et *al.* as already discussed in chapters 1.2.1 and 3.1.[297,303]

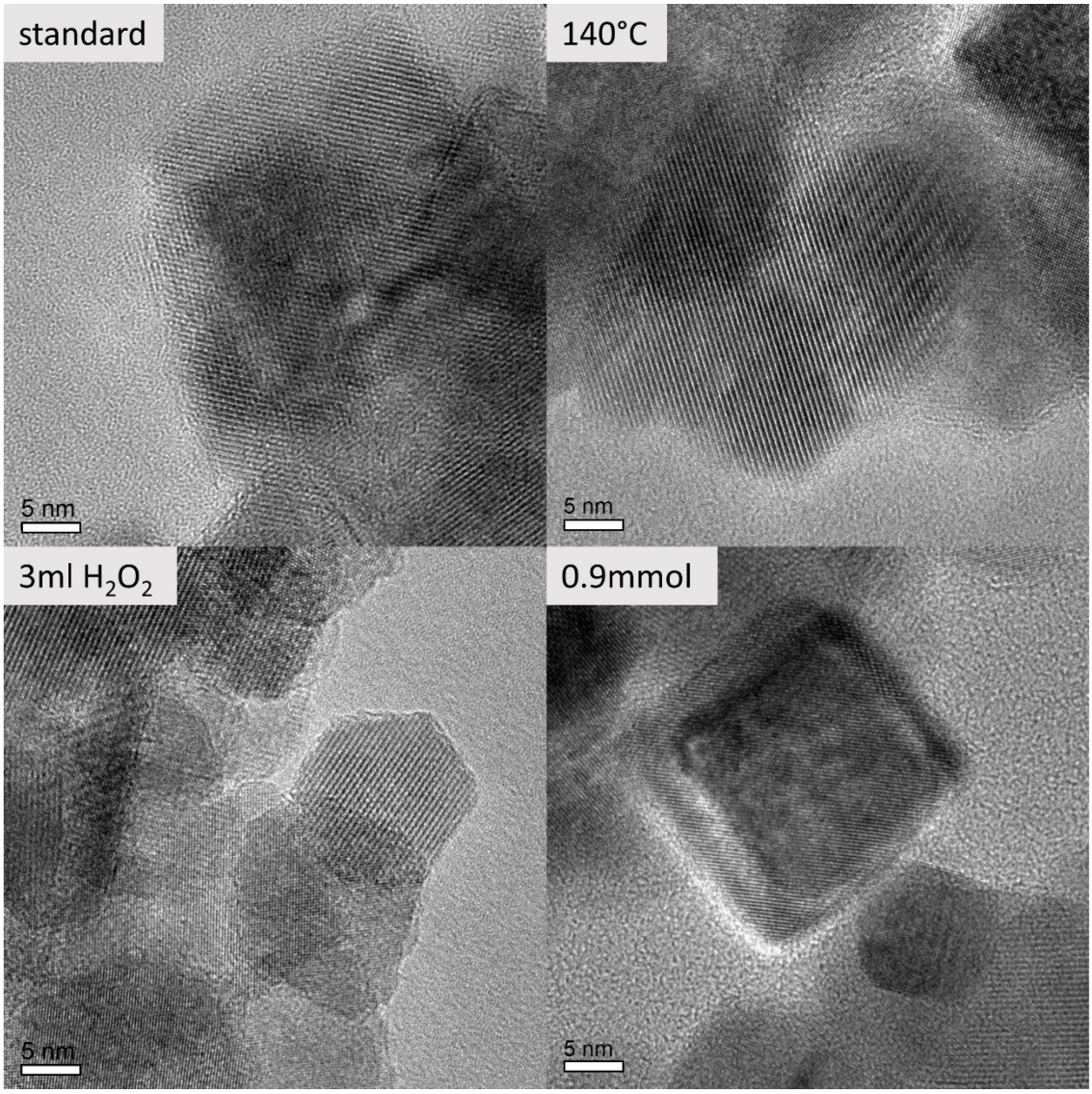

Figure 4-5. High-resolution TEM images of four selected samples: the sample produced at standard synthesis condition, one sample synthesized at lower temperature (140° C), one sample resulting from H_2O_2 addition (3 ml) to the synthesis mixture and one sample in which synthesis less precursor (0.9 mmol) was used.

Deeper insight into the atomic short-range order of the different synthesized Co_3O_4 oxides was obtained through extended X-ray absorption fine structure (EXAFS) analyses. Figure 4-7 shows the fitting of the Fourier-Transformed FT$|k^3\chi(k)|$ of the experimental Co *K*-edge EXAFS spectra $k^3\chi(k)$, for oxides synthesized at different H_2O_2 concentrations of 3 mL and 1.5 mL, low temperatures of 140 °C and 160 °C and at a lower $Co(ac)_2$ concentration of 1.2 mmol. Calculated main values for interatomic distances, atomic coordination numbers (*N*), and Debye-Waller factors (σ^2), are given in Table 4-3. The first peak in the FT$|k^3\chi(k)|$ spectra at $\mathbf{r} \approx 1.55$ Å, arising from backscattering of neighboring O atoms, relates to Co^{2+} and Co^{3+} cations in tetrahedral $\{CoO_4\}$ and octahedral $\{CoO_6\}$ coordination with oxygen atoms at interatomic distances of ≈ 1.914 Å and ≈ 1.899 Å, respectively. Those two shells, however, are too close to be resolved in the FT$|k^3\chi(k)|$ spectra, and hence they convolute to a main Co-O shell with a main interatomic distance Co-O ≈ 1.913 Å and main atomic coordination number N = 5.333. The second and third peaks at $\mathbf{r} \approx 2.49$ and $\mathbf{r} \approx 2.95$ Å due to

backscattering of neighboring Co atoms, relate to the Co_{Oct}-Co_{Oct} ≈ 2.856 Å [N = 4] and Co_{Tet}-Co_{Oct} ≈ 3.365 Å [N = 8] coordination shells, respectively. The fourth peak at **r** ≈ 4.70 Å relates to higher-order Co-O(-Co) coordination shells (Figure 4-7, Table 4-3). The positions of the coordination peaks in FT|$k^3\chi(k)$ and their Wavelet-Transformed (WT) spectra does not change among the different Co_3O_4 oxides. However, both the FT|$k^3\chi(k)$| and WT spectra exhibit a decreasing relative magnitude of the Co-O, Co_{Oct}-Co_{Oct}, Co_{Tet}-Co_{Oct}, and higher Co-Co(-O) coordination peaks. The amplitude decay in the FT|$k^3\chi(k)$| and WT spectra is related with a decreasing in the coordination number (N), or an increase in the mean-square disorder parameter σ^2, which arises from static structural disorder from crystal defects due to slightly different interatomic distances in the same coordination shell. Hence, the weakening in the relative amplitude of high coordination peaks in the FT|$k^3\chi(k)$| and WT spectra provides a direct indication of the extent of crystalline long-range order around the cobalt center.

The Co_3O_4 oxides obtained from standard synthesis, and those synthesized at 30 min holding and at 10 min ramping time, show FT|$k^3\chi(k)$| and WT spectra similar to those of Co_3O_4 synthesized at lower $Co(ac)_2$ concentrations of 0.9 and 1.2 mmol. As shown in Figure 4-7 and Table 4-3, the interatomic distances and the atomic coordination numbers N remain the same, showing that the atomic short-range order of those oxides is very similar regardless of the varying synthesis parameters, and display higher crystallinity among the different synthesized Co_3O_4 oxides. While the main interatomic distances and N-values for Co_3O_4 oxides synthesized at low temperatures of 160 and 140 °C remains quite the same, those oxides show an increasing in the mean-square static disorder σ^2 (Table 4-3). This suggests that these oxides have slightly increased local disorder, and points out to the synthesis temperature as a crucial parameter for controlling the local order and the degree of crystallization of the bulk spinel structure. The static local disorder σ^2 increases more remarkably for Co_3O_4 oxides synthesized at a H_2O_2 concentration of 1.5 and 3 ml (Figure 4-7and Table 4-3), which indicates increased local-disorder and lower crystallization degree in those oxides. The lower crystallinity of these oxides may arise from their formation process. When adding H_2O_2 to the initial suspension ($Co(CH_3COO)_2{\cdot}4H_2O$ + 1.5 ml H_2O + 25% NH_3), some divalent Co^{2+} cations are replaced by trivalent Co^{3+} species. The anions in suspension are then intercalated into the interlayer space to compensate the extra position charge due to Co^{3+} cations, thus leading to the formation of a hydrotalcite-type cobalt compound.[354] Thereafter, upon hydrothermal treatment at 180 °C, the hydrotalcite-cobalt compound is converted into a spinel-type Co_3O_4.[355] This structural transformation induces increased local-disorder in the oxides synthesized using H_2O_2 as oxidant. This finding agrees with the results from PXRD and Raman spectra, in which Co_3O_4 oxides synthesized at H_2O_2 concentration of 1.5 and 3 mL show broadened diffraction and Raman peaks due to the local structural dispersion of the Co and O atoms in the spinel structure (Figure 4-2).

Table 4-3 Main interatomic distances, atomic coordination numbers (N) and Debye-Waller factors (σ^2) calculated from the fitting of the experimental Co K-edge FT|$k^3\chi(k)$| | spectra of Co_3O_4 (phase uncorrected) (Table created by Carlos A. Triana).

Sample	Bond	*N*	σ^2	**r** (A)
1.2 mmol Co	Co-O	5.33	0.00291	1.9127
S_0^2≈0.752	Co_{Octa}-Co_{Octa}	4.00	0.00325	2.8558
E_0≈-1.252 eV	Co_{Tetra}-Co_{Octa}	8.00	0.00653	3.3496
	Co-Co	8.00	0.00354	4.9621
30 min holding	Co-O	5.33	0.00289	1.91245
S_0^2≈0.752	Co_{Octa}-Co_{Octa}	4.00	0.00324	2.85655
E_0≈-1.296	Co_{Tetra}-Co_{Octa}	8.00	0.00833	3.36713
	Co-Co	8.00	0.00437	4.96613
Standard	Co-O	5.33	0.00305	1.91274
S_0^2≈0.752	Co_{Octa}-Co_{Octa}	4.00	0.00341	2.85696
E_0≈-1.222	Co_{Tetra}-Co_{Octa}	8.00	0.00878	3.36580
	Co-Co	8.00	0.00463	4.96822
10 min ramping	Co-O	5.33	0.00299	1.91224
S_0^2≈0.752	Co_{Octa}-Co_{Octa}	4.00	0.00339	2.85667
E_0≈-1.203	Co_{Tetra}-Co_{Octa}	8.00	0.00890	3.36746
	Co-Co	8.00	0.00461	4.96724
0.9 mmol Co	Co-O	5.33	0.00300	1.91561
S_0^2≈0.752	Co_{Octa}-Co_{Octa}	4.00	0.00315	2.85892
E_0≈-0.549	Co_{Tetra}-Co_{Octa}	8.00	0.00522	3.35031
	Co-Co	8.00	0.00424	4.97378
160 °C	Co-O	5.33	0.00300	1.9136
S_0^2≈0.752	Co_{Octa}-Co_{Octa}	4.00	0.00346	2.8577
E_0≈-0.966 eV	Co_{Tetra}-Co_{Octa}	8.00	0.00675	3.3548
	Co-Co	8.00	0.00410	4.9670
140 °C	Co-O	5.33	0.00310	1.9153
S_0^2≈0.752	Co_{Octa}-Co_{Octa}	4.00	0.00354	2.8576
E_0≈-0.687 eV	Co_{Tetra}-Co_{Octa}	8.00	0.00697	3.3509
	Co-Co	8.00	0.00428	4.9672
1.5 ml H_2O_2	Co-O	5.33	0.00323	1.9127
S_0^2≈0.752	Co_{Octa}-Co_{Octa}	4.00	0.00358	2.8585
E_0≈-0.985 eV	Co_{Tetra}-Co_{Octa}	8.00	0.00718	3.3921
	Co-Co	8.00	0.00503	4.9672
3 ml H_2O_2	Co-O	5.33	0.00342	1.9135
S_0^2≈0.752	Co_{Octa}-Co_{Octa}	4.00	0.00381	2.8604
E_0≈-0.959 eV	Co_{Tetra}-Co_{Octa}	8.00	0.00797	3.3618

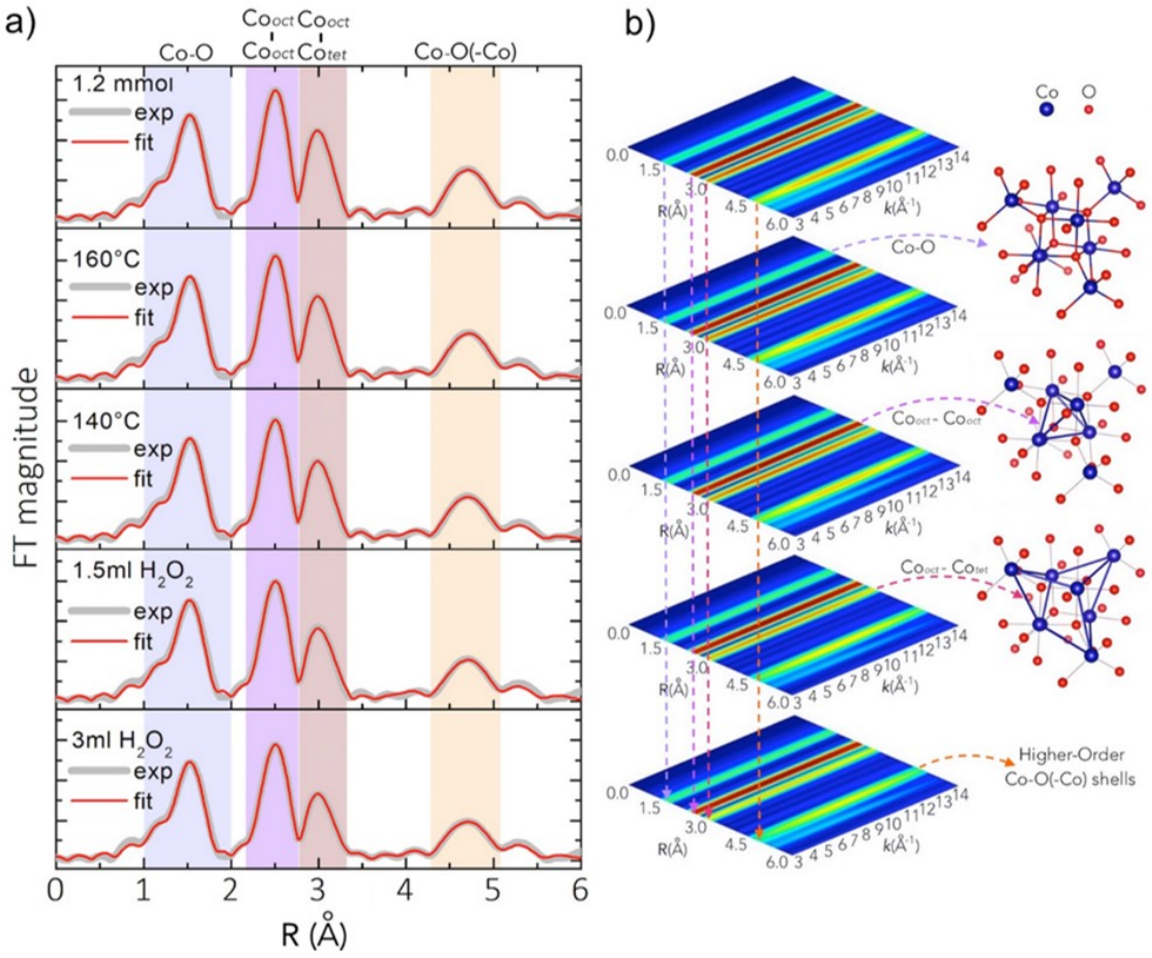

Figure 4-6. Fitting (red) of the FT|$k^3\chi(k)$| spectra (gray) for Co_3O_4 oxides synthesized at different H_2O_2 added amounts of 3 and 1.5 ml, low temperatures of 140 and 160 °C, and lower $Co(ac)_2$ concentration of 1.2 mmol (phase uncorrected). The background 2D contour plots are the WT of the $k^3\chi(k)$ spectra and their shaded regions highlight the decreasing of the peak intensity due to increases in the local-disorder parameter σ^2 for the Co-O, Co_{Oct}-Co_{Oct}, Co_{Tet}-Co_{Oct} and higher Co-Co(-O) coordination shells (Figure created by Carlos A. Triana).

X-ray absorption near edge structure (XANES) spectra was used to get further insight on the electronic properties and main oxidation state of Co in the synthesized oxides. Figure 4-7 shows the XANES spectra for oxides synthesized at H_2O_2 concentrations of 3 and 1.5 mL, low temperatures of 140 and 160 °C, $Co(ac)_2$ concentration of 1.2 mmol and those of the reference compounds $Co^{II}O$ and $LiCo^{III}O_2$. The Co *K*-edge absorption edge energy of the different Co_3O_4 oxides is located at ≈ 7720.1-.3 eV (Figure 4-7), suggesting that the oxidation state of Co is quite the same for all synthesized Co_3O_4 oxides. From the linear dependence of the Co *K*-edge position at the energy corresponding to $\mu(E) \approx 0.5$ of the normalized XANES spectra of Co_3O_4 and reference oxides $Co^{II}O$, $LiCo^{III}O_2$, the main oxidation state of Co was calculated to be 2.65. This agrees well with the main cobalt oxidation state of a normal spinel structure with 8 Co^{2+} and 16 Co^{3+} cations located on tetrahedral and octahedral sites, respectively. The slight changes in the white line intensity at ≈ 7729.57 eV (Figure 4-7), further indicates the existence of local-disorder and that the density of unoccupied Co *d*-states is slightly different for Co_3O_4 oxides synthesized at H_2O_2 concentrations of 1.5 and 3 ml. This, as previously discussed, could be due to the structural transformations induced when using H_2O_2 as oxidant, and to some extent of charge imbalance due to the interaction of Co^{2+}-Co^{3+} species.[332]

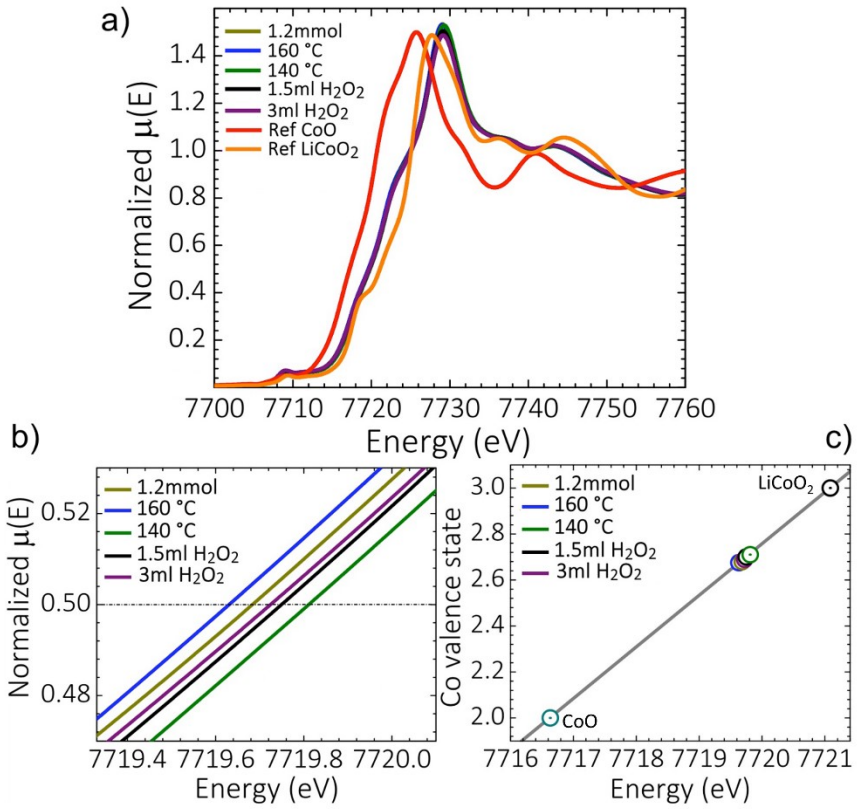

Figure 4-7. a) XANES spectra of selected synthesized Co_3O_4 oxides, and reference compounds $Co^{II}O$ and $LiCo^{III}O_2$, b) the zoom of the Co K-edge absorption of the normalized XANES spectra. c) The average Co valence state determined from the XANES spectra. (Figure created by Carlos A. Triana)

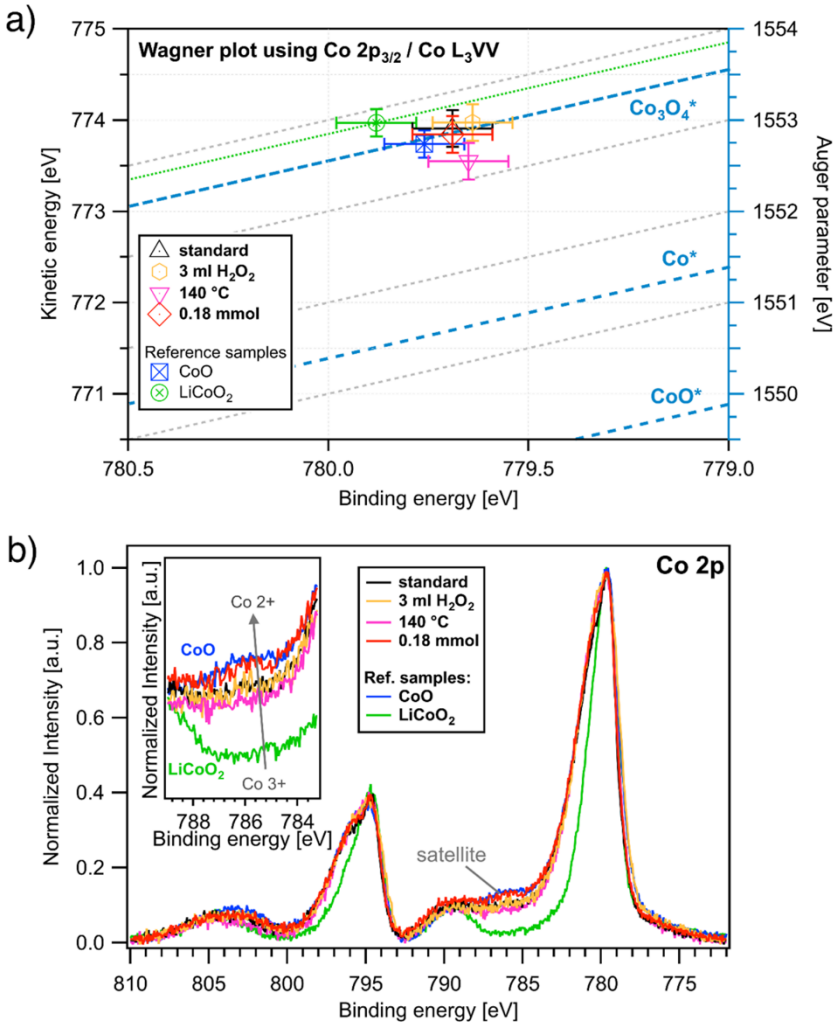

Figure 4-8. a) Wagner plot of the the four most different samples with the kinetic energy of the Co L3VV Auger electron and Co $2p_{3/2}$ core level binding energy with Co*, CoO* and Co_3O_4* references obtained from NIST database.[335] b) XPS spectra of the Co 2p peaks of the same samples and of $Co^{II}O$ and $LiCo^{III}O_2$ reference compounds (inset: satellite of the Co $2p_{3/2}$ peak) (Figure created by Sebastian Siol).

X-ray photoelectron spectroscopy was conducted on the standard, 3 mL H_2O_2, 140 °C and 0.18 mmol samples, the latter corresponding to the three synthesis conditions deviating most widely from the standard protocol. The Co 2p spectra are shown in Figure 5b with similar binding energies for all samples of ≈ 780 eV for the Co $2p_{3/2}$ and ≈ 795 eV for the Co $2p_{1/2}$ peak, which corresponds to literature values.[335] The spectra of the reference compounds $Co^{II}O$ and $LiCo^{III}O_2$ are shown in the same graph, indicating an increase in surface oxidation state in the order 0.18 mmol < standard ≈ 3 mL H_2O_2 < 140°C, which is in accordance with the XANES data shown in Figure 4-7. The oxidation states were determined from the intensity of the shake-up satellite at 785-786 eV (inset in Figure 4-8b), which originates exclusively from Co^{2+}, since the binding energies of Co^{2+} and Co^{3+} are too close to be distinguished.[336] For this reason, a Wagner plot containing the kinetic energies of the Co L_3VV Auger electrons vs the corresponding binding energies of the Co $2p_{3/2}$ core level photoelectrons is shown in Figure 4-8a. Wagner plots facilitate chemical state analysis, by illustrating shifts in photoelectron lines and X-ray excited Auger electron lines as well as the modified Auger parameter (AP) which is defined as the sum of the Auger electron kinetic energy and the corresponding core-level photoelectron binding energy.[262] Due to its insensitivity to static charging and variations in the energy scale calibration the AP is particularly useful to compare spectra of insulating samples with literature data and spectra acquired with different instruments. Reference values for the modified AP for CoO, Co and Co_3O_4 are indicated in Figure 5a as diagonal blue lines.[335] The APs of the as-synthesized Co_3O_4 samples are in agreement with previous values reported in literature, while only the parameter of the sample synthesized at low temperature (140 °C) is somewhat lower but still within the error range.

4.4.2 Water Oxidation Activity

EIS measurements were evaluated by S. Esmael Balaghi.

The obtained materials were furthermore compared for their water oxidation activity. Water oxidation tests were performed using two different methods, chemical and electrocatalytic water oxidation. In the first method, the water oxidation activity was assessed using cerium ammonium nitrate (CAN) which is a standard oxidant for water oxidation with a redox potential of 1.75 V vs NHE.[82] The formed oxygen was measured with a luminescent dissolved oxygen electrode and is shown as a function of the catalyst amount in Figure 4-9. The dark red bar at the beginning of each group represents the reference yield obtained from Co_3O_4 synthesized with standard parameters. Obviously, any change of synthesis parameters in the standard protocol leads to a better oxygen evolution. For the first three parameters, i.e. temperature, H_2O_2 and Co-precursor concentration, the oxygen concentration shows an upward trend whereas for the ramping time an optimum was obtained for 20 min ramping time. With shorter reaction (holding) time and faster stirring speed the activity was only marginally increased.

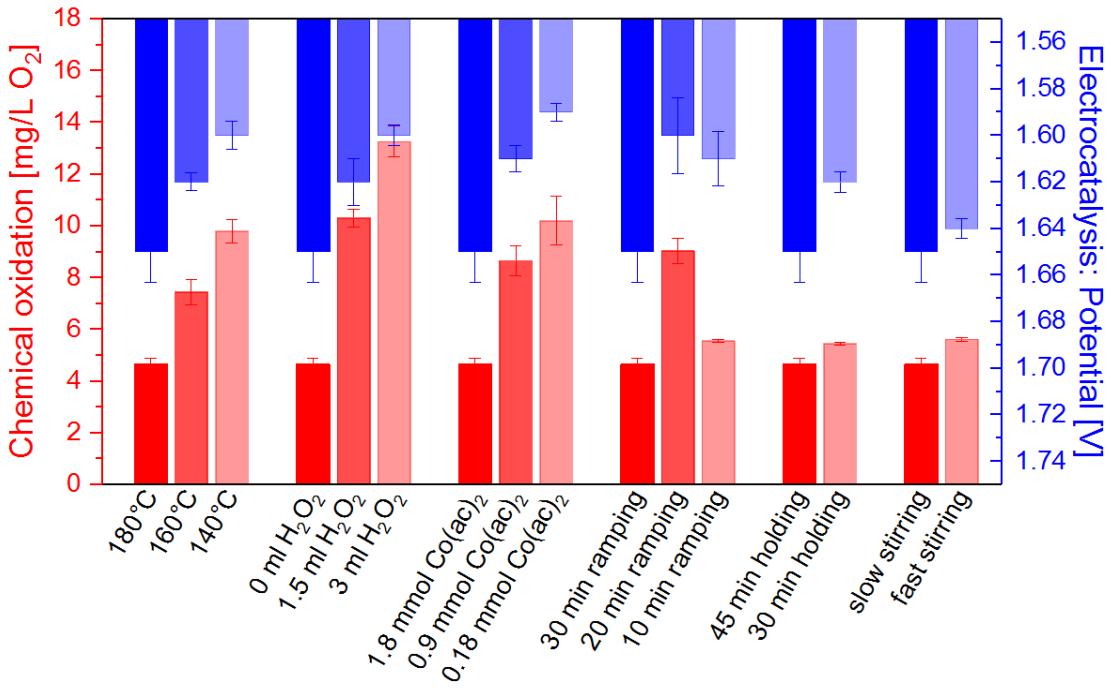

Figure 4-9. Water oxidation activity (chemical: red, electrocatalytic: blue) of the spinel samples synthesized with one parameter varying from the standard synthesis method (most intense colour, always on the left of each group). Chemical oxidation was assessed with 146 mM cerium(IV) ammonium nitrate (CAN) and the electrocatalytic activity was compared by the potentials vs. RHE at 1 mA/cm^2 in 1 M KOH.

Electrocatalytic measurements were performed with a standard three electrode setup using Ag/AgCl as reference and Pt as counter electrode in alkaline environment. The applicability of these two electrodes was shown in the previous chapter. To evaluate electrocatalytic water oxidation activity, stepwise chronoamperometry from 0.45 V to 0.65 V vs Ag/AgCl was performed. To obtain the bare Faradaic current without diffusion current, the current density value after 5 min holding at the same potential was considered and plotted against the applied potential. To facilitate comparison between the samples, the potential at 1 mA/cm^2 current density is shown at the left of each triad in Figure 4-9 (dark blue bars). Notably, the exact same trends for water oxidation activity were obtained by the two different methods. Both chemical and electrochemical activity could be increased by either shorter synthesis times, addition of hydrogen peroxide or lower precursor concentrations. The optimal ramping time was found to be 20 min. Shorter synthesis holding times had a more productive influence on the electrocatalytic performance than on the chemical oxidation activity, and stirring speed was the least important parameter in both assays.

To check, whether the increased catalytic activity arises from lower resistivity for OER on the electrode surface, two representative samples were chosen for EIS analysis – Co_3O_4 synthesized at 140°C and 180°C (standard synthesis). The Nyquist plots of both electrodes show a semicircle in the frequency range of 0.1-50 kHz (Figure 4-10 (a)), which can mainly be correlated to charge transfer resistance (R_{ct}) of the cobalt oxide catalysts. The diameter of the semicircle in the Nyquist diagram of Co_3O_4 synthesized at 140 °C is smaller in comparison with the standard sample, showing lower R_{ct}, due to reduced resistivity of OER on the electrode surface of the 140 °C sample. A coated electrode equivalent electrical circuit was used to fit the EIS data. The R_{ct} of the sample synthesized at 140 °C at 1.69 V (vs RHE) is estimated to be 6.20 Ω cm^{-2}, lower than that of the standard sample (8.40 Ω cm^{-2}) (see Table 4-4). This is presented in the Bode plots (Figure 4-10 (b)) as well, where the sample synthesized at 140 °C shows smaller resistance (Log |Z|). Therefore, it was confirmed that the sample synthesized with standard conditions suffer from higher OER resistivity in the applied potential window, whereas the lower OER resistivity of the sample synthesized at 140 °C leads to higher charge transfer properties.

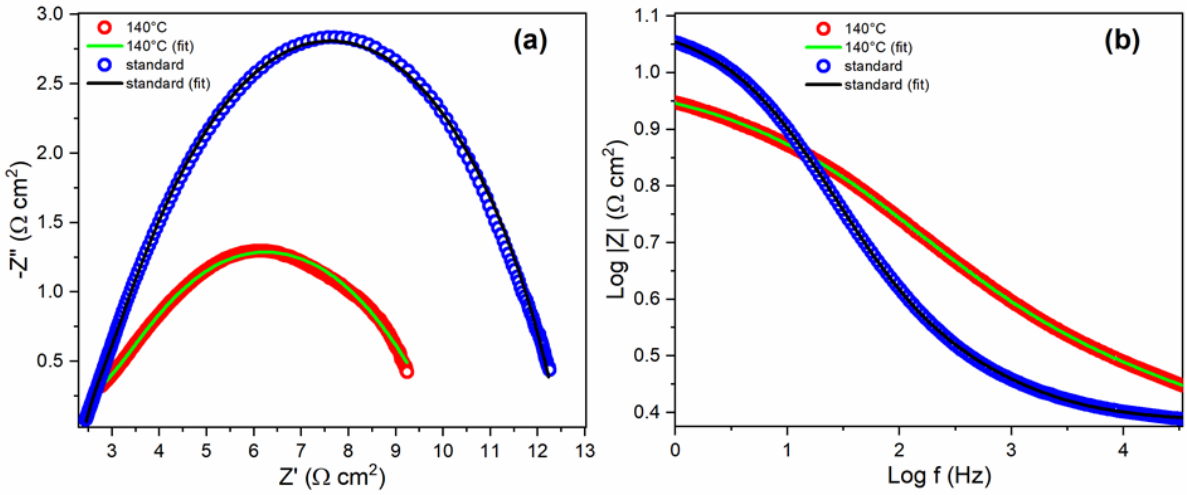

Figure 4-10. (a) Nyquist and (b) Bode plots of 140 °C and Standard samples in 1.0 M KOH at 1.69 V vs RHE applied potential in the frequency range of 0.1 Hz–50 kHz (Figure created by S. Esmael Balaghi).

Table 4-4 Equivalent circuit and its parameters for Carbon paper/catalyst in 1.0 M KOH solution obtained from the Nyquist plots of Figure 4-10 (Table created by S. Esmael Balaghi).

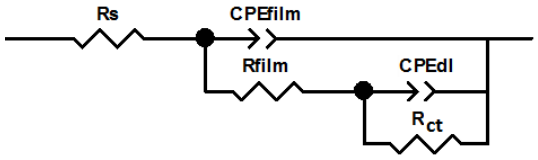

	Value	
Element	**140 °C**	**Standard**
R_S	2.03	2.41
CPE_{film}-T	8.09×10^{-3}	3.54×10^{-3}
CPE_{film}-P	0.37	0.66
R_{film}	1.77	1.66
CPE_{dl}-T	6.57×10^{-3}	3.98×10^{-3}
CPE_{dl}-P	0.48	0.67
R_{ct}	**6.20**	**8.40**

To evaluate the durability of the catalysts for water oxidation, long-term chronoamperometry was carried out at 2.19 V vs RHE in 1.0 M KOH for more than 20 hours with the same two representative samples as above. In comparison with the standard sample, the sample synthesized at 140 °C showed also higher current density in the long-term measurement. As shown in Figure 4-11, a current density of ~10.0 mA/cm^{-2} was recorded for the sample synthesized at 140 °C which was higher compared to the sample synthesized at standard conditions (~7.0 mA cm^{-2}). The activity loss with time can be explained by surface amorphization or decrease in the physical stability of the Nafion layer on the electrode surface.

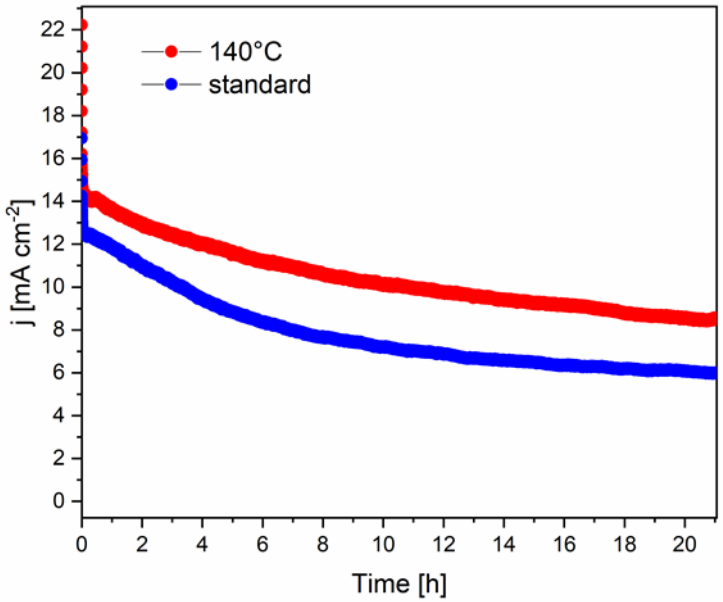

Figure 4-11. Long-term chronoamperometry of the samples synthesized at 140 °C and 180 °C (standard) in 1.0 M KOH at 1.64 V vs RHE (Figure created by S. Esmael Balaghi).

Compared to our abovementioned study (chapter 3) where the influence of substantially different synthetic methods on the electrochemical activity was rather marginal, the present variations in electrocatalytic performance after changing a single synthetic parameter are somewhat higher and display a trend. In contrast, parameter-dependent chemical water oxidation activity differences were slightly smaller compared to the previous study covering a wider range of methods (Figure 4-12).

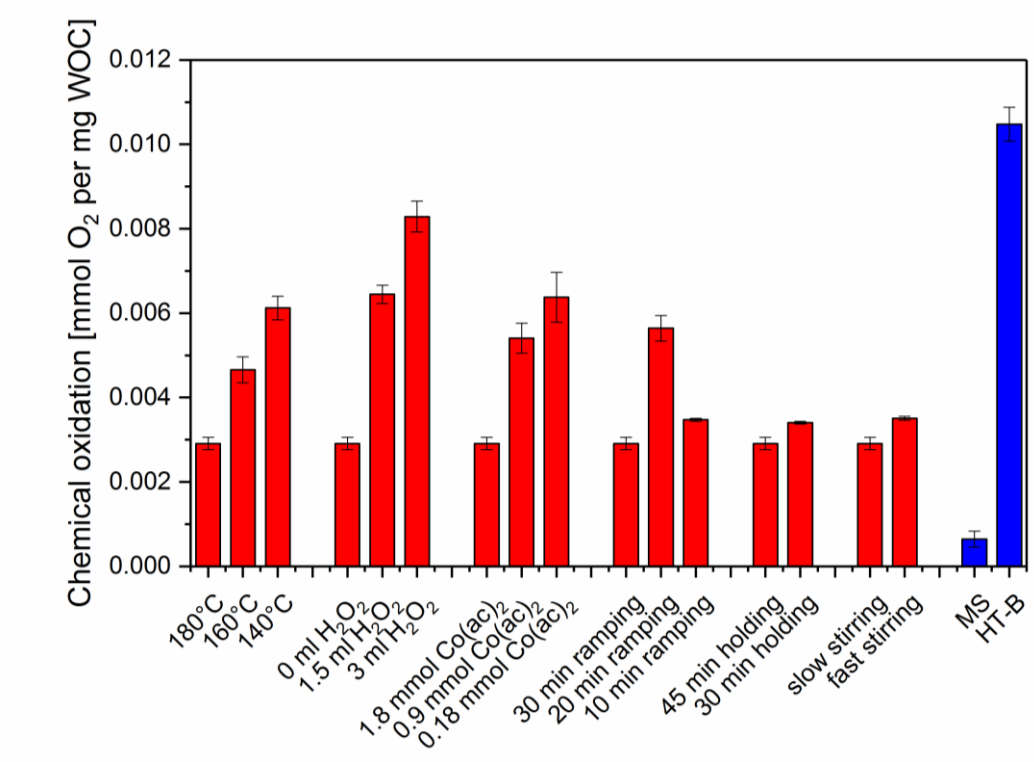

Figure 4-12. Chemical water oxidation activity values from this chapter compared to the least and most active samples from the comparison of Co_3O_4 synthesis methods introduced in Chapter 3.

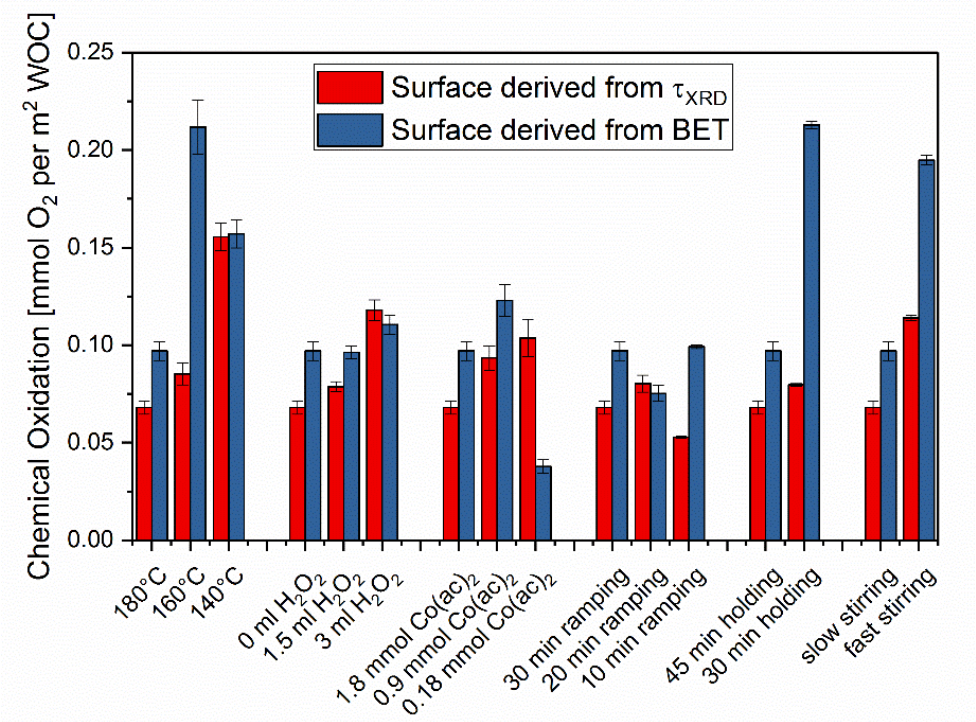

Figure 4-13. Chemical water oxidation activity normalized to the WOC surface area determined from two different methods: calculated from crystallite size determined by the Scherrer equation at FWHM of the PXRD patterns or derived from BET measurements.

Interestingly, for surface normalized activity (Figure 4-13) no correlation to any determined material parameter could be found. The lack of correlation between these activities and surface area is also obvious from comparison with calculated crystallite size and BET-determined surface area (Figure 4-14). The errors in BET and τ_{XRD} are in the range of 1-5 % (0.65 m^2g^{-1} for BET, determined by fourfold measurement of commercial Co_3O_4 with similar crystallite size than most of the here investigated samples and 0.2-1 nm for τ_{XRD}, determined from error propagation from PXRD peak FWHM determination). In light of the key role of the {HO-Co_2(μ-O/OH)$_2$-OH} edge site in Co_3O_4 assisted water oxidation revealed by Frei *et al.*[39], we tentatively plotted non normalized chemical water oxidation activities vs the bond length and disorder of Co_{Oct}-Co_{Oct} as determined by EXAFS fitting (cf. below, Figure 4-14). Other than for the other structural parameters (Co-O and Co_{Oct}-Co_{Tet}, see Table 4-3), a trend was about to emerge here, but more precise data are required to establish a truly significant correlation. In comparison, other materials characteristics such as oxidation state and crystallinity did not display any clear correlations with the water oxidation activity. As an overall trend, however, smaller particles with larger surface area as well as lower sample crystallinity with higher disorder result in higher water oxidation activities.

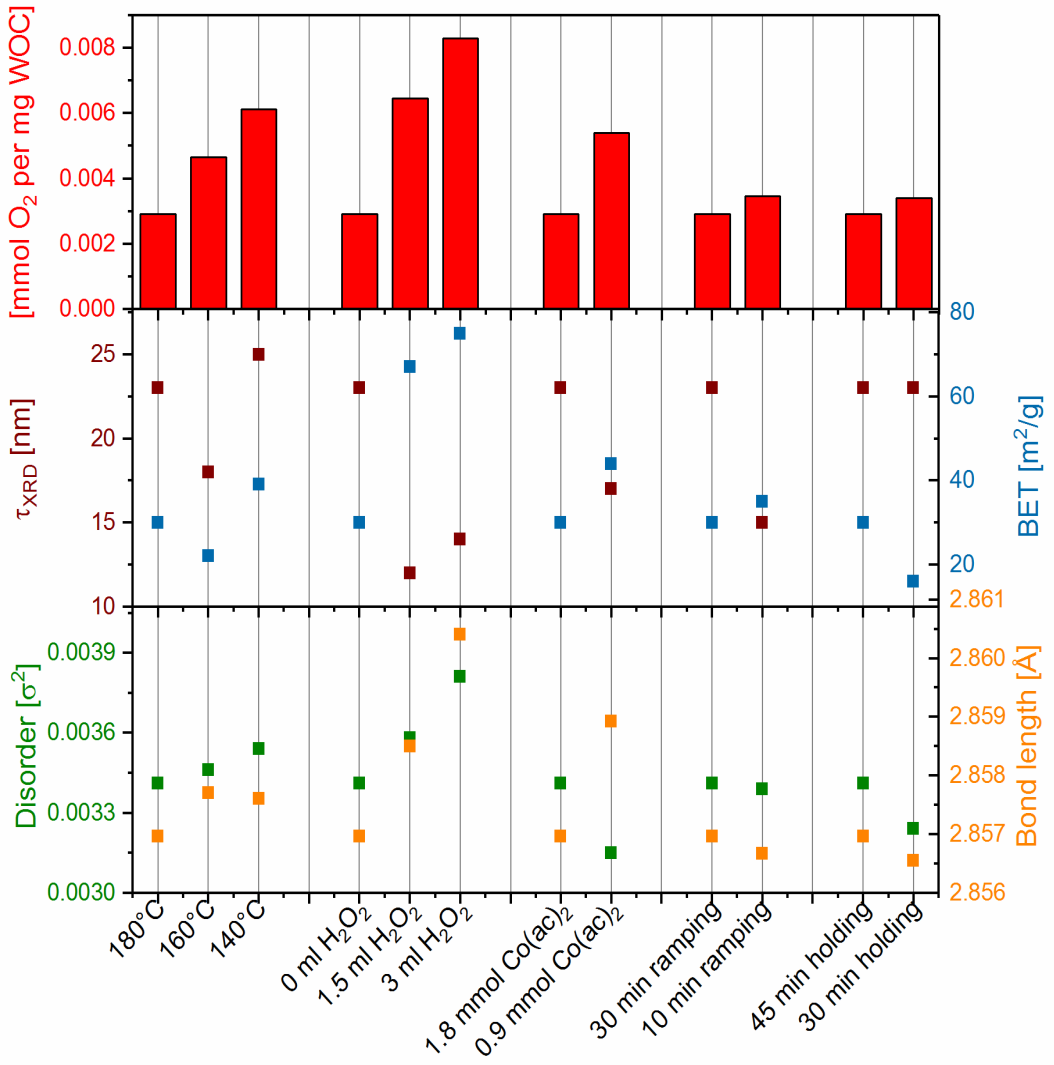

Figure 4-14. Chemical water oxidation activity, together with the respective particle size determined by the Scherrer equation at FWHM of the PXRD patterns (t_{XRD}), the BET surface area as well as and the mean-square disorder parameter σ^2 and the bond length, both of Co_{Oct} – Co_{Oct}, determined from EXAFS fitting. Error bars for BET and t_{XRD} are not shown, but are in the range of 1 – 5 % (0.65 m^2g^{-1} for BET, determined by fourfold measurement of commercial Co_3O_4 of similar size than most here investigated samples and 0.2 – 1 nm for t_{XRD} , determined from error propagation from PXRD peak FWHM determination). Error estimation for disorder σ^2 and bond length are given in table S1 as significant decimal digits.

4.5 Conclusion

The present study demonstrates new insights into the importance of synthetic parameters in microwave-hydrothermal synthesis. This synthetic approach is a tunable and rapid method for the production of nanoscale spinel-type Co_3O_4 water oxidation catalysts, therefore holding great potential for industrial applications. Starting from a standard microwave protocol, the influence of six key synthetic parameters on the properties of the resulting cobalt oxide samples was first screened. In particular, shorter ramping times and addition of hydrogen peroxide were shown to reduce crystallite and particle size. The crystallinity of the Co_3O_4 catalysts was decreased most significantly by hydrogen peroxide addition and by lower synthesis temperatures. Therefore, hydrogen peroxide addition was found to be the most influential synthesis parameter, even though the bulk cobalt oxidation state of the emerging spinels was not notably influenced as shown by XANES investigations.

The obtained Co_3O_4 spinels were characterized with respect to their synthesis parameters using a wide range of analytical methods, including PXRD, BET, XAS, XPS, and Raman spectroscopy as well as electron microscopy. Next, they were compared with respect to their chemical and electrocatalytic water oxidation activity. Significant changes in the respective water oxidation activities were observed as a result of the synthetic parameter variations. In particular, H_2O_2 addition during synthesis yielded much more active catalysts. Furthermore, lower synthesis temperature, cobalt precursor concentrations and shorter ramping times exerted a beneficial influence on the oxygen evolution performance. Stirring speed and holding time were found to be the least impactful parameters.

Correlations of the observed activity changes with the detailed materials parameters of the Co_3O_4 spinels indicate that not only the surface area and the crystallite size, but possibly also structural parameters, such as disorder and Co_{Oct}-Co_{Oct} bond distances as present in the surface edge-site motif determine the water oxidation activity. These results illustrate the key importance of synthetic parameter tuning in heterogeneous catalyst production. Therefore, systematic explorations of the synthetic parameter space along with insight into the underlying mechanisms of catalyst formation and activity are indispensable for informed and efficient design. Future strategies may thus combine rapid machine learning parameter screening with well-designed *in situ* monitoring experiments.

5 Outlook: Mixed Spinels

5.1 Introduction

The importance of stable and active water oxidation catalyst has already been pointed out in the introduction of this thesis. Co_3O_4 was discussed in depth in the previous chapters as a promising and important candidate. In this chapter, a wider screening of spinel materials with other combinations of different (transition) metals was performed.

Cobalt as an active WOC center is not only tested and applied in the form of spinel-type cobalt oxide, but many different Co-based catalysts, including molecular catalysts and amorphous solids, were described.[356] Additionally, WOCs containing Mn are highly attractive since nature uses manganese to split water in PS II (see chapter 1.1.1).[65,357,358] Furthermore, it was already shown that spinels containing both metal centers, Co and Mn, were more active for electrocatalytic water oxidation than primary materials.[182,359]

Another biomimetic concept from PS II was also already adapted: besides Mn, the PS II cluster contains one redox inert Ca(II) ion. Its role is still widely discussed for the development of efficient WOCs as already mentioned in chapter 1.1.2.[36,234,360–362] Therefore, many catalysts containing a redox inert ion were developed, either with Ca as in PS II but also with other cations like Li^+, K^+, Ga^{3+} or lanthanides. [36,234,361–363]

Another very active water oxidation catalyst group are nickel-iron compounds.[364] Iron was long known to "pollute" $Ni(OH)_2$ electrodes which causes serious deterioration in alkaline batteries by lowering the overpotential of oxygen evolution, which on the other side has a very beneficial effect for WOCs.[365,366] This was already introduced in more detail before (chapters 1.1.2.1 & 1.1.2.3). Today, many basic but also highly engineered Ni-Fe catalysts exist which exhibit great potential for the water oxidation reaction.[114,367,368] Moreover, spinel-type Ni-Fe oxide, $NiFe_2O_4$, was found to be active for water oxidation and doping with other metals even increased its activity.[369–371] Other metal oxide combinations in the spinel matrix were found to be more efficient than the corresponding primary or binary compounds as well.[371–373]

Gallium as redox inert ion in a spinel matrix containing cobalt and manganese was already examined in previous works of our group, namely by Franziska Conrad.[363] In continuation of these studies and to further explore all these above mentioned findings of synergistic effects between different metals and the incorporation of redox inert cations in WOCs, a broader screening study on mixed spinels was planned. The scheme shown in Figure 5-1 was developed as a guideline for the following experiments.

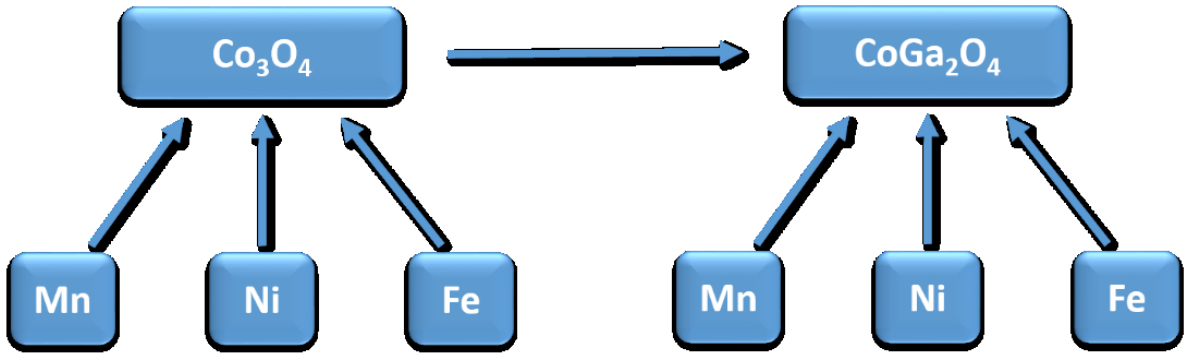

Figure 5-1. Planned investigation scheme for mixed transition metal spinel-type oxides (left) and mixed spinel containing a redox inert Ga ion as biomimetic feature of PSII.

5.2 Aims of the project and summary

The advantages of Co_3O_4 as water oxidation catalyst were already laid out several times in the previous chapters. Therein, Co_3O_4 itself was altered by varying synthesis conditions and methods. In this chapter, the synthesis protocol is mainly kept constant among compared materials, but different precursor combinations were applied to change the transition metal combinations in the spinel matrix with the aim of investigating the presence of synergistic effects. Various spinel materials containing Co, Mn, Ni, Fe and also the redox inert component Ga were produced and compared with respect to photocatalytic water oxidation performance. It became evident that changing the metal content does exert a major influence on the catalytic activity. Interestingly, the pure Co_3O_4 showed the highest activity, and was only slightly improved with the incorporation of iron. However, these results have to be interpreted with caution due to some wider error ranges in the catalytic performance data associated with technical setup issues.

5.3 Experimental

5.3.1 Synthetic Procedures

Syntheses were carried out either hydrothermally or using the sol-gel approach adapted from ref [325]. For hydrothermal synthesis, two different driving forces were used, namely normal heating in the oven or heating by microwave. The microwave synthesis was adapted from ref [363], whereas the hydrothermal protocol were performed similarly as described in ref [374].

Hydrothermal synthesis. For the hydrothermal synthesis of Ga-containing spinel oxides, metallic gallium (1.4 mM) together with the corresponding transition metal salt (e.g. $Co(NO_3)_2 \cdot 6\ H_20$ (0.7 mM)) and 2-aminoethanol (5 ml) were added into a ~ 20 ml Teflon liner and heated in a water bath for about 15 min. Afterwards, the reaction mixture was sealed in a stainless-steel autoclave and heated to 240 °C for 6 days. The products were transferred with MeOH and filtered off. Since metallic cobalt was formed as a side product, the product was redispersed to remove the metallic cobalt with a magnet before a second filtration.

Microwave hydrothermal synthesis. For the microwave hydrothermal synthesis of mixed spinels, a total of 1.8 mmol of the corresponding salts was dissolved in 15 mL H_2O and the pH was adjusted to 11 with NH_3 (25 %) solution. The resulting dispersion was filled into a 50 mL CEM Omni Teflon liner, which can be closed and fixed inside a frame before introducing into the microwave. Reactions were carried out in a MARS5 microwave (CEM cooperation). The synthesis was conducted by controlling the temperature; 30 min ramping to 180°C and then holding this temperature for 60 min (referred to as holding time throughout the chapter) under constant stirring. The temperature and pressure were measured from the reference vessel, which was equipped with appropriate sensors. After letting the dispersions cool down to room temperature, the product was separated by centrifugation and washed with H_2O.

Sol-Gel (SG).[325] A variation of the sol-gel method from the Pechini method[249] was applied: a total 1.8 mmol of the corresponding transition metal salts and 2.7 mmol of citric acid were dissolved in 25 mL H_2O. The solution was heated up slowly while stirring until a gel was formed. It was heated up to 400 °C for 1 h, then transferred into a ceramic crucible and heated to 700 °C for 10 h yielding spinel-type transition metal oxides.

5.3.2 Photocatalytic Measurements

Photocatalytic water oxidation tests were performed using a standard $[Ru(bpy)_3]^{2+}/S_2O_8^{2-}$ protocol.[165] Photocatalytic reaction suspensions were handled in a dark environment while shielded from light. According to the protocol, spinel photocatalyst (2 mM), $Na_2S_2O_8$ sacrificial electron acceptor (9.5 mg, 5 mM), and $[Ru(bpy)_3]Cl_2 \cdot 6H_2O$ photosensitizer (6.0 mg, 1 mM) were mixed with borate buffer (8 mL, 80 mM, pH 8.5) in a 10 mL headspace glass vial. The glass vial was subsequently sealed gas-tight with a rubber septum (PTFE) and an aluminum crimp cap and sonicated for 3 min. To remove all the oxygen before starting the test, the suspension was degassed through purging with helium (purity 5.0) for 10 min. Afterward, the catalytic suspension was illuminated with a 460 nm high flux LED light (26.1 mW cm^{-2}, Rhopoint Component LTD) under constant stirring for 30 min. For evaluating the amount of evolved oxygen a 100 µL gas sample was taken from the headspace with a gastight microliter syringe (Hamilton-1825RN) and injected into the gas chromatograph (GC). Gas chromatography (GC) measurements were recorded with an Agilent Technologies 7820A equipped with a thermal conductivity detector (Varian). O_2 and N_2 were separated by passing the sample through a 3 m x 2 mm packed 5 Å molecular sieve 13 x 80-100 column with a helium carrier gas (purity 6.0).

A previously determined linear GC calibration curve was used to quantify the oxygen evolution (air contamination was corrected). The yield was then calculated from obtained oxygen amount relative to the maximum possible amount regarding the sacrificial electron acceptor.

5.3.3 Materials and Methods

All chemicals and solvents were purchased from commercial suppliers: Gallium (Aldrich, pieces, 99.99999% trace metal basis), $Co(NO_3)_2 \cdot 6H_2O$ (Fluka, purum p.a. ≥ 98%), $Ga(NO_3)_3$ (Aldrich, crystalline, 99.9% trace metal basis), $MnSO_4 \cdot 1H_2O$ (Sigma-Aldrich, ReagentPlus®, ≥ 99%), $FeSO_4 \cdot 7H_2O$ (Sigma-Aldrich, ACS reagent, ≥ 99.0%), $Co(CH_3COO)_2 \cdot 4H_2O$ (Sigma-Aldrich, reagent grade), $Ni(CH_3COO)_2 \cdot 4H_2O$ (Aldrich, purum p.a., ≥ 99.0%), 3-aminoethanol (Fluka, puriss. p.a. ≥ 99.0%) $[Ru(bpy)_3]Cl_2 \cdot 6H_2O$ (Sigma–Aldrich, 99.95 %), $Na_2S_2O_8$ (Sigma–Aldrich, 99.0 %), H_2O_2 30 wt.% in H_2O (Sigma–Aldrich, ACS reagent), ammonia solution 25 % (Merck, for analysis), ethanol (VWR Chemicals, absolute), methanol (VWR Chemicals, absolute), citric acid (Merck, anhydrous for synthesis), Cobalt (US Research Nanomaterials, 28 nm, 99.8%, partially passivated w/[O] ~ 0.8%)

PXRD and BET measurements were performed as described in chapter 5.3.3. SEM was measured on a Jeol JSM-6060 equipped with a tungsten filament. EDX measurements and mappings were recorded with a Bruker AXS XFlash ® Detector 4010. TEM measurements were conducted on a JEOL JEM2200fs operated by Yucheng Zhang (EMPA).

5.4 Results & Discussion

Mixed spinels with different transition metal compositions, as illustrated in Figure 5-2, and ratios were synthesized and photocatalytically tested for water oxidation.

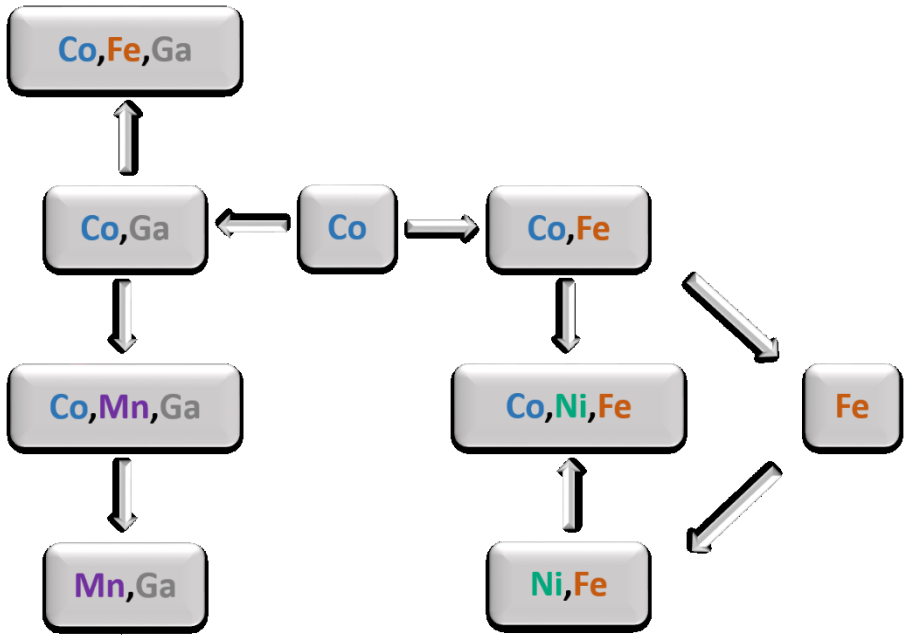

Figure 5-2. Different transition metal combinations obtained and tested for photocatalytic water oxidation.

$CoGa_2O_4$: $CoGa_2O_4$ was prepared via two different methods: First by the hydrothermal approach developed by Walton et *al.* and second by microwave synthesis for a better comparison with the other mixed spinels. The microwave synthesis was found to be much more appropriate, since it was considerably faster (1.5 h instead of 6 days) and secondly also delivered phase pure spinels, whereas in the hydrothermal method metallic cobalt was produced as a side product, which had to be removed from the main phase (see Figure 5-3). Nevertheless, the hydrothermal synthesis opened up an interesting question about catalyst optimization, since we observed that the unseparated product, i.e. a mixture of the metallic cobalt with $CoGa_2O_4$, was more active in photocatalytic water oxidation than after removal of the metallic cobalt (see Table 5-1). This probably indicates the importance of conductivity for active catalysts as discussed in our previous works.[375]

Table 5-1 Different activities (mean values from two measurements) obtained for the product as synthesized or separated (complete separation is not possible with this setup; traces of metallic cobalt remains in $CoGa_2O_4$ and vice versa).

Product treatment	**Photocatalytic O_2 Yield [%]**
Unaltered (→ **Co + $CoGa_2O_4$**)	15.3 ± 4.2
Metallic Co removed (→ **$CoGa_2O_4$**)	8.0 ± 2.2
Removed Co (→ **Co**)	29.3 ± 2.8

Figure 5-3. $CoGa_2O_4$ (light blue) and metallic cobalt after hydrothermal synthesis.

These findings were further investigated by EDX mapping where clearly distinct cobalt spots were seen (see Figure 5-4). Therefore, we presumed from these experiments, that metallic cobalt inside an oxide matrix is able to increase the photocatalytic activity. To test if the increase in activity arises from the metallic particles themselves, or if a mixture or an embedment is needed, metallic nanoparticles were characterized and tested for water oxidation activity. The investigated nanoparticles were defined as partially passivated with ~ 0.8 % [O] by the supplier. PXRD however revealed the presence of $Co(OH)_2$ besides face-centered cubic (fcc, S.G. *Fm-3m*) metallic cobalt (see Figure 5-5a). It was found that the photocatalytic yield was around 30 % and therefore similar to the one obtained for the separated metallic cobalt after hydrothermal synthesis of $CoGa_2O_4$. Besides the $Co(OH)_2$ phase, the nanoparticles contained also Co_3O_4, especially after photocatalytic tests, as evident from PXRD patterns (Figure 5-5b).

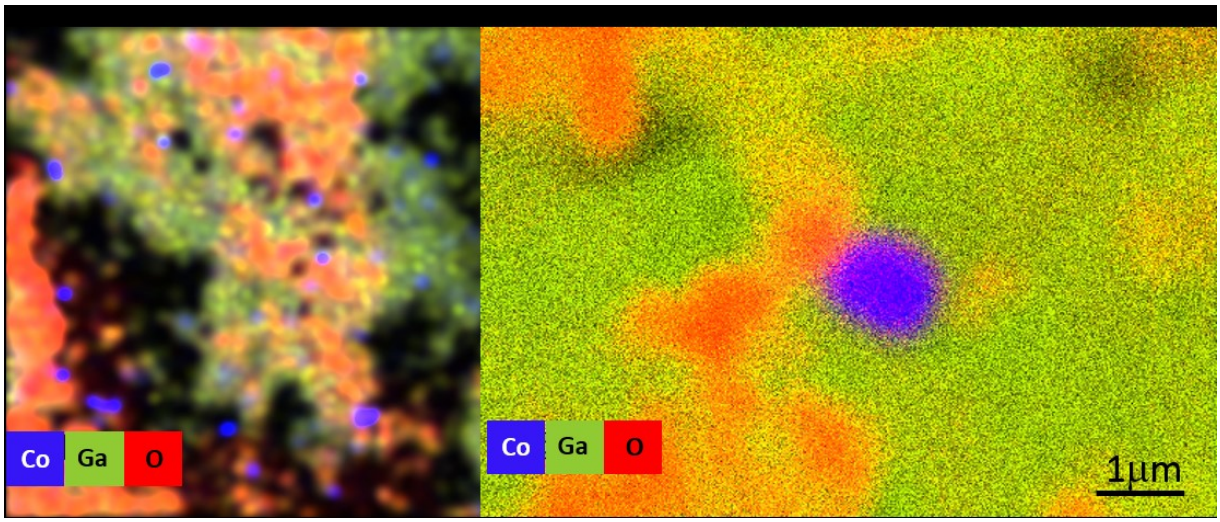

Figure 5-4. EDX mapping of hydrothermally as-synthesised $CoGa_2O_4$ containing metallic cobalt particles.

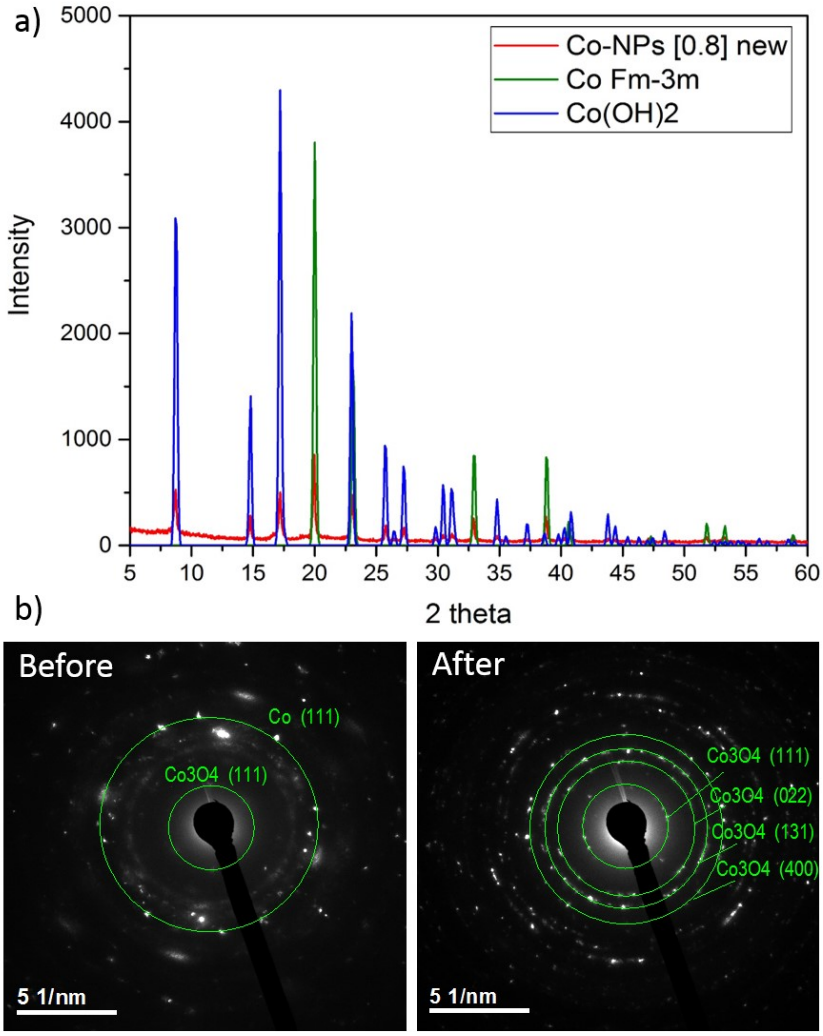

Figure 5-5. PXRD of the purchased cobalt nanoparticles containing 0.8 % [O] (a) and TEM diffraction patterns of these particles before and after water oxidation activity tests (b).

To check if the activity changes with advancing oxidation, the nanoparticles were slowly oxidized in air at 220°C. The temperature was so adjusted that the oxidation process (progress checked by PXRD) was completed in a few hours and therefore samples with different average cobalt oxidation states could be compared. Every 40 min an aliquot was tested for water oxidation activity and the yield was determined as illustrated in Figure 5-6. No trend can be seen from this experiment in spite of significant differences of the yields, varying from 20 to 34 %.

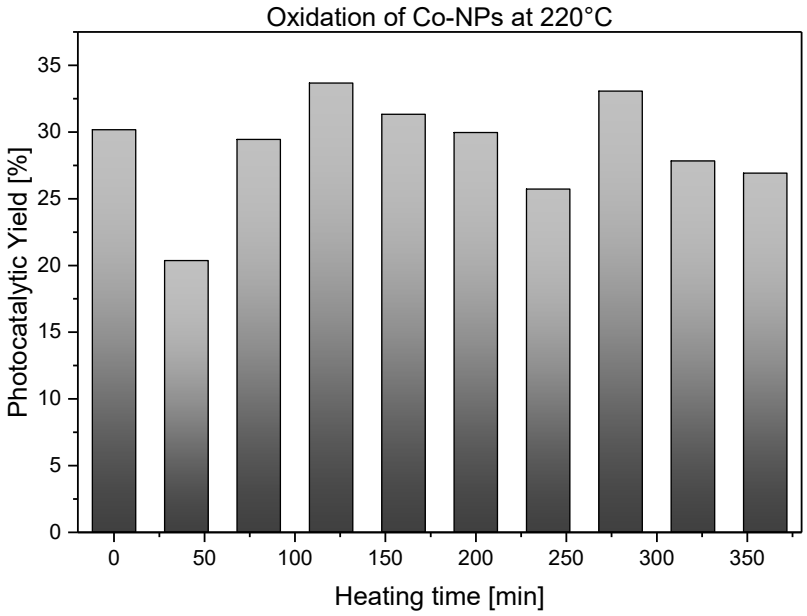

Figure 5-6. Yield in photocatalytic water oxidation obtained from commercial cobalt nanoparticles being oxidized at 220°C for increasing times.

$Co_xMn_{1-x}Ga_2O_4$ and $Co_xFe_{1-x}Ga_2O_4$: The mixed spinels were prepared by microwave synthesis as described in the experimental part of this chapter. All $Co_xMn_{1-x}Ga_2O_4$ samples were synthesized simultaneously by inserting 5 reaction vessels in the microwave together, as well as the $Co_xFe_{1-x}Ga_2O_4$ samples. All samples, except $Co_{0.2}Fe_{0.8}Ga_2O_4$, were obtained in phase pure form (see Figure 5-7). The replacement of Co with Mn was easily possible up to an initial ratio of 1:1 (0.5 in Figure 5-7a). Samples containing more Mn were less crystalline, with $MnGa_2O_4$ being close to amorphous, but still showing the characteristic spinel peaks. Possible explanations could be that the Co^{2+} and Mn^{2+} ions have a similar radius of 70 pm while the more electron-rich Co^{2+} is stronger attracted by the oxygen anions and therefore also leads to a decrease in the unit cell constants.[376–378] This might account for an easier formation of the spinel-type structure. Furthermore, Mn can adapt a wide range of oxidation states and therefore redox potentials and also easily disproportionate, which may lead to less crystalline phases.[379–383]

The sample indicated as $Co_{0.2}Fe_{0.8}Ga_2O_4$ was obtained only as a mixture with iron oxide hydrate and $FeGa_2O_4$ was not obtained from this synthesis route. In both series, the samples ranging from x = 1 to 0.5 show very similar PXRD patterns which renders them comparable for catalysis in the first place.

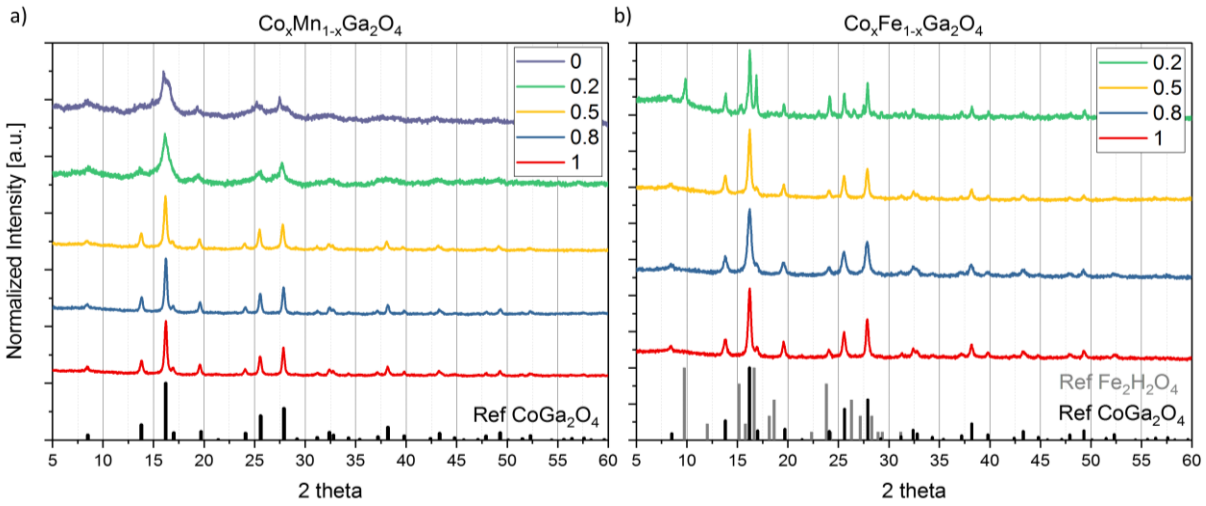

Figure 5-7. PXRD pattern of $Co_xMn_{1-x}Ga_2O_4$ (a) and $Co_xFe_{1-x}Ga_2O_4$ (b) for different x values of the precursor composition.

BET measurements of the $Co_xMn_{1-x}Ga_2O_4$ samples showed increased surface area for the more amorphous $Co_{0.2}Mn_{0.8}Ga_2O_4$ and $MnGa_2O_4$ (Table 5-2). This is expected since a decrease in particle size leads to a peak broadening in the PXRD pattern (see Scherrer equation in chapter 2.2.1). The other three values for $CoGa_2O_4$, $Co_{0.8}Mn_{0.2}Ga_2O_4$ and $Co_{0.5}Mn_{0.5}Ga_2O_4$ are very similar. These values also correspond to the $CoGa_2O_4$ of the $Co_xFe_{1-x}Ga_2O_4$-series. In the latter series, the highest surface area is exhibited by $Co_{0.8}Fe_{0.2}Ga_2O_4$.

Table 5-2 BET surface area values for $Co_xMn_{1-x}Ga_2O_4$ and $Co_xFe_{1-x}Ga_2O_4$ samples

Sample	**BET surface area [m^2g^{-1}]**
$CoGa_2O_4$	68
$Co_{0.8}Mn_{0.2}Ga_2O_4$	63
$Co_{0.5}Mn_{0.5}Ga_2O_4$	82
$Co_{0.2}Mn_{0.8}Ga_2O_4$	114
$MnGa_2O_4$	116
$CoGa_2O_4$	65
$Co_{0.8}Fe_{0.2}Ga_2O_4$	106
$Co_{0.5}Fe_{0.5}Ga_2O_4$	75
$Co_{0.2}Fe_{0.8}Ga_2O_4$	47

Due to earlier investigations, it was expected that the introduction of a certain amount of Mn in $CoGa_2O_4$ would increase the photocatalytic activity.[363] However, as depicted in Figure 5-8, the introduction of all tested amounts of Mn was detrimental for the activity. This decrease in activity is almost linear, with only $Co_{0.5}Mn_{0.5}Ga_2O_4$ showing lower activity. The opposite is the case for the $Co_xFe_{1-x}Ga_2O_4$ series, also illustrated in Figure 5-8. Here, $CoGa_2O_4$ exhibits the lowest activity with an increase upon higher Fe-content. These results show a clear indication of synergistic effects between different transition metals in an oxide matrix. Nevertheless, these results have to be treated with caution, as the reproducibility of the photocatalytic assay was not always given for these complex systems. Experience has demonstrated, that trends usually could be reproduced, but numerical values rather not. This is also obvious from Figure 5-8, where x = 1 corresponds basically to the same material, $CoGa_2O_4$. Although it was synthesized in two different batches which according to PXRD and BET (Figure 5-7 and Table 5-2) are very similar, there are still significantly different values among the Mn- and Fe-series. This may be due to subtle difference in the surfaces and surface oxidation states of such complex spinels upon fluctuations in microwave or other synthesis techniques. Note that even primary Co_3O_4 was already very sensitive towards the synthetic conditions as outlined in detail in the previous chapters.

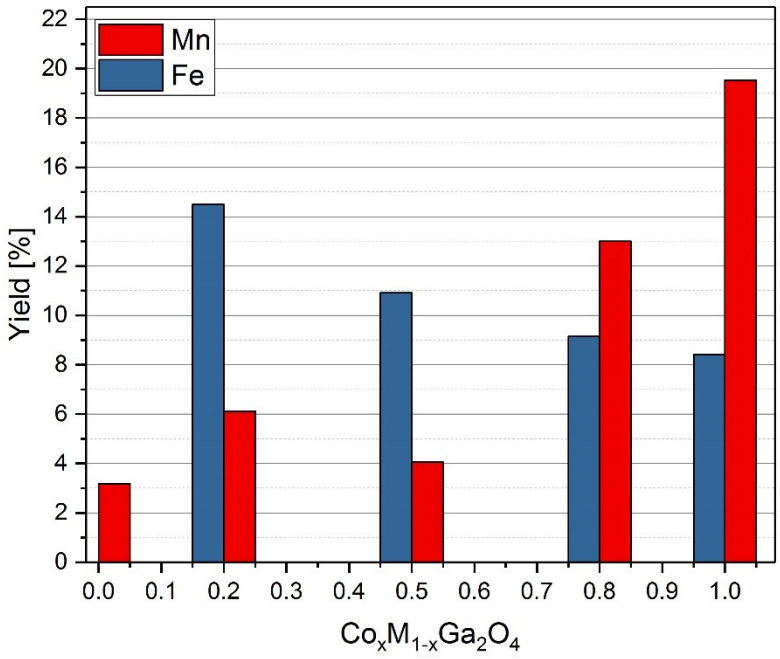

Figure 5-8. Photocatalytic water oxidation activity for $Co_xM_{1-x}Ga_2O_4$ with M = Mn and Fe with ratios from x = 0-1.

Co_3O_4 and Fe_3O_4: In addition to Ga-containing spinels, mixed spinels without redox inactive transition metals were also prepared. As single metal references, primary oxides were synthesized first. Co_3O_4 and Fe_3O_4 could be obtained in phase pure form with the aforementioned microwave synthesis. $Ni(OH)_2$ was obtained when applying the same synthesis conditions instead of Ni_3O_4, which is not surprising, since Ni_3O_4 is not stable and usually is formed only as surface state of NiO and in solid solution with Co_3O_4.[384–387] The same reactions for both Co- and Fe-spinel were carried out at least twice each and these samples were chosen for comparison as well as one sample each (Co_3O_4 and Fe_3O_4) where the reaction was interrupted after 10 min. The latter samples were chosen for further evaluation since they were obtained simultaneously, therefore providing comparability regarding all synthesis parameters except the precursor salt. Better comparability in the photocatalytic tests was also given since they were all performed on the same day with the same reagents. The PXRD patterns of the selected samples are shown in Figure 5-9. All samples are phase pure and exhibit similar peak shapes, indicating related crystallinity and crystallite size. Indeed the BET surface areas are very similar, around 20 m^2g^{-1} for all samples except Fe_3O_4 with 10 min holding time (Fe1 (10 min) in Figure 5-9), where it is 125 m^2g^{-1}. The slight shift of the Fe_3O_4 patterns to smaller angles arise from the larger unit cell of Fe_3O_4 compared to Co_3O_4.[388,389]

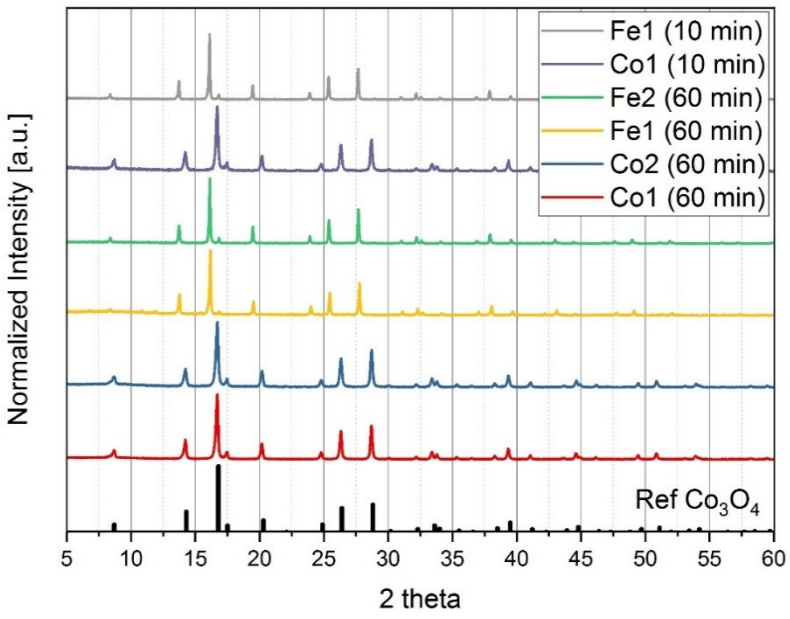

Figure 5-9. PXRD pattern of Co_3O_4 (Co1 (60 min) and Co2 (60 min) being different samples prepared by the same protocol, including 60 min holding time and Co1 (10min) where the reaction was stopped after 10 min) and Fe_3O_4 (same naming).

To ensure that the required testing conditions for Fe_3O_4 are the same as for Co_3O_4, the photocatalytic tests for Fe_3O_4 were carried out at different pH values. The standard pH 8.5 borate buffer used for the evaluation of Co_3O_4 water oxidation activity was also the best choice for Fe_3O_4 amongst the selected buffers (see Figure 5-10) and was therefore selected for further experiments.

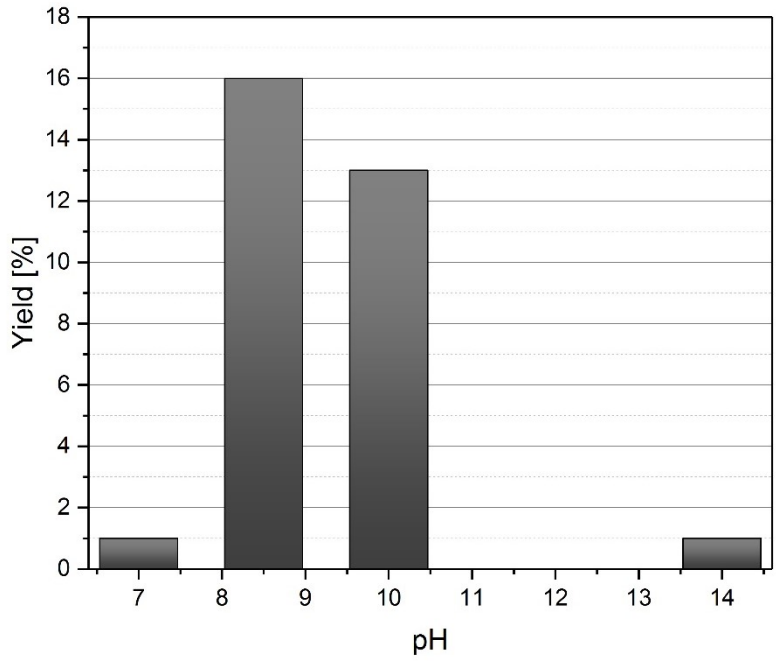

Figure 5-10. Photocatalytic measurements of Fe_3O_4 carried out at different pH values: 50 mM borate buffer (pH 7), 80 mM borate buffer (standard for Co_3O_4, pH 8.5), Britton-Robinson buffer (pH 10) and 1 M NaOH (pH 14).

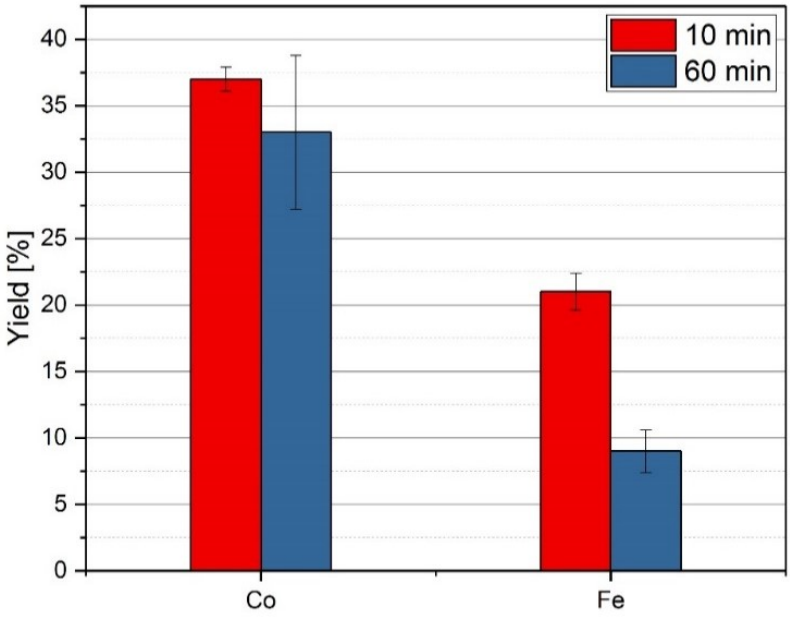

Figure 5-11. Water oxidation activity of Co_3O_4 and Fe_3O_4 synthesized with different holding times. The error bar for the 10 min samples arises from two measurements, whereas in the 60 min samples both two measurements were performed, and two different samples were compared.

If the photocatalytic activity of the selected samples, shown in Figure 5-11, is compared, we directly notice three things: First, Co_3O_4 seems to be more active for water oxidation in the photocatalytic assay for both synthesis temperatures. Second, the samples where the synthesis was interrupted, and the holding time therefore was only 10 min, perform better than the samples where the synthesis holding time was 60 min. This improvement in catalysis for shorter reaction times was already observed for Co_3O_4 in the previous chapter 4. The third observation from Figure 5-11 are the smaller error bars for the "10 min - samples" compared to the "60 min – samples". This can be easily explained by two factors. The 60 min holding time was standard for the microwave syntheses in this project and therefore two different compounds for both measurements, Co_3O_4 and Fe_3O_4, could be selected. But the synthesis was only interrupted once, so only one sample of Co_3O_4 and Fe_3O_4, respectively, with 10 min holding time was produced. For the photocatalytic measurements, both of the latter samples were measured twice in immediate succession, therefore providing better comparability of the test conditions. The samples synthesized for 60 min were prepared and also photocatalytically tested at least days apart, leading to more pronounced deviations in the testing conditions. Furthermore, the Co_3O_4 and Fe_3O_4 samples synthesized with 10 min holding time were produced in the same run and also tested one after another, rendering their comparison more reliable compared to the ones emerging from the 60 min synthesis.

$Co_xFe_{3-x}O_4$ and $Ni_xFe_{3-x}O_4$: After having investigated primary Co_3O_4 and Fe_3O_4 spinels, binary compounds, first of the latter elements and then also of Ni and Fe were studied. Figure 5-12 shows the PXRD patterns of binary spinels. In the $Co_xFe_{3-x}O_4$ series, Co_3O_4 and Fe_3O_4 are the same samples as mentioned above (with 10 min holding time) which were synthesized simultaneously. To compare the binary spinels with these references, the subsequent synthesis of $CoFe_2O_4$ (Co1Fe2 in Figure 5-12a), $Co_{1.5}Fe_{1.5}O_4$ (Co1.5Fe.5) and Co_2FeO_4 (Co2Fe1) was also stopped after 10 min holding time. In this follow-up series, Co_2FeO_4 shows the broadest PXRD peaks, indicating lower crystallinity and smaller particle size. When mixing nickel and iron, only smaller amounts of nickel, up to an initial precursor ratio of 1:5 (Ni0.5Fe2.5) yielded phase pure spinels (see Figure 5-12). With higher amounts of Ni a secondary $Ni(OH)_2$ phase was formed.

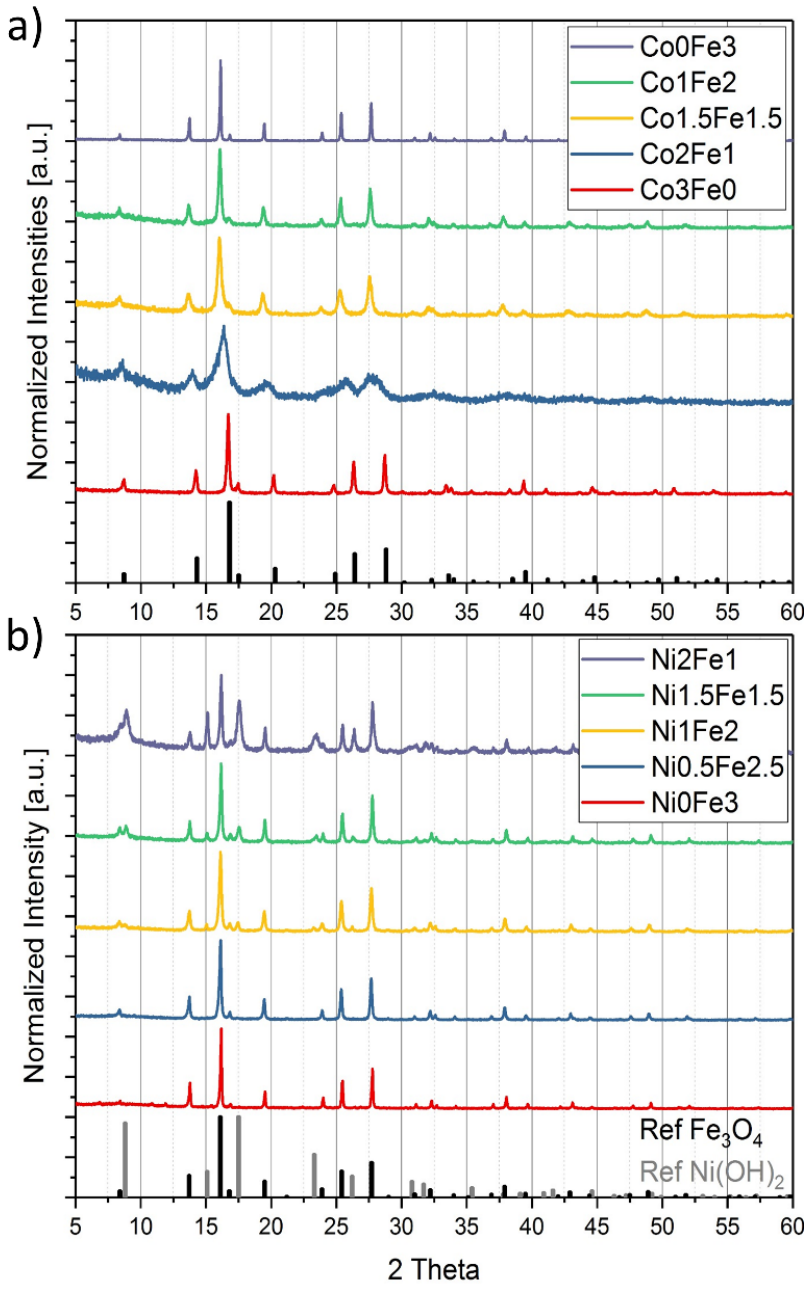

Figure 5-12. PXRD patterns of $Co_xFe_{3-x}O_4$ and $Ni_xFe_{3-x}O_4$. The numbers in the legend (Ni*x*Fe*y)* indicate the ratio of the precursor salts and are not necessarily the ratio in the spinel structure.

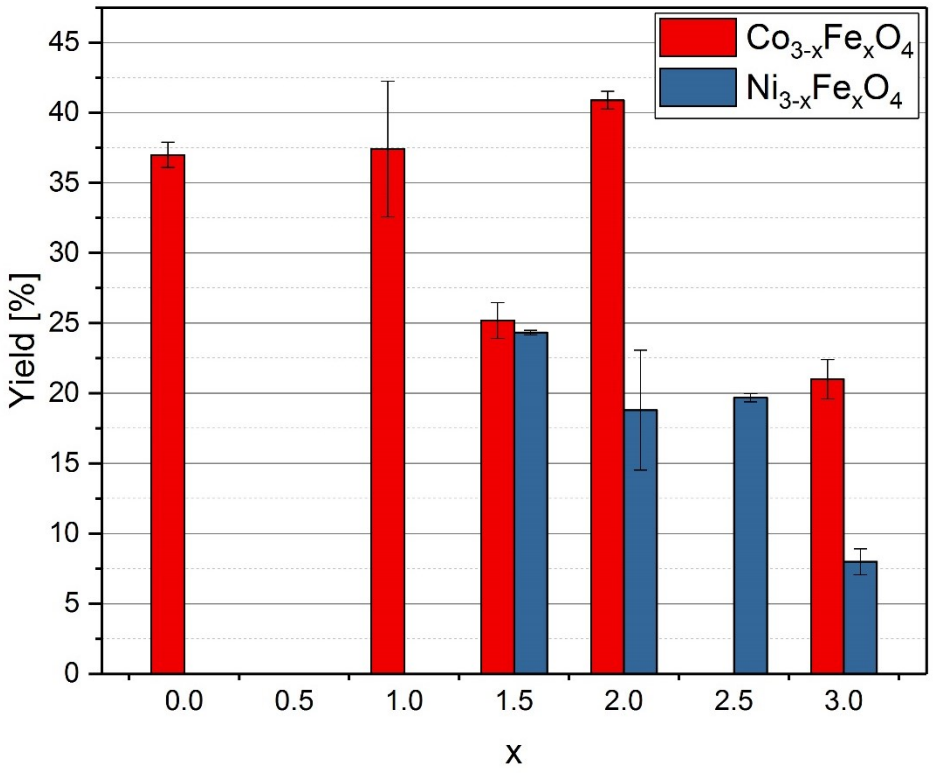

Figure 5-13. Photocatalytic yield of ternary $Co_xFe_{3-x}O_4$ (red) and $Ni_xFe_{3-x}O_4$ (blue) spinels. Errors were derived from 2-3 repeated measurements.

In Figure 5-13 the photocatalytic activities of these binary spinels are depicted. From incorporation of iron in cobalt oxide no systematic trend can be observed, and the highest activity was obtained from $CoFe_2O_4$. With nickel incorporation into Fe_3O_4, an increase in activity can be observed. Unfortunately, samples with a Ni content of 50% or more were not phase pure anymore. Partially large error bars in both series show the reproducibility problems of this test method with more complex structures as already mentioned above.

$Co_xNi_{1-x}Fe_2O_4$: Finally, ternary spinels, containing all three selected transition metals, Co, Ni and Fe, were investigated. For this series, two different synthetic approaches were applied: first, the standard microwave procedure as applied throughout the whole chapter and second the sol-gel procedure as described in the synthetic procedures of this chapter (see chapter 5.3.1). For the $Co_xNi_{1-x}Fe_2O_4$ samples synthesized by microwave techniques, with x ranging from 0 to 1, comparable yields to the above mentioned $Co_xFe_{3-x}O_4$ samples were obtained (see Figure 5-14). No clear trend was observed for this series, and the only evident feature is the low activity for the cobalt free sample (x = 0 in Figure 5-14). In contrast, the samples synthesized by sol-gel methods do exhibit a trend as obvious from Figure 5-14. Here, the activity linearly increases with the Co-content. However, further confirmation studies are necessary here.

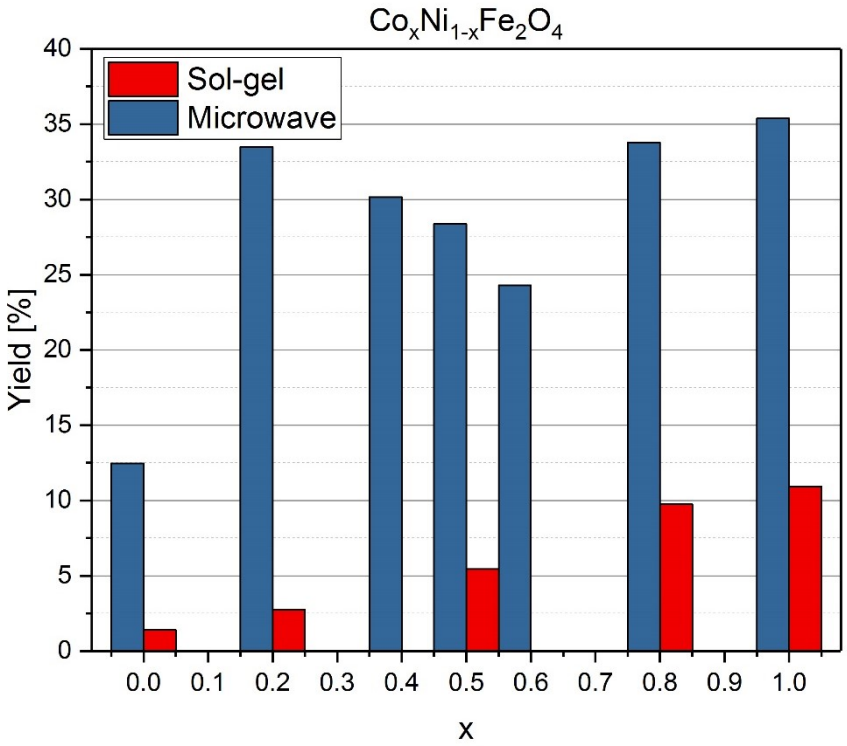

Figure 5-14. Photocatalytic yield of $Co_xNi_{1-x}Fe_2O_4$ with x varying from 0 to 1, synthesized by standard microwave synthesis (blue) or by sol-gel methods (red).

5.5 Perspectives for further research

While investigating $CoGa_2O_4$ synthesized via a hydrothermal method, the occurrence of metallic cobalt suggested new research directions into metallic cobalt compounds as powerful and alternative water oxidation catalysts. Oxides containing metallic cobalt were found to be more active than the corresponding oxides which were free of metallic cobalt.

By introducing manganese and iron into the above described $CoGa_2O_4$ matrix, different results were obtained. While the introduction of Mn was detrimental for the performance of the resulting ternary oxide, Fe incorporation increased the activity. This shows the presence of rather complex synergistic effects between different transition metal combinations which merits further investigations.

When comparing Co_3O_4 with Fe_3O_4 obtained from related synthetic protocols, the superior performance of Co_3O_4 became evident. Furthermore, the difference in synthesis time of microwave-hydrothermal synthesis was compared for these samples. Shorter reaction times led to more active catalysts, which is in agreement with the findings from chapter 4. By substitution of Fe into the Co_3O_4 lattic - or vice versa – a general performance enhancement was achieved to the end that $CoFe_2O_4$ outperformed the other combinations, whereas no overall trend became evident. Further pre-screening with respect to Ni introduction into Fe_3O_4 lead to increased activities, followed by $Ni(OH)_2$ formation above a Ni concentration threshold of $Ni_{1.5}Fe_{1.5}O_4$.

As for tests concerning ternary transition metal spinels containing cobalt, nickel and iron, $Co_xNi_{1-x}Fe_2O_4$ samples displayed no trend when applying the standard microwave method. However, when these samples were produced by the sol-gel approach, a linear increase in water oxidation activity with higher Co/Ni ratios was obtained, even though the general performance was inferior to the samples synthesized by microwave.

By investigating different transition metal combinations in the spinel matrix for photocatalytic water oxidation activity, it became evident that in fact the cation combinations exert a major influence on the performance and open up the potential for further optimization of spinel materials with respect to both synthetic history and cation combinations. The present results pave the way to extended follow-up screening studies in this direction and indicate that a thorough set of analytical bulk and surface characterizations will be necessary to sort out the influence of complex parameter room on the activity of ternary and higher spinel materials.

6 Conclusions & Outlook

Spinel-type transition metal oxides synthesized preferably by microwave hydrothermal synthesis, were investigated for key relations between their synthetic history, materials characteristics and water oxidation activity. To this end, special emphasis was placed on Co_3O_4 as a representative model system.

In Chapter 3 the influence of the synthesis method on the resulting properties and water oxidation activity of Co_3O_4 is discussed in detail. As expected, synthesis methods were shown to have a major influence on the emerging materials properties, regarding crystallinity, disorder, surface area and particle size. Generally, lower crystallinity, higher extents of disorder and smaller particle sizes were obtained from syntheses performed at lower temperatures. Next, the influence of these factors on the activity of Co_3O_4 in different water oxidation catalysis assays was systematically investigated. The chemical water oxidation activity was found to correlate well with the surface area and disorder of the materials. In a related trend, samples synthesized at lower temperatures showed higher activity in photocatalytic water oxidation. In contrast, no evident influence of any investigated materials property on the electrocatalytic water oxidation performance could be identified. These results outline the importance of the selected test and synthesis methods in the assessment and comparison of water oxidation catalyst activities.

Chapter 4 can be considered as a zoom in into the first study: Here, a single synthetic method, namely microwave hydrothermal synthesis, was selected and various synthesis parameters like precursor concentrations, temperature, reactions times etc. were varied. The emerging spinels were thoroughly characterized and tested for chemical and electrochemical water oxidation activity. Interestingly, variations in their activity were almost as significant as in the previous study. In other words, the influence of completely different synthesis methods on the catalytic activity may be comparable to the change of a single synthetic parameter within one specific method. For all investigated parameters, an influence on the water oxidation activity was shown and analogous trends were found for chemical and electrocatalytic water oxidation. This outlines both, the importance of thorough synthetic optimization screenings for water oxidation catalyst production and the difficulties in predicting the influence of a given synthetic parameters variation.

In the explorative third study of Chapter 5, the spinel synthesis parameters were mainly kept constant and the effect of several metal combinations within the spinel matrix was tentatively investigated. While major variations of the photocatalytic water oxidation activity were observed, the performance of pure Co_3O_4 could only be enhanced through incorporation of iron. Surprisingly, all other investigated combinations of Co_3O_4 with Mn, Fe, Co, Ni or with redox inert Ga showed lower activity. In a sideline project, the promising activity of metallic cobalt nanoparticles as an alternative to cobalt spinel was highlighted.

All in all, the present thesis underscores the massive influence of the synthetic parameters on the activity of Co-based spinels as model systems, along with the notable role of the selected test assay in performance comparisons. The studies conducted herein therefore point out the importance of considering all preparative parameters, even when comparing catalysts of related structural types, in search of trends in their properties and catalytic activities. The established guidelines for Co_3O_4 as an attractive noble metal-free water oxidation catalyst model with high robustness pave the way to the systematic exploration of other low-cost spinel types for catalytic applications.

7 References

(1) Hare B. Relationship between increases in global mean temperature and Relationship between increases in global mean temperature impacts on ecosystems, food production, water and socio-economic systemseconomic systems. http://www.pik-potsdam.de/~mmalte/simcap/publications/Hare_submitted_impacts.pdf (accessed September 11, 2018).

(2) Thomas C. D.; Cameron A.; Green R. E.; Bakkenes M.; Beaumont L. J.; Collingham Y. C.; Erasmus B. F. N.; Ferreira de Siqueira M.; Grainger A.; Hannah L.; Hughes L.; Huntley B.; van Jaarsveld A. S.; Midgley G. F.; Miles L.; Ortega-Huerta M. A. A. Townsend Peterson, Oliver L. Phillips & Stephen E. William. Extinction risk from climate change. *Nature* **2004**, 145–148.

(3) Meehl G. A.; Washington W. M.; Collins W. D.; Arblaster J. M.; Hu A.; Buja L. E.; Strand W. G.; Teng H. How Much More Global Warming and Sea Level Rise? *Science*, *2005*, 1763–1772.

(4) Nicholls R. J.; Cazenave A. Sea-Level Rise and Its Impact on Coastal Zones. *Science* **2010**, 1517–1520.

(5) IEA - International Energy Agency. CO2 Emissions from Fuel Combustion - Highlights **2017**.

(6) Herzog, T. World Greenhouse Gas Emissions in 2005. *WRI Working Paper* **2005**, 1–5.

(7) United Nations Population Division | Department of Economic and Social Affairs. World Population Prospects The 2017 Revision: Methodology of the United Nations Population Estimates and Projections. http://www.un.org/en/development/desa/population/publications/index.shtml (accessed September 11, 2018).

(8) World Energy Outlook 2017. https://www.iea.org/weo2017/ (accessed September 11, 2018).

(9) ADVANCING THE GLOBAL RENEWABLE ENERGY TRANSITION: Highlights of the REN21 Renewables 2017 Highlights of the REN21 Renewables 2017 Global Status Report in perspective. *https://www.ren21.net/wp-content/uploads/2019/08/Highlights-2018.pdf* (accessed September 14, 2018).

(10) Society, N. G. Electricity Generation from Renewable Energy. https://www.nationalgeographic.org/maps/electricity-generation-renewable-energy-sources/ (accessed September 14, 2018).

(11) Brown L. R. Sunlight Striking Earth's Surface in Just One Hour Delivers Enough Energy to Power the World Economy for an Entire Year. https://www.alternet.org/environment/sunlight-striking-earths-surface-just-one-hour-delivers-enough-energy-power-world (accessed September 14, 2018).

(12) IEA - International Energy Agency. Key World Energy Statistics **2017**.

(13) Mertens K.. *Photovoltaik: Lehrbuch zu Grundlagen, Technologie und Praxis*; Carl Hanser Verlag München, 2012.

(14) Buhayar N. Musk vs. Buffett: The Billionaire Battle to Own the Sun. https://www.bloomberg.com/features/2016-solar-power-buffett-vs-musk/ (accessed September 15, 2018).

(15) Solar Energy Disadvantages: The Top Drawbacks of Solar Power. https://www.renewableresourcescoalition.org/solar-energy-disadvantages/ (accessed September 15, 2018).

(16) Yachandra, V. K.; Sauer, K.; Klein, M. P. Manganese Cluster in Photosynthesis: Where Plants Oxidize Water to Dioxygen. *Chem. Rev.* **1996**, *96*, 2927–2950.

(17) Pirson A. A study of the nutrition and metabolism of Fontinalis and Chlorella. *Z. Bot.* **1937**, 193–267.

(18) Kok B.; Forbush B.; McGloin M. COOPERATION OF CHARGES IN PHOTOSYNTHETIC O2 EVOLUTION–I. A LINEAR FOUR STEP MECHANISM. *Photochem. Photobiol.* **1970**, 457–475.

(19) Joliot, P.; Barbieri, G.; Chabaud, R. UN NOUVEAU MODELE DES CENTRES PHOTOCHIMIQUES DU SYSTEME II. *Photochem. Photobiol.* **1969**, *10*, 309–329.

(20) Yatabe, T.; Kikkawa, M.; Matsumoto, T.; Nakai, H.; Kaneko, K.; Ogo, S. A model for the water-oxidation and recovery systems of the oxygen-evolving complex. *Dalton Trans.* **2014**, *43*, 3063–3071.

(21) Umena, Y.; Kawakami, K.; Shen, J.-R.; Kamiya, N. Crystal structure of oxygen-evolving photosystem II at a resolution of 1.9 Å. *Nature* **2011**, *473*, 55–60.

(22) Hill R.; Bendall F. Funtion of the two Cytochrome Components in Chloroplasts: A Working Hypothesis. *Nature* **1960**, 136–137.

(23) Tachibana, Y.; Vayssieres, L.; Durrant, J. R. Artificial photosynthesis for solar water-splitting. *Nature Photon* **2012**, *6*, 511–518.

(24) Hetterscheid, D. G. H.; Reek, J. N. H. Mononuclear water oxidation catalysts. *Angew. Chem. Int. Ed.* **2012**, *51*, 9740–9747.

(25) Sala, X.; Maji, S.; Bofill, R.; García-Antón, J.; Escriche, L.; Llobet, A. Molecular water oxidation mechanisms followed by transition metals: state of the art. *Acc. Chem. Res.* **2014**, *47*, 504–516.

(26) Cao, R.; Lai, W.; Du, P. Catalytic water oxidation at single metal sites. *Energy Environ. Sci.* **2012**, *5*, 8134.

(27) Wasylenko, D. J.; Palmer, R. D.; Berlinguette, C. P. Homogeneous water oxidation catalysts containing a single metal site. *Chem. Comm.* **2013**, *49*, 218–227.

(28) Roeser, S.; Farràs, P.; Bozoglian, F.; Martínez-Belmonte, M.; Benet-Buchholz, J.; Llobet, A. Chemical, electrochemical, and photochemical catalytic oxidation of water to dioxygen with mononuclear ruthenium complexes. *ChemSusChem* **2011**, *4*, 197–207.

(29) Gersten S. W.; Samuels G. J.; Meyer T. J. Catalytic oxidation of water by an oxo-bridged ruthenium dimer. *J. Am. Chem. Soc.* **1982**, *104, 14,* 4029-4030

(30) Blakemore, J. D.; Crabtree, R. H.; Brudvig, G. W. Molecular Catalysts for Water Oxidation. *Chem. Rev.* **2015**, *115*, 12974–13005.

(31) McDaniel, N. D.; Coughlin, F. J.; Tinker, L. L.; Bernhard, S. Cyclometalated iridium(III) Aquo complexes: efficient and tunable catalysts for the homogeneous oxidation of water. *J. Am. Chem. Soc.* **2008**, *130*, 210–217.

(32) Kärkäs, M. D.; Verho, O.; Johnston, E. V.; Åkermark, B. Artificial photosynthesis: molecular systems for catalytic water oxidation. *Chem. Rev.* **2014**, *114*, 11863–12001.

(33) Harriman, A.; Pickering, I. J.; Thomas, J. M.; Christensen, P. A. Metal oxides as heterogeneous catalysts for oxygen evolution under photochemical conditions. *J. Chem. Soc., Faraday Trans. 1* **1988**, *84*, 2795.

(34) Morita, M.; Iwakura, C.; Tamura, H. The anodic characteristics of manganese dioxide electrodes prepared by thermal decomposition of manganese nitrate. *Electrochim. Acta* **1977**, *22*, 325–328.

(35) Evangelisti, F.; Güttinger, R.; Moré, R.; Luber, S.; Patzke, G. R. Closer to photosystem II: a Co4O4 cubane catalyst with flexible ligand architecture. *J. Am. Chem. Soc.* **2013**, *135*, 18734–18737.

(36) Evangelisti, F.; Moré, R.; Hodel, F.; Luber, S.; Patzke, G. R. 3d-4f {Co(II)3Ln(OR)4} Cubanes as Bio-Inspired Water Oxidation Catalysts. *J. Am. Chem. Soc.* **2015**, *137*, 11076–11084.

(37) Song, F.; Moré, R.; Schilling, M.; Smolentsev, G.; Azzaroli, N.; Fox, T.; Luber, S.; Patzke, G. R. {Co4O4} and {CoxNi4-xO4} Cubane Water Oxidation Catalysts as Surface Cut-Outs of Cobalt Oxides. *J. Am. Chem. Soc.* **2017**, *139*, 14198–14208.

(38) Wang, L.-P.; van Voorhis, T. Direct-Coupling O 2 Bond Forming a Pathway in Cobalt Oxide Water Oxidation Catalysts. *J. Phys. Chem. Lett.* **2011**, *2*, 2200–2204.

(39) Zhang, M.; Respinis, M. de; Frei, H. Time-resolved observations of water oxidation intermediates on a cobalt oxide nanoparticle catalyst. *Nat. Chem.* **2014**, *6*, 362–367.

(40) Plaisance, C. P.; van Santen, R. A. Structure Sensitivity of the Oxygen Evolution Reaction Catalyzed by Cobalt(II,III) Oxide. *J. Am. Chem. Soc.* **2015**, *137*, 14660–14672.

(41) Geletii, Y. V.; Botar, B.; Kögerler, P.; Hillesheim, D. A.; Musaev, D. G.; Hill, C. L. An all-inorganic, stable, and highly active tetraruthenium homogeneous catalyst for water oxidation. *Angew. Chem. Int. Ed.* **2008**, *47*, 3896–3899.

(42) Sartorel, A.; Carraro, M.; Scorrano, G.; Zorzi, R. de; Geremia, S.; McDaniel, N. D.; Bernhard, S.; Bonchio, M. Polyoxometalate embedding of a tetraruthenium(IV)-oxo-core by template-directed metalation of gamma-SiW10O368-: a totally inorganic oxygen-evolving catalyst. *J. Am. Chem. Soc.* **2008**, *130*, 5006–5007.

(43) Yin, Q.; Tan, J. M.; Besson, C.; Geletii, Y. V.; Musaev, D. G.; Kuznetsov, A. E.; Luo, Z.; Hardcastle, K. I.; Hill, C. L. A Fast Soluble Carbon-Free Molecular Water Oxidation Catalyst Based on Abundant Metals. *Science* **2010**, 1185372.

(44) Evangelisti, F.; Car, P.-E.; Blacque, O.; Patzke, G. R. Photocatalytic water oxidation with cobalt-containing tungstobismutates: tuning the metal core. *Catal. Sci. Technol.* **2013**, *3*, 3117.

(45) Fukuzumi, S.; Hong, D. Homogeneous versus Heterogeneous Catalysts in Water Oxidation. *Eur. J. Inorg. Chem.* **2014**, *2014*, 645–659.

(46) Wu, X.; Li, F.; Zhang, B.; Sun, L. Molecular complexes in water oxidation: Pre-catalysts or real catalysts. *J. Photochem. Photobiol. C* **2015**, *25*, 71–89.

(47) Crabtree, R. H. Deactivation in homogeneous transition metal catalysis: causes, avoidance, and cure. *Chem. Rev.* **2015**, *115*, 127–150.

(48) Fukuzumi, S.; Jung, J.; Yamada, Y.; Kojima, T.; Nam, W. Homogeneous and Heterogeneous Photocatalytic Water Oxidation by Persulfate. *Chem. Asian J.* **2016**, *11*, 1138–1150.

(49) Zhao, Y.; Swierk, J. R.; Megiatto, J. D.; Sherman, B.; Youngblood, W. J.; Qin, D.; Lentz, D. M.; Moore, A. L.; Moore, T. A.; Gust, D.*; et al.* Improving the efficiency of water splitting in dye-sensitized solar cells by using a biomimetic electron transfer mediator. *Proc. Nat. Acad. Sci. U. S. A.* **2012**, *109*, 15612–15616.

(50) Morris, N. D.; Suzuki, M.; Mallouk, T. E. Kinetics of Electron Transfer and Oxygen Evolution in the Reaction of [Ru(bpy) 3] 3+ with Colloidal Iridium Oxide. *J. Phys. Chem. A* **2004**, *108*, 9115–9119.

(51) Gustafson, K. P. J.; Shatskiy, A.; Verho, O.; Kärkäs, M. D.; Schluschass, B.; Tai, C.-W.; Åkermark, B.; Bäckvall, J.-E.; Johnston, E. V. Water oxidation mediated by ruthenium oxide nanoparticles supported on siliceous mesocellular foam. *Catal. Sci. Technol.* **2017**, *7*, 293–299.

(52) Haxel G. B.; Hedrick J. B.; Orris G. J.; Stauffer P. H.; Hendley J. W. Rare Earth Elements—Critical Resources for High Technology | USGS Fact Sheet 087-02. https://pubs.usgs.gov/fs/2002/fs087-02/ (accessed October 24, 2018).

(53) Frame, F. A.; Townsend, T. K.; Chamousis, R. L.; Sabio, E. M.; Dittrich, T.; Browning, N. D.; Osterloh, F. E. Photocatalytic water oxidation with nonsensitized IrO2 nanocrystals under visible and UV light. *J. Am. Chem. Soc.* **2011**, *133*, 7264–7267.

(54) Harriman A.; Richoux M.-C.; Christensen P. A.; Mosseri S.; Neta P. Redox Reactions with Colloidal Metal Oxides. *J. Chem. Soc. Faraday Trans.* **1987**, 3001–3014.

(55) Zhang, Y.; Judkins, E. C.; McMillin, D. R.; Mehta, D.; Ren, T. Mesoporous Silica-Supported Ruthenium Oxide Nanoparticulates as Efficient Catalysts for Photoinduced Water Oxidation. *ACS Catal.* **2013**, *3*, 2474–2478.

(56) Das, S. K.; Dutta, P. K. Synthesis and characterization of a ruthenium oxide–zeolite Y catalyst for photochemical oxidation of water to dioxygen. *Micropor. Mesopor. Mat.* **1998**, *22*, 475–483.

(57) Hong, D.; Yamada, Y.; Nagatomi, T.; Takai, Y.; Fukuzumi, S. Catalysis of nickel ferrite for photocatalytic water oxidation using Ru(bpy)32+ and S2O8(2-). *J. Am. Chem. Soc.* **2012**, *134*, 19572–19575.

(58) Deng, X.; Bongard, H.-J.; Chan, C. K.; Tüysüz, H. Dual-Templated Cobalt Oxide for Photochemical Water Oxidation. *ChemSusChem* **2016**, *9*, 409–415.

(59) Du, X.; Ding, Y.; Li, C. Morphology-Controlled Self-Assembly and Nanostructured NiO: An Efficient and Robust Photocatalytic Water-Oxidation Catalyst. *ChemCatChem* **2015**, *7*, 2370–2376.

(60) Xiang, Q.; Chen, G.; Lau, T.-C. Effects of morphology and exposed facets of α-Fe 2 O 3 nanocrystals on photocatalytic water oxidation. *RSC Adv.* **2015**, *5*, 52210–52216.

(61) Du, X.; Ding, Y.; Xiang, R.; Xiang, X. Ferromagnetic nanocrystallines containing copper as an efficient catalyst for photoinduced water oxidation. *Phys. Chem. Chem. Phys.* **2015**, *17*, 10648–10655.

(62) Yamada, Y.; Yano, K.; Hong, D.; Fukuzumi, S. LaCoO3 acting as an efficient and robust catalyst for photocatalytic water oxidation with persulfate. *Phys. Chem. Chem. Phys.* **2012**, *14*, 5753–5760.

(63) Ressnig, D.; Shalom, M.; Patscheider, J.; Moré, R.; Evangelisti, F.; Antonietti, M.; Patzke, G. R. Photochemical and electrocatalytic water oxidation activity of cobalt carbodiimide. *J. Mater. Chem. A* **2015**, *3*, 5072–5082.

(64) Hong, D.; Yamada, Y.; Nomura, A.; Fukuzumi, S. Catalytic activity of NiMnO3 for visible light-driven and electrochemical water oxidation. *Phys. Chem. Chem. Phys.* **2013**, *15*, 19125–19128.

(65) Robinson, D. M.; Go, Y. B.; Mui, M.; Gardner, G.; Zhang, Z.; Mastrogiovanni, D.; Garfunkel, E.; Li, J.; Greenblatt, M.; Dismukes, G. C. Photochemical water oxidation by crystalline polymorphs of manganese oxides: structural requirements for catalysis. *J. Am. Chem. Soc.* **2013**, *135*, 3494–3501.

(66) Zhao, Y.; Zhang, Y.; Ding, Y.; Chen, M. Hexagonal nanoplates of NiO/CoO/Fe2O3 composite acting as an efficient photocatalytic and electrocatalytic water oxidation catalyst. *Dalton Trans.* **2015**, *44*, 15628–15635.

(67) Yamada, Y.; Oyama, K.; Gates, R.; Fukuzumi, S. High catalytic activity of heteropolynuclear cyanide complexes containing cobalt and platinum ions: visible-light driven water oxidation. *Angew. Chem. Int. Ed.* **2015**, *54*, 5613–5617.

(68) Wang, X.; Maeda, K.; Thomas, A.; Takanabe, K.; Xin, G.; Carlsson, J. M.; Domen, K.; Antonietti, M. A metal-free polymeric photocatalyst for hydrogen production from water under visible light. *Nat. Mater.* **2009**, *8*, 76–80.

(69) Yamada, Y.; Oyama, K.; Suenobu, T.; Fukuzumi, S. Photocatalytic water oxidation by persulphate with a Ca2+ ion-incorporated polymeric cobalt cyanide complex affording O2 with 200% quantum efficiency. *Chem. Comm. (Cambridge, England)* **2017**, *53*, 3418–3421.

(70) Liu, H.; Patzke, G. R. Visible-light-driven water oxidation with nanoscale Co(3)O(4) : new optimization strategies. *Chem. Asian J.* **2014**, *9*, 2249–2259.

(71) Chua, C. S.; Ansovini, D.; Lee, C. J. J.; Teng, Y. T.; Ong, L. T.; Chi, D.; Hor, T. S. A.; Raja, R.; Lim, Y.-F. The effect of crystallinity on photocatalytic performance of Co3O4 water-splitting cocatalysts. *Phys. Chem. Chem. Phys.* **2016**, *18*, 5172–5178.

(72) Maegli, A. E.; Pokrant, S.; Hisatomi, T.; Trottmann, M.; Domen, K.; Weidenkaff, A. Enhancement of Photocatalytic Water Oxidation by the Morphological Control of LaTiO 2 N and Cobalt Oxide Catalysts. *J. Phys. Chem. C* **2014**, *118*, 16344–16351.

(73) Menezes, P. W.; Indra, A.; Littlewood, P.; Schwarze, M.; Göbel, C.; Schomäcker, R.; Driess, M. Nanostructured manganese oxides as highly active water oxidation catalysts: a boost from manganese precursor chemistry. *ChemSusChem* **2014**, *7*, 2202–2211.

(74) Chen, Z.; Duan, Z.; Wang, Z.; Liu, X.; Gu, L.; Zhang, F.; Dupuis, M.; Li, C. Amorphous Cobalt Oxide Nanoparticles as Active Water-Oxidation Catalysts. *ChemCatChem* **2017**, *9*, 3641–3645.

(75) Liu, H.; Zhou, Y.; Moré, R.; Müller, R.; Fox, T.; Patzke, G. R. Correlations among Structure, Electronic Properties, and Photochemical Water Oxidation: A Case Study on Lithium Cobalt Oxides. *ACS Catal.* **2015**, *5*, 3791–3800.

(76) Zhang, N.; Shi, J.; Mao, S. S.; Guo, L. Co3O4 quantum dots: reverse micelle synthesis and visible-light-driven photocatalytic overall water splitting. *Chem. Comm.* **2014**, *50*, 2002–2004.

(77) Liao, L.; Zhang, Q.; Su, Z.; Zhao, Z.; Wang, Y.; Li, Y.; Lu, X.; Wei, D.; Feng, G.; Yu, Q.*; et al.* Efficient solar water-splitting using a nanocrystalline CoO photocatalyst. *Nat. Nanotechnol.* **2014**, *9*, 69–73.

(78) Elizarova, G. L.; Zhidomirov, G. M.; Parmon, V. N. Hydroxides of transition metals as artificial catalysts for oxidation of water to dioxygen. *Catal. Today* **2000**, *58*, 71–88.

(79) Li, J.; Güttinger, R.; Moré, R.; Song, F.; Wan, W.; Patzke, G. R. Frontiers of water oxidation: the quest for true catalysts. *Chem. Soc. Rev.* **2017**, *46*, 6124–6147.

(80) Nair, V.; Deepthi, A. Cerium(IV) ammonium nitrate--a versatile single-electron oxidant. *Chem. Rev.* **2007**, *107*, 1862–1891.

(81) Wadsworth, E.; Duke, F. R.; Goetz, C. A. Present Status of Cerium(IV)-Cerium(III) Potentials. *Anal. Chem.* **1957**, *29*, 1824–1825.

(82) Parent, A. R.; Crabtree, R. H.; Brudvig, G. W. Comparison of primary oxidants for water-oxidation catalysis. *Chem. Soc. Rev.* **2013**, *42*, 2247–2252.

(83) Ikeda-Ohno, A.; Tsushima, S.; Hennig, C.; Yaita, T.; Bernhard, G. Dinuclear complexes of tetravalent cerium in an aqueous perchloric acid solution. *Dalton Trans.* **2012**, *41*, 7190–7192.

(84) Robert, A.; Meunier, B. *New J. Chem.* **1988**, 885.

(85) Limburg, J.; Crabtree, R. H.; Brudvig, G. W. Kinetic analysis of the O2-forming reaction between [Mn(III)(dpa)2]− (dpa=dipicolinate) and potassium peroxomonosulfate. *Inorganica Chim. Acta* **2000**, *297*, 301–306.

(86) Weavers, L. K.; Hua, I.; Hoffmann, M. R. Degradation of triethanolamine and chemical oxygen demand reduction in wastewater by photoactivated periodate. *Water Environ Res* **1997**, *69*, 1112–1119.

(87) Hunter, B. M.; Gray, H. B.; Müller, A. M. Earth-Abundant Heterogeneous Water Oxidation Catalysts. *Chem. Rev.* **2016**, *116*, 14120–14136.

(88) Pourbaix M. Atlas of Electrochemical Equilibria in Aqueous Solutions; *Pergamon Press:* New York, 1966.

(89) Kim, J.; Yin, X.; Tsao, K.-C.; Fang, S.; Yang, H. $Ca_2Mn_2O_5$ as oxygen-deficient perovskite electrocatalyst for oxygen evolution reaction. *J. Am. Chem. Soc.* **2014**, *136*, 14646–14649.

(90) Diaz-Morales, O.; Ledezma-Yanez, I.; Koper, M. T. M.; Calle-Vallejo, F. Guidelines for the Rational Design of Ni-Based Double Hydroxide Electrocatalysts for the Oxygen Evolution Reaction. *ACS Catal.* **2015**, *5*, 5380–5387.

(91) Pokhrel, R.; Goetz, M. K.; Shaner, S. E.; Wu, X.; Stahl, S. S. The "Best Catalyst" for Water Oxidation Depends on the Oxidation Method Employed: A Case Study of Manganese Oxides. *J. Am. Chem. Soc.* **2015**, *137*, 8384–8387.

(92) Gorlin, Y.; Jaramillo, T. F. A bifunctional nonprecious metal catalyst for oxygen reduction and water oxidation. *J. Am. Chem. Soc.* **2010**, *132*, 13612–13614.

(93) Michael E. G Lyons, Michael P Brandon. The Oxygen Evolution Reaction on Passive Oxide Covered Transition Metal Electrodes in Alkaline Solution. Part III – Iron. *Int. J. Electrochem. Sci.* **2008**, 1463–1503.

(94) Cesar, I.; Kay, A.; Gonzalez Martinez, J. A.; Grätzel, M. Translucent thin film Fe2O3 photoanodes for efficient water splitting by sunlight: nanostructure-directing effect of Si-doping. *J. Am. Chem. Soc.* **2006**, *128*, 4582–4583.

(95) Bode, H.; Dehmelt, K.; Witte, J. Zur kenntnis der nickelhydroxidelektrode—I.Über das nickel (II)-hydroxidhydrat. *Electrochim. Acta* **1966**, *11*, 1079-IN1.

(96) Młynarek, G.; Paszkiewicz, M.; Radniecka, A. The effect of ferric ions on the behaviour of a nickelous hydroxide electrode. *J. Appl. Electrochem.* **1984**, *14*, 145–149.

(97) Corrigan, D. A. The Catalysis of the Oxygen Evolution Reaction by Iron Impurities in Thin Film Nickel Oxide Electrodes. *J. Electrochem. Soc.* **1987**, *134*, 377.

(98) McCrory, C. C. L.; Jung, S.; Peters, J. C.; Jaramillo, T. F. Benchmarking heterogeneous electrocatalysts for the oxygen evolution reaction. *J. Am. Chem. Soc.* **2013**, *135*, 16977–16987.

(99) Asnavandi, M.; Yin, Y.; Li, Y.; Sun, C.; Zhao, C. Promoting Oxygen Evolution Reactions through Introduction of Oxygen Vacancies to Benchmark NiFe–OOH Catalysts. *ACS Energy Lett.* **2018**, *3*, 1515–1520.

(100) S. Trasatti. Electrochemistry and Environment: The Role of Electrocatalysis. *Int. J. Hydrogen Energy.* **1995**, 835–844.

(101) Matsumoto, Y.; Sato, E. Electrocatalytic properties of transition metal oxides for oxygen evolution reaction. *Mater. Chem. Phys.* **1986**, *14*, 397–426.

(102) Hall, D. E. Alkaline Water Electrolysis Anode Materials. *J. Electrochem. Soc.* **1985**, *132*, 41C.

(103) Esswein, A. J.; McMurdo, M. J.; Ross, P. N.; Bell, A. T.; Tilley, T. D. Size-Dependent Activity of Co 3 O 4 Nanoparticle Anodes for Alkaline Water Electrolysis. *J. Phys. Chem. C* **2009**, *113*, 15068–15072.

(104) Singh, R. N.; Mishra, D.; Anindita; Sinha, A.S.K.; Singh, A. Novel electrocatalysts for generating oxygen from alkaline water electrolysis. *Electrochem. Commun.* **2007**, *9*, 1369–1373.

(105) Gerken, J. B.; McAlpin, J. G.; Chen, J. Y. C.; Rigsby, M. L.; Casey, W. H.; Britt, R. D.; Stahl, S. S. Electrochemical water oxidation with cobalt-based electrocatalysts from pH 0-14: the thermodynamic basis for catalyst structure, stability, and activity. *J. Am. Chem. Soc.* **2011**, *133*, 14431–14442.

(106) El Wakkad, S. E. S.; Hickling, A. The anodic behaviour of metals. Part VI.—Cobalt. *Trans. Faraday Soc.* **1950**, *46*, 820–824.

(107) Kanan, M. W.; Nocera, D. G. In situ formation of an oxygen-evolving catalyst in neutral water containing phosphate and Co2+. *Science (New York, N.Y.)* **2008**, *321*, 1072–1075.

(108) Lutterman, D. A.; Surendranath, Y.; Nocera, D. G. A self-healing oxygen-evolving catalyst. *J. Am. Chem. Soc.* **2009**, *131*, 3838–3839.

(109) Fan, G.; Li, F.; Evans, D. G.; Duan, X. Catalytic applications of layered double hydroxides: recent advances and perspectives. *Chem. Soc. Rev.* **2014**, *43*, 7040–7066.

(110) Zou, X.; Goswami, A.; Asefa, T. Efficient noble metal-free (electro)catalysis of water and alcohol oxidations by zinc-cobalt layered double hydroxide. *J. Am. Chem. Soc.* **2013**, *135*, 17242–17245.

(111) You, C.; Ji, Y.; Liu, Z.; Xiong, X.; Sun, X. Ultrathin CoFe-Borate Layer Coated CoFe-Layered Double Hydroxide Nanosheets Array: A Non-Noble-Metal 3D Catalyst Electrode for Efficient and Durable Water Oxidation in Potassium Borate. *ACS Sustainable Chem. Eng.* **2018**, *6*, 1527–1531.

(112) Trotochaud, L.; Ranney, J. K.; Williams, K. N.; Boettcher, S. W. Solution-cast metal oxide thin film electrocatalysts for oxygen evolution. *J. Am. Chem. Soc.* **2012**, *134*, 17253–17261.

(113) Gong, M.; Li, Y.; Wang, H.; Liang, Y.; Wu, J. Z.; Zhou, J.; Wang, J.; Regier, T.; Wei, F.; Dai, H. An advanced Ni-Fe layered double hydroxide electrocatalyst for water oxidation. *J. Am. Chem. Soc.* **2013**, *135*, 8452–8455.

(114) Tang D.; Liu, J.; Wu, X.; Liu, R.; Han, X.; Han, Y.; Huang, H.; Liu, Y.; Kang, Z. Carbon quantum dot/NiFe layered double-hydroxide composite as a highly efficient electrocatalyst for water oxidation. *ACS Appl. Mat. Inter.***2014**, *6*, 7918–7925.

(115) Yu, X.; Zhang, M.; Yuan, W.; Shi, G. A high-performance three-dimensional Ni–Fe layered double hydroxide/graphene electrode for water oxidation. *J. Mater. Chem. A* **2015**, *3*, 6921–6928.

(116) Viswanathan, V.; Pickrahn, K. L.; Luntz, A. C.; Bent, S. F.; Nørskov, J. K. Nanoscale limitations in metal oxide electrocatalysts for oxygen evolution. *Nano Lett.* **2014**, *14*, 5853–5857.

(117) Seh, Z. W.; Kibsgaard, J.; Dickens, C. F.; Chorkendorff, I.; Nørskov, J. K.; Jaramillo, T. F. Combining theory and experiment in electrocatalysis: Insights into materials design. *Science (New York, N.Y.)* **2017**, *355*.

(118) Wang, Z.-L.; Xu, D.; Xu, J.-J.; Zhang, X.-B. Oxygen electrocatalysts in metal-air batteries: from aqueous to nonaqueous electrolytes. *Chem. Soc. Rev.* **2014**, *43*, 7746–7786.

(119) Cobo, S.; Heidkamp, J.; Jacques, P.-A.; Fize, J.; Fourmond, V.; Guetaz, L.; Jousselme, B.; Ivanova, V.; Dau, H.; Palacin, S.*; et al.* A Janus cobalt-based catalytic material for electro-splitting of water. *Nat. Mat.* **2012**, *11*, 802–807.

(120) Jiang, N.; You, B.; Sheng, M.; Sun, Y. Electrodeposited cobalt-phosphorous-derived films as competent bifunctional catalysts for overall water splitting. *Angew. Chem. Int. Ed.* **2015**, *54*, 6251–6254.

(121) Hou, Y.; Lohe, M. R.; Zhang, J.; Liu, S.; Zhuang, X.; Feng, X. Vertically oriented cobalt selenide/NiFe layered-double-hydroxide nanosheets supported on exfoliated graphene foil: an efficient 3D electrode for overall water splitting. *Energy Environ. Sci.* **2016**, *9*, 478–483.

(122) Li, K.; Zhang, J.; Wu, R.; Yu, Y.; Zhang, B. Anchoring CoO Domains on CoSe2 Nanobelts as Bifunctional Electrocatalysts for Overall Water Splitting in Neutral Media. *Adv. Sci. (Weinh.)* **2016**, *3*, 1500426.

(123) Masa, J.; Weide, P.; Peeters, D.; Sinev, I.; Xia, W.; Sun, Z.; Somsen, C.; Muhler, M.; Schuhmann, W. Amorphous Cobalt Boride (Co 2 B) as a Highly Efficient Nonprecious Catalyst for Electrochemical Water Splitting: Oxygen and Hydrogen Evolution. *Adv. Energy Mater.* **2016**, *6*.

(124) Jin, H.; Wang, J.; Su, D.; Wei, Z.; Pang, Z.; Wang, Y. In situ cobalt-cobalt oxide/N-doped carbon hybrids as superior bifunctional electrocatalysts for hydrogen and oxygen evolution. *J. Am. Chem. Soc.* **2015**, *137*, 2688–2694.

(125) Popczun, E. J.; McKone, J. R.; Read, C. G.; Biacchi, A. J.; Wiltrout, A. M.; Lewis, N. S.; Schaak, R. E. Nanostructured nickel phosphide as an electrocatalyst for the hydrogen evolution reaction. *J. Am. Chem. Soc.* **2013**, *135*, 9267–9270.

(126) Huang, Z.; Chen, Z.; Chen, Z.; Lv, C.; Meng, H.; Zhang, C. Ni12P5 nanoparticles as an efficient catalyst for hydrogen generation via electrolysis and photoelectrolysis. *ACS Nano* **2014**, *8*, 8121–8129.

(127) Feng, L.-L.; Yu, G.; Wu, Y.; Li, G.-D.; Li, H.; Sun, Y.; Asefa, T.; Chen, W.; Zou, X. High-index faceted Ni3S2 nanosheet arrays as highly active and ultrastable electrocatalysts for water splitting. *J. Am. Chem. Soc.* **2015**, *137*, 14023–14026.

(128) Martindale, B. C. M.; Reisner, E. Bi-Functional Iron-Only Electrodes for Efficient Water Splitting with Enhanced Stability through In Situ Electrochemical Regeneration. *Adv. Energy Mater.* **2016**, *6*, 1502095.

(129) Gao, X.; Zhang, H.; Li, Q.; Yu, X.; Hong, Z.; Zhang, X.; Liang, C.; Lin, Z. Hierarchical NiCo2 O4 Hollow Microcuboids as Bifunctional Electrocatalysts for Overall Water-Splitting. *Angew. Chem. Int. Ed.* **2016**, *55*, 6290–6294.

(130) Li, J.; Wang, Y.; Zhou, T.; Zhang, H.; Sun, X.; Tang, J.; Zhang, L.; Al-Enizi, A. M.; Yang, Z.; Zheng, G. Nanoparticle Superlattices as Efficient Bifunctional Electrocatalysts for Water Splitting. *J. Am. Chem. Soc.* **2015**, *137*, 14305–14312.

(131) Sivanantham, A.; Ganesan, P.; Shanmugam, S. Hierarchical NiCo 2 S 4 Nanowire Arrays Supported on Ni Foam: An Efficient and Durable Bifunctional Electrocatalyst for Oxygen and Hydrogen Evolution Reactions. *Adv. Funct. Mater.* **2016**, *26*, 4661–4672.

(132) Peng, Z.; Jia, D.; Al-Enizi, A. M.; Elzatahry, A. A.; Zheng, G. From Water Oxidation to Reduction: Homologous Ni-Co Based Nanowires as Complementary Water Splitting Electrocatalysts. *Adv. Energy Mater.* **2015**, *5*, 1402031.

(133) Li, S.; Wang, Y.; Peng, S.; Zhang, L.; Al-Enizi, A. M.; Zhang, H.; Sun, X.; Zheng, G. Co-Ni-Based Nanotubes/Nanosheets as Efficient Water Splitting Electrocatalysts. *Adv. Energy Mater.* **2016**, *6*, 1501661.

(134) McKone, J. R.; Lewis, N. S.; Gray, H. B. Will Solar-Driven Water-Splitting Devices See the Light of Day? *Chem. Mater.* **2014**, *26*, 407–414.

(135) Ardo, S.; Fernandez Rivas, D.; Modestino, M. A.; Schulze Greiving, V.; Abdi, F. F.; Alarcon Llado, E.; Artero, V.; Ayers, K.; Battaglia, C.; Becker, J.-P.*; et al.* Pathways to electrochemical solar-hydrogen technologies. *Energy Environ. Sci.* **2018**, *11*, 2768–2783.

(136) Fujishima A.; Honda K. Electrochemical Photolysis of Water. *Nature*, 37–38.

(137) Kudo, A.; Miseki, Y. Heterogeneous photocatalyst materials for water splitting. *Chem. Soc. Rev.* **2009**, *38*, 253–278.

(138) Khaselev O.; Turner J. A. A monolithic photovoltaic-photoelectrochemical device for hydrogen production via water splitting. *Science (New York, N.Y.)* **1998**, *280*, 425–427.

(139) Licht, S. Over 18% solar energy conversion to generation of hydrogen fuel; theory and experiment for efficient solar water splitting. *Int. J. Hydrog. Energy* **2001**, *26*, 653–659.

(140) Youngblood, W. J.; Lee, S.-H. A.; Kobayashi, Y.; Hernandez-Pagan, E. A.; Hoertz, P. G.; Moore, T. A.; Moore, A. L.; Gust, D.; Mallouk, T. E. Photoassisted overall water splitting in a visible light-absorbing dye-sensitized photoelectrochemical cell. *J. Am. Chem. Soc.* **2009**, *131*, 926–927.

(141) Grätzel, M. Photoelectrochemical cells. *Nature* **2001**, *414*, 338–344.

(142) Duret, A.; Grätzel, M. Visible light-induced water oxidation on mesoscopic alpha-Fe2O3 films made by ultrasonic spray pyrolysis. *J. Phys. Chem. B* **2005**, *109*, 17184–17191.

(143) O'Regan B.; Grätzel M. A low-cost, high-efficiency solar cell based on dye-sensitized colloidal TiO2 films. *Nature* **1991**, 737–740.

(144) Brimblecombe, R.; Koo, A.; Dismukes, G. C.; Swiegers, G. F.; Spiccia, L. Solar driven water oxidation by a bioinspired manganese molecular catalyst. *J. Am. Chem. Soc.* **2010**, *132*, 2892–2894.

(145) Maeda, K.; Teramura, K.; Lu, D.; Takata, T.; Saito, N.; Inoue, Y.; Domen, K. Photocatalyst releasing hydrogen from water. *Nature* **2006**, *440*, 295.

(146) Sayama, K.; Mukasa, K.; Abe, R.; Abe, Y.; Arakawa, H. Stoichiometric water splitting into H2 and O2 using a mixture of two different photocatalysts and an IO3 2/I2 shuttle redox mediator under visible light irradiation. *Chem. Commun.* **2001**, 2416–2417.

(147) Kato, H.; Hori, M.; Konta, R.; Shimodaira, Y.; Kudo, A. Construction of Z-scheme Type Heterogeneous Photocatalysis Systems for Water Splitting into H 2 and O 2 under Visible Light Irradiation. *Chem. Lett.* **2004**, *33*, 1348–1349.

(148) Abe, R.; Takata, T.; Sugihara, H.; Domen, K. Photocatalytic overall water splitting under visible light by TaON and WO3 with an IO3-/I- shuttle redox mediator. *Chem. Comm.* **2005**, 3829–3831.

(149) Higashi, M.; Abe, R.; Teramura, K.; Takata, T.; Ohtani, B.; Domen, K. Two step water splitting into H2 and O2 under visible light by ATaO2N (A=Ca, Sr, Ba) and WO3 with IO3-/I- shuttle redox mediator. *Chem. Phys. Lett.* **2008**, *452*, 120–123.

(150) Sasaki, Y.; Nemoto, H.; Saito, K.; Kudo, A. Solar Water Splitting Using Powdered Photocatalysts Driven by Z-Schematic Interparticle Electron Transfer without an Electron Mediator. *J. Phys. Chem. C* **2009**, *113*, 17536–17542.

(151) Santato, C.; Ulmann, M.; Augustynski, J. Photoelectrochemical Properties of Nanostructured Tungsten Trioxide Films. *J. Phys. Chem. B* **2001**, *105*, 936–940.

(152) Khan, S. U. M.; Akikusa, J. Photoelectrochemical Splitting of Water at Nanocrystalline n - Fe 2 O 3 Thin-Film Electrodes. *J. Phys. Chem. B* **1999**, *103*, 7184–7189.

(153) Chen, H. M.; Chen, C. K.; Liu, R.-S.; Wu, C.-C.; Chang, W.-S.; Chen, K.-H.; Chan, T.-S.; Lee, J.-F.; Tsai, D. P. A New Approach to Solar Hydrogen Production: a ZnO-ZnS Solid Solution Nanowire Array Photoanode. *Adv. Energy Mater.* **2011**, *1*, 742–747.

(154) Zhao, Q.; Yan, Z.; Chen, C.; Chen, J. Spinels: Controlled Preparation, Oxygen Reduction/Evolution Reaction Application, and Beyond. *Chem. Rev.* **2017**, *117*, 10121–10211.

(155) Bragg, W. H. The Structure of Magnetite and the Spinels. *Nature* **1915**, 561.

(156) Nishikawa, S. Structure of Some Crystals of Spinel Group. *Proc. Math. Phys. Soc.* **1915**, 199–209.

(157) Müller, U. *Inorganic structural chemistry*, 2. ed.; Inorganic chemistry; Wiley: Hoboken, N.J., 2007.

(158) Principles of General Chemistry - Chapter 23.5: Crystal Field Theory. https://2012books.lardbucket.org/books/principles-of-general-chemistry-v1.0/s27-05-crystal-field-theory.html (accessed December 4, 2018).

(159) West, A. R. *Solid State Chemistry and its Applications*, second edition; Wiley, 2014.

(160) Jeppson, P.; Sailer, R.; Jarabek, E.; Sandstrom, J.; Anderson, B.; Bremer, M.; Grier, D. G.; Schulz, D. L.; Caruso, A. N.; Payne, S. A.*; et al.* Cobalt ferrite nanoparticles: Achieving the superparamagnetic limit by chemical reduction. *J. Appl. Phys.* **2006**, *100*, 114324.

(161) Sonoyama, N.; Kawamura, K.; Yamada, A.; Kanno, R. Electrochemical Luminescence of Rare Earth Metal Ion Doped MgIn[sub 2]O[sub 4] Electrodes. *J. Electrochem. Soc.* **2006**, *153*, H45.

(162) Naveen, A. N.; Manimaran, P.; Selladurai, S. Cobalt oxide (Co3O4)/graphene nanosheets (GNS) composite prepared by novel route for supercapacitor application. *J Mater Sci: Mater Electron* **2015**, *26*, 8988–9000.

(163) Cho, Y.; Lee, S.; Lee, Y.; Hong, T.; Cho, J. Spinel-Layered Core-Shell Cathode Materials for Li-Ion Batteries. *Adv. Energy Mater.* **2011**, *1*, 821–828.

(164) Kushwaha, A. K.; Uğur, Ş.; Akbudak, S.; Uğur, G. Investigation of structural, elastic, electronic, optical and vibrational properties of silver chromate spinels: Normal (CrAg 2 O 4) and inverse (Ag 2 CrO 4). *J. Alloys Compd.* **2017**, *704*, 101–108.

(165) Reith, L.; Lienau, K.; Cook, D. S.; Moré, R.; Walton, R. I.; Patzke, G. R. Monitoring the Hydrothermal Growth of Cobalt Spinel Water Oxidation Catalysts: From Preparative History to Catalytic Activity. *Chem. Eur. J.* **2018**, 18424–18435.

(166) Kaczmarczyk, J.; Zasada, F.; Janas, J.; Indyka, P.; Piskorz, W.; Kotarba, A.; Sojka, Z. Thermodynamic Stability, Redox Properties, and Reactivity of Mn 3 O 4 , Fe 3 O 4 , and Co 3 O 4 Model Catalysts for N 2 O Decomposition: Resolving the Origins of Steady Turnover. *ACS Catal.* **2016**, *6*, 1235–1246.

(167) Molla, A. R.; Kesavulu, C. R.; Chakradhar, R.P.S.; Tarafder, A.; Mohanty, S. K.; Rao, J. L.; Karmakar, B.; Biswas, S. K. Microstructure, mechanical, thermal, EPR, and optical properties of MgAl2O4:Cr3+ spinel glass–ceramic nanocomposites. *J. Alloys Compd.* **2014**, *583*, 498–509.

(168) Yabuuchi, N.; Kubota, K.; Dahbi, M.; Komaba, S. Research development on sodium-ion batteries. *Chem. Rev.* **2014**, *114*, 11636–11682.

(169) Wu, N.; Yang, Z.-Z.; Yao, H.-R.; Yin, Y.-X.; Gu, L.; Guo, Y.-G. Improving the electrochemical performance of the li4 ti5 o12 electrode in a rechargeable magnesium battery by lithium-magnesium co-intercalation. *Angew. Chem. Int. Ed.* **2015**, *54*, 5757–5761.

(170) Zhang, N.; Cheng, F.; Liu, Y.; Zhao, Q.; Lei, K.; Chen, C.; Liu, X.; Chen, J. Cation-Deficient Spinel ZnMn2O4 Cathode in Zn(CF3SO3)2 Electrolyte for Rechargeable Aqueous Zn-Ion Battery. *J. Am. Chem. Soc.* **2016**, *138*, 12894–12901.

(171) Uchaker, E.; Cao, G. The Role of Intentionally Introduced Defects on Electrode Materials for Alkali-Ion Batteries. *Chem. Asian J.* **2015**, *10*, 1608–1617.

(172) Chen, D.; Chen, C.; Baiyee, Z. M.; Shao, Z.; Ciucci, F. Nonstoichiometric Oxides as Low-Cost and Highly-Efficient Oxygen Reduction/Evolution Catalysts for Low-Temperature Electrochemical Devices. *Chem. Rev.* **2015**, *115*, 9869–9921.

(173) Liu, G. Q.; Wen, L.; Wang, X.; Ma, B. Y. Effect of the impurity LixNi1−xO on the electrochemical properties of 5V cathode material LiNi0.5Mn1.5O4. *J. Alloys Compd.* **2011**, *509*, 9377–9381.

(174) Qiao, R.; Wang, Y.; Olalde-Velasco, P.; Li, H.; Hu, Y.-S.; Yang, W. Direct evidence of gradient Mn(II) evolution at charged states in LiNi 0.5 Mn 1.5 O 4 electrodes with capacity fading. *J. Power Sources* **2015**, *273*, 1120–1126.

(175) Shu, C.; Yang, X.; Chen, Y.; Fang, Y.; Zhou, Y.; Liu, Y. Nano-Fe 3 O 4 grown on porous carbon and its effect on the oxygen reduction reaction for DMFCs with a polymer fiber membrane. *RSC Adv.* **2016**, *6*, 37012–37017.

(176) Singh, R.; Singh, J.; Singh, A. Electrocatalytic properties of new spinel-type MMoO4 (M=Fe, Co and Ni) electrodes for oxygen evolution in alkaline solutions. *Int. J. Hydrog. Energy* **2008**, *33*, 4260–4264.

(177) Yang, Z.; Xia, G.; Simner, S. P.; Stevenson, J. W. Thermal Growth and Performance of Manganese Cobaltite Spinel Protection Layers on Ferritic Stainless Steel SOFC Interconnects. *J. Electrochem. Soc.* **2005**, *152*, A1896.

(178) Li, Y.; Maxey, E. R.; Richardson, J. W.; Ma, B. Structural and chemical evolution of Fe・Co・O based ceramics under reduction/oxidation—an in situ neutron diffraction study. *Mat. Sci. Eng. B* **2004**, *106*, 6–26.

(179) Bid, S.; Sahu, P.; Pradhan, S. K. Microstructure characterization of mechanosynthesized nanocrystalline NiFe2O4 by Rietveld's analysis. *Physica E* **2007**, *39*, 175–184.

(180) Hryha, E.; Nyborg, L. Oxide Transformation in Cr-Mn-Prealloyed Sintered Steels: Thermodynamic and Kinetic Aspects. *Metall and Mat Trans A* **2014**, *45*, 1736–1747.

(181) Nie, Y.; Li, L.; Wei, Z. Recent advancements in Pt and Pt-free catalysts for oxygen reduction reaction. *Chem. Soc. Rev.* **2015**, *44*, 2168–2201.

(182) Cady, C. W.; Gardner, G.; Maron, Z. O.; Retuerto, M.; Go, Y. B.; Segan, S.; Greenblatt, M.; Dismukes, G. C. Tuning the Electrocatalytic Water Oxidation Properties of AB 2 O 4 Spinel Nanocrystals: A (Li, Mg, Zn) and B (Mn, Co) Site Variants of LiMn 2 O 4. *ACS Catal.* **2015**, *5*, 3403–3410.

(183) Amri, A.; Jiang, Z.-T.; Pryor, T.; Yin, C.-Y.; Xie, Z.; Mondinos, N. Optical and mechanical characterization of novel cobalt-based metal oxide thin films synthesized using sol–gel dip-coating method. *Surf. Coat. Tech.* **2012**, *207*, 367–374.

(184) Shchukin, D. G.; Yaremchenko, A. A.; Ferreira, M. G. S.; Kharton, V. V. Polymer Gel Templating Synthesis of Nanocrystalline Oxide Anodes. *Chem. Mater.* **2005**, *17*, 5124–5129.

(185) Wang, S.; Ding, Z.; Wang, X. A stable ZnCo2O4 cocatalyst for photocatalytic CO2 reduction. *Chem. Comm.* **2015**, *51*, 1517–1519.

(186) Anu Prathap, M. U.; Srivastava, R. Synthesis of NiCo2O4 and its application in the electrocatalytic oxidation of methanol. *Nano Energy* **2013**, *2*, 1046–1053.

(187) Cai, S.; Zhang, D.; Shi, L.; Xu, J.; Zhang, L.; Huang, L.; Li, H.; Zhang, J. Porous Ni-Mn oxide nanosheets in situ formed on nickel foam as 3D hierarchical monolith de-NO(x) catalysts. *Nanoscale* **2014**, *6*, 7346–7353.

(188) Garg, N.; Basu, M.; Ganguli, A. K. Nickel Cobaltite Nanostructures with Enhanced Supercapacitance Activity. *J. Phys. Chem. C* **2014**, *118*, 17332–17341.

(189) Xing, Z.; Ju, Z.; Yang, J.; Xu, H.; Qian, Y. One-step hydrothermal synthesis of ZnFe2O4 nano-octahedrons as a high capacity anode material for Li-ion batteries. *Nano Res.* **2012**, *5*, 477–485.

(190) Liu, X.; Qiu, G.; Li, X. Shape-controlled synthesis and properties of uniform spinel cobalt oxide nanocubes. *Nanotechnology* **2005**, *16*, 3035–3040.

(191) Acharyya, S. S.; Ghosh, S.; Siddiqui, N.; Sivakumar Konathala, L. N.; Bal, R. Cetyl alcohol mediated synthesis of CuCr 2 O 4 spinel nanoparticles: a green catalyst for selective oxidation of aromatic C–H bonds with hydrogen peroxide. *RSC Adv.* **2015**, *5*, 4838–4843.

(192) Du, J.; Pan, Y.; Zhang, T.; Han, X.; Cheng, F.; Chen, J. Facile solvothermal synthesis of CaMn2O4 nanorods for electrochemical oxygen reduction. *J. Mater. Chem.* **2012**, *22*, 15812.

(193) Jha, A.; Mhamane, D.; Suryawanshi, A.; Joshi, S. M.; Shaikh, P.; Biradar, N.; Ogale, S.; Rode, C. V. Triple nanocomposites of CoMn2O4, Co3O4 and reduced graphene oxide for oxidation of aromatic alcohols. *Catal. Sci. Technol.* **2014**, *4*, 1771.

(194) Lei, W.; Nie, L.; Liu, S.; Zhuo, Y.; Yuan, R. Influence of annealing temperature on microstructure and lithium storage performance of self-templated Cu x Co 3−x O 4 hollow microspheres. *RSC Adv.* **2016**, *6*, 62640–62646.

(195) Singh, N. K.; Tiwari, S. K.; Anitha, K. L.; Singh, R. N. Electrocatalytic properties of spinel-type Mn x Fe 3 –x O 4 synthesized below 100 °C for oxygen evolution in KOH solutions. *J. Chem. Soc., Faraday Trans.* **1996**, *92*, 2397–2400.

(196) Alizadeh-Gheshlaghi, E.; Shaabani, B.; Khodayari, A.; Azizian-Kalandaragh, Y.; Rahimi, R. Investigation of the catalytic activity of nano-sized CuO, Co3O4 and CuCo2O4 powders on thermal decomposition of ammonium perchlorate. *Powder Technol.* **2012**, *217*, 330–339.

(197) Jin, W.; Han, X.; He, Y.; Zhang, B.; Xu, P.; Du, Y. Galvanic replacement mediated synthesis of rGO–Mn 3 O 4 –Pt nanocomposites for the oxygen reduction reaction. *RSC Adv.* **2016**, *6*, 89124–89129.

(198) Alvarez, A.; Ivanova, S.; Centeno, M. A.; Odriozola, J. A. Sub-ambient CO oxidation over mesoporous Co3O4: Effect of morphology on its reduction behavior and catalytic performance. *App. Catal. A Gen.* **2012**, *431-432*, 9–17.

(199) Jang, Y.-I.; Wang, H.; Chiang, Y.-M. Room-temperature synthesis of monodisperse mixed spinel (CoxMn1−x)3O4 powder by a coprecipitation method. *J. Mater. Chem.* **1998**, *8*, 2761–2764.

(200) Ding, R.; Qi, L.; Jia, M.; Wang, H. Facile synthesis of mesoporous spinel $NiCo_2O_4$ nanostructures as highly efficient electrocatalysts for urea electro-oxidation. *Nanoscale* **2014**, *6*, 1369–1376.

(201) Bikkarolla, S. K.; Yu, F.; Zhou, W.; Joseph, P.; Cumpson, P.; Papakonstantinou, P. A three-dimensional Mn 3 O 4 network supported on a nitrogenated graphene electrocatalyst for efficient oxygen reduction reaction in alkaline media. *J. Mater. Chem. A* **2014**, *2*, 14493–14501.

(202) Nakaoka, K.; Nakayama, M.; Ogura, K. Electrochemical Deposition of Spinel-Type Cobalt Oxide from Alkaline Solution of Co[sup 2+] with Glycine. *J. Electrochem. Soc.* **2002**, *149*, C159.

(203) Prabu, M.; Ketpang, K.; Shanmugam, S. Hierarchical nanostructured NiCo2O4 as an efficient bifunctional non-precious metal catalyst for rechargeable zinc-air batteries. *Nanoscale* **2014**, *6*, 3173–3181.

(204) George, S. M. Atomic layer deposition: an overview. *Chem. Rev.* **2010**, *110*, 111–131.

(205) Iwakura, C.; Honji, A.; Tamura, H. The anodic evolution of oxygen on Co3O4 film electrodes in alkaline solutions. *Electrochim. Acta* **1981**, *26*, 1319–1326.

(206) Trasatti, S. Electrocatalysis in the anodic evolution of oxygen and chlorine. *Electrochim. Acta* **1984**, *29*, 1503–1512.

(207) Song, K.; Cho, E.; Kang, Y.-M. Morphology and Active-Site Engineering for Stable Round-Trip Efficiency Li–O 2 Batteries: A Search for the Most Active Catalytic Site in Co 3 O 4. *ACS Catal.* **2015**, *5*, 5116–5122.

(208) Jeon, H. S.; Jee, M. S.; Kim, H.; Ahn, S. J.; Hwang, Y. J.; Min, B. K. Simple Chemical Solution Deposition of Co_3O_4 Thin Film Electrocatalyst for Oxygen Evolution Reaction. *ACS Appl. Mater. Inter.* **2015**, *7*, 24550–24555.

(209) Singh, S. K.; Dhavale, V. M.; Kurungot, S. Low surface energy plane exposed Co3O4 nanocubes supported on nitrogen-doped graphene as an electrocatalyst for efficient water oxidation. *ACS Appl. Mater. Inter.* **2015**, *7*, 442–451.

(210) Kong, F. Synthesis of rod and beadlike Co3O4 and bi-functional properties as air/oxygen electrode materials. *Electrochim. Acta* **2012**, *68*, 198–201.

(211) Wang, H.; Zhuo, S.; Liang, Y.; Han, X.; Zhang, B. General Self-Template Synthesis of Transition-Metal Oxide and Chalcogenide Mesoporous Nanotubes with Enhanced Electrochemical Performances. *Angew. Chem.* **2016**, *128*, 9201–9205.

(212) Zhou, X.; Xia, Z.; Tian, Z.; Ma, Y.; Qu, Y. Ultrathin porous Co 3 O 4 nanoplates as highly efficient oxygen evolution catalysts. *J. Mater. Chem. A* **2015**, *3*, 8107–8114.

(213) Wang, X.; Zheng, Y.; Yuan, J.; Shen, J.; Wang, A.-j.; Niu, L.; Huang, S. Uniform Deposition of Co 3 O 4 Nanosheets on Exfoliated MoS 2 Nanosheets as Advanced Catalysts for Water Splitting. *Electrochim. Acta* **2016**, *212*, 890–897.

(214) Wu, L.-K.; Hu, J.-M. A silica co-electrodeposition route to nanoporous Co3O4 film electrode for oxygen evolution reaction. *Electrochim. Acta* **2014**, *116*, 158–163.

(215) Chen, S.; Zhao, Y.; Sun, B.; Ao, Z.; Xie, X.; Wei, Y.; Wang, G. Microwave-assisted synthesis of mesoporous Co3O4 nanoflakes for applications in lithium ion batteries and oxygen evolution reactions. *ACS Appl. Mater. Inter.* **2015**, *7*, 3306–3313.

(216) Rosen, J.; Hutchings, G. S.; Jiao, F. Ordered mesoporous cobalt oxide as highly efficient oxygen evolution catalyst. *J. Am. Chem. Soc.* **2013**, *135*, 4516–4521.

(217) Zou, X.; Su, J.; Silva, R.; Goswami, A.; Sathe, B. R.; Asefa, T. Efficient oxygen evolution reaction catalyzed by low-density Ni-doped Co3O4 nanomaterials derived from metal-embedded graphitic C3N4. *Chem. Comm.* **2013**, *49*, 7522–7524.

(218) Li, Y.; Hasin, P.; Wu, Y. Ni(x)Co(3-x)O(4) nanowire arrays for electrocatalytic oxygen evolution. *Adv. Mater.* **2010**, *22*, 1926–1929.

(219) Wang, D.; Chen, X.; Evans, D. G.; Yang, W. Well-dispersed Co3O4/Co2MnO4 nanocomposites as a synergistic bifunctional catalyst for oxygen reduction and oxygen evolution reactions. *Nanoscale* **2013**, *5*, 5312–5315.

(220) Grewe, T.; Deng, X.; Tüysüz, H. Influence of Fe Doping on Structure and Water Oxidation Activity of Nanocast Co 3 O 4. *Chem. Mater.* **2014**, *26*, 3162–3168.

(221) Zhang, Q.; Wei, Z. D.; Liu, C.; Liu, X.; Qi, X. Q.; Chen, S. G.; Ding, W.; Ma, Y.; Shi, F.; Zhou, Y. M. Copper-doped cobalt oxide electrodes for oxygen evolution reaction prepared by magnetron sputtering. *Int. J. Hydrog. Energy* **2012**, *37*, 822–830.

(222) Bocca, C. Oxygen evolution on Co3O4 and Li-doped Co3O4 coated electrodes in an alkaline solution. *Int. J. Hydrog. Energy* **1999**, *24*, 699–707.

(223) Song, W.; Ren, Z.; Chen, S.-Y.; Meng, Y.; Biswas, S.; Nandi, P.; Elsen, H. A.; Gao, P.-X.; Suib, S. L. Ni- and Mn-Promoted Mesoporous Co3O4: A Stable Bifunctional Catalyst with Surface-Structure-Dependent Activity for Oxygen Reduction Reaction and Oxygen Evolution Reaction. *ACS Appl. Mater. Inter.* **2016**, *8*, 20802–20813.

(224) Yeo, B. S.; Bell, A. T. Enhanced activity of gold-supported cobalt oxide for the electrochemical evolution of oxygen. *J. Am. Chem. Soc.* **2011**, *133*, 5587–5593.

(225) Zhuang, Z.; Sheng, W.; Yan, Y. Synthesis of monodispere Au@Co3O4 core-shell nanocrystals and their enhanced catalytic activity for oxygen evolution reaction. *Adv. Mater.* **2014**, *26*, 3950–3955.

(226) Musiani, M.; Guerriero, P. Oxygen evolution reaction at composite anodes containing Co3O4 particles. *Electrochim. Acta* **1998**, *44*, 1499–1507.

(227) Suryanto, B. H. R.; Lu, X.; Zhao, C. Layer-by-layer assembly of transparent amorphous Co3O4 nanoparticles/graphene composite electrodes for sustained oxygen evolution reaction. *J. Mater. Chem. A* **2013**, *1*, 12726.

(228) Zhao, M.; Li, X.; Song, L.; Di He; Zhang, Z. Substrate-Assisted Deposition of Metal Oxides on Three-Dimensional Porous Reduced Graphene Oxide Networks as Bifunctional Hybrid Electrocatalysts for the Oxygen Evolution and Oxygen Reduction Reactions. *ChemCatChem* **2016**, *8*, 2808–2816.

(229) Kumar, K.; Canaff, C.; Rousseau, J.; Arrii-Clacens, S.; Napporn, T. W.; Habrioux, A.; Kokoh, K. B. Effect of the Oxide–Carbon Heterointerface on the Activity of Co 3 O 4 /NRGO Nanocomposites toward ORR and OER. *J. Phys. Chem. C* **2016**, *120*, 7949–7958.

(230) Liu, S.; Li, L.; Ahn, H. S.; Manthiram, A. Delineating the roles of Co 3 O 4 and N-doped carbon nanoweb (CNW) in bifunctional Co 3 O 4 /CNW catalysts for oxygen reduction and oxygen evolution reactions. *J. Mater. Chem. A* **2015**, *3*, 11615–11623.

(231) Zhang, C.; Antonietti, M.; Fellinger, T.-P. Blood Ties: Co 3 O 4 Decorated Blood Derived Carbon as a Superior Bifunctional Electrocatalyst. *Adv. Funct. Mater.* **2014**, *24*, 7655–7665.

(232) Koza, J. A.; He, Z.; Miller, A. S.; Switzer, J. A. Electrodeposition of Crystalline Co 3 O 4 —A Catalyst for the Oxygen Evolution Reaction. *Chem. Mater.* **2012**, *24*, 3567–3573.

(233) Liu, D.; Wang, X.; Wang, X.; Tian, W.; Bando, Y.; Golberg, D. Co3O4 nanocages with highly exposed {110} facets for high-performance lithium storage. *Sci. Rep.* **2013**, *3*, 2543.

(234) Risch, M.; Klingan, K.; Ringleb, F.; Chernev, P.; Zaharieva, I.; Fischer, A.; Dau, H. Water oxidation by electrodeposited cobalt oxides--role of anions and redox-inert cations in structure and function of the amorphous catalyst. *ChemSusChem* **2012**, *5*, 542–549.

(235) Zhang, Y.; Ding, F.; Deng, C.; Zhen, S.; Li, X.; Xue, Y.; Yan, Y.-M.; Sun, K. Crystal plane-dependent electrocatalytic activity of Co3O4 toward oxygen evolution reaction. *Catal. Commun.* **2015**, *67*, 78–82.

(236) Chen, Z.; Kronawitter, C. X.; Koel, B. E. Facet-dependent activity and stability of Co_3O_4 nanocrystals towards the oxygen evolution reaction. *Phys. Chem. Chem. Phys.* **2015**, *17*, 29387–29393.

(237) Gedye, R.; Smith, F.; Westaway, K.; Ali, H.; Baldisera, L.; Laberge, L.; Rousell, J. The use of microwave ovens for rapid organic synthesis. *Tetrahedron Lett.* **1986**, *27*, 279–282.

(238) Whittington, B. I.; Milestone, N. B. The mcirowave heating of zeolites. *Zeolites* **1992**, *12*, 815–818.

(239) Munshi, M. Z. A. *Handbook of Solid State Batteries and Capacitors*; WORLD SCIENTIFIC, 1995.

(240) Lan, Y.; Xie, M.; Ouyang, T.; Yue, S. Thermoelectric properties of bulk MoSi 2 synthesized by solid state microwave heating. *Mod. Phys. Lett. B* **2016**, *30*, 1650234.

(241) Choy, M.-T.; Tang, C.-Y.; Chen, L.; Law, W.-C.; Tsui, C.-P.; Lu, W. W. Microwave assisted-in situ synthesis of porous titanium/calcium phosphate composites and their in vitro apatite-forming capability. *Compos. Part B: Eng.* **2015**, *83*, 50–57.

(242) Ebadzadeh, T.; Marzban-Rad, E. Microwave hybrid synthesis of silicon carbide nanopowders. *Mater.Charact.* **2009**, *60*, 69–72.

(243) Vaidhyanathan, B.; Rao, K. J. Synthesis of Ti, Ga, and V Nitrides: Microwave-Assisted Carbothermal Reduction and Nitridation. *Chem. Mater.* **1997**, *9*, 1196–1200.

(244) Tompsett, G. A.; Conner, W. C.; Yngvesson, K. S. Microwave synthesis of nanoporous materials. *Chemphyschem* **2006**, *7*, 296–319.

(245) Rao, K. J.; Vaidhyanathan, B.; Ganguli, M.; Ramakrishnan, P. A. Synthesis of Inorganic Solids Using Microwaves. *Chem. Mater.* **1999**, *11*, 882–895.

(246) Bonaccorsi, L.; Proverbio, E. Microwave assisted crystallization of zeolite A from dense gels. *J. Cryst. Growth* **2003**, *247*, 555–562.

(247) Gash, A. E.; Tillotson, T. M.; Satcher Jr, J. H.; Hrubesh, L. W.; Simpson, R. L. New sol–gel synthetic route to transition and main-group metal oxide aerogels using inorganic salt precursors. *J. Non-Cryst. Solid,* **2001**, *285*, 22–28.

(248) Brinker C. J.; Scherer G. W. Sol-Gel Science: The Physics and Chemistry of Sol-Gel Processing. https://books.google.ch/books?hl=en&lr=&id=CND1BAAAQBAJ&oi=fnd&pg=PP1&dq=sol+gel+metal+oxide&ots=aewNE4Xedy&sig=HZK_O88_Hz-FFyTqWs8iqyM3OYo (accessed January 3, 2019).

(249) Pechini M. P. Method of preparing lead and alkaline earth titanates and niobates and coating method using the same to form a capacitor. *United States Patent 3330697* **1967**

(250) Taghizadeh, F. Fabrication and Investigation of the Magnetic Properties of Co and Co3O4 Nanoparticles. *OPJ* **2016**, *06*, 62–68.

(251) Xu, G.; Ma, H.; Zhong, M.; Zhou, J.; Yue, Y.; He, Z. Influence of pH on characteristics of BaFe12O19 powder prepared by sol–gel auto-combustion. *J. Magn. Magn. Mater* **2006**, *301*, 383–388.

(252) Vaqueiro, P.; López-Quintela, M. A. Influence of Complexing Agents and pH on Yttrium−Iron Garnet Synthesized by the Sol−Gel Method. *Chem. Mater.* **1997**, *9*, 2836–2841.

(253) Hwang, B.J.; Santhanam, R.; Liu, D.G. Effect of various synthetic parameters on purity of LiMn2O4 spinel synthesized by a sol–gel method at low temperature. *J. Power Sources* **2001**, *101*, 86–89.

(254) Danks, A. E.; Hall, S. R.; Schnepp, Z. The evolution of 'sol–gel' chemistry as a technique for materials synthesis. *Mater. Horiz.* **2016**, *3*, 91–112.

(255) Scherrer P. Bestimmung der Grösse und der Inneren Struktur von Kolloidteilchen mittels Röntgenstrahlen. *Göttinger Nachrichten Gesellschaft* **1918**, 98.

(256) Patterson, A. L. The Scherrer Formula for X-Ray Particle Size Determination. *Phys. Rev.* **1939**, *56*, 978–982.

(257) Brunauer, S.; Emmett, P. H.; Teller, E. Adsorption of Gases in Multimolecular Layers. *J. Am. Chem. Soc.* **1938**, *60*, 309–319.

(258) Brame J. A.; Griggs C. S. *Surface Area Analysis Using the Brunauer-Emmett-Teller (BET) Method: Scientific Operating Procedure Series: SOP-C*; Vicksburg, 2016.

(259) Reingruber H. *Rasterelektronenmikroskopie*, 2011.

(260) Wepf R.; Müller E.; Gramm F.; Krumeich F.; Hafner B.; Barthazy E. *Introductory Transmission Electron Microscopy Primer for Users of ScopeM-TEMs*; Zürich.

(261) Biesinger M. C.; Payne B. P.; Grosvenor A. P.; Lau L. W. M.; Gerson A. R.; Smart R. St.C. Resolving surface chemical states in XPS analysis of first row transition metals, oxides and hydroxides: Cr, Mn, Fe, Co and Ni | Elsevier Enhanced Reader. *Appl. Surf. Sci.*, 2717–2730.

(262) Wagner, C. d. Auger lines in x-ray photoelectron spectrometry. *Anal. Chem.* **1972**, *44*, 967–973.

(263) Moretti, G. Auger parameter and Wagner plot in the characterization of chemical states by X-ray photoelectron spectroscopy: a review. *J. Electron Spectrosc.* **1998**, *95*, 95–144.

(264) Dillon, C. T. Synchrotron Radiation Spectroscopic Techniques as Tools for the Medicinal Chemist: Microprobe X-Ray Fluorescence Imaging, X-Ray Absorption Spectroscopy, and Infrared Microspectroscopy. *Aust. J. Chem.* **2012**, *65*, 204.

(265) Newton, M. A.; Dent, A. J.; Evans, J. Bringing time resolution to EXAFS: recent developments and application to chemical systems. *Chem. Soc. Rev.* **2002**, *31*, 83–95.

(266) Hara, M.; Waraksa, C. C.; Lean, J. T.; Lewis, B. A.; Mallouk, T. E. Photocatalytic Water Oxidation in a Buffered Tris(2,2'-bipyridyl)ruthenium Complex-Colloidal IrO 2 System. *J. Phys. Chem. A* **2000**, *104*, 5275–5280.

(267) ATDM CO.LTD. Sodium fluorosilicate, Na2SiF6. https://atdmco.com/wiki-sodium+fluorosilicate++na2sif6-441.html (accessed January 25, 2019).

(268) Limburg, B.; Bouwman, E.; Bonnet, S. Rate and Stability of Photocatalytic Water Oxidation using [Ru(bpy) 3] 2+ as Photosensitizer. *ACS Catal.* **2016**, *6*, 5273–5284.

(269) Ghosh P. K.; Brunschwig B. S.; Chou M.; Creutz C.; Sutin N. Thermal and light-induced reduction of the ruthenium complex cation Ru(bpy)33+ in aqueous solution. *J. Am. Chem. Soc.* 1984, 106, 17, 4772-4783

(270) Akhtar, U. S.; Tae, E. L.; Chun, Y. S.; Hwang, I. C.; Yoon, K. B. Insights into Decomposition Pathways and Fate of Ru(bpy) 32+ during Photocatalytic Water Oxidation with S 2 O 82– as Sacrificial Electron Acceptor. *ACS Catal.* **2016**, *6*, 8361–8369.

(271) Hayes, S. A.; Yu, P.; O'Keefe, T. J.; O'Keefe, M. J.; Stoffer, J. O. The Phase Stability of Cerium Species in Aqueous Systems. *J. Electrochem. Soc.* **2002**, *149*, C623.

(272) Chen, J. G.; Jones, C. W.; Linic, S.; Stamenkovic, V. R. Best Practices in Pursuit of Topics in Heterogeneous Electrocatalysis. *ACS Catal.* **2017**, *7*, 6392–6393.

(273) Wei, C.; Rao, R. R.; Peng, J.; Huang, B.; Stephens, I. E. L.; Risch, M.; Xu, Z. J.; Shao-Horn, Y. Recommended Practices and Benchmark Activity for Hydrogen and Oxygen Electrocatalysis in Water Splitting and Fuel Cells. *Adv. Mater.* **2019**, e1806296.

(274) Cherevko, S.; Zeradjanin, A. R.; Keeley, G. P.; Mayrhofer, K. J. J. A Comparative Study on Gold and Platinum Dissolution in Acidic and Alkaline Media. *J. Electrochem. Soc.* **2014**, *161*, H822-H830.

(275) Song, F.; Busch, M. M.; Lassalle-Kaiser, B.; Hsu, C.-S.; Petkucheva, E.; Bensimon, M.; Chen, H. M.; Corminboeuf, C.; Hu, X. An Unconventional Iron Nickel Catalyst for the Oxygen Evolution Reaction. *ACS Cent. Sci.* **2019**, *5*, 558–568.

(276) Chen, Y.; Zhou, Q.; Zhao, G.; Yu, Z.; Wang, X.; Dou, S. X.; Sun, W. Electrochemically Inert g-C 3 N 4 Promotes Water Oxidation Catalysis. *Adv. Funct. Mater.* **2018**, *28*, 1705583.

(277) Ambrosi, A.; Pumera, M. Multimaterial 3D-Printed Water Electrolyzer with Earth-Abundant Electrodeposited Catalysts. *ACS Sustainable Chem. Eng.* **2018**, *6*, 16968–16975.

(278) Bard, A. J.; Faulkner, L. R. *Electrochemical Methods: Fundamentals and Applications*, 2nd edition; John Wiley & Sons Inc.: New York, 2001.

(279) Bagockii, V. S. *Fundamentals of electrochemistry*, 2. ed.; The Electrochemical Society series; Wiley-Interscience: Hoboken, NJ, 2006.

(280) Yan, Y.; Xia, B. Y.; Zhao, B.; Wang, X. A review on noble-metal-free bifunctional heterogeneous catalysts for overall electrochemical water splitting. *J. Mater. Chem. A* **2016**, *4*, 17587–17603.

(281) Babar, P. T.; Lokhande, A. C.; Pawar, B. S.; Gang, M. G.; Jo, E.; Go, C.; Suryawanshi, M. P.; Pawar, S. M.; Kim, J. H. Electrocatalytic performance evaluation of cobalt hydroxide and cobalt oxide thin films for oxygen evolution reaction. *Appl. Surf. Sci.* **2018**, *427*, 253–259.

(282) Jörissen, L. Bifunctional oxygen/air electrodes. *J. Power Sources* **2006**, *155*, 23–32.

(283) Bergmann, A.; Martinez-Moreno, E.; Teschner, D.; Chernev, P.; Gliech, M.; Araújo, J. F. de; Reier, T.; Dau, H.; Strasser, P. Reversible amorphization and the catalytically active state of crystalline Co3O4 during oxygen evolution. *Nat. Comm.* **2015**, *6*, 8625.

(284) Reith, L.; Lienau, K.; Triana, C. A.; Siol, S.; Patzke, G. R. Preparative History vs Driving Force in Water Oxidation Catalysis: Parameter Space Studies of Cobalt Spinels. *ACS Omega* **2019**, *4*, 15444–15456.

(285) Özer, E.; Pawolek, Z.; Kühl, S.; Nong, H.; Paul, B.; Selve, S.; Spöri, C.; Bernitzky, C.; Strasser, P. Metallic Iridium Thin-Films as Model Catalysts for the Electrochemical Oxygen Evolution Reaction (OER)—Morphology and Activity. *Surfaces* **2018**, *1*, 151–164.

(286) Najafpour, M. M.; Kaboudin, B.; Mostafalu, R.; Shahbazy, M.; Safdari, R.; Kompany-Zareh, M. A proposed mechanism to form nanosized Mn oxides from the decomposition of β-cyclodextrin-Mn complex: Toward nanosized water-splitting catalysts with special morphology. *Int. J. Hydrog. Energy* **2017**, *42*, 11187–11198.

(287) Musić, S.; Popović, S.; Maljković, M.; Dragčević, Đ. Influence of synthesis procedure on the formation and properties of zinc oxide. *J. Alloys Compd.* **2002**, *347*, 324–332.

(288) Xing, Y.; Rosner, D. E. Prediction of Spherule Size in Gas Phase Nanoparticle Synthesis. *J. Nanopart. Res.* **1999**, *1*, 277–291.

(289) Singh, A.; Spiccia, L. Water oxidation catalysts based on abundant 1st row transition metals. *Coord. Chem. Rev.* **2013**, *257*, 2607–2622.

(290) Luo, Y.; Kong, D.; Luo, J.; Wang, Y.; Zhang, D.; Qiu, K.; Cheng, C.; Li, C. M.; Yu, T. Seed-assisted synthesis of Co3O4@α-Fe2O3 core–shell nanoneedle arrays for lithium-ion battery anode with high capacity. *RSC Adv.* **2014**, *4*, 13241.

(291) Gao, R.; Yang, Z.; Zheng, L.; Gu, L.; Liu, L.; Lee, Y.; Hu, Z.; Liu, X. Enhancing the Catalytic Activity of Co 3 O 4 for Li–O 2 Batteries through the Synergy of Surface/Interface/Doping Engineering. *ACS Catal.* **2018**, *8*, 1955–1963.

(292) Wang, D.; Yu, Y.; He, H.; Wang, J.; Zhou, W.; Abruña, H. D. Template-free synthesis of hollow-structured Co3O4 nanoparticles as high-performance anodes for lithium-ion batteries. *ACS Nano* **2015**, *9*, 1775–1781.

(293) Li, W. Y.; Xu, L. N.; Chen, J. Co3O4 Nanomaterials in Lithium-Ion Batteries and Gas Sensors. *Adv. Funct. Mater.* **2005**, *15*, 851–857.

(294) Wang, R. M.; Liu, C. M.; Zhang, H. Z.; Chen, C. P.; Guo, L.; Xu, H. B.; Yang, S. H. Porous nanotubes of Co3O4: Synthesis, characterization, and magnetic properties. *Appl. Phys. Lett.* **2004**, *85*, 2080–2082.

(295) Zhou, M.; Cai, L.; Bajdich, M.; García-Melchor, M.; Li, H.; He, J.; Wilcox, J.; Wu, W.; Vojvodic, A.; Zheng, X. Enhancing Catalytic CO Oxidation over Co 3 O 4 Nanowires by Substituting Co 2+ with Cu 2+. *ACS Catal.* **2015**, *5*, 4485–4491.

(296) Iosub, A. V.; Stahl, S. S. Catalytic Aerobic Dehydrogenation of Nitrogen Heterocycles Using Heterogeneous Cobalt Oxide Supported on Nitrogen-Doped Carbon. *Org. Lett.* **2015**, *17*, 4404–4407.

(297) Zhou, X.; Liu, Z.; Wang, Y.; Ding, Y. Facet effect of Co 3 O 4 nanocrystals on visible-light driven water oxidation. *Appl. Cat. B: Environ.* **2018**, *237*, 74–84.

(298) Wang, H.-Y.; Hung, S.-F.; Chen, H.-Y.; Chan, T.-S.; Chen, H. M.; Liu, B. In Operando Identification of Geometrical-Site-Dependent Water Oxidation Activity of Spinel Co3O4. *J. Am. Chem. Soc.* **2016**, *138*, 36–39.

(299) Cordeiro, P. V. O.; Carvalho, N. M. F. Water Oxidation Reaction Catalyzed by Co 3 O 4 Treated with Organic Compounds. *Ind. Eng. Chem. Res.* **2018**, *57*, 11259–11264.

(300) Zhang, G.; Yang, J.; Wang, H.; Chen, H.; Yang, J.; Pan, F. Co3O4-δ Quantum Dots As a Highly Efficient Oxygen Evolution Reaction Catalyst for Water Splitting. *ACS Appl. Mater. Inter.* **2017**, *9*, 16159–16167.

(301) Wei, R.; Fang, M.; Dong, G.; Lan, C.; Shu, L.; Zhang, H.; Bu, X.; Ho, J. C. High-Index Faceted Porous Co3O4 Nanosheets with Oxygen Vacancies for Highly Efficient Water Oxidation. *ACS Appl. Mater. Inter.* **2018**, *10*, 7079–7086.

(302) Rosen, J.; Hutchings, G. S.; Jiao, F. Synthesis, structure, and photocatalytic properties of ordered mesoporous metal-doped Co3O4. *J. Catal.* **2014**, *310*, 2–9.

(303) Liu, Q.; Chen, Z.; Yan, Z.; Wang, Y.; Wang, E.; Wang, S.; Wang, S.; Sun, G. Crystal-Plane-Dependent Activity of Spinel Co 3 O 4 Towards Water Splitting and the Oxygen Reduction Reaction. *ChemElectroChem* **2018**, *5*, 1080–1086.

(304) Zhou, J.; Li, J.; Zhang, L.; Song, S.; Wang, Y.; Lin, X.; Gu, S.; Wu, X.; Weng, T.-C.; Wang, J.*; et al.* Highly Active Surface Structure in Nanosized Spinel Cobalt-Based Oxides for Electrocatalytic Water Splitting. *J. Phys. Chem. C* **2018**, *122*, 14447–14458.

(305) Grzelczak, M.; Zhang, J.; Pfrommer, J.; Hartmann, J.; Driess, M.; Antonietti, M.; Wang, X. Electro- and Photochemical Water Oxidation on Ligand-free Co 3 O 4 Nanoparticles with Tunable Sizes. *ACS Catal.* **2013**, *3*, 383–388.

(306) Schenk, A. S.; Eiben, S.; Goll, M.; Reith, L.; Kulak, A. N.; Meldrum, F. C.; Jeske, H.; Wege, C.; Ludwigs, S. Virus-directed formation of electrocatalytically active nanoparticle-based Co3O4 tubes. *Nanoscale* **2017**, *9*, 6334–6345.

(307) Zhang, N.; Wang, Y.; Hao, Y.-C.; Ni, Y.-M.; Su, X.; Yin, A.-X.; Hu, C.-W. Ultrathin cobalt oxide nanostructures with morphology-dependent electrocatalytic oxygen evolution activity. *Nanoscale* **2018**, *10*, 20313–20320.

(308) Zhang, R.; Zhang, Y.-C.; Pan, L.; Shen, G.-Q.; Mahmood, N.; Ma, Y.-H.; Shi, Y.; Jia, W.; Wang, L.; Zhang, X.*; et al.* Engineering Cobalt Defects in Cobalt Oxide for Highly Efficient Electrocatalytic Oxygen Evolution. *ACS Catal.* **2018**, *8*, 3803–3811.

(309) Bao, J.; Zhang, X.; Fan, B.; Zhang, J.; Zhou, M.; Yang, W.; Hu, X.; Wang, H.; Pan, B.; Xie, Y. Ultrathin Spinel-Structured Nanosheets Rich in Oxygen Deficiencies for Enhanced Electrocatalytic Water Oxidation. *Angew. Chem. Int. Ed.* **2015**, *54*, 7399–7404.

(310) Xu, L.; Jiang, Q.; Xiao, Z.; Li, X.; Huo, J.; Wang, S.; Dai, L. Plasma-Engraved Co3 O4 Nanosheets with Oxygen Vacancies and High Surface Area for the Oxygen Evolution Reaction. *Angew. Chem. Int. Ed.* **2016**, *55*, 5277–5281.

(311) Tung, C.-W.; Hsu, Y.-Y.; Shen, Y.-P.; Zheng, Y.; Chan, T.-S.; Sheu, H.-S.; Cheng, Y.-C.; Chen, H. M. Reversible adapting layer produces robust single-crystal electrocatalyst for oxygen evolution. *Nat. Comm.* **2015**, *6*, 8106.

(312) Xu, T.; Zhou, X.; Jiang, Z.; Kuang, Q.; Xie, Z.; Zheng, L. Syntheses of Nano/Submicrostructured Metal Oxides with All Polar Surfaces Exposed via a Molten Salt Route. *Cryst. Growth Des.* **2009**, *9*, 192–196.

(313) Ren, G.; Li, Y.; Guo, Z.; Xiao, G.; Zhu, Y.; Dai, L.; Jiang, L. A bio-inspired Co3O4-polypyrrole-graphene complex as an efficient oxygen reduction catalyst in one-step ball milling. *Nano Res.* **2015**, *8*, 3461–3471.

(314) Singh, R. N.; Pandey, J. P.; Singh, N. K.; Lal, B.; Chartier, P.; Koenig, J.-F. Sol-gel derived spinel MxCo3−xO4 (M=Ni, Cu; 0≤x≤1) films and oxygen evolution. *Electrochim. Acta* **2000**, *45*, 1911–1919.

(315) Ji, G.; Gong, Z.; Zhu, W.; Zheng, M.; Liao, S.; Shen, K.; Liu, J.; Cao, J. Simply synthesis of Co3O4 nanowire arrays using a solvent-free method. *J. Alloys Compd.* **2009**, *476*, 579–583.

(316) Wang, K.; Cao, Y.; Hu, J.; Li, Y.; Xie, J.; Jia, D. Solvent-Free Chemical Approach to Synthesize Various Morphological Co3O4 for CO Oxidation. *ACS Appl. Mater. Inter.* **2017**, *9*, 16128–16137.

(317) Xu, R.; Zeng, H. C. Mechanistic Investigation on Salt-Mediated Formation of Free-Standing Co 3 O 4 Nanocubes at 95 °C. *J. Phys. Chem. B* **2003**, *107*, 926–930.

(318) Zhou, K.; Liu, J.; Wen, P.; Hu, Y.; Gui, Z. Morphology-controlled synthesis of Co 3 O 4 by one step template-free hydrothermal method. *Mater. Res. Bull.* **2015**, *67*, 87–93.

(319) Jadhav, A. R.; Puguan, J. M. C.; Kim, H. Microwave-Assisted Synthesis of a Stainless Steel Mesh-Supported Co 3 O 4 Microrod Array As a Highly Efficient Catalyst for Electrochemical Water Oxidation. *ACS Sustainable Chem. Eng.* **2017**, *5*, 11069–11079.

(320) Conrad, F.; Bauer, M.; Weyeneth, S.; Zhou, Y.; Hametner, K.; Günther, D.; Patzke, G. R. Hierarchically structured copper gallium spinels through microwave hydrothermal methods. *Solid State Sci.* **2013**, *24*, 125–132.

(321) Duan, Y.; Zhang, Q.; Song, Z.; Wang, J.; Tang, X.; Liu, Q.; Zhang, T. Effect of preparation methods on the catalytic activity of Co3O4 for the decomposition of N2O. *Res. Chem. Intermed.* **2017**, *43*, 7241–7255.

(322) Hammiche-Bellal, Y.; Djadoun, A.; Meddour-Boukhobza, L.; Benadda, A.; Auroux, A.; Berger, M.-H.; Mernache, F. Effect of the preparation method on the structural and catalytic properties of spinel cobalt-iron oxide. *Mater. Chem. Phys.* **2016**, *177*, 384–397.

(323) Zhu, Z.; Lu, G.; Zhang, Z.; Guo, Y.; Guo, Y.; Wang, Y. Highly Active and Stable Co 3 O 4 /ZSM-5 Catalyst for Propane Oxidation: Effect of the Preparation Method. *ACS Catal.* **2013**, *3*, 1154–1164.

(324) Feng, C.; Zhang, J.; He, Y.; Zhong, C.; Hu, W.; Liu, L.; Deng, Y. Sub-3 nm Co3O4 nanofilms with enhanced supercapacitor properties. *ACS Nano* **2015**, *9*, 1730–1739.

(325) Jacot, R.; Moré, R.; Michalsky, R.; Steinfeld, A.; Patzke, G. R. Trends in the phase stability and thermochemical oxygen exchange of ceria doped with potentially tetravalent metals. *J. Mater. Chem. A* **2017**, *5*, 19901–19913.

(326) Ravel, B.; Newville, M. ATHENA, ARTEMIS, HEPHAESTUS: data analysis for X-ray absorption spectroscopy using IFEFFIT. *J. Synchrotron Radiat.* **2005**, *12*, 537–541.

(327) Ankudinov, A. L.; Ravel, B.; Rehr, J. J.; Conradson, S. d. Real-space multiple-scattering calculation and interpretation of x-ray-absorption near-edge structure. *Phys. Rev. B* **1998**, *58*, 7565–7576.

(328) Hadjiev, V. G.; Iliev, M. N.; Vergilov, I. V. The Raman spectra of Co 3 O 4. *J. Phys. C: Solid State Phys.* **1988**, *21*, L199-L201.

(329) Gawali, S. R.; Gandhi, A. C.; Gaikwad, S. S.; Pant, J.; Chan, T.-S.; Cheng, C.-L.; Ma, Y.-R.; Wu, S. Y. Role of cobalt cations in short range antiferromagnetic Co3O4 nanoparticles: a thermal treatment approach to affecting phonon and magnetic properties. *Sci. Rep.* **2018**, *8*, 249.

(330) Lorite, I.; Romero, J. J.; Fernández, J. F. Effects of the agglomeration state on the Raman properties of Co 3 O 4 nanoparticles. *J. Raman Spectrosc.* **2012**, *43*, 1443–1448.

(331) Hongyan, X.; Jiangtao, D.; Zhenyin, H.; Libo, G.; Qiang, Z.; Jun, T.; Binzhen, Z.; Chenyang, X. A study of the growth process of Co 3 O 4 microcrystals synthesized via a hydrothermal method. *Cryst. Res. Technol.* **2016**, *51*, 123–128.

(332) Dau, H.; Liebisch, P.; Haumann, M. X-ray absorption spectroscopy to analyze nuclear geometry and electronic structure of biological metal centers--potential and questions examined with special focus on the tetra-nuclear manganese complex of oxygenic photosynthesis. *Anal. Bioanal. Chem.* **2003**, *376*, 562–583.

(333) Sahoo, P.; Djieutedjeu, H.; Poudeu, P. F. P. Co3O4 nanostructures: the effect of synthesis conditions on particles size, magnetism and transport properties. *J. Mater. Chem. A* **2013**, *1*, 15022.

(334) Sparks, T. d.; Gurlo, A.; Bekheet, M. F.; Gaultois, M. W.; Cherkashinin, G.; Laversenne, L.; Clarke, D. R. High-temperature structure of Co3O4 : Understanding spinel inversion using in situ and ex situ measurements. *Phys. Rev. B* **2019**, *99*, 33.

(335) Linstrom, P. *NIST Chemistry WebBook, NIST Standard Reference Database 69*.

(336) Yang, J.; Liu, H.; Martens, W. N.; Frost, R. L. Synthesis and Characterization of Cobalt Hydroxide, Cobalt Oxyhydroxide, and Cobalt Oxide Nanodiscs. *J. Phys. Chem. C* **2010**, *114*, 111–119.

(337) Rodriguez, P.; Tichelaar, F. D.; Koper, M. T. M.; Yanson, A. I. Cathodic corrosion as a facile and effective method to prepare clean metal alloy nanoparticles. *J. Am. Chem. Soc.* **2011**, *133*, 17626–17629.

(338) Lopes, P. P.; Strmcnik, D.; Tripkovic, D.; Connell, J. G.; Stamenkovic, V.; Markovic, N. M. Relationships between Atomic Level Surface Structure and Stability/Activity of Platinum Surface Atoms in Aqueous Environments. *ACS Catal.* **2016**, *6*, 2536–2544.

(339) Chen, R.; Yang, C.; Cai, W.; Wang, H.-Y.; Miao, J.; Zhang, L.; Chen, S.; Liu, B. Use of Platinum as the Counter Electrode to Study the Activity of Nonprecious Metal Catalysts for the Hydrogen Evolution Reaction. *ACS Energy Lett.* **2017**, *2*, 1070–1075.

(340) Kalyanasundaram, K. Photophysics, photochemistry and solar energy conversion with tris(bipyridyl)ruthenium(II) and its analogues. *Coord. Chem. Rev.* **1982**, *46*, 159–244.

(341) Bilecka, I.; Niederberger, M. Microwave chemistry for inorganic nanomaterials synthesis. *Nanoscale* **2010**, *2*, 1358.

(342) Hilaire, S.; Süess, M. J.; Kränzlin, N.; Bieńkowski, K.; Solarska, R.; Augustyński, J.; Niederberger, M. Microwave-assisted nonaqueous synthesis of WO 3 nanoparticles for crystallographically oriented photoanodes for water splitting. *J. Mater. Chem. A* **2014**, *2*, 20530–20537.

(343) Meher, S. K.; Justin, P.; Rao, G. R. Microwave-mediated synthesis for improved morphology and pseudocapacitance performance of nickel oxide. *ACS Appl. Mater. Inter.* **2011**, *3*, 2063–2073.

(344) Nissinen, T.; Valo, T.; Gasik, M.; Rantanen, J.; Lampinen, M. Microwave synthesis of catalyst spinel MnCo2O4 for alkaline fuel cell. *J. Power Sources* **2002**, *106*, 109–115.

(345) Nissinen, T. A.; Kiros, Y.; Gasik, M.; Leskelä, M. MnCo 2 O 4 Preparation by Microwave-Assisted Route Synthesis (MARS) and the Effect of Carbon Admixture. *Chem. Mater.* **2003**, *15*, 4974–4979.

(346) Yang, M.; Huang, Q.; Jin, X. Microwave synthesis of porous ZnGaNO solid solution for improved visible light photocatalytic performance. *Solid State Sci.* **2012**, *14*, 465–470.

(347) Zhang, Z.; Yang, X.; Hedhili, M. N.; Ahmed, E.; Le Shi; Wang, P. Microwave-assisted self-doping of TiO2 photonic crystals for efficient photoelectrochemical water splitting. *ACS Appl. Mater. Inter.* **2014**, *6*, 691–696.

(348) Nüchter, M.; Ondruschka, B.; Bonrath, W.; Gum, A. Microwave assisted synthesis – a critical technology overview. *Green Chem.* **2004**, *6*, 128–141.

(349) Koziej, D.; Floryan, C.; Sperling, R. A.; Ehrlicher, A. J.; Issadore, D.; Westervelt, R.; Weitz, D. A. Microwave dielectric heating of non-aqueous droplets in a microfluidic device for nanoparticle synthesis. *Nanoscale* **2013**, *5*, 5468–5475.

(350) Moura, A. P.; Cavalcante, L. S.; Sczancoski, J. C.; Stroppa, D. G.; Paris, E. C.; Ramirez, A. J.; Varela, J. A.; Longo, E. Structure and growth mechanism of CuO plates obtained by microwave-hydrothermal without surfactants. *Adv. Powder Technol.* **2010**, *21*, 197–202.

(351) Zeng, G.; Caputo, R.; Carriazo, D.; Luo, L.; Niederberger, M. Tailoring Two Polymorphs of LiFePO 4 by Efficient Microwave-Assisted Synthesis: A Combined Experimental and Theoretical Study. *Chem. Mater.* **2013**, *25*, 3399–3407.

(352) Conrad, F.; Zhou, Y.; Yulikov, M.; Hametner, K.; Weyeneth, S.; Jeschke, G.; Günther, D.; Grunwaldt, J.-D.; Patzke, G. R. Microwave-Hydrothermal Synthesis of Nanostructured Zinc-Copper Gallates. *Eur. J. Inorg. Chem.* **2010**, *2010*, 2036–2043.

(353) Conrad, F.; Massue, C.; Kühl, S.; Kunkes, E.; Girgsdies, F.; Kasatkin, I.; Zhang, B.; Friedrich, M.; Luo, Y.; Armbrüster, M.*; et al.* Microwave-hydrothermal synthesis and characterization of nanostructured copper substituted ZnM2O4 (M = Al, Ga) spinels as precursors for thermally stable Cu catalysts. *Nanoscale* **2012**, *4*, 2018–2028.

(354) Yang Y.-P.; Liu R.-S.; Huang K.-L.; Wang L.-P.; Liu S.-Q.; Zeng W.-W. Preparation and electrochemical performance of nanosized Co3O4 via hydrothermal method. *Trans. Nonferrous Met. Soc. China*, 1334–1338.

(355) Hashemi Amiri S. E.; Vaezi M. R.; Kandjani A. E. A comparison between hydrothermally prepared Co3O4 via H2O2 assisted and calcination methods. *J. Ceram. Process. Res.* **2011**, 327–331.

(356) Artero, V.; Chavarot-Kerlidou, M.; Fontecave, M. Splitting water with cobalt. *Angew. Chem. Int. Ed.* **2011**, *50*, 7238–7266.

(357) Brimblecombe, R.; Dismukes, G. C.; Swiegers, G. F.; Spiccia, L. Chapter 9. Energy from Photosystem II: Manganese Water Oxidation Catalysts. In *Molecular solar fuels*; Wydrzynski, T. J., Ed.; RSC energy and environment series 5; RSC Publ: Cambridge, 2012; pp 249–272.

(358) Wiechen, M.; Najafpour, M. M.; Allakhverdiev, S. I.; Spiccia, L. Water oxidation catalysis by manganese oxides: learning from evolution. *Energy Environ. Sci.* **2014**, *7*, 2203.

(359) Menezes, P. W.; Indra, A.; Gutkin, V.; Driess, M. Boosting electrochemical water oxidation through replacement of Oh Co sites in cobalt oxide spinel with manganese. *Chem. Comm.* **2017**, *53*, 8018–8021.

(360) Schilling, M.; Luber, S. Computational Modeling of Cobalt-Based Water Oxidation: Current Status and Future Challenges. *Front. Chem.* **2018**, *6*, 100.

(361) Chen, C.; Zhang, C.; Dong, H.; Zhao, J. Artificial synthetic Mn(IV)Ca-oxido complexes mimic the oxygen-evolving complex in photosystem II. *Dalton Trans.* **2015**, *44*, 4431–4435.

(362) Najafpour, M. M.; Heidari, S.; Balaghi, S. E.; Hołyńska, M.; Sadr, M. H.; Soltani, B.; Khatamian, M.; Larkum, A. W.; Allakhverdiev, S. I. Proposed mechanisms for water oxidation by Photosystem II and nanosized manganese oxides. *BBA Bioenergetics* **2017**, *1858*, 156–174.

(363) Conrad, F.; Bauer, M.; Sheptyakov, D.; Weyeneth, S.; Jaeger, D.; Hametner, K.; Car, P.-E.; Patscheider, J.; Günther, D.; Patzke, G. R. New spinel oxide catalysts for visible-light-driven water oxidation. *RSC Adv.* **2012**, *2*, 3076.

(364) Gong M.; Dai H. A mini review on NiFe-based materials as highly active oxygen evolution reaction electrocatalysts. *Nano Res.* **2015**, 23–39.

(365) Hickling, A.; Hill, S. Oxygen overvoltage. Part I. The influence of electrode material, current density, and time in aqueous solution. *Discuss. Faraday Soc.* **1947**, *1*, 236.

(366) Tichenor, R. L. Nickel Oxides-Relation Between Electrochemical and Foreign Ion Content. *Ind. Eng. Chem.* **1952**, 973–977.

(367) Lu, Z.; Xu, W.; Zhu, W.; Yang, Q.; Lei, X.; Liu, J.; Li, Y.; Sun, X.; Duan, X. Three-dimensional NiFe layered double hydroxide film for high-efficiency oxygen evolution reaction. *Chem. Comm.* **2014**, *50*, 6479–6482.

(368) Miller, E. L. Electrochemical Behavior of Reactively Sputtered Iron-Doped Nickel Oxide. *J. Electrochem. Soc.* **1997**, *144*, 3072.

(369) Singh, R. N.; Singh, J. P.; Lal, B.; Thomas, M.J.K.; Bera, S. New NiFe2−xCrxO4 spinel films for O2 evolution in alkaline solutions. *Electrochim. Acta* **2006**, *51*, 5515–5523.

(370) Anindita; Singh, A.; Singh, R. N. Effect of V substitution at B-site on the physicochemical and electrocatalytic properties of spinel-type NiFe2O4 towards O2 evolution in alkaline solutions. *Int. J. Hydrog. Energy* **2010**, *35*, 3243–3248.

(371) Chanda, D.; Hnát, J.; Paidar, M.; Bouzek, K. Evolution of physicochemical and electrocatalytic properties of NiCo2O4 (AB2O4) spinel oxide with the effect of Fe substitution at the A site leading to efficient anodic O2 evolution in an alkaline environment. *Int. J. Hydrog. Energy* **2014**, *39*, 5713–5722.

(372) Duan, Y.; Sun, S.; Sun, Y.; Xi, S.; Chi, X.; Zhang, Q.; Ren, X.; Wang, J.; Ong, S. J. H.; Du, Y.*; et al.* Mastering Surface Reconstruction of Metastable Spinel Oxides for Better Water Oxidation. *Adv. Mater.* **2019**, *31*, e1807898.

(373) Kumar, M.; Awasthi, R.; Sinha, A.S.K.; Singh, R. N. New ternary Fe, Co, and Mo mixed oxide electrocatalysts for oxygen evolution. *Int. J. Hydrog. Energy* **2011**, *36*, 8831–8838.

(374) Playford, H. Y.; Hannon, A. C.; Tucker, M. G.; Lees, M. R.; Walton, R. I. Total neutron scattering investigation of the structure of a cobalt gallium oxide spinel prepared by solvothermal oxidation of gallium metal. *J. Phys-Condens. Mat.* **2013**, *25*, 454212.

(375) Liu, H.; Moré, R.; Grundmann, H.; Cui, C.; Erni, R.; Patzke, G. R. Promoting Photochemical Water Oxidation with Metallic Band Structures. *J. Am. Chem. Soc.* **2016**, *138*, 1527–1535.

(376) Metallic, Covalent and Ionic Radii(r)*. http://www.wiredchemist.com/chemistry/data/metallic-radii (accessed April 24, 2019).

(377) Casado, P. G.; Rasines, I. Crystal data for the spinels MGa 2 O 4 (M = Mg, Mn). *Zeitschrift für Kristallographie* **1982**, *160*, 33–37.

(378) Christensen, A. N.; Norby, P.; Hanson, J. C. A synchrotron X-ray powder diffraction study of CoAl2O4 and CoGa2O4 by PSD diffractometer technique. *Powder Diffr.* **1995**, *10*, 185–188.

(379) Kaufman, G. B. Inorganic chemistry: principles of structure and reactivity, 4th ed. (Huheey, James E.; Keiter, Ellen A.; Keiter, Richard L.). *J. Chem. Educ.* **1993**, *70*, A279.

(380) Antoni, H.; Xia, W.; Masa, J.; Schuhmann, W.; Muhler, M. Tuning the oxidation state of manganese oxide nanoparticles on oxygen- and nitrogen-functionalized carbon nanotubes for the electrocatalytic oxygen evolution reaction. *Phys. Chem. Chem. Phys.* **2017**, *19*, 18434–18442.

(381) 4.3: Latimer and Frost diagrams. https://chem.libretexts.org/Bookshelves/Inorganic_Chemistry/Book%3A_Inorganic_Chemistry_(Wikibook)/Chapter_04%3A_Redox_Stability_and_Redox_Reactions/4.3%3A_Latimer_and_Frost_diagrams (accessed April 24, 2019).

(382) Benedek, R. Role of Disproportionation in the Dissolution of Mn from Lithium Manganate Spinel. *J. Phys. Chem. C* **2017**, *121*, 22049–22053.

(383) Housecroft, C. E.; Sharpe, A. G. *Anorganische Chemie*, 2., aktualisierte Aufl. [der engl. Ausg.], [Nachdr.]; Che - Chemie; Pearson- Studium: München, 2008], c 2006.

(384) McCloy, J. S.; Jiang, W.; Bennett, W.; Engelhard, M.; Lindemuth, J.; Parmar, N.; Exarhos, G. J. Electrical and Magnetic Properties Modification in Heavy Ion Irradiated Nanograin Ni x Co (3– x) O 4 Films. *J. Phys. Chem. C* **2015**, *119*, 22465–22476.

(385) Wang, L.; Maxisch, T.; Ceder, G. A First-Principles Approach to Studying the Thermal Stability of Oxide Cathode Materials. *Chem. Mater.* **2007**, *19*, 543–552.

(386) Kuboon, S.; Hu, Y. H. Study of NiO−CoO and Co 3 O 4 −Ni 3 O 4 Solid Solutions in Multiphase Ni−Co−O Systems. *Ind. Eng. Chem. Res.* **2011**, *50*, 2015–2020.

(387) Buckett, M. I.; Marks, L. d. Formation of a Ni3O4 Spinel Phase on the Surface of NiO During Electron Irradiation. *MRS Proc.* **1988**, *129*, 191.

(388) Fleet, M. E. The structure of magnetite. *Acta Crystallogr B Struct Crystallogr Cryst Chem* **1981**, *37*, 917–920.

(389) Picard, J. P.; Baud, G.; Besse, J. P.; Chevalier, R. Croissance cristalline et étude structurale de Co3O4. *J. Less Common Met.* **1980**, *75*, 99–104.


CMSZH
GRADUATE SCHOOL
CHEMICAL MOLECULAR SCIENCES ZURICH